

# Étalonnage du calorimètre électromagnétique ATLAS et mesure des propriétés du Boson $W$ à $\sqrt{s} = 5$ et $13$ TeV avec le détecteur ATLAS au LHC.

Hicham Atmani

## ► To cite this version:

Hicham Atmani. Étalonnage du calorimètre électromagnétique ATLAS et mesure des propriétés du Boson  $W$  à  $\sqrt{s} = 5$  et  $13$  TeV avec le détecteur ATLAS au LHC.. Physique des Hautes Energies - Expérience [hep-ex]. Université Paris-Saclay, 2020. Français. NNT: 2020UPASP070 . tel-03224873

HAL Id: tel-03224873

<https://tel.archives-ouvertes.fr/tel-03224873>

Submitted on 12 May 2021

**HAL** is a multi-disciplinary open access archive for the deposit and dissemination of scientific research documents, whether they are published or not. The documents may come from teaching and research institutions in France or abroad, or from public or private research centers.

L'archive ouverte pluridisciplinaire **HAL**, est destinée au dépôt et à la diffusion de documents scientifiques de niveau recherche, publiés ou non, émanant des établissements d'enseignement et de recherche français ou étrangers, des laboratoires publics ou privés.

# Calibration of the ATLAS Electromagnetic Calorimeter and Measurement of W Boson Properties at $\sqrt{s} = 5$ and 13 TeV with the ATLAS Detector at the LHC

## Thèse de doctorat de l'Université Paris-Saclay

École doctorale n° 576, Particules, Hadrons, Énergie, Noyau,  
Instrumentation, Imagerie, Cosmos, Simulation (PHENIICS)

Spécialité de doctorat: La physique des particules.

Unité de recherche: Université Paris-Saclay, CNRS, IJCLab,  
91405, Orsay, France.

Référent: Faculté des sciences d'Orsay.

Thèse présentée et soutenue à Orsay, le 03/12/2020, par

## HICHAM ATMANI

### Composition du jury:

<b>Maire-Hélène Schune</b>	Présidente de jury
Directrice de recherche, Université Paris-Saclay (IJCLAB)	
<b>Alexandre Glazov</b>	Rapporteur
Chercheur, Desy Laboratory	
<b>Aram Apyan</b>	Rapporteur
Research Associate, Fermi Laboratory	
<b>Anne-Catherine Le Bihan</b>	Examinateuse
Chargée de recherche, l'Université de Strasbourg (IPHC)	
<b>Maarten Boonekamp</b>	Examinateur
Directeur de Recherche, CEA Saclay	
<b>Zhiqing ZHANG</b>	Directeur de thèse
Directeur de recherche, Université Paris-Saclay (IJCLAB)	
<b>Louis FAYARD</b>	Co-directeur de thèse
Directeur de recherche, Université Paris-Saclay (IJCLAB)	

**Titre:** Étalonnage du calorimètre électromagnétique ATLAS et mesure des propriétés du Boson  $W$  à  $\sqrt{s} = 5$  et  $13$  TeV avec le détecteur ATLAS au LHC.

**Mots clés:** Masse, Mesure de précision, Boson  $W$ , ATLAS, LHC

**Résumé:** Cette thèse se compose de deux parties principales. La première partie correspond à un étalonnage in-situ du calorimètre électromagnétique à l'aide d'électrons et de positrons provenant de désintégrations du boson  $Z$  sélectionnées parmi toutes les données nominales collectées par ATLAS lors du Run 2 entre 2015 et 2018, ainsi que pendant des runs spéciaux, caractérisés par un faible nombre d'interactions par croisement afin d'améliorer la résolution expérimentale de la mesure du recul des bosons  $Z$  et  $W$  et de la reconstruction des différentes variables cinématiques nécessaires à la détermination de la masse du boson  $W$ . Les

données nominales ont été collectées à une énergie dans le centre de masse de  $13$  TeV correspondant à une luminosité intégrée d'environ  $140 \text{ fb}^{-1}$ , alors que les runs spéciaux ont été collectés à  $5$  et  $13$  TeV, correspondant à  $258 \text{ pb}^{-1}$  et  $340 \text{ pb}^{-1}$ , respectivement. La deuxième partie porte sur la mesure des propriétés du boson  $W$  à l'aide des données des runs spéciaux, y compris une mesure de l'impulsion transverse du boson  $W$ , des mesures des sections efficaces fiducielles, simple et double différentielles, et une évaluation préliminaire des incertitudes statistiques et systématiques expérimentales sur la détermination de la masse du boson  $W$ .

**Title:** Calibration of the ATLAS Electromagnetic Calorimeter and Measurement of  $W$  Boson Properties at  $\sqrt{s} = 5$  and  $13$  TeV with the ATLAS Detector at the LHC.

**Keywords:** Mass, Precision measurement,  $W$  boson, ATLAS, LHC

**Abstract:** This thesis consists of two main parts. The first part corresponds to an in-situ calibration of the electromagnetic calorimeter using electrons and positrons from  $Z$  boson decays selected from all nominal data samples taken by ATLAS during Run 2 between 2015 and 2018, as well as during special runs, characterised by a low number of interactions per bunch crossing in order to improve the experimental resolution of the recoil measurement of  $Z$  and  $W$  bosons and of the reconstruction of various kinematic variables needed for the  $W$  boson mass determination. The nominal data

samples were taken at a center of mass energy of  $13$  TeV corresponding to an integrated luminosity of about  $140 \text{ fb}^{-1}$ , whereas the special runs were taken at  $5$  and  $13$  TeV, corresponding to  $258 \text{ pb}^{-1}$  and  $340 \text{ pb}^{-1}$ , respectively. The second part is on the measurement of  $W$  boson properties using data from the special runs, including a measurement of the transverse momentum of the  $W$  boson, a measurement of fiducial, single and double differential cross sections, and a preliminary evaluation of the statistical and experimental uncertainties of the  $W$  mass determination.

# 1 Introduction

2 After the discovery of  $W$  and  $Z$  bosons at the Super Proton Synchrotron (SPS) at  
 3 CERN, particles responsible of weak interactions, the efforts have been geared to-  
 4 wards measuring their properties with high precision to test the consistency of the  
 5 Standard Model. The Standard Model has 25 free parameters to describe particles  
 6 and their interactions, some of them are measured directly, sometimes with great  
 7 precision, the other parameters are constrained by the measurement of physical  
 8 quantities related by the theory. For example, the  $W$  boson mass  $M_W$ , by includ-  
 9 ing radiative corrections, is related to the masses of the  $Z$  boson, Higgs boson and  
 10 quark top. The  $Z$  boson mass is measured with high precision at LEP experiments,  
 11 and after the discovery of the Higgs boson in 2012 at the LHC, the  $W$  boson mass  
 12 can be predicted theoretically and the comparison between the predicted and mea-  
 13 sured values is considered as a solid test for the consistency of the Standard Model.  
 14

15 This thesis describes the measurement of the  $W$  boson properties using data  
 16 collected with the ATLAS detector at the LHC at a center-of-mass energy of 5 and  
 17 13 TeV, corresponding to an integrated luminosity of  $258 \text{ pb}^{-1}$  at  $\sqrt{s} = 5 \text{ TeV}$  and  
 18  $340 \text{ pb}^{-1}$  at  $\sqrt{s} = 13 \text{ TeV}$ . The data used are collected using special runs, with low  
 19 number of interactions per bunch crossing, in order to improve the experimental  
 20 resolution of the recoil measurement and the reconstruction of the missing trans-  
 21 verse momentum and of the transverse mass. In this work, we are interested in the  
 22 leptonic decays of the  $W$  boson, and the charged products of this decay, electron or  
 23 muon, are accompanied by a neutrino. The neutrino can not be measured directly  
 24 in the detector but can be measured indirectly using the lepton and the hadronic  
 25 system which recoils against the  $W$  boson.  
 26

27 Chapter 1 describes the Standard Model with a brief review of the spontaneous  
 28 symmetry breaking mechanism. Also the  $W$  boson production in  $pp$  collisions at  
 29 the LHC is described. Finally, a brief history of  $W$  boson mass measurements is  
 30 given, focusing on last results published by the ATLAS collaboration, with a de-  
 31 scription of all the dominant sources of uncertainties.  
 32

33 Chapter 2 briefly describes the LHC machine, gives a review of the LHC ac-  
 34 celeration chain and describes the machine performance. Then, the ATLAS de-  
 35 tector is described with its different parts focusing mainly on the electromagnetic  
 36 calorimeter, an important element of this thesis.  
 37

38 Chapter 3 gives a detailed explanation of the calibration procedure of electro-  
 39 magnetic particles, electrons and photons, in the ATLAS detector. To reach a high  
 40 precision in our measurement, a precise calibration of electron energy is required.  
 41 My personal contribution is basically the extraction of the energy scale factors, re-  
 42 sponsible of the correction of the mis-calibration of the electromagnetic calorime-  
 43 ter, for the nominal runs collected during Run 2, and for special runs collected  
 44 with low number of interactions per bunch crossing, to be used in a precise mea-  
 45 surement of the  $W$  mass. For the special runs, and because of the low statistics, we

46 proposed a new approach for the extraction of the energy scale factors.

47  
48 Chapter 4 presents a theoretical description of the unfolding problem, focusing  
49 on the iterative Bayesian unfolding method used in the high energy physics to cor-  
50 rect undesired detector effects. The unfolding is used in the measurement of the  
51 transverse momentum of the  $W$  boson, the measurement of the differential cross  
52 sections and the measurement of the  $W$  boson mass.

53  
54 Chapter 5 gives a detailed study on the measurement of the  $W$ -boson trans-  
55 verse momentum distribution at 5 and 13 TeV. A precise measurement of  $p_T^W$  will  
56 provide a direct comparison with predictions, and a direct measurement may re-  
57 duce the QCD modeling uncertainties by a factor of two. My personal contribu-  
58 tion concerns the unfolding of distributions at the detector level, the propagation  
59 of uncertainties through the unfolding, the estimation of the unfolding bias (a bias  
60 introduced with the unfolding procedure), and finally an optimisation study of  
61 one of the unfolding parameters.

62  
63 Chapter 6 reports results for the measurement of the  $W$  boson fiducial cross  
64 sections using the unfolded distributions of  $p_T^W$ .

65  
66 Chapter 7 presents detailed studies of the measurement of differential and dou-  
67 ble differential cross section of the  $W$  boson at 5 and 13 TeV. The measurements are  
68 based on the unfolded distributions of  $p_T^\ell$  and  $\eta_\ell$ . My personal contribution is the  
69 unfolding of  $p_T^\ell$  and  $\eta_\ell$  distributions at the detector level and the estimation of the  
70 corresponding uncertainties.

71  
72 Chapter 8 gives preliminary results for the uncertainties of the  $W$  boson mass  
73 determination, using the template method introduced in Run 1, focusing on the  
74 statistical and systematic experimental uncertainties.

## 75 0.1 Résumé

76 **Motivation.** Au 20<sup>e</sup> siècle, les physiciens ont commencé à construire un modèle  
77 qui décrit toutes les particules de la nature et leurs interactions, à l’exception de  
78 celles dues à la gravité, que l’on appelle le modèle standard. Ce modèle est la com-  
79 binaison de deux théories qui décrivent les particules et leurs interactions dans un  
80 cadre unique. Les deux composantes du modèle standard sont la théorie électro-  
81 faible, qui décrit les interactions via les forces électromagnétiques et faibles, et la  
82 chromodynamique quantique (QCD), la théorie de la force nucléaire forte. Ces  
83 deux théories sont des théories de champ de jauge, qui décrivent les interactions  
84 entre particules en termes d’échange de particules intermédiaires «messagères».  
85 Avec le développement technologique au début des années 1970, des expériences  
86 ont été construites pour étudier les particules du modèle standard et leurs interac-  
87 tions.

88

89 Après la découverte des bosons  $W$  et  $Z$  au Super Synchrotron à Protons du  
90 CERN, particules responsables d’interactions faibles, les efforts ont été orientés  
91 vers la mesure de leurs propriétés avec une grande précision pour tester la co-  
92 hérence du modèle standard. Le modèle standard dispose de 25 paramètres libres  
93 pour décrire les particules et leurs interactions, certains d’entre eux sont mesurés  
94 directement, parfois avec une grande précision, les autres paramètres sont con-  
95 traints par la mesure des grandeurs physiques liées par la théorie. Par exemple, la  
96 masse  $M_W$  du boson  $W$ , en incluant des corrections radiatives, est liée aux masses  
97 du boson  $Z$ , du boson de Higgs et du quark top. La masse du boson  $Z$  est mesurée  
98 avec une grande précision par les expériences LEP, et après la découverte du boson  
99 de Higgs en 2012 au LHC, la masse du boson  $W$  peut être prédite théoriquement  
100 et la comparaison entre les valeurs prédites et mesurées est considérée comme un  
101 test solide pour la cohérence du modèle standard.

102

103 Cette thèse décrit la mesure des propriétés du boson  $W$  à partir de données col-  
104 lectées avec le détecteur ATLAS au LHC à deux énergies dans le centre de masse  
105 de 5 et 13 TeV, correspondant à une luminosité intégrée de  $258 \text{ pb}^{-1}$  à  $\sqrt{s} = 5 \text{ TeV}$   
106 et  $340 \text{ pb}^{-1}$  à  $\sqrt{s} = 13 \text{ TeV}$ . Les données utilisées sont collectées à l’aide des runs  
107 spéciaux, avec un faible nombre d’interactions par croisement, afin d’améliorer la  
108 résolution expérimentale de la mesure du recul et la reconstruction de l’impulsion  
109 transverse manquante et de la masse transverse. Dans ce travail, nous nous in-  
110 téressons aux désintégrations leptонiques du boson  $W$ , et les produits chargés  
111 de cette désintégration, électron ou muon, sont accompagnés d’un neutrino. Le  
112 neutrino ne peut pas être mesuré directement dans le détecteur mais peut être  
113 mesuré indirectement à l’aide du lepton et du système hadronique qui recule con-  
114 tre le boson  $W$ . Cette thèse est divisée en deux parties, la première partie étudie  
115 la calibration du calorimètre électromagnétique du détecteur ATLAS, utilisé pour  
116 déterminer l’énergie des électrons et des photons avec une grande précision. La

117 deuxième partie est consacrée à la mesure des propriétés du boson  $W$ .

118  
119 **Le calorimètre électromagnétique du détecteur ATLAS au LHC.** Le LHC est  
120 un collisionneur de particules à haute énergie, approuvé en 1996, avec les premiers  
121 faisceaux en 2008 à l'organisation européenne pour la recherche nucléaire (CERN)  
122 à la frontière entre la France et la Suisse. Avec une circonférence de 27 km et qua-  
123 tre points d'interaction pour quatre grandes expériences (ATLAS, CMS, ALICE  
124 et LHCb), le LHC est actuellement le plus grand et le plus puissant accélérateur  
125 de la planète. Le LHC est conçu pour accélérer deux faisceaux de protons à plus  
126 de 99,99% de la vitesse de la lumière, qui se déplacent dans des directions op-  
127 posées autour de l'accélérateur et entrent en collision aux emplacements des qua-  
128 tre expériences principales. ATLAS (A Toroidal LHC ApparatuS) est un détecteur  
129 polyvalent développé pour étudier différents programmes de physique : interac-  
130 tions électrofaible, production du boson de Higgs, QCD et signatures possibles  
131 de la physique au-delà du modèle standard. Le détecteur ATLAS est situé à 100  
132 mètres sous terre au premier point d'interaction du LHC, d'environ 44 mètres de  
133 long et 25 mètres de diamètre, pesant environ 7 000 tonnes. Le détecteur ATLAS  
134 est composé de différents sous-détecteurs qui présentent une couverture uniforme  
135 autour du tube de faisceau et mesurent différentes propriétés des particules dans  
136 les collisions proton-proton au LHC. Près du centre, nous commençons par les  
137 détecteurs de trace internes, qui mesurent les trajectoires des particules chargées  
138 à proximité du point d'interaction. Les calorimètres électromagnétiques (EM) et  
139 hadroniques, qui mesurent l'énergie déposée par les électrons, les photons et les  
140 jets hadroniques. Les calorimètres sont entourés par le spectromètre à muons, la  
141 couche la plus externe, qui est conçu pour mesurer la trajectoire des muons.

142  
143 Les particules électromagnétiques, électrons et photons, sont utilisées essen-  
144 tiellement dans toutes les analyses notamment dans les études des propriétés du  
145 boson de Higgs et dans la mesure de précision des paramètres électrofaible tels que  
146 la masse du boson  $W$ , permettant un test de cohérence pour le modèle standard.  
147 Les particules électromagnétiques sont arrêtées et mesurées dans le calorimètre  
148 EM. Pour atteindre une bonne précision dans nos mesures, un étalonnage précis  
149 de l'énergie des électrons et des photons est nécessaire. La procédure d'étalonnage  
150 est basée sur des échantillons  $Z \rightarrow ee$ , en raison des statistiques élevées et de  
151 l'état final propre qui caractérise ce canal. Dans cette thèse, nous discuterons de  
152 l'étalonnage de l'énergie des électrons et des photons pour les données nominales  
153 en utilisant un étalonnage "in-situ" du calorimètre EM. L'idée principale de cette  
154 méthode est de comparer les distributions de la masse invariante  $m_{ee}$  des données  
155 et de la simulation, et en utilisant cette comparaison nous pouvons déduire deux  
156 facteurs de correction que nous appliquons aux données et aux simulations pour  
157 la calibration du calorimètre électromagnétique. En plus des runs appelés runs  
158 nominaux, on discute aussi de la calibration des runs spéciaux, utilisé pour des  
159 mesures de précision, caractérisés par un faible nombre d'interactions par croise-  
160 ment ( $\mu \approx 2$ ). Pour ces runs, nous proposons deux approches différentes pour  
161 l'étalonnage des énergies des électrons, la première est similaire à ce que nous  
162 faisons pour les runs nominaux, la seconde consiste à faire une extrapolation des  
163 résultats des runs nominaux, ce qui permet de réduire les incertitudes statistiques.

164

165 **La mesure de la distribution d'impulsion transverse du boson  $W$ .** L'une des  
 166 sources d'incertitudes théoriques la plus importante dans la mesure de la masse  
 167 du boson  $W$  est l'extrapolation de la distribution en  $p_T$  du boson  $Z$  au boson  $W$  ( $\approx$   
 168 6 MeV), où les prédictions d'ordre supérieur de la QCD ne sont pas suffisamment  
 169 précises pour décrire les données. Une mesure précise du  $p_T^W$  fournira une com-  
 170 paraison directe avec les prédictions QCD, cela revient à dire que le remplacement  
 171 de l'extrapolation théorique de  $p_T^Z$  par une telle mesure directe de la distribution  
 172  $p_T^W$  améliorera la précision de la mesure de  $M_W$ . La mesure de la distribution du  
 173  $p_T^W$  dans la région du  $p_T^W$  faible ( $p_T^W < 30$  GeV) avec une incertitude  $\sim 1\%$  dans un  
 174 bin de 5 GeV réduira l'incertitude de modélisation QCD dans la mesure de  $M_W$   
 175 d'un facteur deux. La distribution de  $p_T^W$  est reconstruite à l'aide d'événements  
 176  $W \rightarrow \ell\nu$ , où les leptons chargés sont mesurés dans les différents détecteurs de  
 177 trace ou dans le calorimètre EM, tandis que le neutrino quitte le détecteur sans  
 178 être directement mesuré. C'est la raison pour laquelle, la distribution  $p_T^W$  est re-  
 179 construite par le recul hadronique,  $u_T$ , défini comme la somme vectorielle de tous  
 180 les dépôts d'énergie à l'exclusion de l'énergie du lepton. L'impulsion transverse  
 181 du boson  $W$  est définie par:

$$\vec{p}_T^W = -\vec{u}_T. \quad (1)$$

182 Dans la plupart des cas, les distributions des observables physiques sont affectées  
 183 par des effets de détecteur: efficacité limitée, migration entre les bins etc. Dans  
 184 cette thèse on discute de la mesure de la distribution d'impulsion transverse du  
 185 boson  $W$  et de la correction des effets indésirables du détecteur avec la méthode  
 186 d'unfolding. L'utilisation de la technique d'unfolding en physique des hautes én-  
 187 ergies permet d'obtenir des résultats indépendants des effets de détection et de  
 188 reconstruction. Par conséquent, les résultats d'unfolding peuvent être comparés  
 189 directement à des prédictions théoriques ou à d'autres expériences.

190

191 L'idée principale de l'unfolding consiste à construire une matrice à partir de la  
 192 simulation, appelée matrice de migration, qui contient des informations au niveau  
 193 de la vérité et de la reconstruction. L'application de l'inverse de la matrice de  
 194 migration à la distribution des données permet de passer au niveau de la vérité  
 195 correspondant aux données, qui ne contient aucun effet de détecteur. Aussi cette  
 196 thèse discute la propagation des différents sources d'incertitude par l'unfolding,  
 197 en utilisant des techniques de bootstrapping, fit, etc. Au final, les résultats pour  
 198 la mesure du  $p_T^W$  après l'unfolding sont comparés aux différentes prédictions  
 199 théoriques.

200

201 Les distributions d'impulsion transverse du boson  $W$ ,  $p_T^W$ , sont utilisées aussi  
 202 pour la mesure des sections efficaces fiducielles, ce qui permet de comparer nos ré-  
 203 sultats avec les prédictions disponibles, incluant les corrections de QCD (NNLO)  
 204 et EW (NLO). Les sections efficaces sont mesurées en utilisant deux méthodes :  
 205 une avec la correction bin-par-bin qui consiste à appliquer un factor  $C_i$ , déduit  
 206 de la comparaison des niveaux vérité et reconstruit de la simulation. Alors que la  
 207 deuxième consiste à utiliser les distributions d'unfolding.

208

209 **Mesure des sections efficaces simple et double différentielles.** Les sections

210 efficaces différentielles sont mesurées en fonction de différentes variables ( $\eta_\ell, p_T^\ell$ )  
211 en utilisant les distributions après l'unfolding. La mesure des sections efficaces  
212 différentes dans ce processus fournit des tests rigoureux de la théorie QCD,  
213 cruciaux pour une compréhension approfondie et la modélisation des interactions  
214 QCD. De plus, la dépendance en fonction de la rapidité de la production de boson  
215  $W$  dans le processus Drell–Yan fournit des contraintes sur les fonctions de distribu-  
216 tion des partons (PDFs), qui sont actuellement la source d'incertitude dominante  
217 dans la mesure de la masse  $W$  ( $\approx 9,2$  MeV).

218 En parallèle, un unfolding à 2 dimensions est réalisé pour mesurer les sections  
219 efficaces double différentielles dans les bins de ( $\eta_\ell - p_T^\ell$ ). Une technique est util-  
220 isée pour transférer l'unfolding bidimensionnel à un unfolding unidimensionnel  
221 tel qu'utilisé pour les sections efficaces différentielles de  $\eta_\ell$  et  $p_T^\ell$  séparément. Dans  
222 les deux cas, les différentes sources d'incertitudes (statistiques, systématiques et bi-  
223 ais) sont propagées par l'unfolding en utilisant la même approche que celle de  
224 l'analyse de  $p_T^W$ .

225 **La mesure de la masse du boson  $W$ .** Le boson  $W$  est une particule instable qui  
226 se désintègre en un lepton chargé et un neutrino. La masse du boson  $W$  est déter-  
227 minée en utilisant les distributions de la masse transverse du boson  $W$  ( $m_T^W$ ) et de  
228 l'impulsion transverse du lepton ( $p_T^\ell$ ). L'idée de base de la méthode, appelée "tem-  
229 plates" (utilisée pour le Run 1), consiste à calculer les distributions simulées par  
230 Monte Carlo (MC) de  $p_T^\ell$  et  $m_T^W$  pour différentes valeurs supposées de  $M_W$  ("tem-  
231 plates"), et la comparaison entre les "templates" et les données donne la meilleure  
232 valeur de la masse du boson  $W$ . En plus de la méthode des "templates", il existe  
233 une approche différente consistant à utiliser les distributions au niveau unfolded  
234 au lieu des distributions au niveau reconstruit. L'idée principale est d'utiliser  
235 des distributions déjà corrigées par la procédure d'unfolding et ne conterant pas  
236 d'effets de détecteur indésirables. La masse du boson  $W$  et les différentes sources  
237 d'incertitudes (statistiques et systématiques) sont calculées en utilisant les distri-  
238 butions de  $p_T^\ell$  et  $m_T^W$  séparément puis combinées pour le résultat final. Puisque  
239 nos distributions d'intérêt sont générées à partir des mêmes événements, nous de-  
240 vons prendre en compte la corrélation entre ces deux variables. La corrélation est  
241 calculée à l'aide des "Toys" de MC, générés en faisant varier les distributions  $p_T^\ell$   
242 et  $m_T^W$  simultanément avec une variation aléatoire de Poisson. Cette thèse, donne  
243 des résultats préliminaires pour la mesure de la masse du boson  $W$  avec les in-  
244 certitudes statistiques et expérimentales correspondantes, en utilisant les données  
245 des runs spéciaux collectés avec un faible nombre d'interactions par croisement ( $\mu$   
246  $\approx 2$ ).

# 248 **Contents**

249	<b>0.1 Résumé</b>	5
250	<b>1 Theoretical overview</b>	1
251	1.1 Introduction	1
252	1.2 The Standard Model	1
253	1.2.1 Elementary particles	1
254	1.2.1.1 Fermions	1
255	1.2.1.2 Gauge bosons	2
256	1.2.2 Fields and interactions	3
257	1.2.2.1 Lagrangian formalism and symmetries	3
258	1.2.2.2 Quantum chromodynamics	4
259	1.2.2.3 Electroweak interaction	5
260	1.3 $W$ boson production in $pp$ collision	6
261	1.4 Properties of the $W$ boson	10
262	1.4.1 $W$ boson mass	10
263	1.4.2 Experimental determinations of $W$ boson mass	11
264	<b>2 Experimental Setup: The ATLAS experiment at the LHC</b>	15
265	2.1 The large hadron collider	15
266	2.1.1 The LHC acceleration chain	15
267	2.1.2 LHC performance	16
268	2.2 The ATLAS detector	17
269	2.2.1 Coordinate system	18
270	2.2.2 Inner tracking detectors	19
271	2.2.3 Electromagnetic and hadronic calorimeters	20
272	2.2.3.1 The electromagnetic calorimeter	21
273	2.2.3.2 The ATLAS tile hadronic calorimeter	25
274	2.2.4 Muon spectrometer and toroidal magnets	25
275	2.2.5 ATLAS trigger and data acquisition system	26
276	2.3 Reconstruction of physics objects	27
277	2.3.1 Electron reconstruction	27
278	2.3.2 Electron identification	31
279	<b>3 Calibration of the electromagnetic calorimeter</b>	33
280	3.1 Introduction	33
281	3.2 Overview of the calibration procedure	33
282	3.3 Energy scale and resolution determination with electrons from $Z \rightarrow ee$ decays	34
283	3.3.1 Overview	34
284	3.3.2 Definition of the correction factors	35
285	3.3.3 Effect of the scale factors ( $\alpha, c'$ ) on the di-electrons mass $m_{ee}$	36

287	3.4	Template method for the energy scale factors . . . . .	37
288	3.4.1	Methodology of the template method . . . . .	37
289	3.4.2	Inversion procedure . . . . .	38
290	3.5	Selections and corrections . . . . .	39
291	3.5.1	Binning . . . . .	41
292	3.6	Results . . . . .	41
293	3.6.1	Extraction of the correction factors ( $\alpha, c'$ ) . . . . .	41
294	3.6.2	Systematic uncertainties . . . . .	44
295	3.6.3	Data to simulation comparison . . . . .	46
296	3.7	Calibration for low pile-up runs . . . . .	47
297	3.7.1	Introduction . . . . .	47
298	3.7.2	Energy scale factors for low pile-up runs . . . . .	47
299	3.7.3	Extrapolation method . . . . .	50
300	3.7.4	Extrapolation results . . . . .	53
301	3.7.5	Uncertainties for the extrapolation method . . . . .	55
302	3.7.6	Data to simulation comparison for low pile-up runs . . . . .	56
303	3.8	Future of the calibration . . . . .	57
304	<b>4</b>	<b>Statistical overview: Unfolding</b>	<b>59</b>
305	4.1	Introduction . . . . .	59
306	4.2	Unfolding in high energy physics . . . . .	59
307	4.3	Iterative Bayesian unfolding . . . . .	61
308	4.3.1	Migration matrix . . . . .	62
309	4.4	Uncertainties with unfolding . . . . .	63
310	4.4.1	Propagation of the statistical uncertainty . . . . .	64
311	4.4.2	Propagation of systematic uncertainties . . . . .	65
312	4.4.3	Bias uncertainty with unfolding . . . . .	65
313	4.5	Optimisation of the number of iterations . . . . .	67
314	4.6	Bin-by-bin unfolding . . . . .	67
315	<b>5</b>	<b>Measurement of the <math>W</math>-boson transverse momentum distribution</b>	<b>71</b>
316	5.1	Introduction . . . . .	71
317	5.2	Data and simulated distributions . . . . .	72
318	5.2.1	Selections . . . . .	72
319	5.2.2	Control plots for the $p_T^W$ distribution . . . . .	72
320	5.3	Data unfolding . . . . .	77
321	5.3.1	Unfolding description . . . . .	77
322	5.3.2	Experimental systematic uncertainties . . . . .	79
323	5.3.3	Propagation of statistical uncertainties . . . . .	81
324	5.3.4	Propagation of systematic uncertainties . . . . .	81
325	5.3.5	Comparison of the uncertainties . . . . .	84
326	5.3.6	Unfolding bias . . . . .	87
327	5.4	Results of $p_T^W$ measurement . . . . .	88
328	<b>6</b>	<b><math>W</math> boson production cross sections</b>	<b>91</b>
329	6.1	Introduction . . . . .	91
330	6.2	Fiducial cross-section methodology . . . . .	91
331	6.2.1	The bin-by-bin method . . . . .	91

332	6.2.2	The Bayesian unfolding method . . . . .	92
333	6.2.3	Results . . . . .	94
334	6.2.4	Comparison with theoretical predictions . . . . .	94
335	<b>7</b>	<b>Measurement of single and double differential cross sections</b>	<b>97</b>
336	7.1	Introduction . . . . .	97
337	7.2	Data and simulation distributions . . . . .	98
338	7.2.1	Fiducial phase space . . . . .	98
339	7.2.2	Experimental systematic uncertainties . . . . .	98
340	7.2.3	Data and MC comparison . . . . .	99
341	7.2.4	Unfolding of data distributions . . . . .	99
342	7.2.5	Propagation of the statistical and systematic uncertainties .	102
343	7.2.6	Unfolding bias . . . . .	103
344	7.2.7	Optimisation of the number of iterations in iterative Bayesian unfolding . . . . .	103
345	7.3	Differential cross sections . . . . .	106
346	7.4	Comparison of electron and muon channels . . . . .	119
347	7.5	Comparison with theoretical predictions . . . . .	121
348	7.6	Double differential cross sections in $p_T^{\ell}$ and $\eta_{\ell}$ bins . . . . .	122
349	7.6.1	Introduction . . . . .	122
350	7.6.2	Migration matrix . . . . .	123
351	7.6.3	Statistical uncertainty . . . . .	123
352	7.6.4	Unfolding bias . . . . .	123
353	7.6.5	Double differential cross sections . . . . .	126
354	<b>8</b>	<b>Measurement of the <math>W</math>-boson mass</b>	<b>131</b>
355	8.1	Introduction . . . . .	131
356	8.2	Template fit method methodology . . . . .	131
357	8.3	$W$ boson mass using the unfolded distribution . . . . .	132
358	8.4	Statistical uncertainty . . . . .	134
359	8.5	Systematic uncertainties . . . . .	135
360	8.6	Statistical uncertainty with the unfolded distribution . . . . .	139
361	<b>9</b>	<b>Conclusion</b>	<b>143</b>
362	<b>A</b>	<b>Control plots</b>	<b>145</b>
363	<b>B</b>	<b>Breakdown of uncertainties</b>	<b>151</b>
364	<b>C</b>	<b>Uncertainties for the differential cross sections</b>	<b>159</b>



## <sup>366</sup> Chapter 1

# <sup>367</sup> Theoretical overview

### <sup>368</sup> 1.1 Introduction

<sup>369</sup> For a long time, understand the nature of the matter that surrounds us was one of  
<sup>370</sup> the most interesting questions of philosophers. The first idea to explain the nature  
<sup>371</sup> of matter is due to ancient Greek philosophers in the 6<sup>th</sup> century B.C., who intro-  
<sup>372</sup>duced the term "atom" to describe the small and indivisible object we can find in  
<sup>373</sup> nature. The next huge step in the understanding of the matter came in the 18<sup>th</sup>  
<sup>374</sup> century, where the chemists started to classify the materials on observed proper-  
<sup>375</sup>ties and also proposed predictions. However, near the end of the 19th century,  
<sup>376</sup> physicists discovered that atoms are not the fundamental particles of nature, but  
<sup>377</sup> conglomerates of even smaller particles.

<sup>378</sup> In the 20<sup>th</sup> century, physicists started to build a model that describes all the  
<sup>379</sup> particles in nature and their interactions except those due to gravity, which is so  
<sup>380</sup> called the Standard Model (SM). This model is the combination of two theories  
<sup>381</sup> that describe particles and their interactions into a single framework. The two  
<sup>382</sup> components of the SM are the electroweak theory, which describes interactions via  
<sup>383</sup> the electromagnetic and weak forces, and quantum chromodynamics, the theory  
<sup>384</sup> of the strong nuclear force. Both these theories are gauge field theories, which  
<sup>385</sup> describe the interactions between particles in terms of exchange of intermediary  
<sup>386</sup> "messenger" particles. This chapter gives an overview of the particles and their  
<sup>387</sup> interactions in the SM.

### <sup>388</sup> 1.2 The Standard Model

#### <sup>389</sup> 1.2.1 Elementary particles

<sup>390</sup> The particles in the SM, are divided in two groups called fermions and bosons,  
<sup>391</sup> and are interacting with each other through three known interactions. The classi-  
<sup>392</sup>fication of particles is based on their physical properties.

##### <sup>393</sup> 1.2.1.1 Fermions

<sup>394</sup> The fermions [118] in the SM are separated into two groups, leptons and quarks.  
<sup>395</sup> Leptons are assumed to be elementary with no inner structure, while the quarks  
<sup>396</sup> are constituent of other particles, hadrons, combined by the strong interaction [154].

397 The SM fermion sector is organised in three generations as shown in Table 1.1. Ac-  
 398 cording to the predictions of relativistic quantum mechanics [80], each fermion has  
 399 a corresponding anti-particle.

400 **Leptons:** They are one of the three classes of particles in the SM. There are six  
 401 known leptons and they occur in pairs called generations. The three charged  
 402 leptons ( $e^-$ ,  $\mu^-$ ,  $\tau^-$ ) are: electron, mu-lepton or muon and the tau-lepton or  
 403 tau. The three charged leptons have the same charge  $Q = -e$ . In addition  
 404 to charged leptons, there are three neutral leptons-neutrinos ( $\nu_{e^-}$ ,  $\nu_{\mu^-}$ ,  $\nu_{\tau^-}$ )  
 405 called the electron neutrino, muon neutrino and tau neutrino respectively,  
 406 having very small masses.

407 **Quarks:** Considered as elementary particles and without inner structure, quarks  
 408 are combined by the strong interactions to form the hadrons. Quarks can  
 409 not be isolated because of the “color confinement” (Sec. 1.2.2.2). The strong  
 410 interaction regroups quarks with different charges and color charges, to form  
 411 hadrons. The most well known and stable hadrons are protons and neutrons.

TABLE 1.1: Generations of quarks and leptons with their masses and charges [63].

	1 <sup>st</sup> Generation	2 <sup>nd</sup> Generation	3 <sup>rd</sup> Generation	Charge[e]
Quarks	Up ( $u$ ) $m = 2.3$ MeV	Charm ( $c$ ) $m = 1.275$ GeV	Top ( $t$ ) $m = 173.2$ GeV	+2/3
	Down ( $d$ ) $m = 4.8$ MeV	Strange ( $s$ ) $m = 95$ MeV	Bottom ( $b$ ) $m = 4.18$ GeV	-1/3
Leptons	Electron ( $e^-$ ) $m = 511$ keV	Muons ( $\mu^-$ ) $m = 105.7$ MeV	Tau ( $\tau^-$ ) $m = 1.8$ GeV	-1
	Electron neutrino ( $\nu_e$ ) $m < 2$ eV	Muon neutrino ( $\nu_\mu$ ) $m < 0.19$ MeV	Tau neutrino ( $\nu_\tau$ ) $m < 18.2$ MeV	0

### 412 1.2.1.2 Gauge bosons

413 Called also messenger particles or intermediate particles, the gauge bosons (Ta-  
 414 ble 1.2) give rise to the interactions between particles. Photons are the intermediate  
 415 particles of electromagnetic interactions, which bond the electrons to the nucleus  
 416 to form the atoms, and which also bond the atoms together to form the molecules.  
 417 The  $W$  and  $Z$  bosons, discovered at CERN in 1983 by the UA1 and UA2 collabora-  
 418 tions [90], are the weak interaction messengers. Unlike photons, these particles are  
 419 characterised by a non-zero mass, and their masses were found to be about 80 GeV  
 420 and 91 GeV, respectively [71]. Exchange of gluons, the intermediate particles for  
 421 strong interactions are analogous to the exchange of photons in the electromag-  
 422 netic force between two charged particles, but for strong interactions, they “glue”  
 423 quarks together, forming hadrons such as protons and neutrons. The Higgs boson  
 424 has, contrary to the gauge bosons, a spin 0 and has been discovered at CERN in  
 425 2012 by the ATLAS and CMS collaborations [4, 126].

TABLE 1.2: The SM bosons with their masses and charges, and corresponding interaction types [130].

Boson	Mass	Charge	Spin	Interaction	Range	Act on
Photon	0	0	1	Electromagnetism	Infinite	Charge
8 gluons	0	0	1	Strong	$10^{-15}\text{m}$	Colour
$W^\pm$	80.4 GeV	$\pm$	1	Weak	$10^{-18}\text{m}$	Weak isospin
$Z$	91.2 GeV	0	1	Weak	$10^{-18}\text{m}$	Weak isospin and hypercharge
Higgs	125 GeV	0	0			

## 1.2.2 Fields and interactions

In the SM, there are quantum fields associated to the bosons that are responsible of the interactions between particles. The SM is a theory describing the electromagnetic, weak, and strong interactions by a class of quantum field theories constrained by various symmetry principles.

### 1.2.2.1 Lagrangian formalism and symmetries

The Lagrangian formalism is an efficient method used to describe variety of physical systems including systems with finite (particles) and an infinite number of degrees of freedom (fields). In the SM, we describe all the interactions with the notion of field, and they are built using the Lagrangian formalism.

The easiest way to understand this formalism, is to take an example of an isolated system in classical physics, where the Lagrangian can be written as:

$$\mathcal{L}(x, \dot{x}, t) = T - V, \quad (1.1)$$

where  $T$  and  $V$  are the kinetic and potential energy, respectively. In the simple case of a system of a particle of mass  $m$  moving along a dimension  $x$  in a potential  $V(x)$ , the Lagrangian can be written as:

$$\mathcal{L}(x, \dot{x}, t) = \frac{1}{2}m\dot{x}^2 - V(x). \quad (1.2)$$

On the other hand, the principle of least action [35] tells us that the action:

$$S = \int_{t_1}^{t_2} \mathcal{L}(x, \dot{x}, t) dt, \quad (1.3)$$

must be minimised or maximised [35], which implies that:

$$\delta S = \int_{t_1}^{t_2} \left( \frac{\partial \mathcal{L}}{\partial q} \delta q + \frac{\partial \mathcal{L}}{\partial \dot{q}} \delta \dot{q} \right) dt = 0, \quad (1.4)$$

leading finally to the Lagrangian equation which describes the movement of the system:

$$\frac{\partial}{\partial t} \frac{\partial \mathcal{L}}{\partial \dot{q}} - \frac{\partial \mathcal{L}}{\partial q} = 0. \quad (1.5)$$

445 For the example introduced in equation (1.2), by injecting equation (1.2) in (1.5) we  
 446 find:

$$m\ddot{q} = -\frac{\partial V}{\partial q}, \quad (1.6)$$

447 which is none other than Newton's first law. On the other hand and from the  
 448 equation (1.5) we find that

$$\frac{d}{dt} \left[ \frac{\partial \mathcal{L}}{\partial \dot{q}} \dot{q} - \mathcal{L} \right] = 0, \quad (1.7)$$

449 which leads us to another important theorem, Noether theorem [88], which means  
 450 that for any continuous symmetry of a system, there is a constant associated to the  
 451 movement (in our case here temporal). This notion of symmetry, or invariance, is  
 452 a key element in the construction of the SM as a gauge theory.

### 453 1.2.2.2 Quantum chromodynamics

454 Quantum chromodynamics (QCD) [84] is the gauge field theory which describes  
 455 the strong interactions. The QCD is a local gauge symmetry under the  $SU(3)_c$   
 456 group [84]. This symmetry generates eight gluons, massless gauge bosons consid-  
 457 ered as intermediate particle for strong interactions. Gluons are characterised by a  
 458 conserved quantum number called the color charge (there are eight color states of  
 459 gluons, composed by the three colors: red, green or blue, and the three anti-colors).  
 460 The associated Lagrangian of QCD is:

$$\mathcal{L}_{\text{QCD}} = \bar{\psi}_{q,a} (i\gamma^\mu \partial_\mu \delta_{ab} - g_s \gamma^\mu t_{ab}^c A^c \mu^c - m_q \delta_{ab}) \psi_{q,a} - \frac{1}{4} F_{\mu\nu}^A F^{A\mu\nu}. \quad (1.8)$$

461 The  $\gamma^\mu$  are the Dirac  $\gamma$ -matrices, the  $\psi_{q,a}$  represent the field of quark of flavor  $q$  [84]  
 462 and  $a$  is the color index (quarks come in three colors). The  $A^c \mu^c$  correspond to gluon  
 463 fields, with  $c$  running from 1 to  $N_c^2 - 1 = 8$  representing the number of existing  
 464 gluons. The  $g_s$  is the strong coupling constant and is universal for all gluons. The  
 465 constant  $g_s (g_s^2 = 4\pi\alpha_s)$  is a fundamental parameter of QCD and can be written as  
 466 a function of the energy scale  $Q$  as:

$$\alpha_s (Q^2) \approx \frac{1}{\beta_0 \ln (Q^2/\Lambda^2)}, \quad (1.9)$$

467 where  $\beta_0$  is a constant term related to the number of quark flavors and  $\Lambda$  is the scale  
 468 of the QCD. The dependence of  $\alpha_s$  as a function of the energy scale  $Q$ , plotted in  
 469 Figure 1.1, defines the characteristic properties of QCD interactions:

- 470 • Asymptotic freedom: it means that at large  $Q^2$  (small distance) the coupling  
 471 between quarks becomes weak.
- 472 • Quark confinement: it means that at small  $Q^2$  (large distance) the coupling  
 473 between quarks becomes strong and we cannot find a quark as an isolated  
 474 particle.

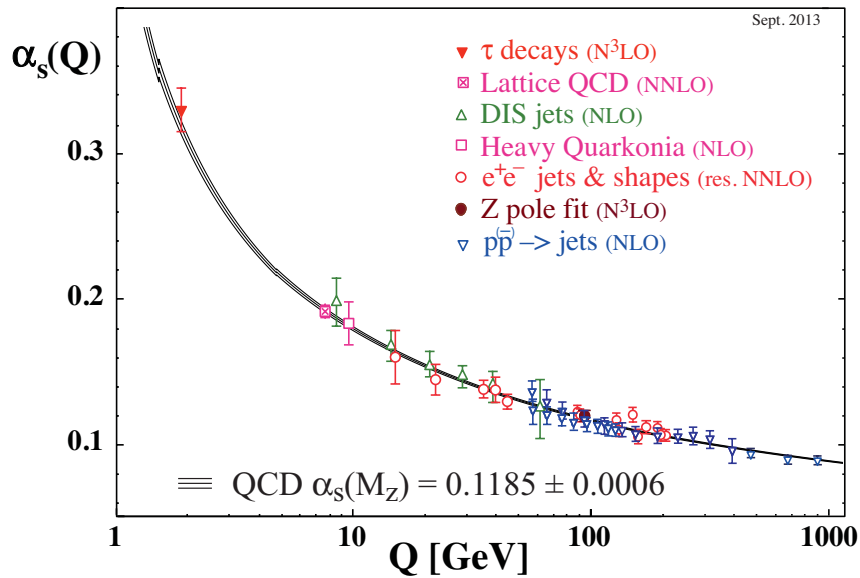


FIGURE 1.1: Evolution of the strong coupling constant as a function of the energy scale measured by various experiments [61].

#### 475 1.2.2.3 Electroweak interaction

476 In the SM, the electromagnetic and weak interactions are considered as two dif-  
 477 ferent low-energy aspects of a single electroweak (EW) interaction, this theory de-  
 478 veloped by Glashow, Weinberg, and Salam being known as “GWS theory” [133].  
 479 This theory is described by an  $SU(2)_L \otimes U(1)_Y$  gauge group, with the exchange of  
 480 four mediator bosons: photon,  $Z$ ,  $W^+$  and  $W^-$ . The Lagrangian of the EW theory  
 481 is described as:

$$\mathcal{L}_{EW} = \sum_{\Psi} \bar{\Psi} [i\gamma^{\mu} D_{\mu}] \Psi - \frac{1}{4} W_{\mu\nu}^a W_a^{\mu\nu} - \frac{1}{4} B_{\mu\nu} B^{\mu\nu}, \quad (1.10)$$

$$D_{\mu} = \partial_{\mu} + igT^a W_{\mu}^a + ig' \frac{1}{2} T_Y B_{\mu}, \quad (1.11)$$

482 where  $T^a$  and  $T_Y$  are the generators of  $SU(2)_L$  and  $U(1)_Y$ ,  $g$  and  $g'$  are the weak and  
 483 electromagnetic couplings.  $B_{\mu}$  and  $W_{\mu}^a$  are gauge fields which give rise to the four  
 484 mediator bosons. The bosons photon,  $Z$ ,  $W^+$  and  $W^-$  can be written as:

$$A_{\mu} = B_{\mu} \cos \theta_W + W_{\mu}^3 \sin \theta_W, \quad (1.12)$$

$$Z_{\mu} = -B_{\mu} \sin \theta_W + W_{\mu}^3 \cos \theta_W, \quad (1.13)$$

$$W_{\mu}^{\pm} = \frac{1}{\sqrt{2}} (W_{\mu}^1 \mp W_{\mu}^2), \quad (1.14)$$

485 where  $\theta_W$  is a mixing parameter called the weak mixing (Weinberg) angle which  
 486 is precisely measured by experiments:  $\sin^2(\theta_W) = 0.23153 \pm 0.00006$ , in the scheme  
 487 where  $\theta_W$  is the effective leptonic weak mixing angle [89], and can be expressed in

488 terms of the coupling constants as:

$$\cos \theta_W = \frac{g}{\sqrt{g^2 + g'^2}}, \quad (1.15)$$

$$\sin \theta_W = \frac{g'}{\sqrt{g^2 + g'^2}}, \quad (1.16)$$

489 according to the EW Lagrangian (1.11). The fermionic and bosonic fields must be  
 490 massless to preserve the  $SU(2)_L \otimes U(1)_Y$  gauge symmetry. On the other hand, the  
 491 experimental observations show the existence of massive bosons and fermions. In  
 492 1964, the Brout-Englert-Higgs mechanism [32] proposed a solution to solve this  
 493 conflict with experiments by adding an additional scalar boson called the (Brout-  
 494 Englert-) Higgs boson and generating a “Higgs field” which interacts with all the  
 495 particles. This mechanism is called “spontaneous symmetry breaking”. The La-  
 496 grangian of the Higgs field can be written as:

$$\mathcal{L}_{\text{Higgs}} = -\frac{1}{4}F^{\mu\nu}F_{\mu\nu} + (D^\mu\Phi)^\dagger(D_\mu\Phi) - V(\Phi), \quad (1.17)$$

$$V(\Phi) = -\mu^2|\Phi|^2 + \lambda(|\phi|^2)^2, \quad (1.18)$$

497 where  $(D^\mu\Phi)^\dagger(D_\mu\Phi)$  contains the interaction between Higgs and gauge bosons.  
 498 The Higgs boson mass term is expressed as:  $m_H^2 = 2|\mu|^2 = 2\lambda v^2$ , while the gauge  
 499 bosons masses are written as:

$$m_W^2 = \frac{1}{4}g^2v^2, \quad m_Z^2 = \frac{1}{4}(g^2 + g'^2)v^2. \quad (1.19)$$

### 500 1.3 $W$ boson production in $pp$ collision

501 At the LHC [148], the electroweak gauge bosons  $W$  and  $Z$  are produced from  
 502 proton–proton collisions (at Tevatron they were produced by proton–antiproton  
 503 collisions). Each proton is composed of two quarks up ( $u$ ) and one quark  
 504 down ( $d$ ) which interact through strong interactions by exchange of gluons.  
 505 Quarks  $u$  and  $d$ , containing valence quarks, determine the quantum numbers of  
 506 proton. The production of  $W$  and  $Z$  bosons at leading order is dominated by  
 507 quark–antiquark annihilation processes, as seen in Figure 1.2, with  $q\bar{q} \rightarrow W$ ,  
 508  $q\bar{q} \rightarrow Z$  with no momentum in the plane transverse to the beam [132]. However,  
 509 high order corrections can include radiation of gluons or quarks, where the glu-  
 510 ons can self-interact and produce more gluons, and each gluon can also produce a  
 511 quark and anti-quark pairs, called *sea* quarks, also shown in Figure 1.2.

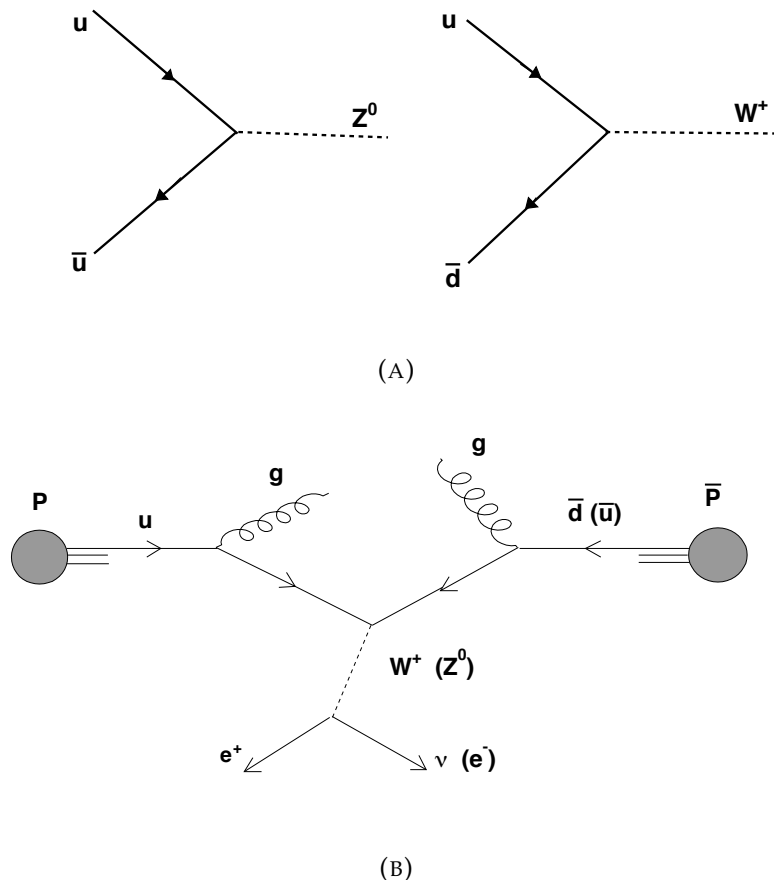


FIGURE 1.2: (A) First-order production diagrams for the  $W$  and  $Z$  boson. (B) Basic production and leptonic decay for  $W/Z$  bosons with radiated gluons.

512     Eventually, the production of the EW gauge bosons in proton–proton collisions  
 513     with high order of QCD corrections, is mainly related to the distributions of  
 514     partons inside each proton. The partonic structure is studied in particular in scat-  
 515     tering processes like Deep Inelastic Scattering (DIS) [76], and the resulting Parton  
 516     Distribution Functions (PDFs) [75] represent the probability density to find par-  
 517     tons (quarks and gluons) carrying a momentum fraction  $x$  at an energy scale  $Q$ .  
 518     PDF sets cannot be calculated analytically but are obtained by fits to a large num-  
 519     ber of cross section data points from many experiments [76]. Figure 1.3 shows  
 520     examples of parton distributions in the proton at two energy scales  $Q = 2$  GeV  
 521     and  $Q = 100$  GeV.

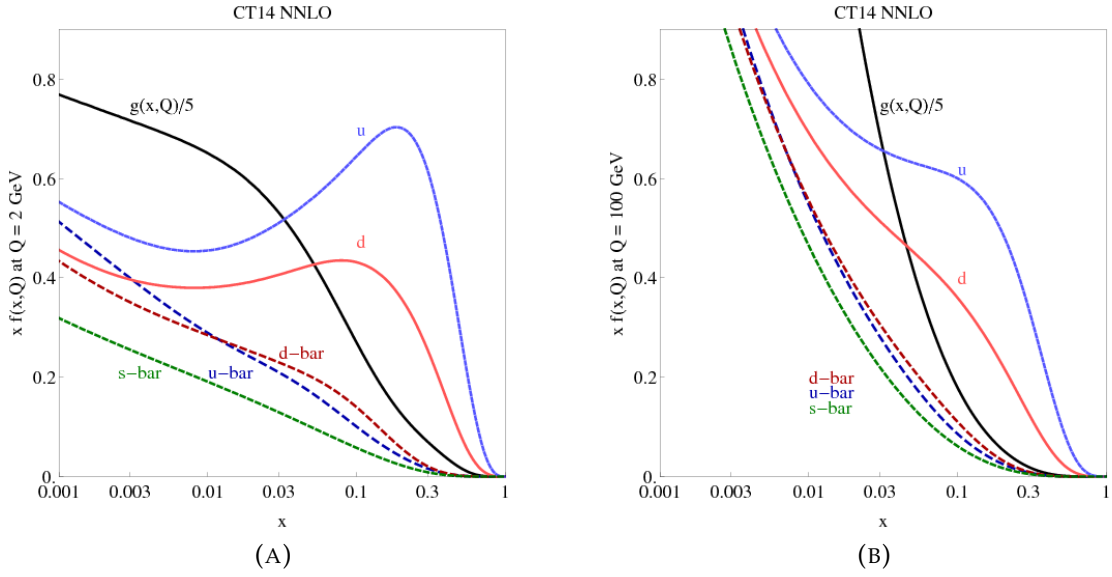


FIGURE 1.3: The CT14 parton distribution functions at  $Q = 2$  GeV (A) and  $Q = 100$  GeV (B) for  $u, \bar{u}, d, \bar{d}, s = \bar{s}$  and  $g$  [65]

522 In proton–proton collisions, the hadrons interactions can be separated in two  
 523 types, hard QCD and soft QCD. The hard QCD process for the  $W$  boson produc-  
 524 tion corresponds to a production with large momentum transfer  $Q$ , and the  $W$   
 525 boson production cross-section ( $p_1 + p_2 \rightarrow V + X$ ) can be determined using the  
 526 *Factorization Theorem* [66] and the PDFs  $f_i(x, Q)$ :

$$\sigma_V(h_1(p_1), h_2(p_2)) = \sum_{a,b} \int_0^1 dx_a dx_b f_{a/h_1}(x_a, \mu_F^2) f_{b/h_2}(x_b, \mu_F^2) \times \sigma_{ab \rightarrow V}(x_a p_1, x_b p_2, \mu_F^2). \quad (1.20)$$

527 where  $x_{1,2}$  are the fractions of the momenta of the hadrons and  $f_{i,j}$  are the corre-  
 528 sponding distributions of quark and anti-quark ( $a,b$ ),  $\mu_F$  is the factorization scale  
 529 that separates hard and soft QCD regimes. The generalisation of equation (1.20)  
 530 for higher order corrections that can contribute to the  $W$  boson production is writ-  
 531 ten as:

$$\sigma_{ab \rightarrow V} = \sigma_0 + \alpha_s(\mu_R^2) \sigma_1 + \alpha_s^2(\mu_R^2) \sigma_2 + \dots \quad (1.21)$$

532 where  $\mu_R$  is the renormalisation scale of the QCD running coupling constant, and  
 533  $\sigma_0$  corresponds to the cross section at Leading Order (LO). The terms  $\alpha_s(\mu_R^2) \sigma_1$  and  
 534  $\alpha_s^2(\mu_R^2) \sigma_2$  correspond to the cross-sections at Next-Leading Order (NLO) and Next-  
 535 to-Next-Leading Order (NNLO). For Drell-Yan processes, the scale parameters  $\mu_F$   
 536 and  $\mu_R$  are chosen as  $\mu_F = \mu_R = M$  [46]. The predictions at NLO order for some  
 537 important SM cross sections in proton–proton and proton–antiproton collisions  
 538 are shown in Figure 1.4.

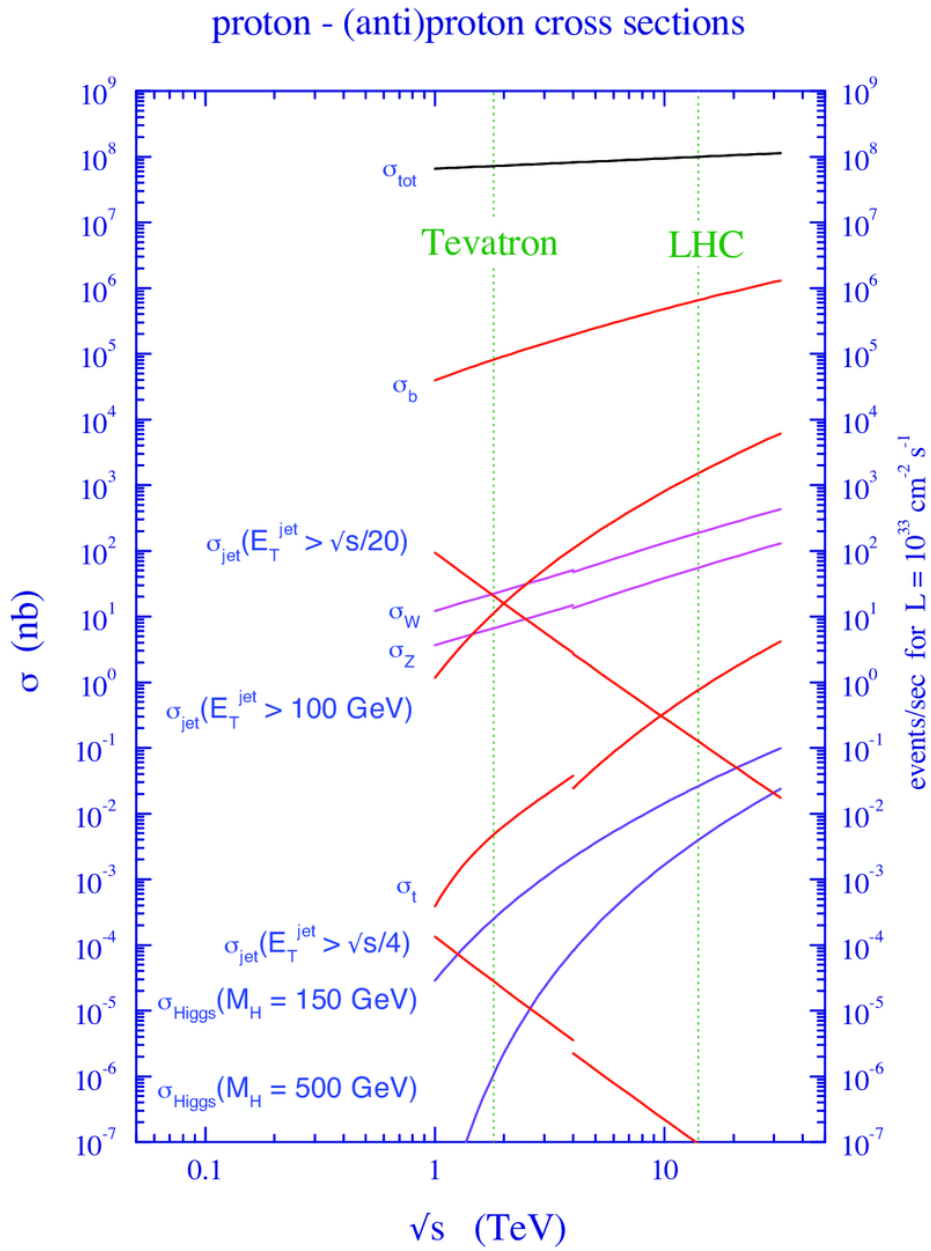


FIGURE 1.4: Standard Model cross sections at the Tevatron and LHC colliders, calculated at next-to-leading order in perturbation theory [141].

## 539 1.4 Properties of the $W$ boson

### 540 1.4.1 $W$ boson mass

541 As described in Sec. 1.2.2.3 for the spontaneous symmetry breaking, the fundamental parameters of the electroweak interactions are: the mass of the Higgs boson, the weak mixing angle  $\theta_W$ , and the coupling constants  $(g, g')$ . At lowest order in the EW theory, the  $W$  boson mass can be expressed as a function of the fine-structure constant  $\alpha (= e^2/4\pi)$ , the Fermi constant  $G_F$  and the mass of the  $Z$  boson.  
 542 The Fermi constant  $G_F$  is a function of the the coupling constant  $g$  and calculated  
 543 using the Fermi model [144]. The  $Z$  boson mass is determined with high precision  
 544 from the  $Z$  lineshape scan at LEP1 [138]:

$$\alpha^{-1} = 137.035999074(44), \quad (1.22)$$

$$G_F = 1.1663787(6) \times 10^{-5} \text{ GeV}^{-2}, \quad (1.23)$$

$$M_Z = 91.1876(21) \text{ GeV}. \quad (1.24)$$

545 At this level, the  $W$  boson mass can be expressed as:

$$M_W^2 = M_Z^2 \left( \frac{1}{2} + \sqrt{\frac{1}{4} - \frac{\alpha\pi}{\sqrt{2}G_F M_Z^2}} \right). \quad (1.25)$$

546 It predicts a  $W$  mass value of  $M_W = 80.939 \pm 0.0026$  GeV. However, higher-order  
 547 EW corrections introduce an additional dependence on the gauge couplings and  
 548 the mass of heavy particles of the SM. The  $W$  mass boson can be expressed with  
 549 an additional parameter  $\Delta r$  containing all the high-order corrections:

$$M_W^2 = M_Z^2 \left( \frac{1}{2} + \sqrt{\frac{1}{4} - \frac{\alpha\pi}{\sqrt{2}G_F M_Z^2(1 - \Delta r)}} \right). \quad (1.26)$$

550 In summary, the additional parameter  $\Delta r$  depends on the vacuum polarisation  
 551 contribution of leptons and light quarks, as well as the top-quark and Higgs boson  
 552 masses and may be sensitive to additional particles and interactions beyond the  
 553 SM. All those effects make the  $W$  mass boson an extremely important parameter of  
 554 the SM. Producing a  $W$  mass measurement with excellent accuracy is accordingly  
 555 of high importance for testing the overall consistency of the SM, by comparing the  
 556 experimental measurement of  $M_W$  to the theoretical predictions. The determina-  
 557 tion of the  $W$  boson mass at the NLO order (2-loop EW), with some leading NNLO  
 558 and few N<sup>3</sup>LO QCD contributions, is performed with a global fit [28, 89] (see also  
 559 Refs. [146, 39]) of electroweak parameters. The resulting  $W$  mass value is:

$$M_W = 80.359 \pm 0.006 \text{ GeV}. \quad (1.27)$$

### 1.4.2 Experimental determinations of $W$ boson mass

After the first detection of the  $W$  boson by the UA1 [21] and UA2 [29] collaborations [90] in proton–antiproton collisions at the SPS collider in 1983, the obtained  $M_W$  value was  $81 \pm 5$  GeV [72] and it was difficult to determine it precisely at this accelerator [60]. However, UA2 produced finally a determination  $M_W = 80.35 \pm 0.37$  GeV in 1991 [11]. Later, the  $W$  mass was determined [137] in Large Electron-Positron (LEP) collider at CERN [1995-2000] [83]. LEP was accelerating electrons and positrons to reach a center-of-mass energy up to 209 GeV. The direct measurement of the  $W$  boson mass at LEP experiments (ALEPH, DELPHI, L3 and OPAL) gives the following result:

$$M_W^{\text{LEP}} = 80.376 \pm 0.025_{\text{stat}} \pm 0.022_{\text{syst}} \text{ GeV.} \quad (1.28)$$

Later, a new determination of  $M_W$  was performed in Tevatron experiments (CDF and D0) at Fermilab [2002-2011] [59]. The Tevatron collider was a proton–antiproton collider, where the center of mass energy can reach 1.96 TeV [125]. The  $M_W$  was determined from the comparison of kinematical distributions of  $W \rightarrow l\nu$  with simulated distributions characterised with different  $M_W$  values. The direct determination of the  $W$  boson mass by the Tevatron experiments (CDF and D0) gives the following result [5]:

$$M_W^{\text{Tevatron}} = 80.387 \pm 0.016 \text{ GeV,} \quad (1.29)$$

The Tevatron and LEP combined results lead to the world average value:

$$M_W = 80.385 \pm 0.015 \text{ GeV,} \quad (1.30)$$

The latest  $M_W$  determination is carried out with the ATLAS detector at the LHC [115, 17], using proton–proton collision at a center of mass energy of 7 TeV collected during Run 1 in 2011. The  $M_W$  is determined using the lepton transverse momentum ( $p_T^\ell$ ) and transverse mass ( $m_T^W$ ) distributions from  $W \rightarrow l\nu$  with the template approach [115]. The  $W$  boson transverse mass,  $m_T^W$ , is derived from the missing transverse momentum ( $p_T^{\text{miss}}$ ) and from  $p_T^\ell$  as follows:

$$m_T^W = \sqrt{2p_T^\ell p_T^{\text{miss}}(1 - \cos \Delta\phi)}, \quad (1.31)$$

where  $\Delta\phi$  is the azimuthal opening angle between the charged lepton and the missing transverse momentum. The different sources of uncertainties are described in the Table 1.3, and the dominant systematic uncertainties are:

**Lepton calibration:** The measurement of lepton momentum and energy is derived using information from the  $Z$  decay due to its very clean final state. The Run 1 corrections for the leptons with their uncertainties are described in [23, 41, 67] and are studied in detail for this analysis in [158, 152]. Electron energy calibration will be discussed in Chapter 3.

**Hadronic recoil uncertainty:** It is defined as the uncertainty from the hadronic recoil (HR) calibration [48]. The study for the Run 1 analysis is shown in [140].

598 The uncertainties in HR calibration are mainly driven by data statistics in the  
 599 resolution and response corrections [155, 101].

600 **Backgrounds in the  $W$  boson sample:** The  $W$  boson background contributions  
 601 are estimated using simulation, except for the multijet background using  
 602 data-driven techniques [155, 157]. The study for the Run 1 analysis is shown  
 603 in [17].

604 **QCD corrections:** The NNLO is used to describe the differential cross-section as  
 605 a function of boson rapidity and angular coefficient [143, 16]. The QCD un-  
 606 certainties are coming from the uncertainties in the fixed-order predictions,  
 607 parton-shower predictions and angular coefficients [115].

608 **Electroweak corrections:** Dominated by QED final-state radiation (FSR) [33], the  
 609 uncertainties are evaluated by comparing the distributions with different  
 610 computations.

611 **PDF uncertainties:** Uncertainties in the PDFs are the dominant source of physics-  
 612 modelling uncertainty, due to our imperfect knowledge of the PDFs affecting  
 613 the differential cross section as a function of boson rapidity, the angular co-  
 614 efficients, and the  $W$  boson transverse momentum distribution.

615 The ATLAS experiment gives the following results:

$$M_W^{\text{ATLAS}} = 80.370 \pm 0.019 \text{ GeV.} \quad (1.32)$$

616 The  $W$  boson mass results of ATLAS in comparison with other determinations are  
 617 shown in Figure 1.5.

TABLE 1.3: The ATLAS  $M_W$  result with statistical and systematic uncertainties [115].

Combined categories	Value MeV	Stat. Unc.	Muon Unc.	Elec. Unc.	Recoil Unc.	Bckg. Unc.	QCD Unc.	EW Unc.	PDF Unc.	Total Unc.
$m_T^W, p_T^\ell$	80369.5	6.8	6.6	6.4	2.9	4.5	8.3	5.5	9.2	18.5

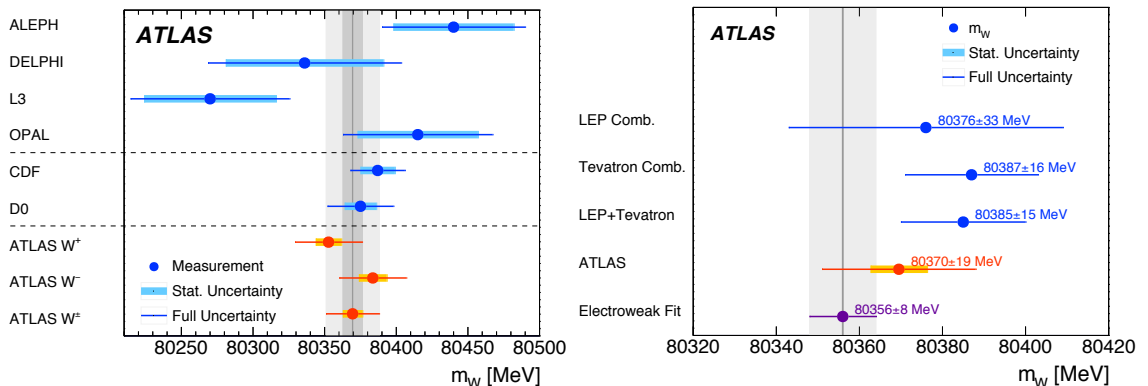


FIGURE 1.5: Left: The  $M_W$  results of ATLAS [115] in comparison with other published results from the LEP experiments ALEPH, DELPHI, L3 and OPAL, and from the Tevatron collider experiments CDF and D0. The vertical bands show the statistical and total uncertainties of the ATLAS determination, and the horizontal bands and lines show the statistical and total uncertainties of the other published results. Right: The ATLAS result compared to the SM prediction from the global electroweak fit, and to the combined values determined at LEP and at Tevatron.



## 618 Chapter 2

# 619 Experimental Setup: The ATLAS 620 experiment at the LHC

621 The results presented in this thesis are based on data collected during Run 2 by the  
622 ATLAS experiment at the Large Hadron Collider (LHC). This chapter provides an  
623 overview of the LHC [81] and of the ATLAS experiment [102], with a description  
624 focused on the components relevant for the analysis.

## 625 2.1 The large hadron collider

626 The LHC is a high-energy particle collider, approved in 1996, with the first beams  
627 in 2008 at the European Organization for Nuclear Research (CERN) [30] at the bor-  
628 der of France and Switzerland. With a circumference of 27 km and with four inter-  
629 action points for four large experiments (ATLAS, CMS, ALICE and LHCb [122]),  
630 the LHC is currently the largest and most powerful accelerator on Earth. The LHC  
631 is designed to accelerate two beams of protons to more than 99.99% the speed of  
632 light, which travel in opposite directions around the accelerator and collide at the  
633 locations of the four major experiments. In the LHC, the particles are grouped to-  
634 gether in about 2000 bunches in each beam, which can contain  $10^{11}$  particles per  
635 bunch [92], and reach an energy up to 6.5 TeV per beam. The beams are therefore  
636 at a center of mass energy up to 13 TeV [92] and collide every 25 nanoseconds.

### 637 2.1.1 The LHC acceleration chain

638 Before being injected in the LHC, particles are accelerated through a series of  
639 lower energy accelerators that successively increase the energy of the colliding  
640 beams [145]. The starting point is a cylinder of hydrogen gas, where the electrons  
641 are stripped from hydrogen atoms before injecting the protons in the linear accel-  
642 erator LINAC2 to begin the first phase of acceleration up to an energy of 50 MeV [81].  
643 Afterwards, the beam of protons is injected into the Proton Synchrotron Booster  
644 (PSB) which accelerates them to an energy of 1.4 GeV. The proton bunches are  
645 then injected into the Proton Synchrotron (PS) in which they are accelerated to an  
646 energy of 26 GeV. After the PS, the 7 km long Super Proton Synchrotron (SPS) ac-  
647 celerates them to reach an energy of 450 GeV. In the last step, the proton beams are  
648 injected in the LHC where they are accelerated to their current maximal energy  
649 6.5 TeV [81].

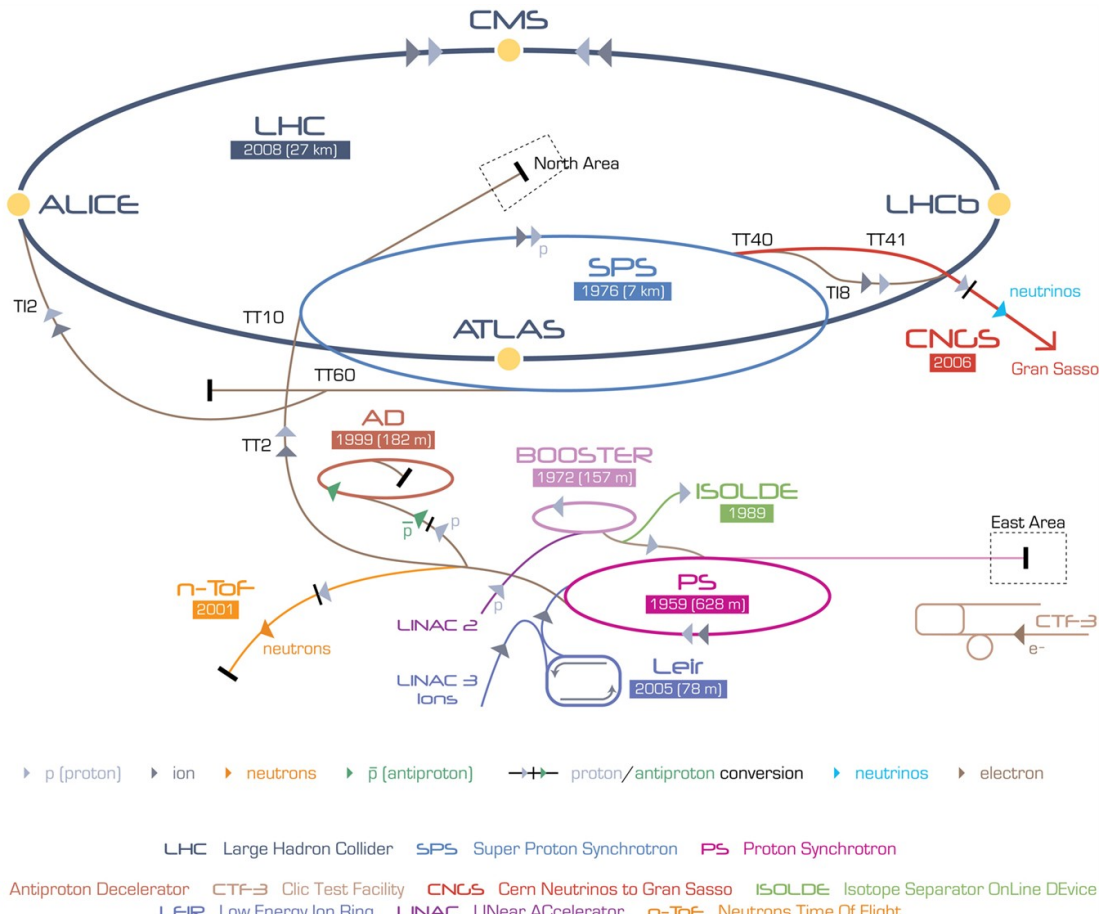


FIGURE 2.1: An overview of the LHC acceleration chain at CERN [119]

### 2.1.2 LHC performance

The performance of the LHC can be parameterised with two factors, the center of mass-energy which allows to estimate the energy available for the production of new processes, and the instantaneous luminosity [105] (expressed in units  $\text{cm}^{-2}\text{s}^{-1}$ ) which represents the rate of physics process a collider is able to produce. The instantaneous luminosity (in the limit of no crossing angle between the beams) is defined as:

$$L_{\text{inst}} = \frac{N_1 N_2 f_r n_b}{4\pi \sigma_x \sigma_y}, \quad (2.1)$$

where  $n_b$  is the number of bunches in a beam,  $f_r$  is the bunch revolution frequency in the LHC,  $N_1$  and  $N_2$  are the number of protons per colliding bunch,  $\sigma_x$  and  $\sigma_y$  are the horizontal and vertical beam size (about  $7 \mu\text{m}$  for the Run 2 in the standard working point). The integrated luminosity is the integral over the data taking time of the instantaneous luminosity:

$$L_{\text{int}} = \int L_{\text{inst}}(t) d(t), \quad (2.2)$$

and it is directly connecting the number of events to the cross-section by:

$$L_{\text{int}} \times \sigma_{\text{process}} = N_{\text{process}}. \quad (2.3)$$

Another significant parameter for our analysis is the pileup, which is the number of inelastic proton–proton interactions per bunch crossing. The average number of proton–proton collisions per bunch crossing is named as  $\langle \mu \rangle$  [124]. The dataset used in our analysis is a special dataset characterised with low pileup ( $\langle \mu \rangle = 2$ ) taken in 2017 and 2018 during Run 2.

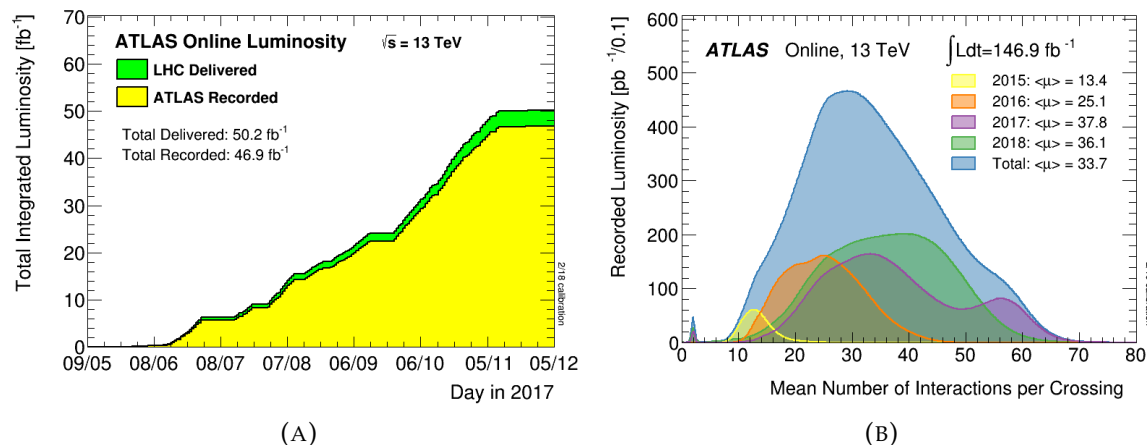


FIGURE 2.2: (A) Integrated luminosity versus time delivered (green) and recorded (yellow) by ATLAS during stable beams for  $pp$  collisions at 13 TeV center of mass energy. (B) Mean number of interactions per crossing  $\langle \mu \rangle$  per year in Run 2 [106]

## 2.2 The ATLAS detector

ATLAS (A Toroidal LHC ApparatuS) [52] is a general-purpose detector developed to study different physics programs: SM electroweak interactions, Higgs boson production, hard QCD and possible signatures of BSM physics. An overview of the ATLAS detector components can be seen in Figure 2.3. The ATLAS detector is located 100 meters underground at the LHC first interaction point, approximately 44 meters long and 25 meters in diameter, weighing around 7000 tons [50]. The ATLAS detector is composed of different sub-detectors [52] which give uniform coverage around the beam pipe and measure different properties of particles in proton–proton collisions at the LHC [24]. Near the center, we start by the inner tracker detectors, which measure the trajectories of charged particles close to the interaction point. The electromagnetic and hadronic calorimeters, which measure the energy deposited by electrons, photons and hadronic jets. The calorimeters are surrounded by the muon spectrometer, the outermost layer, which is designed to measure the trajectory of muons.

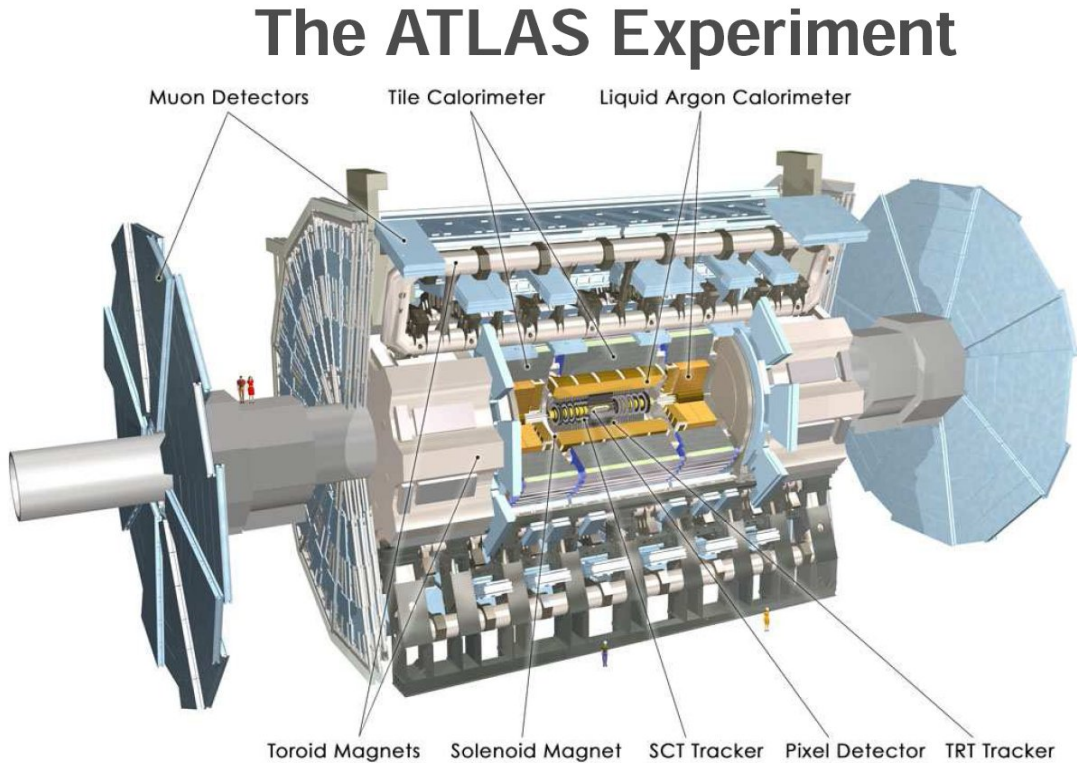


FIGURE 2.3: An overview of the ATLAS detector at CERN [42].

### 683 2.2.1 Coordinate system

684 The nominal interaction point of  $pp$  collisions is defined as the origin of the ATLAS  
 685 coordinate system. The beam direction defines the  $z$ -axis where the positive direc-  
 686 tion is defined as oriented counter clockwise to the LHC ring, while the  $x$  is hori-  
 687 zontal, orthogonal to the beam pipe and pointing towards the center of the LHC .  
 688 The  $y$  direction is defined as orthogonal to the beam pipe and pointing upwards.  
 689 The  $(x, y, z)$  frame is a right handed frame. Because of the symmetry of the AT-  
 690 LAS detector, a polar coordinate system  $(\phi, \theta, z)$  is used, with  $\phi$  being defined with  
 691 respect to the  $x$ -axis and  $\theta$  with respect to the  $z$ -axis, as shown in Figure 2.4. The  
 692 angle  $\theta = 0$  is parallel to the  $z$ -axis while  $\theta = \pi/2$  is in the  $xy$ -plane. In most cases,  
 693 the pseudo-rapidity  $\eta$  is used to instead of  $\theta$  and is defined as  $\eta = -\ln[\tan(\theta/2)]$ ,  
 694 where  $\Delta\eta$  is invariant under boosts along the  $z$ -axis. Another important variable  
 695  $\Delta R$  is used to calculate the distances between two particles in the  $\theta - \eta$  space and  
 696 is defined as  $\Delta R = \sqrt{(\Delta\theta)^2 + (\Delta\eta)^2}$ .

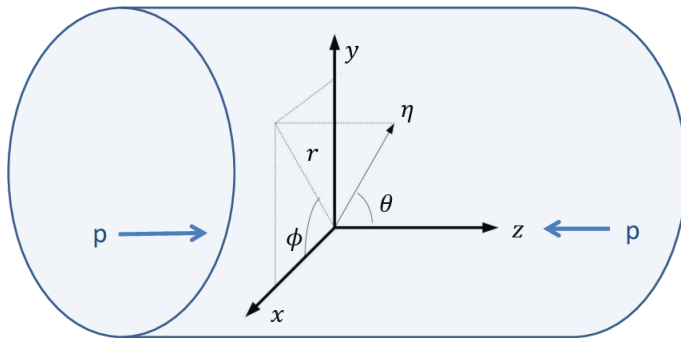


FIGURE 2.4: An overview of the ATLAS coordinate system [128].

### 2.2.2 Inner tracking detectors

The ATLAS Inner Detector (ID) [149] is the closest detector to the collision point, and it is responsible for the reconstruction of the tracks of charged particles emitted in  $pp$  collisions. In the normal (high) pileup mode one has approximately 1000 particles produced in a bunch crossing within the acceptance of the ID (each 25 ns). The inner detector contributes also with the calorimeter and muons spectrometer to the identification of electron, photon and muon. As shown in Figure 2.5, the ID consists of three sub-detectors: the silicon pixel detector, the Semiconductor Tracker (SCT) and Transition Radiation Tracker (TRT):

**Silicon pixel detector [150]:** It is built with four concentric cylindrical layers around the beampipe (in the barrel). The most-inner layer is called the Insertable B-Layer (IBL) and was installed between Run 1 and Run 2. The pixel detector is reconstructed with a pixel size of  $50\mu\text{m} \times 400\mu\text{m}$  ( $50\mu\text{m} \times 250\mu\text{m}$  for the IBL). The pixel detector is used for  $b$ -tagging and track reconstruction.

**Semi-conductor tracker [147]:** It is the second part of the inner detector, with four layers of silicon microstrips (in the barrel). The SCT is used for the measurement of momentum and to identify the vertex of charged particles.

**Transition Radiation Tracker [129]:** This sub-detector surrounds the SCT sub-detector, and consists of multiple layers of straw tubes with a diameter of 4 mm. The TRT is used for momentum measurement and provides discrimination between electrons and hadrons.

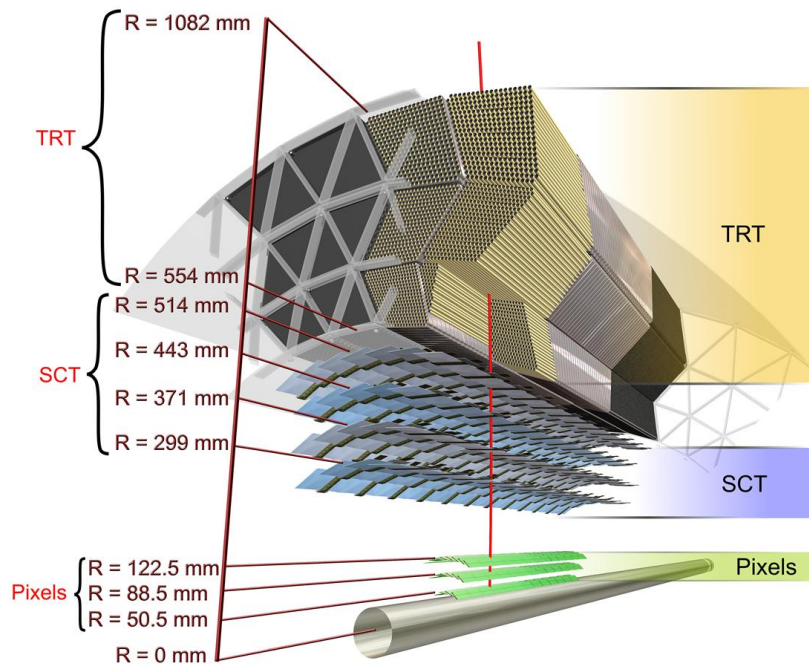


FIGURE 2.5: Schematic showing the ATLAS inner detector [134].

### 718 2.2.3 Electromagnetic and hadronic calorimeters

719 The ATLAS calorimeters system is composed of two main sub-detectors: the elec-  
 720 tromagnetic (EM) [10] and hadronic [79] calorimeters. The two calorimeters are  
 721 designed to stop and measure the energy of particles coming from  $pp$  collisions  
 722 (or other processes) and sensitive to electromagnetic or strong interactions: the  
 723 EM calorimeter, which targets EM showers and measures the energies of electrons  
 724 and photons, and the hadronic calorimeter, which targets hadronic showers and  
 725 measures the energy of hadrons. The inner sub-detector is the EM calorimeter, sur-  
 726 rounded by the hadronic calorimeter. Both calorimeters are composed of the barrel  
 727 and two symmetric end-caps, as shown in Figure 2.6, and cover the acceptance up  
 728 to  $|\eta| = 4.9$ .

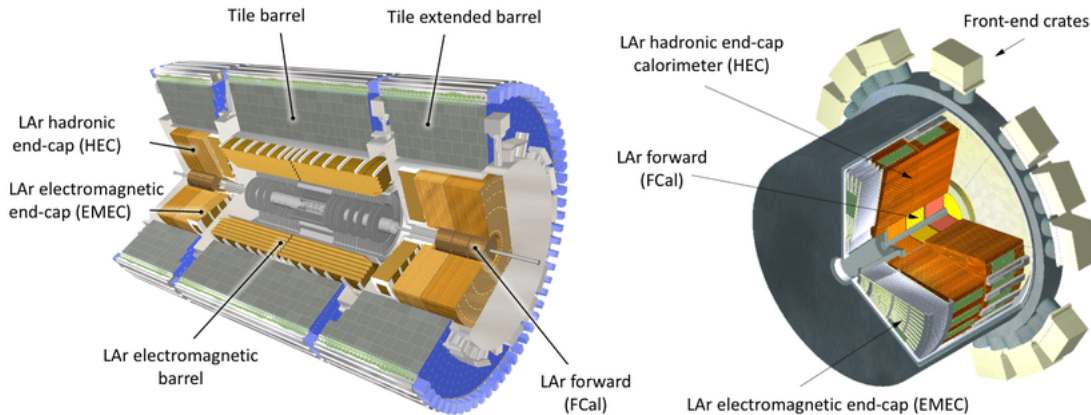


FIGURE 2.6: An overview of ATLAS calorimeter system [142].

### 2.2.3.1 The electromagnetic calorimeter

The ATLAS EM calorimeter is the most relevant sub-detector for this thesis. In this paragraph, the EM showers and the different components of the ATLAS EM calorimeter are described:

**EM shower:** An EM shower begins when a high-energy particle (electron, positron or photon) enters a material. Depending on their properties (charge, mass ...), particles interact differently with matter. In our case we are interested in high-energy electrons and photons interactions. Figure 2.7 shows the fraction of energy loss by electrons in lead (used as an absorber in the ATLAS EM calorimeter) and the photon interaction cross-section as a function of their energies. **Electrons** with low energies lose their energy mainly through ionisation and excitation (collisions with the atoms and molecules of the material and the transferred energy is enough to unbind an electron from this atom), while electrons with energies larger than  $\simeq 10$  MeV, lose their energy with bremsstrahlung (interaction of the incoming particle in the electric field of an atom and emission of a high energy photon). **Photons** with low energies, lose their energy through Compton scattering (photons mainly scatter on the electrons of the atoms constituting the medium) and photoelectric effect (emission of electrons). For photons with energies larger than  $\simeq 10$  MeV, interactions result in conversion, produce electron–positron pairs. **Electrons and photons** with high energy ( $\geq 1$  GeV) interact with matter to produce secondary photons by bremsstrahlung and electron–positron by pair-production with lower energy. These in turn will interact with the matter with the same mechanisms as described before until they lose their energy. This avalanche of produced electrons, positrons, and photons is known as an **EM shower**.

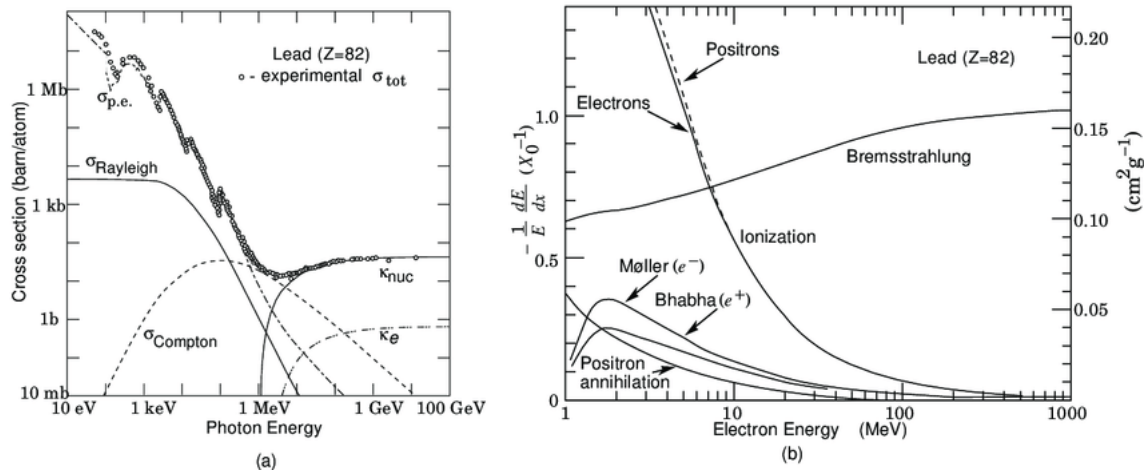


FIGURE 2.7: (a) Photon energy loss in lead as a function of its energy. (b) Electron energy loss in lead as a function of its energy [98].

755 **Energy resolution of an EM calorimeter:** The energy resolution of an EM  
 756 calorimeter can be described by [70]:

$$\left(\frac{\sigma}{E}\right)^2 = \left(\frac{S}{\sqrt{E}}\right)^2 + \left(\frac{N}{E}\right)^2 + C^2 \quad (2.4)$$

757 where the first term on the right side is the stochastic ( $S$ ) term, being due  
 758 to the fluctuations related to the physical development of the shower [73],  
 759 the second term is a noise ( $N$ ) term, coming from the electronic noise of the  
 760 signal readout chain and the pileup noise, the last term is a constant ( $C$ ) term,  
 761 coming from instrumental defects that cause variations of the calorimeter  
 762 response [73], and is independent of the particle energy.

763 The ATLAS EM calorimeter is a lead liquid Argon (LAr) sampling calorimeter.  
 764 It is designed with an accordion geometry, an original idea of D. Fournier [78], in  
 765 order to avoid azimuthal cracks in the detector ( $\phi$  symmetry) [26]. The EM shower  
 766 is generated when particles interact with the absorber (lead). Secondary particles  
 767 produced by these interaction ionise the argon and produce ionisation electrons.  
 768 These ionisation electrons drift towards the anode following the electric field lines  
 769 produced by the high voltage connected to the electrodes. During their drift, these  
 770 ionisation electrons induce on the electrodes (see Figure 2.8) an electric current  
 771 proportional to the number of electrons drifting in the medium, and at the end  
 772 proportional to the energy deposited.

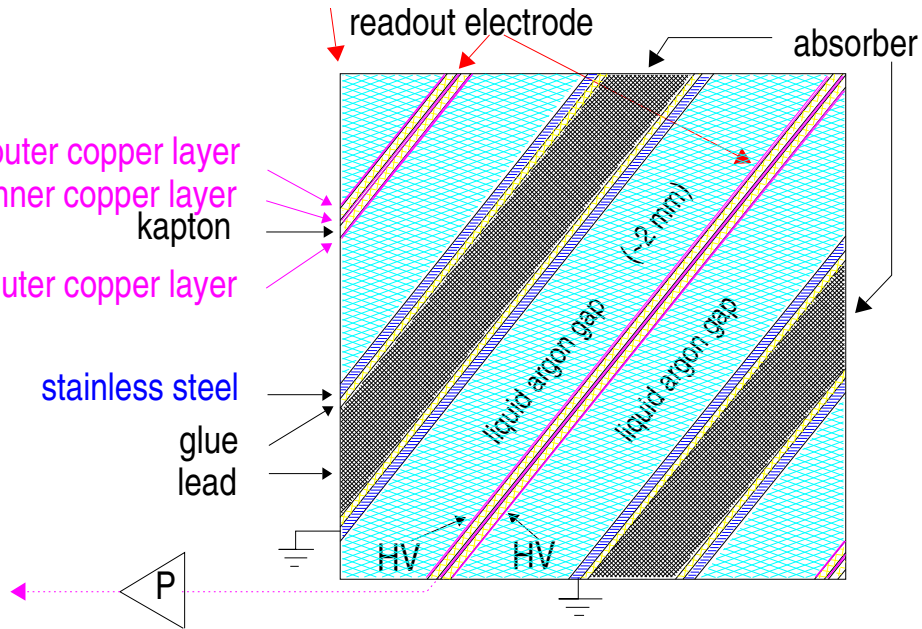


FIGURE 2.8: A sketch of the LAr EM calorimeter [123].

773 The EM calorimeter [26] has two main parts: the **Barrel** which consists of two  
 774 half-barrels separated with a gap of 4mm and covers the regions  $|\eta| < 1.37$ , and two  
 775 **end-caps** placed at each end of the barrel which cover the regions  $1.52 < |\eta| < 3.2$ .  
 776 The part of the end-cap used for precise measurements stops at  $|\eta| \approx 2.4$ . The  
 777 region between the barrel and the end-cap is called the transition region and cor-  
 778 responds to  $1.37 < \eta < 1.52$ , characterised by the presence of a large amount of  
 779 dead material and is not used in precision measurements like the decay of the  
 780 Higgs boson into two photons. For the Run 1  $W$  mass analysis [14] a larger part of  
 781 the detector, corresponding to  $1.2 < \eta < 1.82$  was excluded, due to the higher qual-  
 782 ity wanted and small mismodeling in this region [96]. More details about the EM  
 783 calorimeter can be found in different theses [6, 13, 141, 31, 82]. The EM calorimeter  
 784 is divided in three layers: front, middle and back (as shown in Figure 2.9):

- 785 • Front layer (L1): It has a very fine segmentation along  $\eta$ :  $\Delta\eta \times \Delta\phi = 0.0031 \times$   
 786  $0.1$  in the barrel and  $\Delta\eta \times \Delta\phi$  varying between  $0.0031 \times 0.1$  and  $0.0062 \times 0.1$   
 787 in the end-cap. The fine granularity in  $\eta$  allows to separate a single photon  
 788 from photons coming from:  $\pi^0 \rightarrow \gamma\gamma$ .
- 789 • Middle layer (L2): it is where the particles deposit most of their energy. The  
 790 cells in the middle layer are of size  $\eta$ :  $\Delta\eta \times \Delta\phi = 0.025 \times 0.025$  in the barrel  
 791 and in the end-cap.
- 792 • Back layer (L3): it is where part of the shower leaking after L2 is measured.  
 793 The cells in the middle layer are of size  $\eta$ :  $\Delta\eta \times \Delta\phi = 0.05 \times 0.025$  in the barrel  
 794 and the end-cap.

795 In front of the LAr EM calorimeter, there is for  $0 < |\eta| < 1.8$  a presampler, which  
 796 is also based on LAr technology. A detailed description of the LAr EM calorimeter  
 797 and of the presampler can be found in Table 2.1.

TABLE 2.1: Description of the composition of the LAr calorimeter [25].

		Barrel	End-cap			
<b>EM calorimeter</b>						
Number of layers and $ \eta $ coverage						
Presampler	1	$ \eta  < 1.52$	1	$1.5 <  \eta  < 1.8$		
Calorimeter	3	$ \eta  < 1.35$	2	$1.375 <  \eta  < 1.5$		
	2	$1.35 <  \eta  < 1.475$	3	$1.5 <  \eta  < 2.5$		
			2	$2.5 <  \eta  < 3.2$		
Granularity $\Delta\eta \times \Delta\phi$ versus $ \eta $						
Presampler	$0.025 \times 0.1$	$ \eta  < 1.52$	$0.025 \times 0.1$	$1.5 <  \eta  < 1.8$		
Calorimeter 1st layer	$0.025/8 \times 0.1$	$ \eta  < 1.40$	$0.050 \times 0.1$	$1.375 <  \eta  < 1.425$		
	$0.025 \times 0.025$	$1.40 <  \eta  < 1.475$	$0.025 \times 0.1$	$1.425 <  \eta  < 1.5$		
			$0.025/8 \times 0.1$	$1.5 <  \eta  < 1.8$		
			$0.025/6 \times 0.1$	$1.8 <  \eta  < 2.0$		
			$0.025/4 \times 0.1$	$2.0 <  \eta  < 2.4$		
			$0.025 \times 0.1$	$2.4 <  \eta  < 2.5$		
			$0.1 \times 0.1$	$2.5 <  \eta  < 3.2$		
Calorimeter 2nd layer	$0.025 \times 0.025$	$ \eta  < 1.40$	$0.050 \times 0.025$	$1.375 <  \eta  < 1.425$		
	$0.075 \times 0.025$	$1.40 <  \eta  < 1.475$	$0.025 \times 0.025$	$1.425 <  \eta  < 2.5$		
			$0.1 \times 0.1$	$2.5 <  \eta  < 3.2$		
Calorimeter 3rd layer	$0.050 \times 0.025$	$ \eta  < 1.35$	$0.050 \times 0.025$	$1.5 <  \eta  < 2.5$		
Number of readout channels						
Presampler	7808		1536 (both sides)			
Calorimeter	101760		62208 (both sides)			
<b>LAr hadronic end-cap</b>						
$ \eta $ coverage			$1.5 <  \eta  < 3.2$			
Number of layers			4			
Granularity $\Delta\eta \times \Delta\phi$			$0.1 \times 0.1$	$1.5 <  \eta  < 2.5$		
			$0.2 \times 0.2$	$2.5 <  \eta  < 3.2$		
Readout channels			5632 (both sides)			
<b>LAr forward calorimeter</b>						
$ \eta $ coverage			$3.1 <  \eta  < 4.9$			
Number of layers			3			
Granularity $\Delta x \times \Delta y$ (cm)			FCal1: $3.0 \times 2.6$ FCal1: ~ four times finer FCal2: $3.3 \times 4.2$ FCal2: ~ four times finer FCal3: $5.4 \times 4.7$ FCal3: ~ four times finer	$3.15 <  \eta  < 4.30$ $3.10 <  \eta  < 3.15$ , $4.30 <  \eta  < 4.83$ $3.24 <  \eta  < 4.50$ $3.20 <  \eta  < 3.24$ , $4.50 <  \eta  < 4.81$ $3.32 <  \eta  < 4.60$ $3.29 <  \eta  < 3.32$ , $4.60 <  \eta  < 4.75$		
Readout channels			3524 (both sides)			
<b>Scintillator tile calorimeter</b>						
	Barrel		Extended barrel			
$ \eta $ coverage	$ \eta  < 1.0$		$0.8 <  \eta  < 1.7$			
Number of layers	3		3			
Granularity $\Delta\eta \times \Delta\phi$	$0.1 \times 0.1$		$0.1 \times 0.1$			
Last layer	$0.2 \times 0.1$		$0.2 \times 0.1$			
Readout channels	5760		4092 (both sides)			

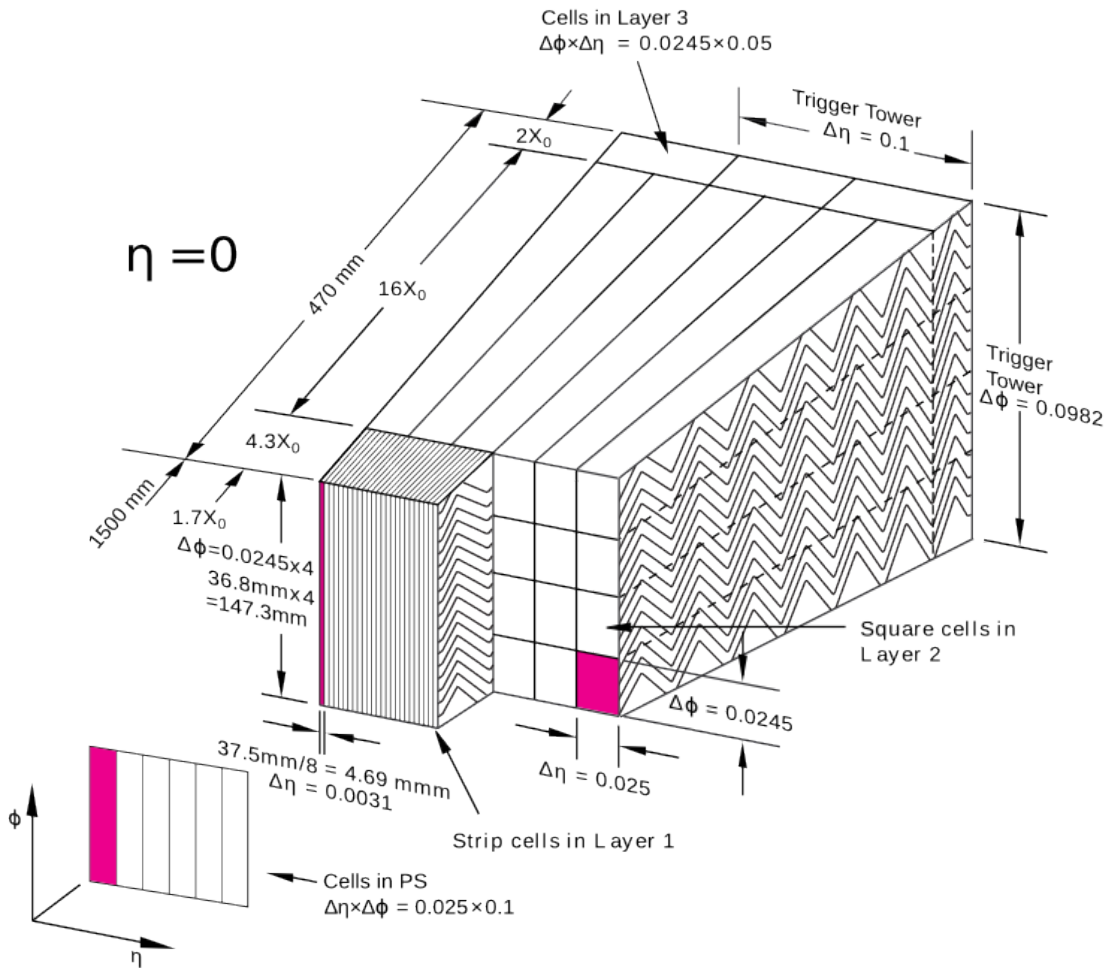


FIGURE 2.9: A sketch of the LAr EM calorimeter layers [135].

798 2.2.3.2 The ATLAS tile hadronic calorimeter

799 The tile hadronic calorimeter is located behind the EM calorimeter and operates in  
800 a similar way but uses iron as an absorber and scintillating tiles as active material.  
801 The tile hadronic calorimeter is composed of three layers covering the range  $|\eta| <$   
802 1.7. The first two layers have the same granularity  $\Delta\eta \times \Delta\phi = 0.1 \times 0.1$  while  
803  $\Delta\eta \times \Delta\phi = 0.2 \times 0.1$  is the granularity of the last layer. The tile hadronic calorimeter  
804 is used to measure the position and energy of the jets.

805 2.2.4 Muon spectrometer and toroidal magnets

806 The ATLAS muon spectrometer, shown in Figure 2.10, is the outermost part of  
807 the ATLAS detector and is designed to measure the position and the energy of  
808 particles that are able to pass through the inner detectors [86]. Since the muons  
809 pass through the calorimeter system with little interaction and therefore conserving  
810 most of their initial energy, they are detected with high efficiency in the Muon  
811 Spectrometer (MS). It consists of four main types of detectors:

812 **Monitor Drift Tubes (MDTs):** They are used for the precision measurement of  
813 muon momentum and cover the entire MS detection region  $|\eta| < 2.7$ . They

814 are built with straw aluminum tubes with 30 mm diameter and each tube is  
 815 filled with an Ar/CO<sub>2</sub> mixture (93% and 7%). The muons ionise the gas and  
 816 signals of the ionisation electrons are measured.

817 **Cathode Strip Chambers (CSCs):** Because of the radiation level in  $2.0 < |\eta| <$   
 818 2.7 [19], the CSCs replace the MDTs in the most inner layer and provide a  
 819 precise track measurement.

820 **Resistive Plate Chambers (RPCs):** In the RPCs two parallel plates are separated  
 821 by a thin layer of gas filled with C<sub>2</sub>H<sub>2</sub>F<sub>4</sub> and SF<sub>6</sub>. The RPCs provide a track  
 822 identification and trigger measurements in the barrel region  $|\eta| < 1.05$ .

823 **Thin Gap Chambers (TGCs):** TGCs are multi-wire proportional chambers filled  
 824 with n-C<sub>5</sub>H<sub>12</sub>. The purpose of the TGCs is to replace RPCs in the end-cap  
 825 regions,  $1.05 < |\eta| < 2.4$ .

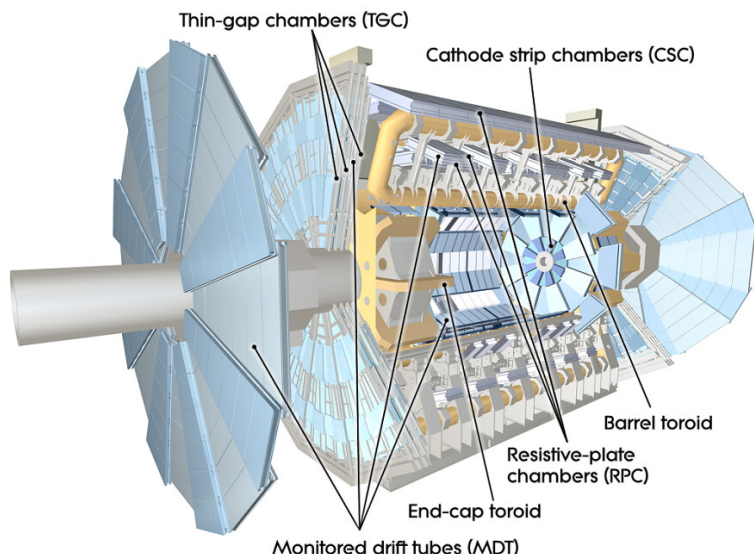


FIGURE 2.10: An overview of ATLAS muon system [3].

### 826 2.2.5 ATLAS trigger and data acquisition system

827 Within the ATLAS detector the proton bunches collide every 25 ns, and can pro-  
 828 duce nearly 600 terabytes of raw data every second [128]. Because of the limited  
 829 storage (each event is characterised with a size of the order of 1 Mb) it is impossi-  
 830 ble to record all these interactions. The aim of the trigger system is to select events  
 831 having desired signatures. The trigger system selects between 100 and 1000 events  
 832 per second out of 1000 million in total [128]. During Run 2, the trigger system [136],  
 833 was divided in two parts (as shown in Figure 2.11):

834 **The L1 trigger:** It is a hardware trigger and performs the first stage of the trig-  
 835 ger. The L1 trigger uses inputs from the muon spectrometer and the  
 836 calorimeter systems and searches for signatures from high- $p_T$  muons, elec-  
 837 trons/photons, jet and  $\tau$ -lepton decays in order to choose desired events. The

838 L1 trigger reduces the event rate from the LHC bunch crossing of 40 MHz to  
 839 about  $> 100$  kHz.

840 **The High Level Trigger (HLT):** The events that have been triggered by the L1 are  
 841 then filtered by the HLT in order to reduce the rate to 1 kHz. The HLT recon-  
 842 structs events using a finer granularity of the data with ID tracks to remove  
 843 most of the pre-selected events.

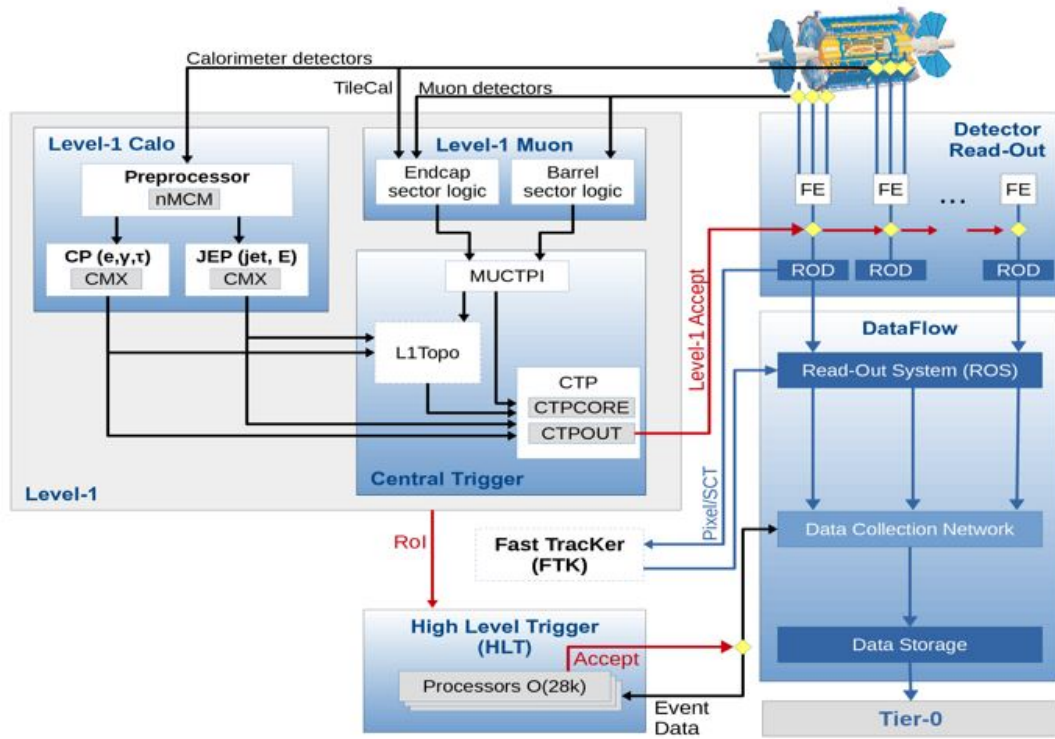


FIGURE 2.11: An overview of ATLAS trigger system [136].

## 844 2.3 Reconstruction of physics objects

845 This section gives an overview of the identification of the electrons and their re-  
 846 construction by the ATLAS detector. The electrons will be used for the calibration  
 847 of the ATLAS EM calorimeter as discussed in Chapter 3.

### 848 2.3.1 Electron reconstruction

849 Electrons and photons are reconstructed in the EM calorimeter (see Chapter 3).  
 850 When electrons and photons enter to the EM calorimeter, they interact with the  
 851 lead absorbers and create the EM showers. The EM showers ionise the liquid  
 852 argon and the ionisation electrons will drift thanks to a high voltage which pro-  
 853 duces an electric field between the electrodes. During their drift, these ionisation  
 854 electrons induce on the electrode an electric current. The charge collection time

855 in the electrode is  $t_d \approx 450$  ns and the induced signal has a triangular shape as  
 856 shown in Figure 2.12. Since the charge collection time (450 ns) is longer than the  
 857 time difference between two bunch crossings at the LHC (25 ns), we will integrate  
 858 in the charge collection time several bunch crossings and include a lot of pileup  
 859 events. In order to reduce this effect, the signals are passed through a bipolar filter  
 860 which shape the signals as shown in Figure 2.12 in order to be more peaked and  
 861 therefore to have a smaller contribution from pileup.

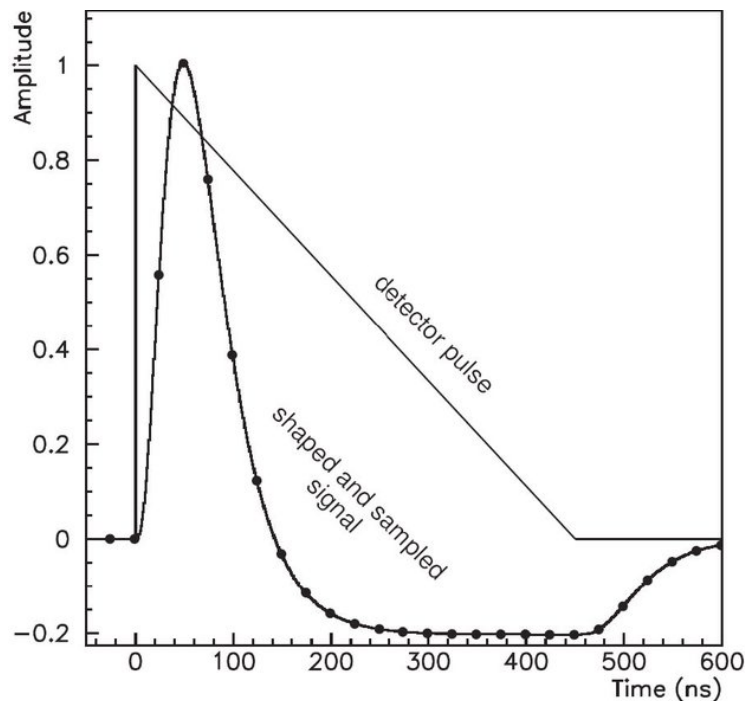


FIGURE 2.12: The pulse shape in the ATLAS LAr calorimeters. The triangular shape is the current pulse generated in the liquid argon by ionisation electrons. The dots shows the positions of the samples separated by 25 ns [127].

862 The pulses recorded for a cell are used to reconstruct the cell energy in MeV  
 863 with the formula:

$$E_{\text{cell}} = F_{\mu A \rightarrow \text{MeV}} \times F_{\text{DAC} \rightarrow \mu A} \times \frac{1}{\frac{M_{\text{phys}}}{M_{\text{cali}}}} \times G \times A \quad (2.5)$$

864 where:

- 865 •  $F_{\mu A \rightarrow \text{MeV}}$ : relates the current from ionisation electrons to the energy de-  
 866 posited in the EM cell [116].
- 867 •  $F_{\text{DAC} \rightarrow \mu A}$ : is a conversion factor related to the digital-to-analog converter  
 868 (DAC).
- 869 •  $\frac{M_{\text{phys}}}{M_{\text{cali}}}$ : is used to correct the gain to take into account the fact that the injected  
 870 calibration signal is exponential while the physics signal is triangular (see  
 871 Figure 2.12), and have therefore slightly different maximum amplitudes after  
 872 the bipolar shaping. It can be obtained from delayed calibration runs, as it is  
 873 described in [54].

- $G$ : represents the cell gain, measured during the calibration runs (expressed in ADC  $\rightarrow$  DAC).
- $A$ : is the signal amplitude extracted using the optimal filtering method [51, 13].

The procedure to reconstruct electrons starts by building a cluster using the measured cell energies in the EM calorimeter, these energies being obtained by equation (2.5). At the beginning of Run 2, a sliding-window clustering algorithm was used, but since 2017, a new algorithm called “dynamical topological cell clustering algorithm” is used. This new algorithm improves the measurement of the electron and photon energy, specially when an electron is emitting a photon by bremsstrahlung [69]. The main difference between the “sliding-window clustering” and the “topological clustering” algorithms, is that the first one is characterised by a fixed-size window, unlike the topological clustering where the selection of cells in a cluster depends on a parameter,  $\varsigma_{\text{cell}}^{\text{EM}}$ , called cell significance, and computed as:

$$\varsigma_{\text{cell}}^{\text{EM}} = \left| \frac{E_{\text{cell}}^{\text{EM}}}{\sigma_{\text{noise,cell}}^{\text{EM}}} \right| \quad (2.6)$$

where  $E_{\text{cell}}^{\text{EM}}$  is the absolute cell energy at the EM scale [69] and  $\sigma_{\text{noise,cell}}^{\text{EM}}$  is the expected cell noise (electronic and pileup noise). This algorithm starts by building clusters of EM cells, called *topo-cluster*. Each *topo-cluster* is built using the same procedure:

- A *topo-cluster* includes cells characterised by  $\varsigma > 4$ .
- The neighboring cells with  $\varsigma > 2$  are added to the *topo-cluster*.
- All neighboring cells with  $\varsigma > 0$  are added to the *topo-cluster*.

The procedure of grouping cells in *topo-cluster* is called also 4 – 2 – 0 which refers to the values of the thresholds on  $\varsigma$ . Figure 2.13 shows an overview of the topo-cluster construction.

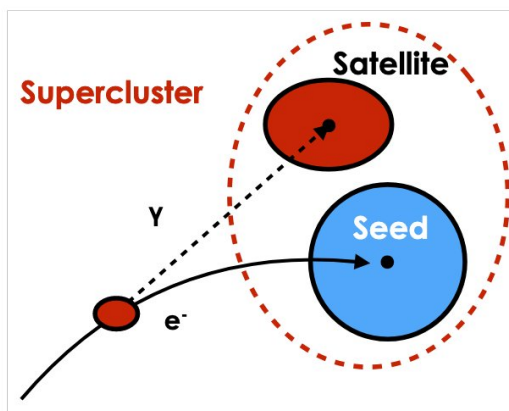


FIGURE 2.13: Illustration of a *topo-cluster* construction [69].

In addition to the procedure described above, there are other selections applied to a topo-cluster to ensure a large rejection of pileup, and to isolate clusters that

901 are primarily from showers in the EM calorimeter. Those selections are based on  
 902 the factor  $f_{\text{EM}}$  computed as:

$$f_{\text{EM}} = \frac{E_{\text{L1}} + E_{\text{L2}} + E_{\text{L3}}}{E_{\text{Cluster}}} \quad (2.7)$$

903 where  $E_{\text{L1}}$ ,  $E_{\text{L2}}$  and  $E_{\text{L3}}$  are the energies deposited in the first, second and last  
 904 layers,  $E_{\text{Cluster}}$  is the energy in the cluster. At the end, only topo-clusters with  
 905  $f_{\text{EM}} > 0.5$  and  $E_{\text{Cluster}} > 400$  MeV are kept. As shown in Figure 2.14, the selection  
 906  $f_{\text{EM}} > 0.5$  allows to reject over than  $\approx 60\%$  of pileup clusters without changing the  
 907 reconstruction efficiency of true electron topo-clusters [69].

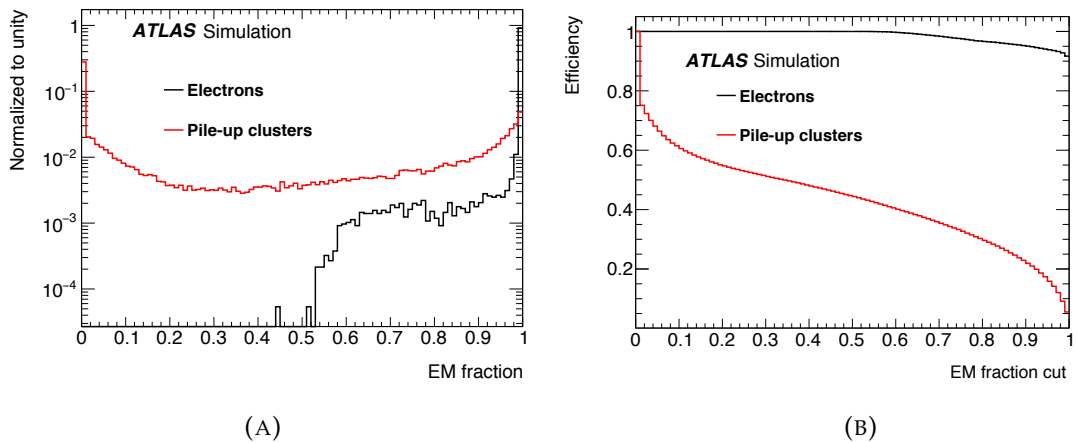


FIGURE 2.14: (A) Distribution of  $f_{\text{EM}}$ . (B) Reconstruction efficiency as a function of  $f_{\text{EM}}$  [69].

### 2.3.2 Electron identification

In fact, not all of the electrons reconstructed by the “topological clustering” algorithms are prompt electrons. In order to reject background objects, an identification algorithm is used to select prompt electrons and photons from the backgrounds coming from hadronic jets, prompt electrons from photon conversions, and QCD jets. The identification algorithm is based on a likelihood-based (LH) identification, where we use information from the tracking system and the calorimeter system. The discriminant variables are based on the EM shower information, and are shown in Table 2.2.

TABLE 2.2: List of the discrimination variables used in the electron and photon identification [68].

Category	Description	Name	Usage
Hadronic leakage	Ratio of $E_T$ in the first layer of the hadronic calorimeter to $E_T$ of the EM cluster (used over the ranges $ \eta  < 0.8$ and $ \eta  > 1.37$ )	$R_{\text{had}_1}$	$e/\gamma$
	Ratio of $E_T$ in the hadronic calorimeter to $E_T$ of the EM cluster (used over the range $0.8 <  \eta  < 1.37$ )	$R_{\text{had}}$	$e/\gamma$
EM third layer	Ratio of the energy in the third layer to the total energy in the EM calorimeter	$f_3$	$e$
EM second layer	Ratio of the sum of the energies of the cells contained in a $3 \times 7 \eta \times \phi$ rectangle (measured in cell units) to the sum of the cell energies in a $7 \times 7$ rectangle, both centred around the most energetic cell	$R_\eta$	$e/\gamma$
	Lateral shower width, $\sqrt{(\sum E_i \eta_i^2)/(\sum E_i) - ((\sum E_i \eta_i)/(\sum E_i))^2}$ , where $E_i$ is the energy and $\eta_i$ is the pseudorapidity of cell $i$ and the sum is calculated within a window of $3 \times 5$ cells	$w_{\eta_2}$	$e/\gamma$
	Ratio of the sum of the energies of the cells contained in a $3 \times 3 \eta \times \phi$ rectangle (measured in cell units) to the sum of the cell energies in a $3 \times 7$ rectangle, both centred around the most energetic cell	$R_\phi$	$e/\gamma$
EM first layer	Total lateral shower width, $\sqrt{(\sum E_i (i - i_{\text{max}})^2)/(\sum E_i)}$ , where $i$ runs over all cells in a window of $\Delta\eta \approx 0.0625$ and $i_{\text{max}}$ is the index of the highest-energy cell	$w_{\text{s tot}}$	$e/\gamma$
	Lateral shower width, $\sqrt{(\sum E_i (i - i_{\text{max}})^2)/(\sum E_i)}$ , where $i$ runs over all cells in a window of 3 cells around the highest-energy cell	$w_{\text{s 3}}$	$\gamma$
	Energy fraction outside core of three central cells, within seven cells	$f_{\text{side}}$	$\gamma$
	Difference between the energy of the cell associated with the second maximum, and the energy reconstructed in the cell with the smallest value found between the first and second maxima	$\Delta E_s$	$\gamma$
	Ratio of the energy difference between the maximum energy deposit and the energy deposit in a secondary maximum in the cluster to the sum of these energies	$E_{\text{ratio}}$	$e/\gamma$
	Ratio of the energy measured in the first layer of the electromagnetic calorimeter to the total energy of the EM cluster	$f_1$	$e/\gamma$
Track conditions	Number of hits in the innermost pixel layer	$n_{\text{innermost}}$	$e$
	Number of hits in the pixel detector	$n_{\text{pixel}}$	$e$
	Total number of hits in the pixel and SCT detectors	$n_{\text{Si}}$	$e$
	Transverse impact parameter relative to the beam-line	$d_0$	$e$
	Significance of transverse impact parameter defined as the ratio of $d_0$ to its uncertainty	$ d_0/\sigma(d_0) $	$e$
	Momentum lost by the track between the perigee and the last measurement point divided by the momentum at perigee	$\Delta p/p$	$e$
Track–cluster matching	Likelihood probability based on transition radiation in the TRT	$e_{\text{ProbabilityHT}}$	$e$
	$\Delta\eta$ between the cluster position in the first layer of the EM calorimeter and the extrapolated track	$\Delta\eta_1$	$e$
	$\Delta\phi$ between the cluster position in the second layer of the EM calorimeter and the momentum-rescaled track, extrapolated from the perigee, times the charge $q$	$\Delta\phi_{\text{res}}$	$e$
	Ratio of the cluster energy to the measured track momentum	$E/p$	$e$



## 917 Chapter 3

# 918 Calibration of the electromagnetic 919 calorimeter

## 920 3.1 Introduction

921 Electromagnetic particles, electrons and photons, are used essentially in all analy-  
 922 ses in particular in the studies of the Higgs boson properties and in the precision  
 923 measurement of electroweak parameters such as the  $W$  boson mass, allowing for  
 924 a consistency test for the Standard Model. As described in Chapter 2, electromag-  
 925 netic particles are stopped and measured in the EM calorimeter. To reach a good  
 926 precision in our measurements, a precise electron and photon energy calibration  
 927 is required. The calibration procedure is based on  $Z \rightarrow ee$  samples, because of the  
 928 high statistics and clean final state which characterises this channel. In this chap-  
 929 ter, we will discuss the electron and photon energy calibration for the nominal and  
 930 low pile-up data collected during Run 2 with the ATLAS detector.

## 931 3.2 Overview of the calibration procedure

932 The calibration of the EM calorimeter is a complex procedure and was established  
 933 during Run 1 [67]. The aim of the calibration procedure, summarised in Figure 3.1,  
 934 is to measure the energy of electrons and photons with the best precision and reso-  
 935 lution. In order to estimate the signal and background contribution, the generated  
 936 events are passed through a full simulation of the ATLAS detector using GEANT4  
 937 [8].

938 The calibration procedure starts with the energy in EM calorimeter clusters (see  
 939 Chapter 2), and can be described as follows:

940 **Step 1:** based on a MultiVariate Algorithm (MVA) [107], it allows to determine  
 941 the energy of electrons and photons using the calorimeter cluster properties,  
 942 measured by the EM calorimeter. The MVA is performed separately for elec-  
 943 trons, converted and unconverted photons [67, 100, 151].

944 **Step 2:** this step is related to the EM calorimeter design. In fact, the energy of  
 945 electrons and photons is obtained using the energy deposit in different layers  
 946 of the EM calorimeter. This step equalises the energy scales of the different  
 947 longitudinal layers between data and simulation [67].

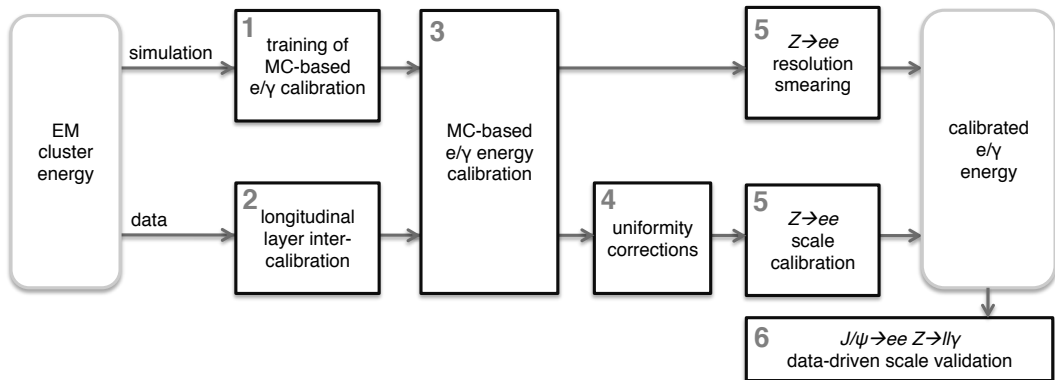


FIGURE 3.1: Schematic overview of the procedure used to calibrate the energy response of electrons and photons in ATLAS [67].

948 **Step 3:** the MC-based calibration determined in previous steps is applied to the  
 949 energy of the clusters in data and simulation.

950 **Step 4:** the aim of this step is to include corrections which take into account the  
 951 uniformity of the calorimeter energy reconstruction as: high-voltage inho-  
 952 mogeneities [18], (where a perfect correction is taken into account in the de-  
 953 tector simulation for the zones where there is a "stable" problem) geometric  
 954 effects such as the inter-module widening (IMW) [113] which are not taken  
 955 into account in the detector simulation, or biases related to the EM in the  
 956 detecteceletronic calibration [18].

957 **Step 5:** at this step of the calibration procedure, the electron response in data is  
 958 calibrated to match the expected value in simulation. Also, an additional  
 959 correction factor aiming to correct the resolution is applied to the simulation,  
 960 in order to match the data. This step is an important part of this thesis and  
 961 will be discussed in Sec. 3.3.

962 **Step 6:** is the last step, and it does the validation of the scale extracted in step 5  
 963 using  $J/\psi \rightarrow ee$  and  $Z \rightarrow ll\gamma$  processes.

964 In this thesis we will focus on the extraction of the energy scale factors showed  
 965 in step 5 of Figure 3.1, for the nominal runs and low pile-up runs used for the  
 966 precise measurement of  $M_W$ . As the  $Z$  boson mass is precisely measured in LEP  
 967 experiments [58] and there is a large statistics of  $Z$  bosons in ATLAS, the  $Z$  boson  
 968 decay channel ( $Z \rightarrow ee$ ) is used for the extraction of the energy scale factors.

### 969 3.3 Energy scale and resolution determination with 970 electrons from $Z \rightarrow ee$ decays

#### 971 3.3.1 Overview

972 After applying the first steps of the calibration procedure (steps 1 to 4 described in  
 973 Figure 3.1), we still observe an important difference between data and simulation.  
 974 The sources of the difference are not precisely known. This difference between

975 data and simulation can be seen in the Figure 3.2, which shows the di-electron invariant mass  $m_{ee}$  at the step 4 of the calibration procedure, as defined in Figure 3.1,  
 976 and computed as:  
 977

$$m_{ee} = \sqrt{2E_1 E_2 (1 - \cos \theta_{12})}, \quad (3.1)$$

978 where  $\theta_{12}$  is the angle between the two electrons measured by the track, and  $E_1, E_2$  are their energies. The discrepancies showed in Figure 3.2 affect the central value

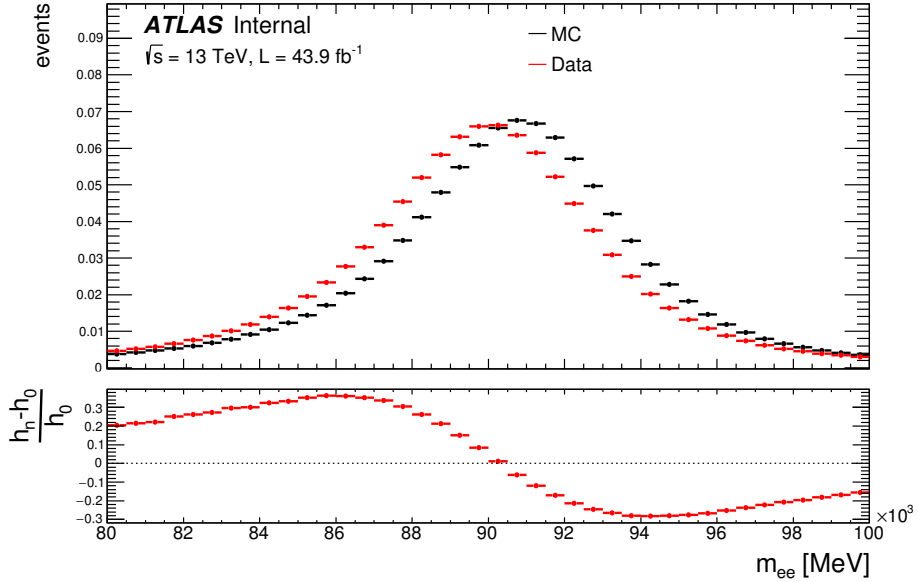


FIGURE 3.2: The di-electron invariant mass  $m_{ee}$  after step 4 of the calibration procedure, Figure 3.1, for data and simulation.

979 of the energy response and the energy resolution. To correct for this difference  
 980 between data and simulation, two correction factors are extracted. The next para-  
 981 graph will discuss the methodology used to extract those correction factors.  
 982

### 983 3.3.2 Definition of the correction factors

984 As discussed in the previous paragraph, two correction factors are extracted from  
 985 the  $Z \rightarrow ee$  channel. The correction factors are called the energy scale factors  $\alpha$   
 986 and the additional constant term  $c'$ . The factors  $(\alpha, c')$  will be expressed in  $\eta$  bin  $i$ ,  
 987 defined in sec. 3.5.1, as  $(\alpha_i, c'_i)$ :

- 988 • The energy scale factor  $\alpha$ : it is applied to the data in order to match the  
 989 energy response of the simulation:

$$E_i^{\text{corr}} = \frac{E_i^{\text{data}}}{1 + \alpha_i} \quad (3.2)$$

990 where  $E^{\text{data}}$  is the measured energy and  $E^{\text{corr}}$  is the corrected energy.

991 • The additional constant term  $c'$ : it is applied to the simulation to be in agree-  
 992 ment with the energy resolution of the data:

$$\left( \frac{\sigma(E)}{E} \right)_i^{\text{corr}} = \left( \frac{\sigma(E)}{E} \right)_i^{\text{MC}} \oplus c'_i \quad (3.3)$$

993 where  $\sigma(E)^{\text{corr}}$  is the resolution of the simulation after applying  $c'$ , supposed  
 994 to be equal to  $\sigma(E)^{\text{data}}$ , which is the resolution of the data, and  $\sigma(E)^{\text{MC}}$  is the  
 995 resolution of the simulation before applying  $c'$ .

### 996 3.3.3 Effect of the scale factors ( $\alpha, c'$ ) on the di-electrons mass $m_{ee}$

997 The scale factors ( $\alpha, c'$ ) are computed using the comparison of the di-electrons  
 998 invariant mass between data and simulation. Before discussing the method used  
 999 for the extraction of the scale factors, we will discuss in this part the effect of the  
 1000 scale factors ( $\alpha, c'$ ) on the invariant mass  $m_{ee}$ :

$$m_{ee}^{\text{MC}} = \sqrt{2E_1^{\text{MC}}E_2^{\text{MC}}(1 - \cos\theta_{12})}, \quad (3.4)$$

1001 by replacing  $E_1^{\text{MC}}$  and  $E_2^{\text{MC}}$  with their expressions as shown in equation (3.2). The  
 1002 effect of the scale factor  $\alpha$  on  $m_{ee}$  is expressed as:

$$m_{ee}^{\text{data}} = m_{ee}^{\text{MC}} \sqrt{(1 + \alpha_i)(1 + \alpha_j)}, \quad (3.5)$$

1003 where  $i$  and  $j$  are  $\eta_{\text{calo}}$  bins where each electron falls in. By neglecting the term of  
 1004 the second order ( $\alpha_i \times \alpha_j$ ) the invariant mass is expressed as:

$$m_{ee}^{\text{data}} = m_{ee}^{\text{MC}}(1 + \alpha_{i,j}), \quad (3.6)$$

1005 and  $\alpha_{i,j}$  is written as:

$$\alpha_{i,j} = \frac{\alpha_i + \alpha_j}{2}. \quad (3.7)$$

1006 Contrary to the scale factor  $\alpha$ , we can not relate directly the additional constant  
 1007 term  $c'$  and the resolution on the invariant mass. Instead, the di-electron invariant  
 1008 mass resolution is expressed in term of the relative energy resolution as:

$$\begin{aligned} \left( \frac{\sigma(m)}{m} \right)_{\text{data}}^2 &\simeq \frac{1}{4} \left( \left( \frac{\sigma(E_1)}{E_1} \right)_{\text{data}}^2 + \left( \frac{\sigma(E_2)}{E_2} \right)_{\text{data}}^2 \right) \\ &= \frac{1}{4} \left( \left( \frac{\sigma(E_1)}{E_1} \right)_{\text{MC}}^2 + c_i'^2 + \left( \frac{\sigma(E_2)}{E_2} \right)_{\text{MC}}^2 + c_j'^2 \right) \\ &= \left( \frac{\sigma(m)}{m} \right)_{\text{MC}}^2 + \frac{c_i'^2 + c_j'^2}{4}. \end{aligned} \quad (3.8)$$

1009 What is done is to apply to both electrons (with independent random numbers) an  
 1010 effective correction  $c'_{i,j}$  and the resolution is therefore expressed as:

$$\left(\frac{\sigma(m)}{m}\right)_{\text{data}}^2 = \left(\frac{\sigma(m)}{m}\right)_{\text{MC}}^2 + \frac{c_i'^2 + c_j'^2}{4} = \left(\frac{\sigma(m)}{m}\right)_{\text{MC}}^2 + \frac{c_{ij}'^2}{2}, \quad (3.9)$$

1011 and  $c'_{i,j}$  is written as:

$$c_{ij}'^2 \equiv \frac{c_i'^2 + c_j'^2}{2}. \quad (3.10)$$

1012 Finally, the calibration of the EM calorimeter is simplified to the extraction of the  
 1013 correction factors  $\alpha_{i,j}$  and  $c'_{i,j}$ . To extract these correction factors, the template  
 1014 method in [36, 38] is used for the early Run 2 analysis with a sliding window  
 1015 clustering algorithm, and in [15] for the final Run 2 algorithm with the dynamical  
 1016 topo-cell clustering algorithm (see Chapter 2). The next paragraph will give a  
 1017 detailed explanation of this method.

## 1018 3.4 Template method for the energy scale factors

### 1019 3.4.1 Methodology of the template method

1020 The template method described in [82] was established during Run 1 for the ex-  
 1021 traction of the correction factors  $\alpha_{i,j}$  and  $c'_{i,j}$ . The corrections are determined inde-  
 1022 pendently in each  $(\eta_{\text{calo}}^i, \eta_{\text{calo}}^j)$  configuration. The idea of the template method is to  
 1023 apply hypothesized values of the scale factors to simulation. For each MC event,  
 1024 the di-electron invariant mass is modified and expressed as:

$$m_{ee}^{\text{template}} = m_{ee}^{\text{MC}} \sqrt{((1 + c'_{i,j} \times N_i(0, 1)) (1 + c'_{i,j} \times N_j(0, 1)) (1 + \alpha_{i,j}) (1 + \alpha_{i,j})).} \quad (3.11)$$

1025 For each couple  $(\alpha_{i,j}, c'_{i,j})$ , the new mass distribution is called a template. The  
 1026 comparison between the template and data distributions is done using a  $\chi^2$  test,  
 1027 by default for mass values between 80 and 100 GeV:

$$\chi^2 = \sum_{k=1}^{N_{\text{bins}}} \frac{\left(m_{ee,k}^{\text{template}} - m_{ee,k}^{\text{data}}\right)^2}{\left(\sigma_k^{\text{template}}\right)^2 + \left(\sigma_k^{\text{data}}\right)^2}, \quad (3.12)$$

1028 where  $N_{\text{bins}}$  is the number of mass bins used,  $m_{ee,k}^{\text{template}}$  and  $m_{ee,k}^{\text{data}}$  are the bin con-  
 1029 tents of the invariant mass distributions in bin  $k$  and  $\sigma_k^{\text{template}}$  and  $\sigma_k^{\text{data}}$  are the  
 1030 corresponding uncertainties in the bin. By repeating this procedure for all the tem-  
 1031 plates, we can plot a 2D scan of the  $\chi^2$  as shown in the Figure 3.3. The minimum of  
 1032 the distribution gives the final correction factors  $(\hat{\alpha}_{i,j}, \hat{c}'_{i,j})$ , which correspond to the  
 1033 best agreement between data and simulation. The determination of the correction  
 1034 factors is related to the determination of the minimum of  $\chi^2$ .

1035 There is in Figure 3.3 a small correlation between  $\alpha$  and  $c'$  and the minimum  
 1036 of this 2D distributions is obtained using several 1D fits. The minimisation proce-  
 1037 dure [82] is shown in Figure 3.4 and can be summarised in the steps below:

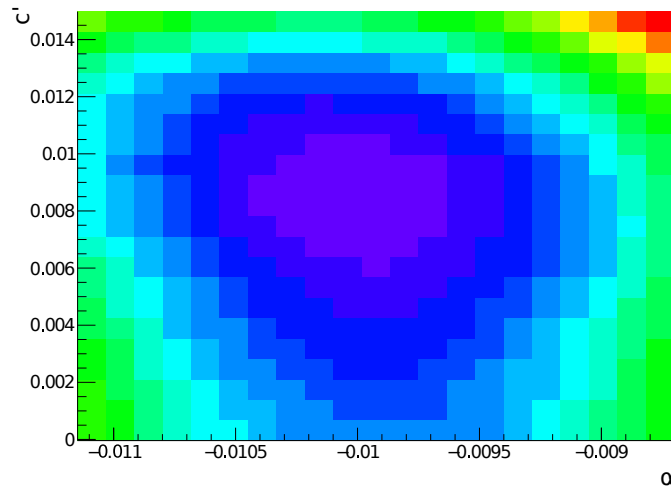


FIGURE 3.3: Distribution of  $\chi^2$  test between data and templates, as a function of the energy scale factor and the resolution factor.

- For a fixed value of  $c'_{ij}$ , we look at the  $\chi^2$  distribution as a function of  $\alpha_{ij}$ , as can be seen as a line in Figure 3.3, and the resulting  $\chi^2$  is fitted using a parabolic shape function:

$$\chi^2(\alpha_{ij}, c'_{ij}) = a_0(c'_{ij}) + \frac{(\alpha_{ij} - \alpha_{ij,\min}(c'_{ij}))^2}{(\delta\alpha_{ij}(c'_{ij}))^2} \quad (3.13)$$

where  $\delta\alpha_{ij}(c'_{ij})$  is the uncertainty on  $\alpha_{ij,\min}(c'_{ij})$  determined by  $\Delta\chi^2 = 1$  around the minimum.

- All the  $c'_{ij}$  lines of Figure 3.3 are scanned, and the  $\chi^2_{\min}(c'_{ij})$  is plotted as a function of  $c'_{ij}$  and fitted using a 3<sup>rd</sup> polynomial function characterised with the parameters  $(b_0, b_1, b_2)$ :

$$\chi^2_{\min}(c'_{ij}) = b_0 + \frac{(c'_{ij} - \hat{c}'_{ij})^2}{b_2^2} + b_1 \frac{(c'_{ij} - \hat{c}'_{ij})^3}{b_2^3}. \quad (3.14)$$

The minimum of this distribution  $\hat{c}'_{ij}$  is the most probable value (MPV) for the additional constant term in the configuration  $(\eta_1, \eta_2)$ . The uncertainty on  $\hat{c}'_{ij}$  is determined by  $\Delta\chi^2 = 1$ .

- Finally,  $\alpha_{ij,\min}(c'_{ij})$  is plotted as a function of  $\hat{c}'_{ij}$  and a linear fit is performed around  $\hat{c}'_{ij}$ . The most probable value  $\hat{\alpha}'_{ij}$  is defined as the value corresponding to  $\hat{c}'_{ij}$ .

### 3.4.2 Inversion procedure

- As the values of  $\alpha_{ij}$  and  $c'_{ij}$  are computed for each configuration  $(\eta_1, \eta_2)$  as described above, the correction factors  $\alpha_i$  and  $c'_i$  must then be computed. For the

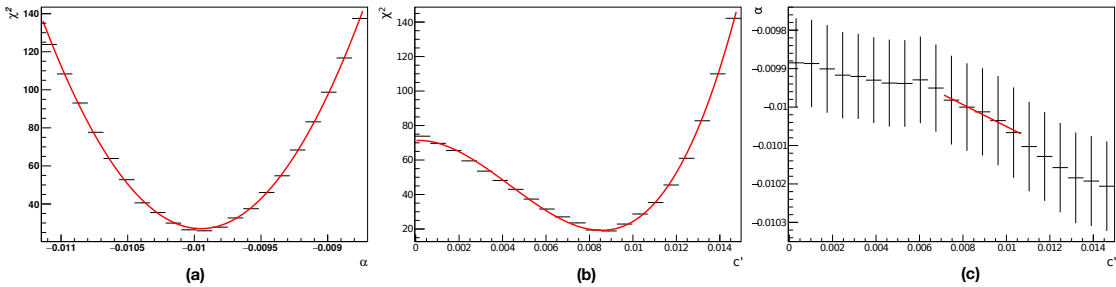


FIGURE 3.4: (a):  $\chi^2$  as a function of  $\alpha_{i,j}$  for a given value of  $c'_{ij}$ . (b):  $\chi^2_{\min}(c'_{ij})$  as a function of  $c'_{ij}$ . (c):  $\alpha_{ij,\min}(c'_{ij})$  as a function of  $c'_{ij}$ .

1055 energy scale factor, and because of the linear equation (3.7),  $\alpha_i$  can be computed  
 1056 by the minimisation of a  $\chi^2_\alpha$  described as:

$$\chi^2_\alpha = \sum_{i,j \leq i} \frac{(\alpha_i + \alpha_j - 2\alpha_{ij})^2}{(\Delta\alpha_{ij})^2}. \quad (3.15)$$

1057 On the other hand, the extraction of the additional constant term  $c'_i$  is more com-  
 1058 plicated because of the non-linearity of equation (3.10) describing the relation be-  
 1059 tween  $c'_{i,j}$  and  $(c'_i, c'_j)$ . The extraction of the constant  $c'_i$  is based on the likelihood  
 1060 minimisation [83, 108] using the formula:

$$\chi^2_{c'} = \sum_{i,j \leq i} \frac{\left( \sqrt{\frac{c_i'^2 + c_j'^2}{2}} - c'_{ij} \right)^2}{(\delta c'_{ij})^2}. \quad (3.16)$$

## 1061 3.5 Selections and corrections

1062 The results presented in this thesis are based on data collected during Run 2 with  
 1063 the ATLAS detector, corresponding to an integrated luminosity of  $139 \text{ fb}^{-1}$  col-  
 1064 lected in 2015, 2016, 2017 and 2018. The data samples are detailed in [156]. To  
 1065 select  $Z \rightarrow ee$  events, electrons candidates must pass the triggers shown in Table  
 1066 3.1.

TABLE 3.1: Triggers used for data collected during Run 2.

Year	Trigger
2015	HLT_2e12_lhloose_L12EM10VH
2016	HLT_2e17_lhvloose_nod0
2017	HLT_2e24_lhvloose_nod0
2018	HLT_2e24_lhvloose_nod0    HLT_2e17_lhvloose_nod0_L12EM15VHI

1067 In addition, electron events must pass the MediumLH identification (ID) and  
 1068 loose isolation criteria in order to reduce mis-identified electrons and to suppress  
 1069 the QCD background [82]. Also, electrons are required to have  $p_T^\ell > 27 \text{ GeV}$  and

1070  $|\eta_{\text{track}}| < 2.47$ . Finally, events which pass all the selections mentioned above and  
 1071 with opposite charge are selected in the range  $0 < m_{ee} < 180$  GeV. The number of  
 1072 selected events is shown in Table 3.2.

TABLE 3.2: Number of selected events which passes the selections used for the  $Z \rightarrow ee$  analysis.

	2015	2016	2017	2018
Data	1.62 M	15.6 M	19.2 M	25.4 M
Simulation	6.53 M (MC16a)	18.5 M (MC16a)	20.2 M (MC16d)	28.8 M (MC16e)

1073 In Table 3.2, MC16a, MC16d and MC16e indicate the tag of simulation samples.  
 1074 Additional corrections in terms of weights to match the data need to be applied to  
 1075 the simulation. One of the corrections is the pile-up reweighting, used to repro-  
 1076 duce the distribution of the number of  $pp$  collisions per bunch crossing in the data.  
 1077 Figure 3.5 shows an example of the actual number of interactions per bunch cross-  
 1078 ing in data compared to simulation after the pile-up reweighting.

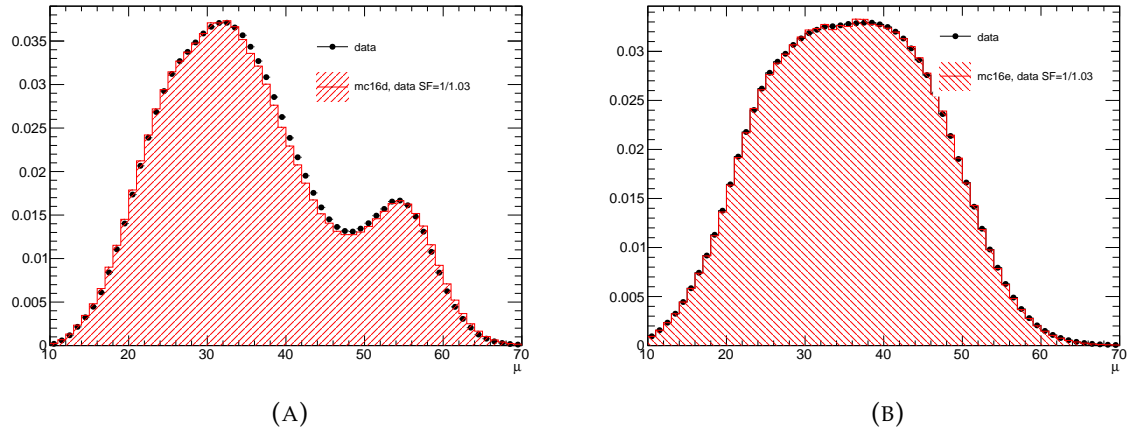


FIGURE 3.5: The actual number of interactions per bunch crossing of data which is re-scaled by a factor 1/1.03 and simulation for 2017 (A) and 2018 (B), after the pile-up reweighting procedure.

1079 Also, the difference between data and simulation for the reconstruction, iden-  
 1080 tification, isolation and trigger efficiencies is taken into account by applying cor-  
 1081 responding scale factors to the simulation. As shown in Figure 3.6, the changes  
 1082 in the invariant mass distribution of the MC before and after applying the pile-  
 1083 up reweighting correction and the different scale factors is typically small. In the  
 1084 current analysis, the electroweak background has been neglected. It is included in  
 1085 the systematic uncertainty (Table 3.4) and its contribution is smaller than 0.05% for  
 1086 invariant mass  $m_{ee}$  between 75 and 97 GeV.

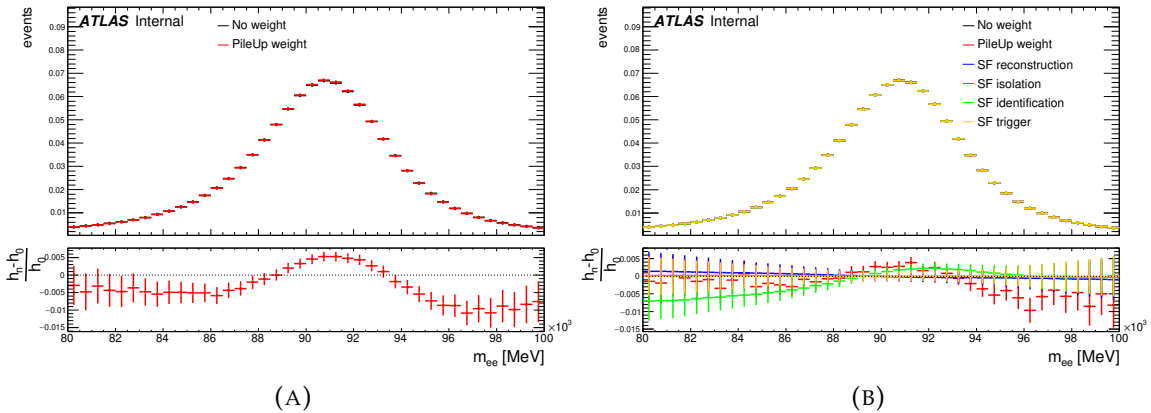


FIGURE 3.6: Effect of the pile-up reweighting (A) and different efficiency scale factors (B) corrections on the normalized  $Z \rightarrow ee$  mass distribution in simulation. The bottom plot shows the fractional differences of the invariant mass distribution without any scale factors (labelled  $h_0$ ) and with the application of different efficiency scale factors or reweightings (labelled  $h_n$ ) separately.

### 1087 3.5.1 Binning

1088 During Run 1, the energy scale factor  $\alpha$  was extracted in 34 bins along  $\eta$ . For  
 1089 Run 2 and because of the high statistics of the data collected, the energy scale  
 1090 factors  $\alpha$  are extracted using 68 bins, which correspond to Run 1 binning splitted  
 1091 by two. The small binning allows a better correction of data. For the additional  
 1092 constant term, the Run 1 binning is kept in order to maximise the statistics in each  
 1093 configuration. Table 3.3 shows the new binning used for  $\alpha$  and  $c'$  in the barrel and  
 end-cap regions.

TABLE 3.3: Absolute values of  $\eta_{\text{calo}}$  bin boundaries for energy scale factors  $\alpha$  and resolution constant terms  $c'$  used in the calibration of electromagnetic calorimeter during Run 2.

Barrel															
$\alpha_i$	0	0.1	0.2	0.3	0.4	0.5	0.6	0.7	0.8	0.9	1	1.1	1.2	1.285	1.37
$c'_i$	0		0.2		0.4		0.6		0.8		1		1.2		1.37
End-cap															
$\alpha_i$	1.55	1.59	1.63	1.6775	1.725	1.7625	1.8	1.9	2	2.05	2.1	2.2	2.3	2.35	2.4
$c'_i$	1.55						1.8	2			2.3			2.435	2.47

1094

## 1095 3.6 Results

### 1096 3.6.1 Extraction of the correction factors ( $\alpha, c'$ )

1097 The results of the energy scale factors  $\alpha$  for Run 2 data sets are presented in Figure  
 1098 3.7. The results are extracted separately for each year to take into account the

1099 data taking conditions. The observed differences (up to  $\pm 0.005$ ) in the end-cap  
 1100 region between the different years are related to two effects [2]:

1101 **Change of luminosity:** at high luminosity, a larger current  $I$  is induced on HV  
 1102 lines due to a larger amount of energy deposited in the liquid argon gaps.  
 1103 The HV in the detector is reduced by  $R \times I$ , where  $R$  is the resistance between  
 1104 the power supply where the voltage is set to a constant value and the LAr  
 1105 gap. This effect is called high voltage drop and is dominated by luminosity  
 1106 effects.

1107 **Change of LAr temperature:** this effect is related to the change of liquid argon  
 1108 temperature between the different data taking periods. Studies [97, 31] show  
 1109 that the energy response change by  $-2\% / K^0$ .

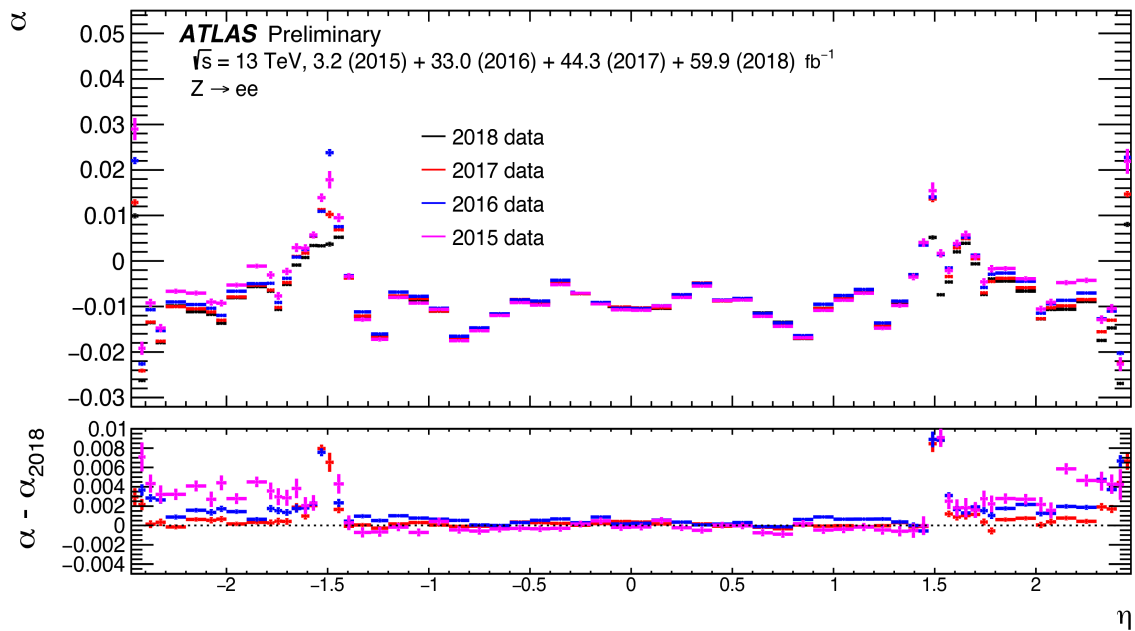


FIGURE 3.7: Energy scale factors extracted for 2015, 2016, 2017 and 2018 data taking during Run 2 as a function of  $\eta_{\text{calo}}$ . The bottom panel shows the differences between 2015, 2016 and 2017 to the 2018 data measurements.

1110 For the additional constant term  $c'$ , the results are shown in the same way for  
 1111 different years of Run 2 in Figure 3.8. Ideally, the additional constant term is inde-  
 1112 pendent of luminosity, but, as shown in Figure 3.8, the constant  $c'$  decreases as a  
 1113 function of the year. Studies [15] show that this effect is related to mis-modelling  
 1114 of the pile-up noise in simulation: the pile-up noise in the calorimeter increases  
 1115 with  $\langle \mu \rangle$  in data and this effect is not well modelled in simulation, and therefore is  
 1116 absorbed by the additional constant  $c'$ .

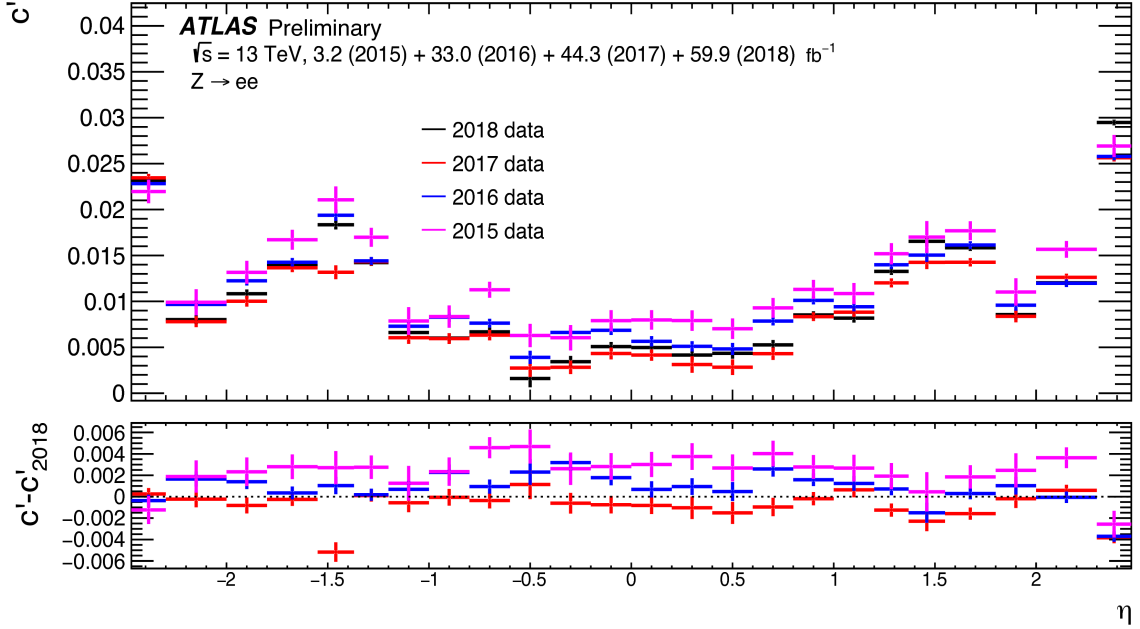


FIGURE 3.8: Additional constant term  $c'$  extracted for 2015, 2016, 2017 and 2018 data taking during Run 2 as a function of  $\eta_{\text{calo}}$ . The bottom panel shows the differences between 2015, 2016 and 2017 to the 2018 data measurements.

1117 This effect is due to the fact that , in order to simulate the charged distribution and  
 1118 the calorimeter distribution of the data , different tunings of the pile-up reweighting  
 1119 are needed [99]. This is also dependent on the beam crossing configuration at  
 1120 LHC [153] as seen for instance in [121] . The official ATLAS pile-up reweighting  
 1121 correction factor of 1.03 ( see figure 3.5) can be changed to 1.2 or 1.3, depending  
 1122 of the beam crossing configuration and the additional constant terms of different  
 1123 years are much more similar [131].

### 3.6.2 Systematic uncertainties

Different sources of systematic uncertainties of the correction factors ( $\alpha$  and  $c'$ ) are evaluated using 64 bins for the energy scale factor  $\alpha$  and 24 bins for the additional constant term  $c'$  described in Table 3.3, then symmetrised in bins of  $\eta_{\text{calo}}$  to reduce the statistical fluctuations. The systematic sources can be summarised in:

**Mass window:** the energy scale factors depend on the invariant mass window of the fit, due to the fact that the distribution tails are not well modelled in simulation [96]. The impact of the mass window is estimated by changing the window from [80, 100] to [87, 94.5] GeV, and the difference is taken as a systematic uncertainty.

**Mass threshold:** in the template method, we use only configurations with  $m_{ee}^{\text{th}} > 70$  GeV. This threshold mass is computed [82] based on the fact that the mass of the  $Z$  boson, when both electrons have the same  $E_T$  and are at opposite  $\phi$ , is equal to  $M_Z = E_T \sqrt{2 \cdot \cosh(\eta_j - \eta_i)}$ . Since the selection requires electrons to have at least  $E_T = 27$  GeV, the threshold mass for an  $(i,j)$  configuration is defined as  $m_{ee}^{\text{th}} = 27 \cdot \sqrt{2 \cdot \cosh(\eta_j - \eta_i)}$ . This choice is arbitrary and a systematic uncertainty, defined by comparing the scale factors using  $m_{ee}^{\text{th}} > 70$  and  $m_{ee}^{\text{th}} > 77$  GeV, is added to take into account the impact of the selection.

**Background:** in the template method, the electroweak background has been neglected. This systematic uncertainty is computed by comparing the scale factors with and without the background.

**Electron reconstruction efficiencies:** this uncertainty is added to take into account the scale factors (reconstruction, isolation, identification and trigger) applied to MC in order to match data. These efficiency factors are characterised by uncertainties propagated by the template method and considered as systematic uncertainties in  $\alpha$  and  $c'$ .

**Electron reconstruction quality:** as shown in Sec. 3.5, electrons must pass medium ID requirement. A systematic uncertainty is evaluated by comparing medium and tight ID electrons. In addition, another systematic uncertainty is added to take into account the uncertainty on the emission of photon by bremsstrahlung in the calorimeter.

**Method comparison:** in addition to the template method used on this thesis, there is another method called the “lineshape method” [74]. A systematic uncertainty is defined by the difference between the two methods.

**Method accuracy:** this uncertainty is used to take into account the intrinsic bias of the template method. It is evaluated by injecting known values in a MC sample and try to measure these values using the template method. The difference between the measured and injected values is defined as the systematic uncertainty.

The systematic uncertainties in the scale factors are listed in Table 3.4. The total uncertainty is calculated by the quadratic sum of all the effects described above.

TABLE 3.4: Ranges of systematic uncertainties in  $\alpha$  and  $c'$  for different  $\eta$  ranges [74].

$ \eta $ range	Uncertainty in $\alpha_i \times 10^3$				Uncertainty in $c_i \times 10^3$	
	0 – 1.2	1.2 – 1.8	1.8 – 2.4	0 – 1.2	1.2 – 1.8	1.8 – 2.4
Uncertainty source						
Method accuracy	(0.01 – 0.04)	(0.04 – 0.10)	(0.02 – 0.08)	(0.1 – 0.7)	(0.2 – 0.4)	(0.1 – 0.2)
Method comparison	(0.1 – 0.3)	(0.3 – 1.2)	(0.1 – 0.4)	(0.1 – 0.5)	(0.7 – 2.0)	(0.2 – 0.5)
Mass range	(0.1 – 0.5)	(0.2 – 4.0)	(0.2 – 1.0)	(0.2 – 0.8)	(1.0 – 3.5)	1.0
Region selection	(0.02 – 0.08)	(0.02 – 0.2)	(0.02 – 0.2)	(0 – 0.1)	0.1	(0.2 – 1.0)
Bkg. with prompt electrons	(0 – 0.05)	(0 – 0.1)	(0 – 0.5)	(0.1 – 0.4)	0.2	(0.1 – 0.2)
Electron isolation requirement	(0 – 0.02)	(0.02 – 5.0)	(0.02 – 0.20)	(0.1 – 0.9)	(0.1 – 1.5)	(0.5 – 1.5)
Electron identification criteria	(0 – 0.30)	(0.20 – 2.0)	(0.20 – 0.70)	(0 – 0.5)	0.3	0.0
Electron bremsstrahlung removal	(0 – 0.30)	(0.05 – 0.7)	(0.20 – 1.0)	(0.2 – 0.3)	(0.1 – 0.8)	(0.2 – 1.0)
Electron efficiency corrections	0.10	(0.1 – 5.0)	(0.10 – 0.20)	(0 – 0.3)	(0.1 – 3.0)	(0.1 – 0.2)
Total uncertainty	(0.2 – 0.7)	(0.5 – 10)	(0.6 – 2.0)	(0.3 – 1.2)	(1.0 – 6.0)	(2.0 – 3.0)

### 3.6.3 Data to simulation comparison

After deriving the energy correction factors, they are applied to data and MC events and the final distributions are compared in Figure 3.9. The energy scale factors  $\alpha$  are applied to data in order to match the energy response of the simulation and MC events are smeared according to  $c'$  factors in order to match the slightly worse resolution in data. The lower panel shows the data to simulation ratio and the total systematic uncertainty on the energy scale and resolution corrections from [36]. The deviations are largest in the tails where they can reach 3% and are mostly covered by uncertainties.

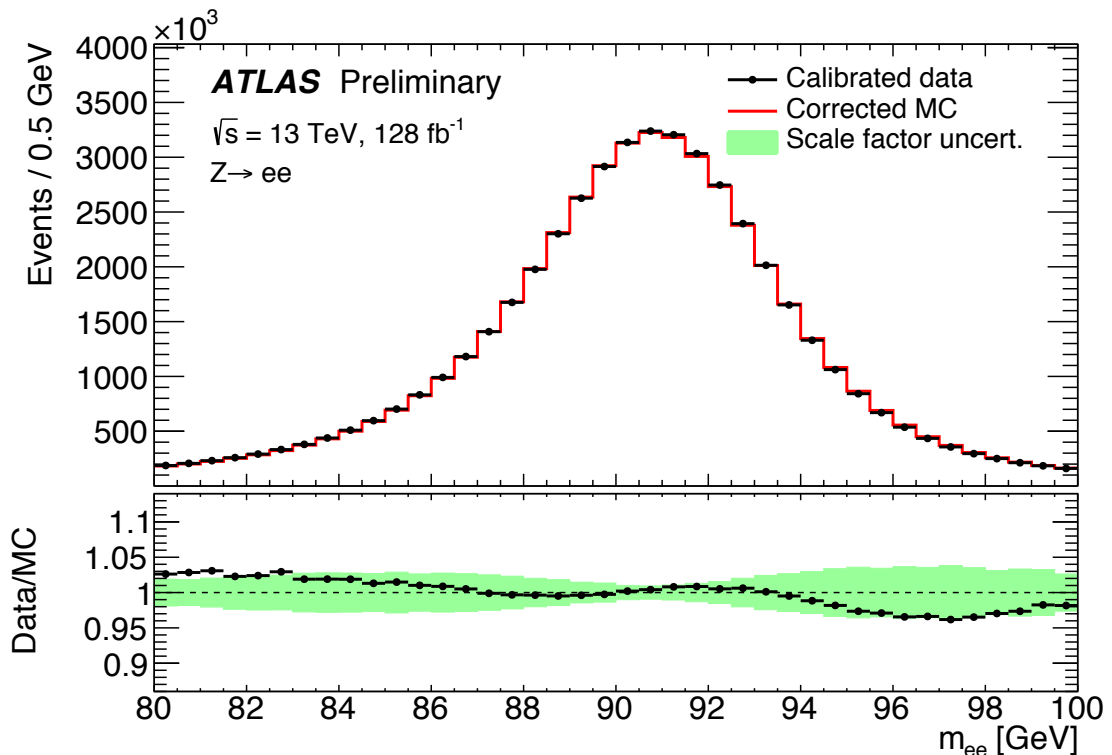


FIGURE 3.9: Inclusive di-electron invariant mass distribution from  $Z \rightarrow ee$  decays in data compared to MC after applying the full calibration. The simulation is normalized to data. The lower panel shows the data to simulation ratio, together with the uncertainty from the energy scale and resolution corrections.

The systematic uncertainties (see Table 3.4) are dominated by the electron identification, the method comparison, the mass range and the electron Bremsstrahlung removal. However, for the  $W$ -mass measurement [115] some improvements [41] were achieved with respect to the Run 1 calibration [67]: in particular restricting the  $\eta$  range by excluding  $1.2 < |\eta| < 1.8$ , using broader  $\eta$  bins in order to compute the systematic uncertainties and neglecting some uncertainties when we apply the calibration to electrons, like in  $W \rightarrow e\nu$ , for instance the uncertainty related to the electron ID as well as the uncertainty related to Bremsstrahlung emission since the analysis is inclusive in Bremsstrahlung.

## 3.7 Calibration for low pile-up runs

### 3.7.1 Introduction

In addition to the data collected for the nominal Run 2 analyses, called nominal runs, there are other runs dedicated to special studies. For the measurement of the  $W$  boson mass, we use low pile-up runs characterised with low number of interactions per crossing ( $\langle\mu\rangle \approx 2$ ), as shown in Figure 3.10. These data sets were collected by ATLAS in autumn 2017 ( $258 \text{ pb}^{-1}$  at  $\sqrt{s} = 5 \text{ TeV}$  and  $148 \text{ pb}^{-1}$  at  $\sqrt{s} = 13 \text{ TeV}$ ) and in summer 2018 (an additional  $193 \text{ pb}^{-1}$  at  $\sqrt{s} = 13 \text{ TeV}$ ). The low pile-up samples are detailed in [95]. For low pile-up runs, we use the the same selections as for the nominal runs described in Sec. 3.5, except for the trigger where we use `HLT_e15_lhloose_nod0_L1EM12` for 2017 and 2018 data. The number of selected events for low pile-up runs is shown in Table 3.5.

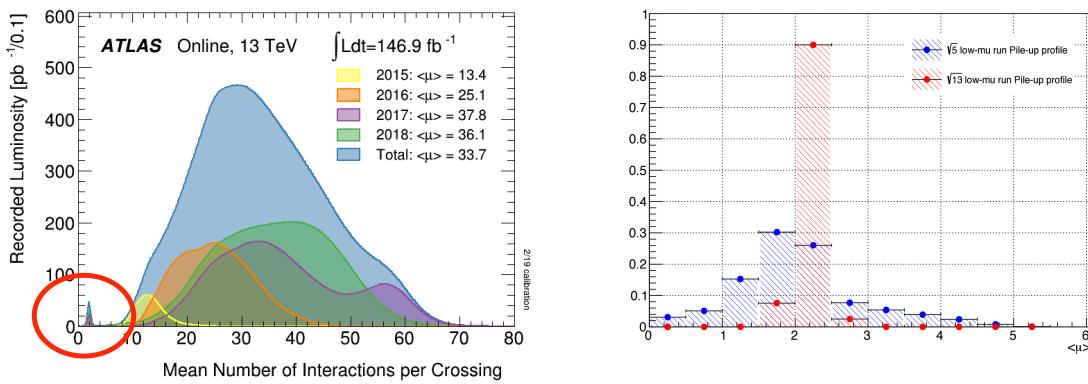


FIGURE 3.10: **left:** low pile-up runs at  $\langle\mu\rangle \approx 2$  showed in the red circle. **right:** the pile-up distribution of simulated low pile-up data at  $\sqrt{s} = 5$  and  $13 \text{ TeV}$ .

TABLE 3.5: The number of  $Z \rightarrow ee$  candidate events selected after applying all the selections for low pile-up runs at  $\sqrt{s} = 5$  and  $13 \text{ TeV}$ .

	5 TeV(2017)	13 TeV(2017)	13 TeV(2018)
Data	58.7 k	79.9 k	107.2 k
Simulation	2.14 M	1.38 M	1.41 M

The correction factors related to the reconstruction, identification, isolation and trigger efficiencies are applied also for the low pile-up runs. All these correction factors are obtained from the low pile-up runs except for the reconstruction efficiencies. In the same way, the pile-up reweighting is applied to MC in order to reproduce the distribution of the number of  $pp$  collisions per bunch crossing in data. Figure 3.11 shows the distribution of  $\langle\mu\rangle$  in data and MC.

### 3.7.2 Energy scale factors for low pile-up runs

For the low pile-up runs, the same procedure described above is used to derive  $\alpha$  and  $c'$  correction factors to equalise the response and resolution of data and MC.

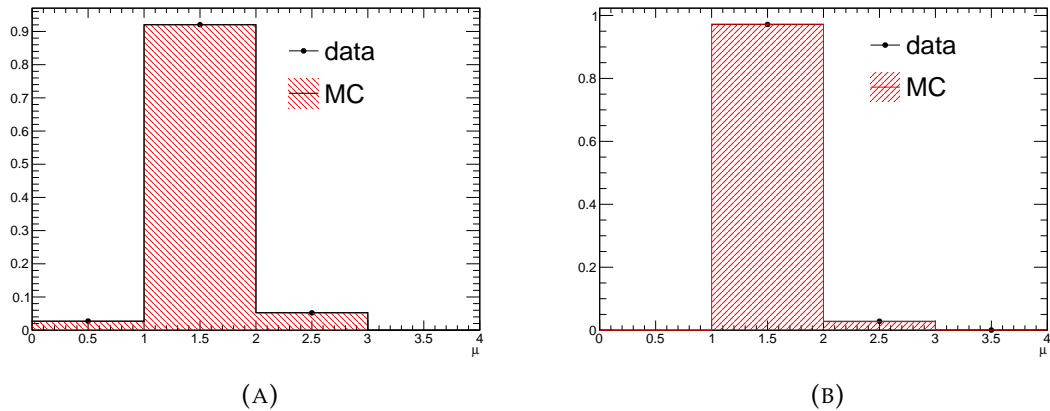


FIGURE 3.11: The average number of interaction per bunch crossing of data and simulation with low pile-up  $\sqrt{s} = 13$  TeV runs for 2017 (A), 2018 (B) after the pile-up reweighting procedure.

1204 For the nominal high pile-up data, the energy scale factors corrections are derived  
 1205 in 68  $\eta_{\text{calo}}$  bins. Because of the smaller number of  $Z \rightarrow ee$  events in the low pile-up  
 1206 runs, the scale factors extracted with the same 68 bins result have large statistical  
 1207 fluctuation and systematic bias, especially in the end-cap region, as shown in the  
 1208 Figure 3.12. To avoid this problem, two binnings were studied combining some  
 1209 bins of the 68  $\eta_{\text{calo}}$  bins:

- 1210 • either 48 bins in total with bins of larger size only in the end-cap
- 1211 • or 24 bins in total with bins of larger size in both the barrel and the end-cap  
 1212 regions, as shown in Figure 3.12 and Table 3.6.

TABLE 3.6: Values of  $\eta_{\text{calo}}$  bin boundaries for energy scale  $\alpha$  for 24 bins.

-2.47	-2.4	-2.1	-1.8	-1.55	-1.37	-1.2	-1	-0.8	-0.6	-0.4	-0.2	0	0.2	0.4	0.6	0.8	1	1.2	1.37	1.55	1.8	2.1	2.4	2.47
-------	------	------	------	-------	-------	------	----	------	------	------	------	---	-----	-----	-----	-----	---	-----	------	------	-----	-----	-----	------

1213 The results obtained from these binnings are shown in Figure 3.12. As can be  
 1214 seen, the instability for the end-cap bins disappears. As the  $\alpha$  factors do not vary  
 1215 strongly between the 48 and 24 bins versions, the baseline chosen is 24 bins. The  
 1216 additional constant term  $c'_i$  applied to MC to account for the worse resolution in  
 1217 data is shown in Figure 3.13. As the  $c'_i$  values were previously observed to be de-  
 1218 pendent on the pile-up and data taking conditions, it is best to extract and use the  
 1219 constants from the respective data set under study. This is further discussed in  
 1220 Sec. 3 of Ref. [15]. The physics analyses currently use directly the in-situ cali-  
 1221 brations as derived in this section. The main uncertainties are given by the statistical  
 1222 uncertainties of the  $\alpha_i$  and  $c'_i$  factors. As these are significantly larger than other  
 1223 uncertainties, another approach is used to extract the energy scale factor  $\alpha_i$  and  
 1224 explained in Sec. 3.7.3.

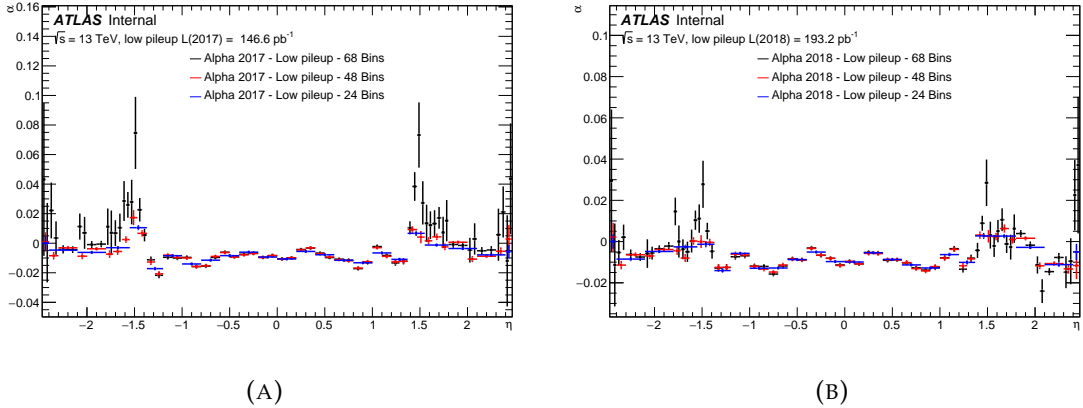


FIGURE 3.12: Energy scale factors  $\alpha$  for low pile-up runs of 2017 (A) and 2018 (B) using 68, 48 and 24  $\eta$  bins. It can be seen, that the extraction is unstable in case of 68 bins, resulting in  $\alpha$  factors with very large uncertainties.

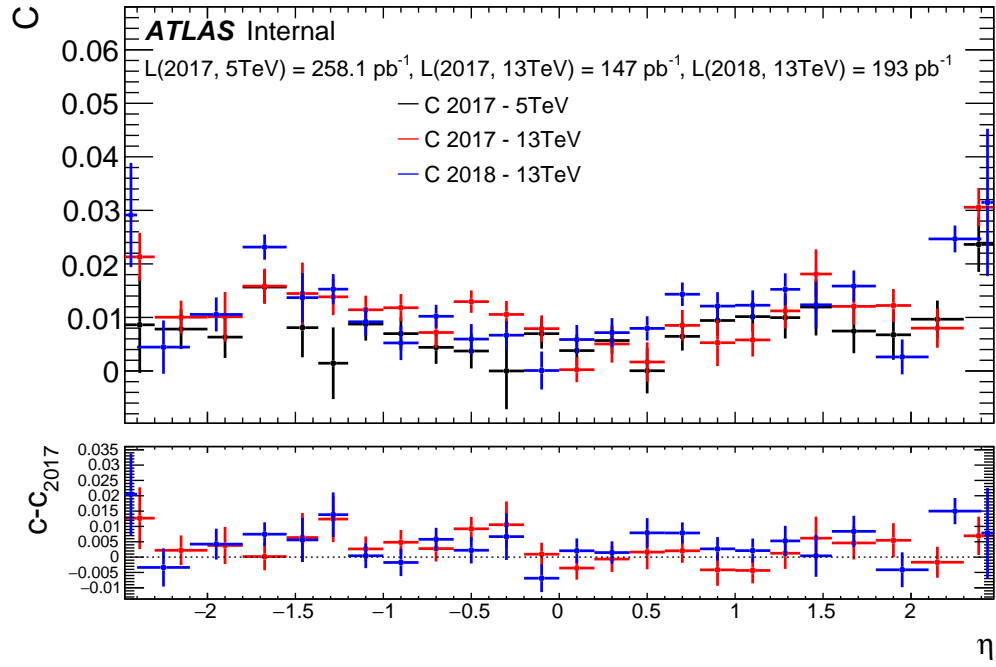


FIGURE 3.13: Additional constant term  $c'_i$  for low pile-up runs of 2017 (13 TeV), 2018 (13 TeV) and 2017 (5 TeV) using 24 bins. The lower panel shows the difference of  $c'_i$  to 2017 (5 TeV) results.

### 3.7.3 Extrapolation method

An alternative method to derive the energy correction scale factors for the low pile-up data is to study the dependence of the factor  $\alpha$  for high pile-up data sets and to perform an extrapolation to  $\langle\mu\rangle \approx 2$ . This method exploits the large sample of the high pile-up data, but requires additional work to ensure the extrapolation is under control. The extrapolation proceeds by separating the high pile-up data into intervals of  $\langle\mu\rangle$  and applying the template method to extract the energy scale factors as a function of  $\langle\mu\rangle$ , i.e.  $\alpha(\langle\mu\rangle)$ . Using a (linear) fit  $\alpha(\langle\mu\rangle)$  can be extrapolated to  $\langle\mu\rangle \approx 2$ . The  $\langle\mu\rangle$  intervals are defined in Table 3.7. The extrapolation for two example  $\eta$  bins is shown in Figure 3.14. Figures 3.15 and 3.16 show the extrapolation from high pile-up to low pile-up data for all  $\eta$  bins comparing the negative and positive  $\eta$  bins in a same plot. The asymmetric effect observed between the negative and positive  $\eta$  bins could be due mainly to temperature effects which may not be symmetric. Over the  $\langle\mu\rangle$  range samples in the high pile-up data a linear fit is found to be sufficient. In many bins the slope of  $\alpha(\langle\mu\rangle)$  is found to be small, but in particularly in the end-cap region the slopes are often significant.

TABLE 3.7: The  $\mu$  intervals used for extrapolation study.

[ 0 : 26 ]	[ 26 : 33 ]	[ 33 : 40 ]	[ 40 : 50 ]	[ 50 : 80 ]
------------	-------------	-------------	-------------	-------------

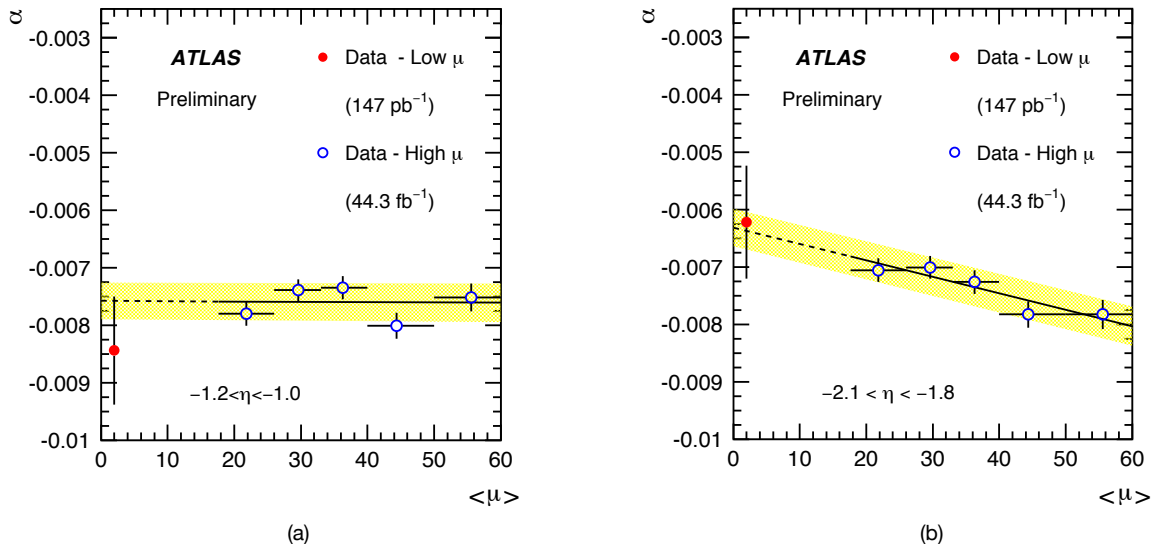


FIGURE 3.14: Examples of the energy scale extrapolation from high pile-up to low pile-up in the barrel (a) and end-cap (b). The blue points show the energy scale factors  $\alpha$  for the high pile-up data set as a function of  $\langle\mu\rangle$ , the black lines show the extrapolation to  $\langle\mu\rangle \approx 2$  using a linear function and 5 intervals of  $\langle\mu\rangle$ , the band represents the uncertainty in the extrapolation. The extrapolation results are compared to the energy scale factors  $\alpha$  extracted from the low pile-up data set, represented by the red point.

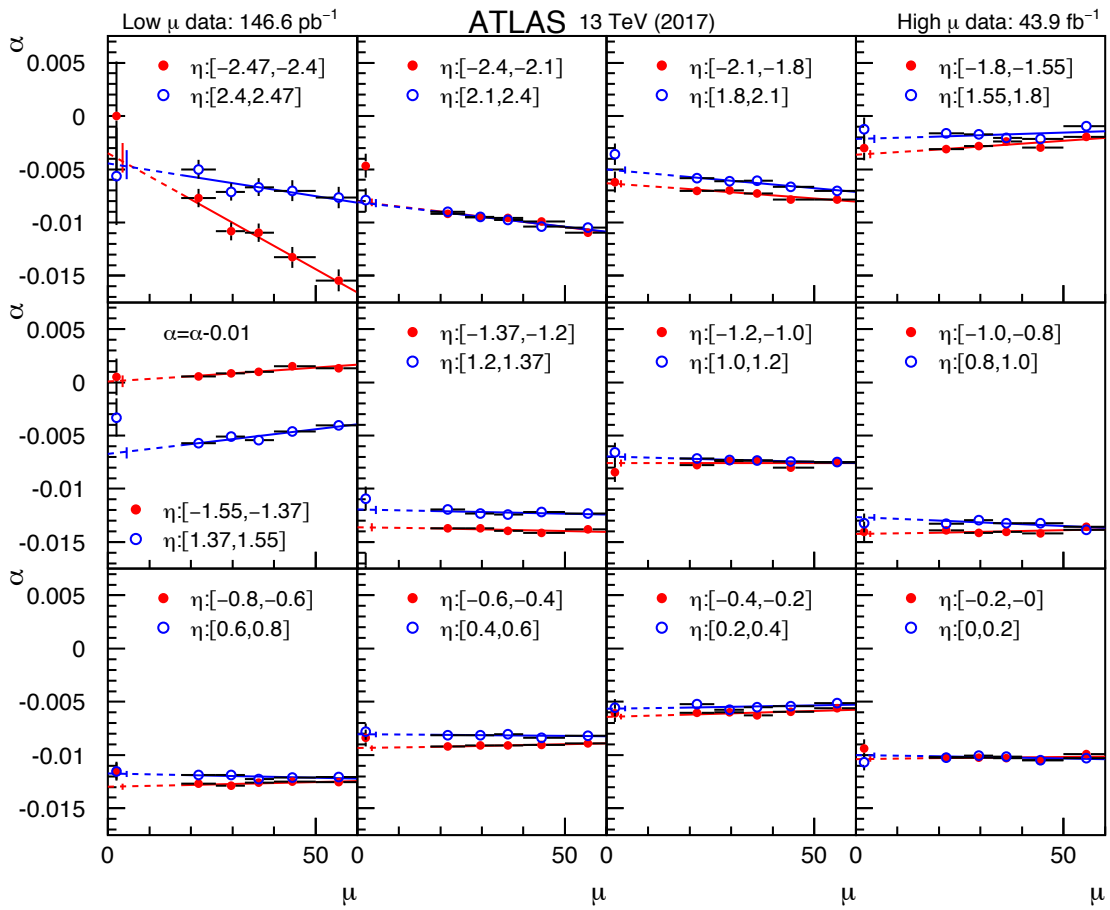


FIGURE 3.15: Energy scale extrapolation from 2017 high pile-up to low pile-up for 2017 (at 13 TeV) low pile-up data. The blue and red points show the energy scale factors  $\alpha$  for the high pile-up data set as a function of  $\langle \mu \rangle$  for different  $\eta$  regions, the dotted lines show the extrapolation to  $\langle \mu \rangle \approx 2$  using a linear function and 5 intervals of  $\langle \mu \rangle$ . The values of  $\alpha$  determined using the low  $\langle \mu \rangle$  data sets are also shown at  $\langle \mu \rangle \approx 2$ . The size of the vertical lines near the low  $\alpha$  points represents the uncertainty of the extrapolation.

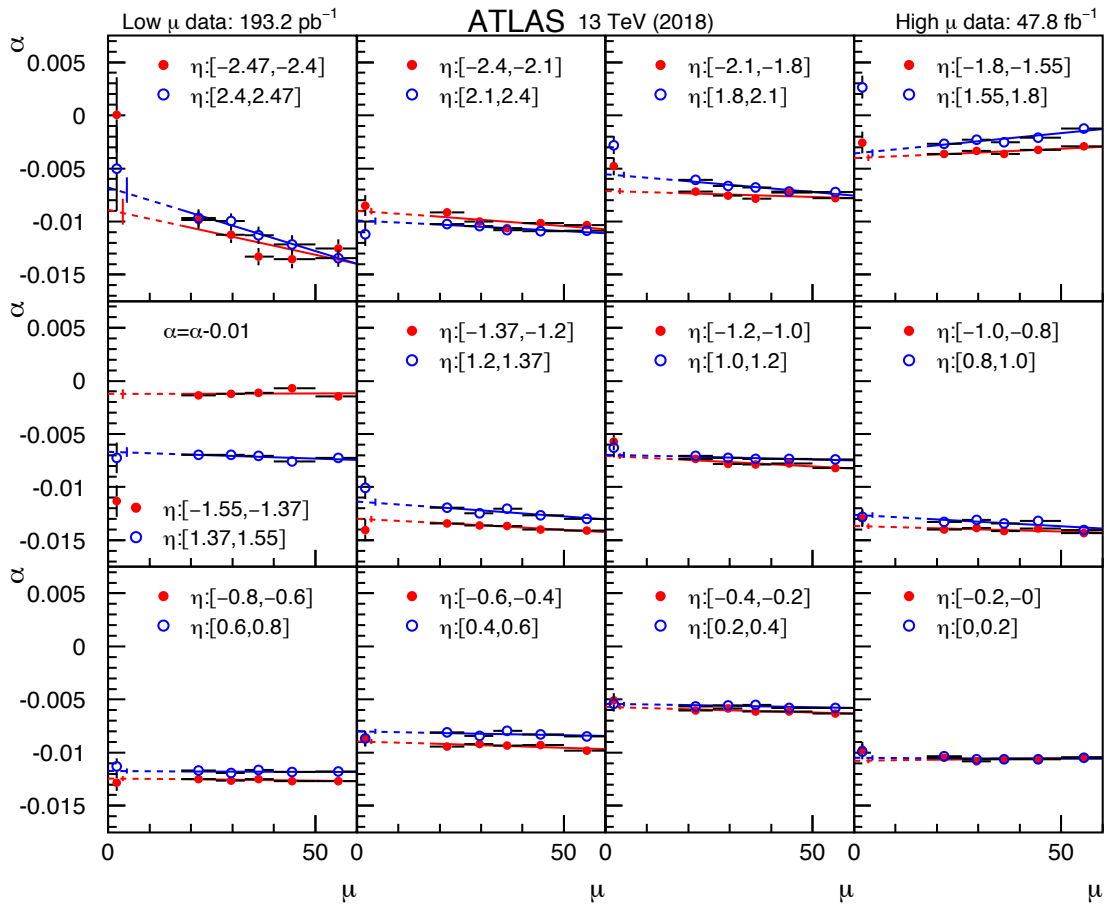


FIGURE 3.16: Energy scale extrapolation from 2018 high pile-up to low pile-up for 2018 (13 TeV) low pile-up data. The blue and red points show the energy scale factors  $\alpha$  for the high pile-up data set as a function of  $\langle \mu \rangle$  for different  $\eta$  regions, the dotted lines show the extrapolation to  $\langle \mu \rangle \approx 2$  using a linear function and 5 intervals of  $\langle \mu \rangle$ . The values of  $\alpha$  determined using the low  $\langle \mu \rangle$  data sets are also shown at  $\langle \mu \rangle \approx 2$ . The size of the vertical lines near the low  $\alpha$  points represents the uncertainty of the extrapolation.

### 3.7.4 Extrapolation results

After extrapolating the results to  $\langle \mu \rangle \approx 2$ , it could be expected that the energy scale factors coincide with those extracted directly using the low pile-up data within uncertainties. However, this is not always the case as it is shown in Figure 3.17, where it is observed that the extrapolation results are in fact closer to the high pile-up results without extrapolation than to the low pile-up results.

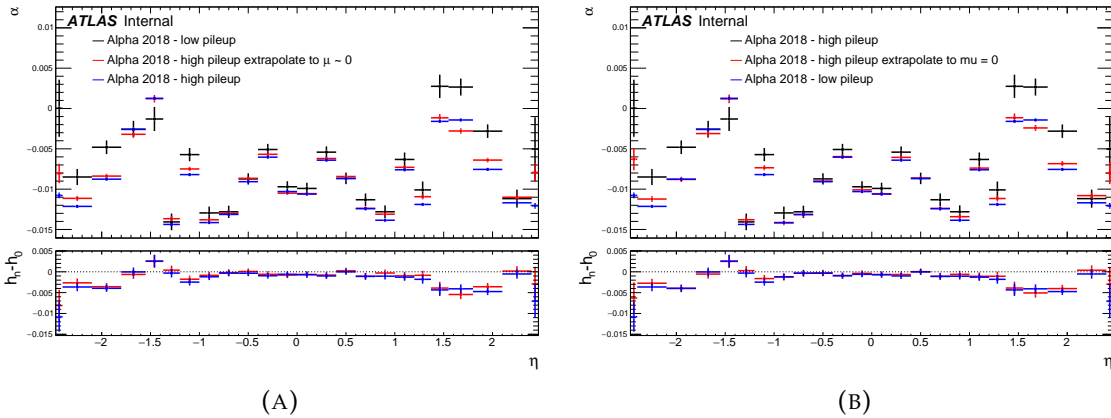


FIGURE 3.17: The energy scale factors  $\alpha$  for 2017 (A) and 2018 (B) data, respectively. The results are shown using directly the low (black) and high (blue) pile-up data and extrapolating the high pile-up results to  $\langle \mu \rangle \approx 2$  (red). The bottom panels show the absolute differences between the high-pile-up  $\alpha$  factors with and without extrapolation correction (labelled  $h_n$ ) to the in-situ low pile-up derived  $\alpha$  factors (labelled  $h_0$ ).

This behavior of the extrapolated results was understood to be due to the different settings of the topo-cluster noise thresholds at reconstruction level: for the low pile-up data these were set to correspond to  $\langle \mu \rangle = 0$  (to improve the hadronic recoil reconstruction), while the nominal high pile-up data is reconstructed with a threshold corresponding to  $\langle \mu \rangle = 40$ . The lower noise threshold used for the low pile-up data leads to more cells added to the topo-clusters and thus to a higher energy as shown in Figure 3.18. The effect of different noise thresholds on the energy scale factors  $\alpha$  is studied with a dedicated processing of the data and MC (as described in Sec. 3.3) where the noise thresholds are set to the nominal high pile-up values.

Using the template method, the energy scale factors for the low pile-up data are extracted separately for low and high noise thresholds and compared in Figure 3.19 (A). As an alternative method, the difference of the average energy response  $(E^{\text{low-threshold}} - E^{\text{high-threshold}})/E^{\text{low-threshold}}$  electron-by-electron reconstructed with low and high noise thresholds can be compared between data and simulation, as shown in Figure 3.19 (B). This second method is chosen because it reduces the statistical fluctuations. After correcting the threshold effect by applying the correction from Figure 3.19 (B), the extrapolation results in 24 bins of  $\eta$  are closer to the low pile-up results extracted directly with the template method, as shown in Figure 3.20. As can be seen from this figure, the difference between the extrapolated and low pile-up results is of the order of 0.1% (absolute difference in  $\alpha$  of 0.001) in the barrel region, but increases to 0.5% (absolute difference in  $\alpha$  of 0.005)

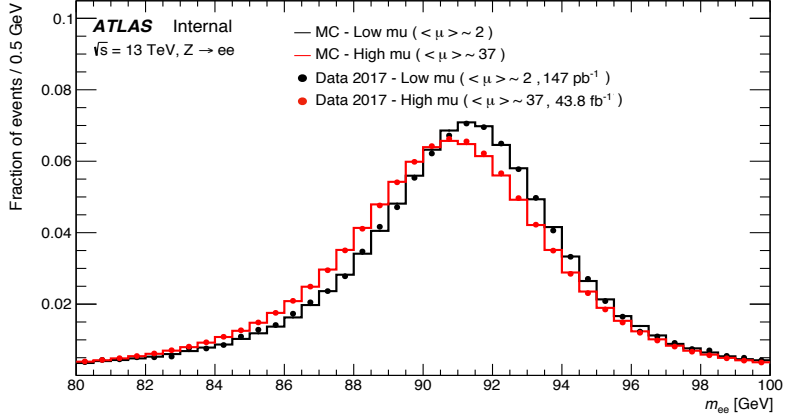


FIGURE 3.18: Comparison of the di-electron invariant mass distribution  $m_{ee}$  for data and simulation between high and low pile-up runs.

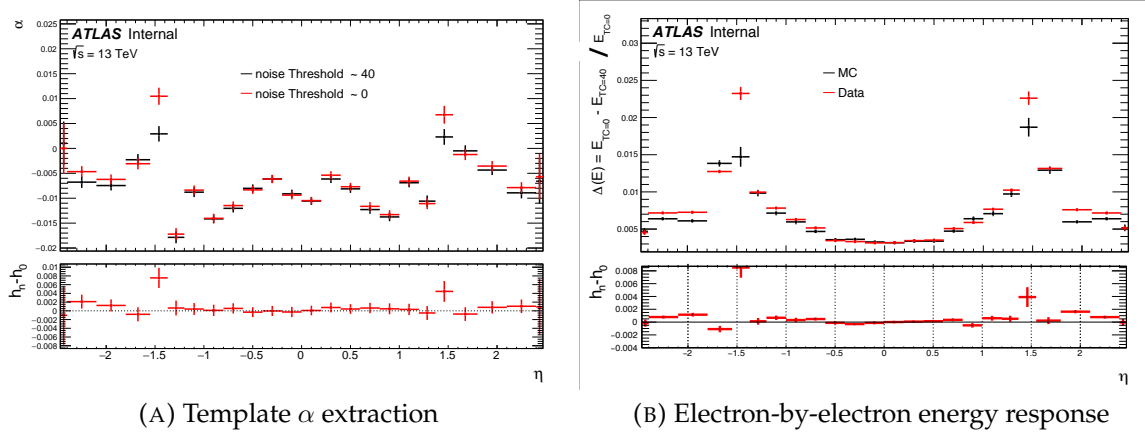


FIGURE 3.19: (A): The effect of the noise threshold corresponding to  $\mu = 0$  (red) or  $\mu = 40$  (black) on the energy scale factors  $\alpha$  using the template extraction. The bottom panel shows the absolute differences of  $\alpha$ -factors obtained with high pile-up (labelled  $h_n$ ) to those obtained with the low pile-up (labelled  $h_0$ ) topo-cluster thresholds. (B): The difference in the energy response from the noise threshold settings extracted electron-by-electron on MC (black) and data (red). The bottom panel shows the absolute differences between data (labelled  $h_n$ ) to MC (labelled  $h_0$ ).

1269 in the end-cap region (excluding the “crack” region). The additional constant term  
 1270  $c'$  in any case will be taken from the direct results from the template method using  
 1271 low pile-up samples without extrapolation from high pile-up data, as the calibration  
 uncertainties are dominated by the scale factors  $\alpha_i$  corrections.

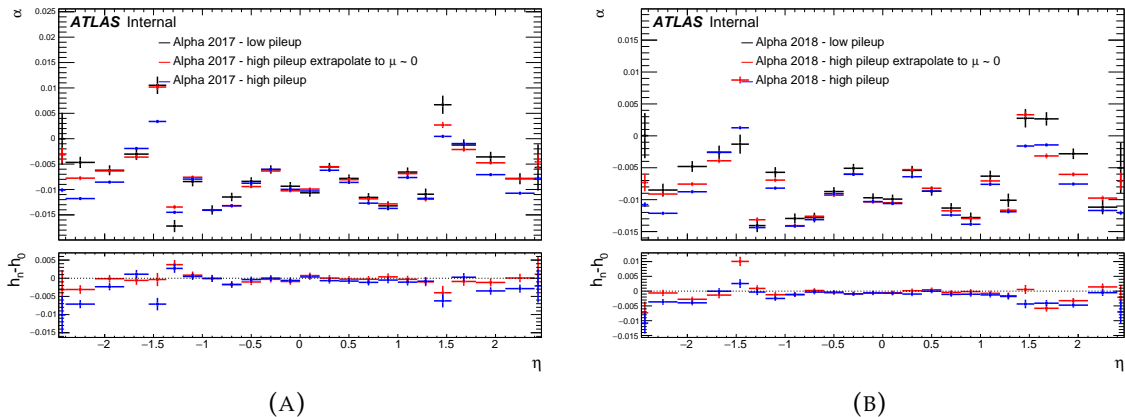


FIGURE 3.20: The extrapolation results for the energy correction factors  $\alpha$  before (blue) and after (red) correcting the effects of the difference of the noise threshold for 2017 (A) and 2018 (B). The results are compared to the in-situ low pile-up results (black). The bottom panels show the absolute differences between the extrapolated results (labelled  $h_n$ ) to the in-situ results (labelled  $h_0$ ).

1272

### 1273 3.7.5 Uncertainties for the extrapolation method

1274 As the high pile-up results are used in the extrapolation procedure, the systematic  
 1275 uncertainties of high pile-up samples evaluated in Sec.3.6.2 are relevant also at  
 1276 low pile-up. In addition to high pile-up systematic uncertainties, there are other  
 1277 uncertainties mainly related to the difference between high and low pile-up runs  
 1278 and to the extrapolation procedure:

1279 **Threshold correction:** for low pile-up data set a different topo-cluster noise  
 1280 threshold for the energy reconstruction is used, and a systematic uncertainty  
 1281 is evaluated to take into account this difference. This systematic uncertainty  
 1282 is defined as the statistical error on the difference of threshold, shown in the  
 1283 bottom plot panel in Figure 3.19 (B).

1284 **Extrapolation systematic uncertainties:** The extrapolation uncertainty is consid-  
 1285 ered as the quadratic sum of the following two effects:

- 1286 1. The choice of the polynomial functions used in the extrapolation: the  
 1287 baseline extrapolation is performed with a polynomial of order 1. The  
 1288 difference between using a first or a second order polynomial function  
 1289 is included as discussed in [15].
- 1290 2. The number of  $\langle \mu \rangle$  intervals used in the extrapolation: for the baseline  
 1291 extrapolation, we used five intervals in  $\langle \mu \rangle$ . The effect of using three  
 1292 intervals is considered [15].

1293 **Temperature uncertainty:** for nominal runs, there is a systematic uncertainty  
 1294 which includes the changes of LAr calorimeter response with temperature,  
 1295 but this effect is not linear with  $\mu$ . Indeed, since it takes some time (few  
 1296 hours) for the liquid argon calorimeter to heat, there is a rough delay be-  
 1297 tween the increase or decrease of luminosity and the corresponding increase  
 1298 or decrease of temperature. This introduces [99] a systematic uncertainty of  
 1299 0.03% in the barrel and 0.1% in the end-cap region for low pile-up runs.

1300 Figure 3.21 shows an overview of all the sources on the energy scale factor  $\alpha$  for  
 the 2017 low pile-up run at  $\sqrt{s} = 13$  TeV while using the extrapolation method.

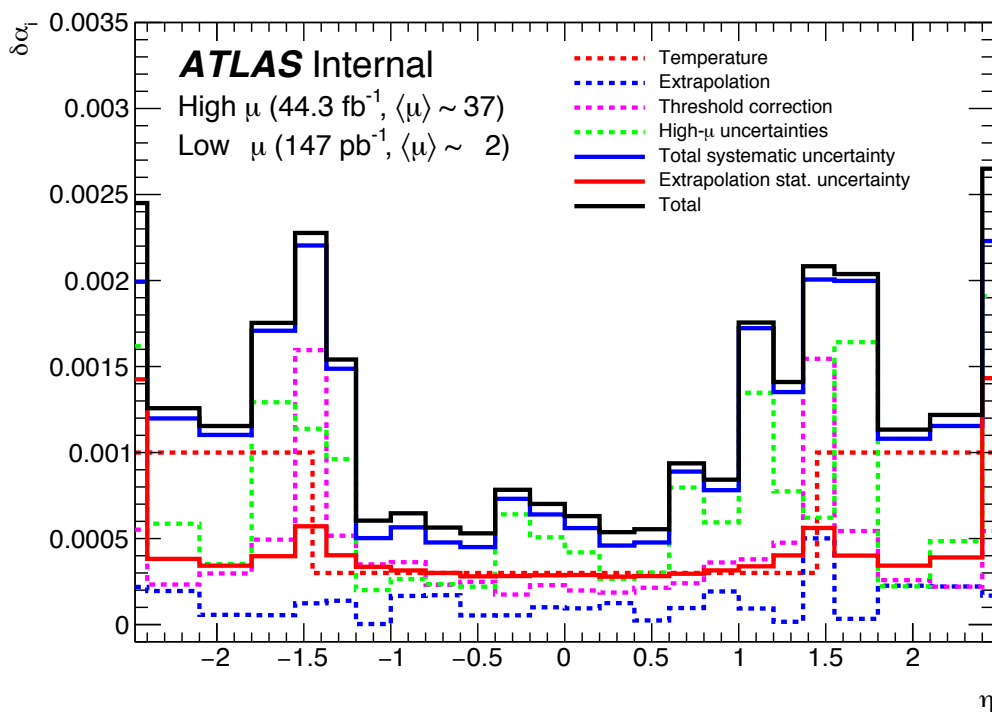


FIGURE 3.21: Uncertainties on the energy scale corrections as a function of  $\eta$  for the 2017 low pile-up runs at  $\sqrt{s} = 13$  TeV.

### 1302 3.7.6 Data to simulation comparison for low pile-up runs

1303 After having calculated the energy correction factor  $\alpha$ , we apply them to data and  
 1304 MC events and the final distributions are compared in Figure 3.22. The lower panel  
 1305 shows the data to simulation ratio with the statistical uncertainty in the energy  
 1306 scale.

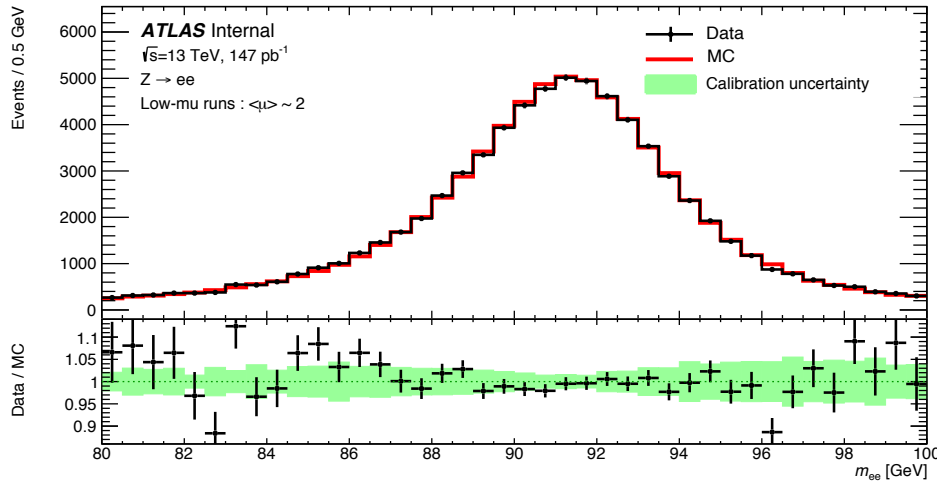


FIGURE 3.22: Inclusive di-electron invariant mass distribution for low pile-up runs from  $Z \rightarrow ee$  decays in data compared to MC after applying the full calibration. The simulation is normalized to data. The lower panel shows the data to simulation ratio, together with the statistical uncertainty from the energy scale corrections.

## 3.8 Future of the calibration

1307 A lot of efforts have been made on the  $e/\gamma$  calibration, in Run 1 and Run 2, however  
 1308 there remain several problems. In particular there a small mismodeling of the  
 1309 lineshape by the Monte Carlo as seen in Figure 3.9. Several ideas have been studied  
 1310 (or will be studied) to understand and solve this problem:

- 1312 • It was noticed [41, 97, 115] that excluding the  $1.2 < |\eta| < 1.8$  region gives a  
 1313 better agreement. This was confirmed and scrutinized with more in depth in  
 1314 recent analysis [131, 85].
- 1315 • Non linearity [57, 85] checks have been performed using a method [38] simi-  
 1316 lar to the template method described in Sec 3.4. The non linearity has been  
 1317 computed but the improvement in the mismodeling is marginal. Additional  
 1318 test of non linearity will be test using  $E/p$  as a measure.
- 1319 • Additional non Gaussian tails could be at the origin of this effect. However  
 1320 simple tests using additional material in front of the calorimeter did not show  
 1321 any significant improvement of the mismodeling [85]. Following work on  
 1322 the forward calorimeter [44], a study as started [94] in order to study these  
 1323 non Gaussian tails in the EM calorimeter.



1324 **Chapter 4**

1325 **Statistical overview: Unfolding**

1326 **4.1 Introduction**

1327 In this chapter we will discuss the theoretical part of the unfolding problem [139],  
 1328 used in chapter 7, to calculate the fiducial and differential cross sections, and in  
 1329 chapter 5 for the measurement of the boson transverse momentum and in the  
 1330 chapter 8 for the measurement of  $W$  mass. The need for unfolding stems from the  
 1331 fact that any quantity measured at the LHC detectors is affected by the not com-  
 1332 pletely well known detector effects (like acceptance and resolution). The goal of  
 1333 the unfolding is to correct data distributions and estimate the true physical distri-  
 1334 butions of the observables of interest without detector effects [40]. In high energy  
 1335 physics, several unfolding methods are used [49], and in our analysis, the iterative  
 1336 Bayesian unfolding [55] is used.

1337 **4.2 Unfolding in high energy physics**

1338 In high energy physics, we are interested in distributions of the observables of  
 1339 interest. In most of the cases, different distributions are affected by detector effects  
 1340 with different sizes. For example, the transverse mass of the  $W$  boson is more  
 1341 affected by detector effects than the transverse momentum of the lepton in  $W \rightarrow$   
 1342  $\ell + \nu$ . Figure 4.1 shows the comparison between simulated distributions without  
 1343 detector effects (particle level), with detector effects (reconstructed level) and after  
 1344 the unfolding for  $m_T^W$  and  $p_T^\ell$ .

1345 The reconstructed distributions are different from truth distributions because  
 1346 of two effects:

- 1347 • Limited acceptance: it reflects the fact that not all events are observed by the  
 1348 detector, it is called the detector acceptance and it is smaller than 1 [120].
- 1349 • Migration: due to limited detector resolution, an event originating from bin  
 1350  $i$  can be measured in another bin  $j$ . This effect is taken into account with the  
 1351 migration matrix explained in Sec. 4.3.1.

1352 For a mathematical presentation of the unfolding problem, let's consider that we  
 1353 have just MC simulation vector  $x$  ( $y$ ) of dimension  $N_x$  ( $N_y$ ), where the elements  $x_i$   
 1354 ( $y_i$ ) represent the number of events in bin  $i$  in our distribution at the truth (recon-  
 1355 structed) level. Both vectors  $x$  and  $y$  are related with a matrix  $R$ , called response  
 1356 matrix:

$$R \times x = y. \quad (4.1)$$

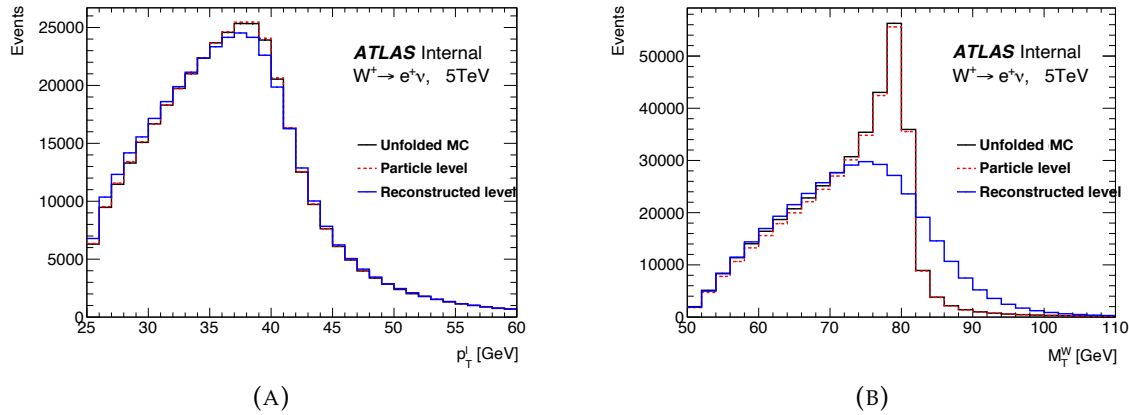


FIGURE 4.1:  $p_T^l$  (A) and  $m_T^W$  (B) distributions before and after detector effects, with the unfolded distributions.

1357 The elements  $R_{i,j}$  of the response matrix  $R$  represent the probability that an event  
 1358 generated in bin  $j$  is measured in bin  $i$ . The number of background events must be  
 1359 removed from the vector  $y$ . In a real case, the response matrix  $R$  is calculated from  
 1360 the migration matrix  $M$ , where the  $M_{i,j}$  are estimated using information from MC  
 1361 simulation:

$$M_{i,j} = N_{i,j}^{\text{rec} \wedge \text{gen}}, \quad (4.2)$$

1362 where  $N_{i,j}^{\text{rec} \wedge \text{gen}}$  represents the number of event generated in truth bin  $j$  and recon-  
 1363 structed in bin  $i$ . If  $N_j^{\text{gen}}$  represents the number of event generated in truth bin  $j$ ,  
 1364 the response matrix is then defined as:

$$R_{i,j} = \frac{M_{i,j}}{N_j^{\text{gen}}}. \quad (4.3)$$

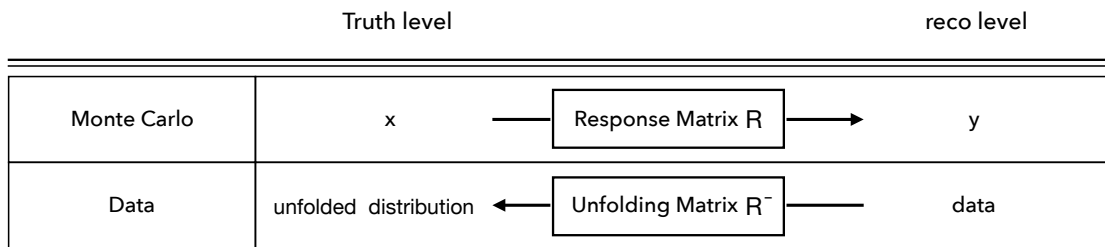
1365 In our case, we are using a slightly modified response matrix  $R'_i, j$  defined as

$$R'_{i,j} = \frac{M_{i,j}}{N_j^{\text{rec} \wedge \text{gen}}} \quad (4.4)$$

1366 where  $N_j^{\text{rec} \wedge \text{gen}}$  is the number of events generated and reconstructed in bin  $j$ . The  
 1367 ratio of  $R$  by  $R'$  is a function of the truth bin  $j$  and is equal to the acceptance  
 1368 correction (Sec. 4.3.1)

$$A_j = \frac{N_j^{\text{rec} \wedge \text{gen}}}{N_j^{\text{gen}}}. \quad (4.5)$$

1369 Now let's take the case of real data, where we don't have any information about  
 1370 distributions at the truth level, the idea of unfolding is to apply the inverse of the  
 1371 response matrix calculated using MC simulation to real data to estimate the true  
 1372 physical distributions. At this moment, the unfolding problem is an inversion  
 1373 problem of the response matrix:



1374 The use of the unfolding technique in high energy physics allows to obtain  
 1375 results which are independent from detector and reconstruction effects. Conse-  
 1376 quently, the unfolding results can be compared directly to theoretical predictions  
 1377 or to other experiments. They also can be used for the precision measurements  
 1378 as the  $W$  boson mass  $M_W$  measurement. On the other hand, there are some cases  
 1379 where the unfolding is not needed. Mainly, the unfolding is used for observables  
 1380 characterised by a large migration between truth and reconstruction distributions.  
 1381 In other words, for the observables with small migration between the truth and  
 1382 reco level, a bin-by-bin correction is sufficient to determine the true physical dis-  
 1383 tributions of the observables of interest. Applying the inverse of the migration  
 1384 matrix to the reconstructed simulation distribution is considered as a closure test  
 1385 for the unfolding.

### 1386 4.3 Iterative Bayesian unfolding

1387 In this thesis, the iterative Bayesian unfolding [56] is used for the unfolding of our  
 1388 variables of interest with RooUnfold [7]. This paragraph will give an overview of  
 1389 the method, with a detailed description of the propagation of the source uncer-  
 1390 tainties through the unfolding. The iterative Bayesian unfolding is based on Bayes  
 1391 theorem, which describes the probability of an effect based on prior knowledge  
 1392 of causes related to the effect. Let us consider a list of causes and effects ( $C, E$ ),  
 1393 where causes ( $C$ ) correspond to the true values and effects ( $E$ ) to the values after  
 1394 smearing. Each effect ( $E$ ) results from several causes. The unfolding problem can  
 1395 be summarised in the estimation of  $P(C_i|E_j)$  which corresponds to the probability  
 to observe a cause  $C_i$  responsible of observed effects  $E_j$ .

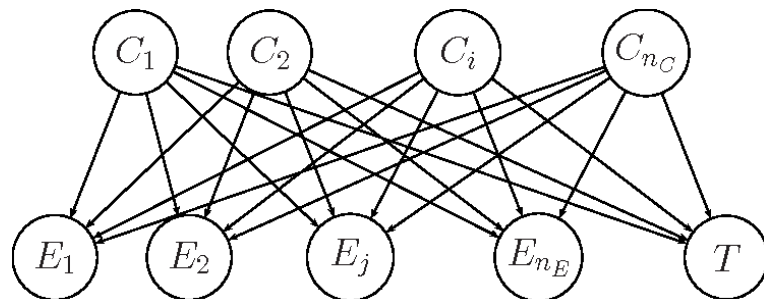


FIGURE 4.2: Probabilistic links from causes to effects. The node T corresponds to undetected events [56].

1397 In the Bayes theorem, the probability  $P(C_i|E_j)$  can be calculated as:

$$P(C_i|E_j) = \frac{P(E_j|C_i) \cdot P(C_i)}{\sum_{l=1}^{n_c} P(E_j|C_l) \cdot P(C_l)}, \quad (4.6)$$

1398  $n_c$  corresponds to the number of possible causes,  $P(E_j|C_i)$  represents the probability 1399 to observe the effect  $E_j$  knowing  $C_i$  and  $P(C_i)$  is the probability to observe the 1400 cause ( $i$ ). Finally the number of events in the cause bin ( $i$ ) can be expressed as:

$$\hat{n}(C_i) = \frac{1}{\epsilon_i} \sum_{j=1}^{n_E} n(E_j) \cdot P(C_i|E_j), \quad \epsilon_i \neq 0, \quad (4.7)$$

1401  $n(E_j)$  corresponds to the number of events in the effect bin ( $j$ ) and  $P(C_i|E_j)$  is 1402 calculated with formula (4.6) which is using  $P(E_j|C_i)$  based on simulation. The 1403 iterative Bayesian unfolding is characterised by a bias [139] that we introduce with 1404 the unfolding procedure. To reduce the unfolding bias, a regularization parameter 1405 is used. The regularization consists in repeating the unfolded procedure several 1406 times, as will be discussed later in Sec. 4.4.3. The migration matrix can be de- 1407 termined from simulation by filling a two-dimensional histogram for all selected 1408 events with a common matching of truth and reconstructed values (TR) [20].

### 1409 4.3.1 Migration matrix

1410 The migration matrix is a matrix containing information from the truth and 1411 reconstructed level, with e.g. the  $x$ -axis corresponding to reconstructed bins and the 1412  $y$ -axis to truth bins. The example in Figure 4.3 shows the migration matrix for two 1413 variables,  $p_T^\ell$  and  $m_T^W$ . Comparing  $m_T^W$  to  $p_T^\ell$  matrix, the transverse mass is char- 1414 acterised with a larger migration between the truth and reconstructed level because of the detector effects which affect more the transverse mass  $m_T^W$ .

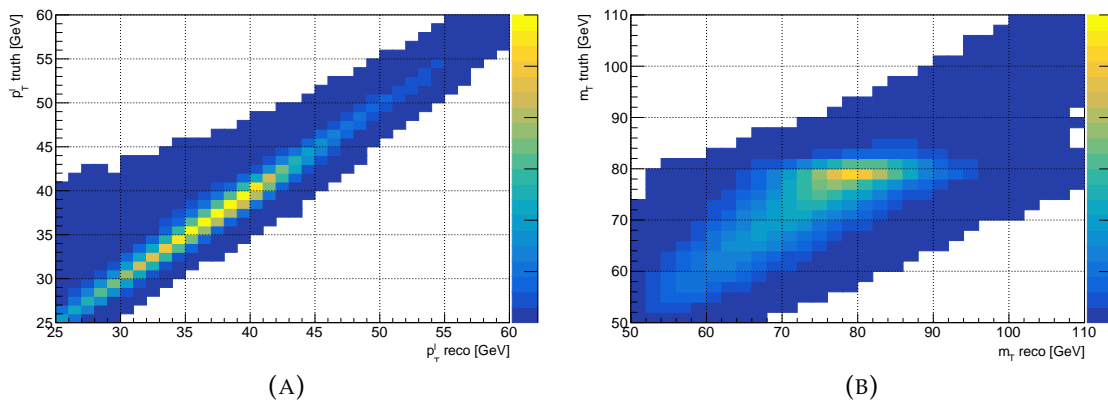


FIGURE 4.3: Example of the migration matrix for  $p_T^\ell$  (A) and  $m_T^W$  (B).

1415 In addition to the migration and response matrix, there are two important fac- 1416 tors, as shown in Figure 4.4, that we apply before and after the unfolding, and will 1417 be used later especially for the measurement of the differential cross sections: 1418

1419 **The efficiency correction:** It is defined as the fraction of events passing recon-  
 1420 structed and truth level selections ( $N^{\text{reco,truth}}$ ) to the number of events that  
 1421 meet the selection criteria at reconstruction level ( $N^{\text{reco}}$ ):

$$\epsilon_i = \frac{N^{\text{reco,truth}}}{N^{\text{reco}}}. \quad (4.8)$$

1422 It is defined as a function of the reconstructed bin number  $i$ . The efficiency  
 1423 correction is applied before unfolding to correct data distributions since the  
 1424 data events pass reconstructed selections only.

1425 **The acceptance correction:** It is defined as the fraction of events that passing re-  
 1426 constructed and truth level selections ( $N^{\text{reco,truth}}$ ) to the number of events that  
 1427 meet the selection criteria at truth level ( $N^{\text{truth}}$ ):

$$A_i = \frac{N^{\text{reco,truth}}}{N^{\text{truth}}}. \quad (4.9)$$

1428 It is defined as a function of the truth bin number  $i$ . The inverse of the ac-  
 1429 ceptance is applied to the unfolded distribution in order to extrapolate to  
 1430 the truth fiducial phase space. This has to be done because the unfolding is  
 1431 done with a response matrix  $R'$  obtained with events satisfying both truth  
 1432 and reconstructed criteria.

1433 It is worth to note that the events passing  $N^{\text{reco,truth}}$  and  $N^{\text{reco}}$  selections receive  
 1434 both reconstructed and truth weights i.e. SF efficiency, hadronic recoil, calibration,  
 1435 polarisation, generator weights, while the events passing  $N^{\text{truth}}$  have only truth  
 weights applied.

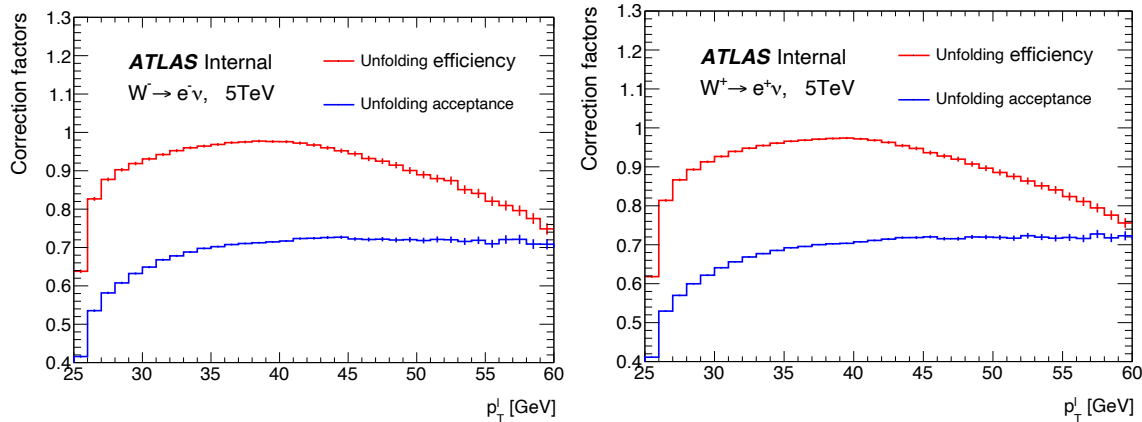


FIGURE 4.4: Example of the acceptance and efficiency factors for  $p_T^\ell$ .

## 1436 4.4 Uncertainties with unfolding

1438 The propagation of the statistical and systematic uncertainties through unfolding  
 1439 is a crucial technical aspect when the unfolding is applied to an analysis. In this

part, we discuss the propagation of the uncertainties in the iterative Bayesian unfolding.

#### 4.4.1 Propagation of the statistical uncertainty

The propagation of the statistical uncertainties through the unfolding is done using pseudo-data (toys). Basically, the idea is to fluctuate the unfolding inputs (data distributions) with Poisson variations [37] to generate toys. Then, for each toy we redo the unfolding procedure using the nominal (not modified) migration matrix. The covariance matrix for the statistical uncertainty is calculated by comparing the unfolded distributions for each toy using:

$$\text{Cov}(i, j) = \frac{1}{n-1} \sum_{k=1}^n (X_i^k - \bar{X}_i) (X_j^k - \bar{X}_j)^T, \quad (4.10)$$

where  $X_i^k$  ( $X_j^k$ ) corresponds to the content of bin  $i$  ( $j$ ) of the unfolded toy  $k$ ,  $\bar{X}_i$  ( $\bar{X}_j$ ) corresponds to the content of bin  $i$  ( $j$ ) of the average of all toys. The correlation matrix between bins for the statistical uncertainty is calculated using the covariance matrix by the formula:

$$\text{Corr}(i, j) = \frac{\text{Cov}(i, j)}{\sqrt{\text{Cov}(i, i)} \times \sqrt{\text{Cov}(j, j)}}. \quad (4.11)$$

Propagation of the statistical uncertainty for MC simulation is treated differently from data. In fact, the statistical uncertainty for simulation is treated as a systematic uncertainty, and the unfolding for simulation toys is done with a modified migration matrix instead of the nominal migration matrix. Figure 4.5 shows an example of the statistical uncertainty with the correlation matrix for the unfolded distribution.

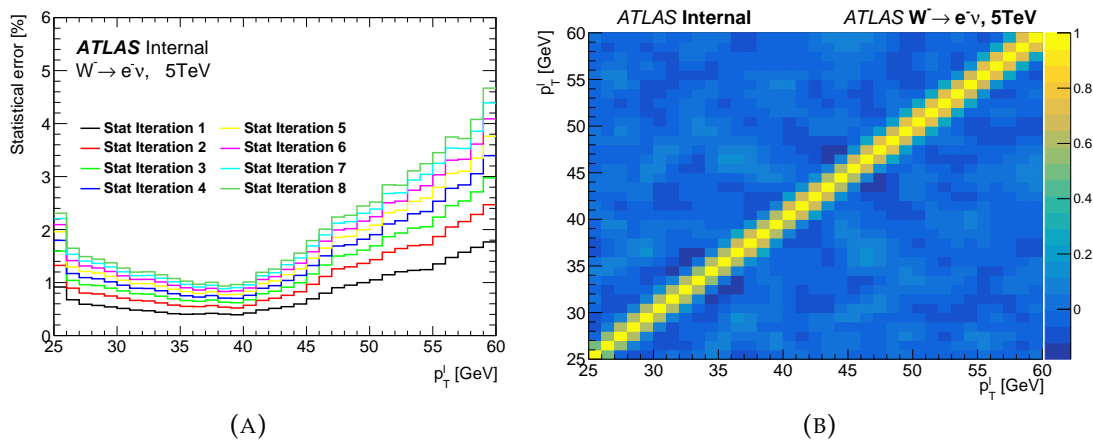


FIGURE 4.5: (A) Example of the statistical uncertainty for different iterations. (B) Example of the correlation matrix for the statistical uncertainty of the unfolding distribution.

Because of the correlation between truth and reconstruction level for our variables of interest, the statistical uncertainty increases with the number of iterations,

1461 as shown in Figure 4.5. Along with the increase of uncertainty with the number of  
 1462 iterations, the anti-correlation between bins increases also to ensure that the sta-  
 1463 tistical uncertainty is independent of the number of iterations when we integrate  
 1464 over all the bins.

#### 1465 4.4.2 Propagation of systematic uncertainties

1466 The estimation of systematic uncertainties at the unfolded level is based on simu-  
 1467 lated distributions. For a given systematic uncertainty, we varied the inputs distri-  
 1468 butions (reconstructed distributions and migration matrix) according to this sys-  
 1469 tematic uncertainty. The propagation of the systematic uncertainty through un-  
 1470 folding is estimated as the the difference between the unfolding of the nominal  
 1471 distribution and the unfolding of the modified distribution. For the same reason  
 1472 of migration between bins, the systematic uncertainties increase with the number  
 1473 of iterations as seen in Sec. 4.6. After the unfolding, all the systematic uncertainties  
 1474 are assumed to be fully correlated between the bins, and the covariance matrix ( $V$ )  
 1475 is calculated as:

$$V_{i,j} = \sigma_i \times \sigma_j, \quad (4.12)$$

1476 where  $\sigma_i$  ( $\sigma_j$ ) is the systematic uncertainty in bin  $i$  ( $j$ ). Figure 4.6 shows as an  
 1477 example the calibration systematic uncertainty as a function of iteration and the  
 1478 corresponding correlation matrix. In fact, the systematic uncertainties must be  
 1479 independent of the number of iterations, and the variation with the number of it-  
 1480 erations is related to statistical fluctuations in the systematic variations. For the  
 1481 choice of the number of iterations, the systematic uncertainties are not included in  
 the optimisation study described in Sec. 4.5.

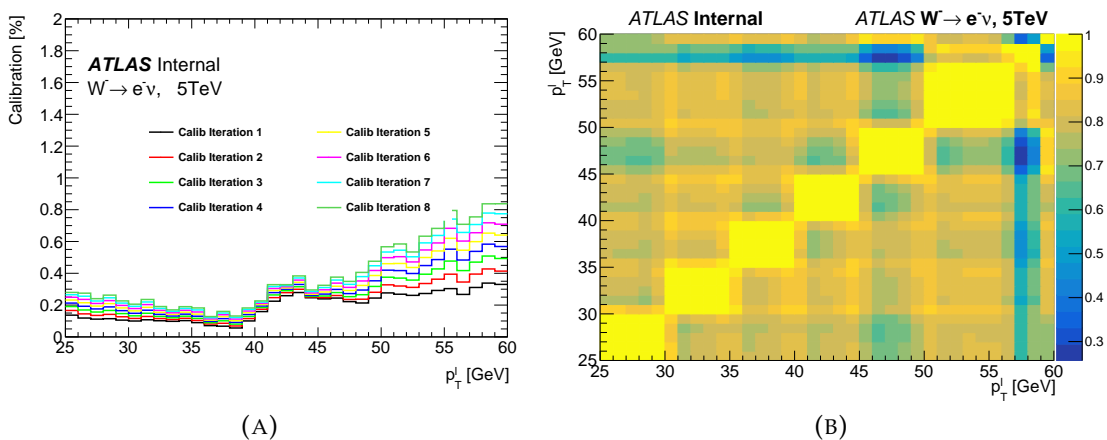


FIGURE 4.6: (A) Example of the systematic uncertainty for different iterations. (B) Exam-  
 ple of the correlation matrix. The calibration uncertainty is defined as the sum of several  
 variations.

1482

#### 1483 4.4.3 Bias uncertainty with unfolding

1484 In addition to the statistical and systematic uncertainties, there is the unfolding  
 1485 bias that we have to take into account. This bias is related mainly to the unfolding

method and can be estimated with different approaches. The approach used in this chapter is a simple one used for the unfolding of a variable with small migration between reconstruction and truth level, like for  $p_T^\ell$  and  $\eta_\ell$ . For the unfolding of a variable with larger migration like  $p_T^W$ , a more involved approach is used and will be described later. The procedure to estimate the bias, through a "data-driven closure test" using the data/MC shape differences for the unfolded observable, can be summarised in two steps: (Figure 4.7) [111]:

- Reweight the MC distribution at truth level with the fitted ratio of data over simulation, in such a way that the reconstructed distribution after the reweighting matches the data in which the background has been subtracted. As shown in Figure 4.8, as we expect, the ratio data/MC is closer to 1 for the reconstruction-weighted distribution.
- The bias is estimated as the difference between the unfolding of the reconstruction-weighted distribution and the truth-weighted distribution.

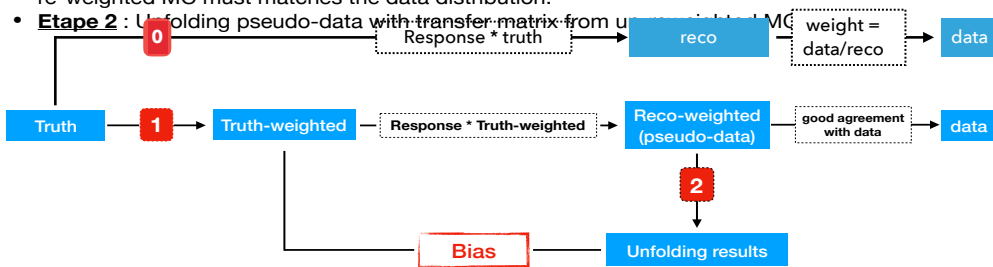


FIGURE 4.7: An overview of the procedure used to estimate the unfolding bias.

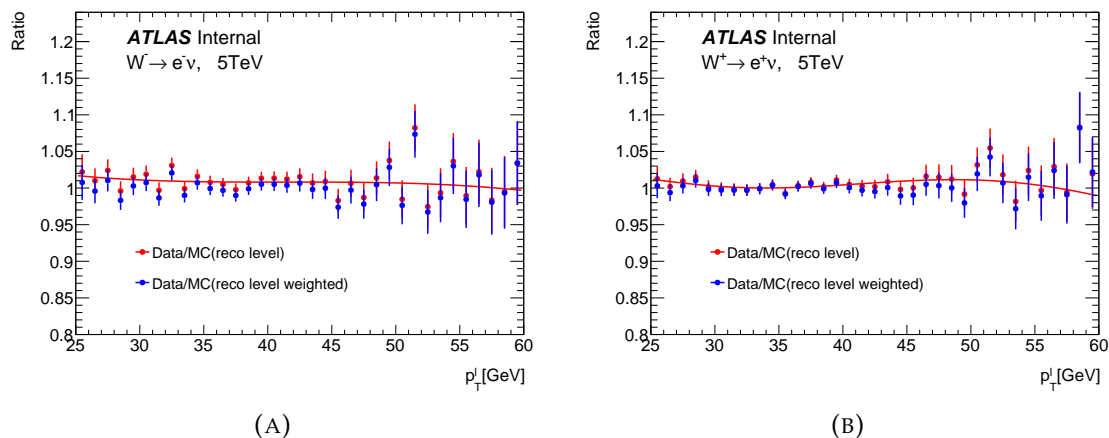


FIGURE 4.8: Comparison of the ratio data/MC using the reconstruction and weighted reconstruction-distributions, for  $W^-$  (A) and  $W^+$  (B) at 5 TeV.

In general, the unfolding bias decreases with the number of iterations, as shown in Figure 4.9. Also, as the unfolding does not change the normalisation of

1502 the input distributions, the total integrated unfolding bias when we take the corre-  
 1503 lation (anti-correlation) between bins into account must be equal to 0. Contrary to  
 1504 other source of uncertainties, the bias decreases with the number of iterations and  
 1505 the anti-correlation between bins increases with the number of iterations to ensure  
 that the integrated bias is zero.

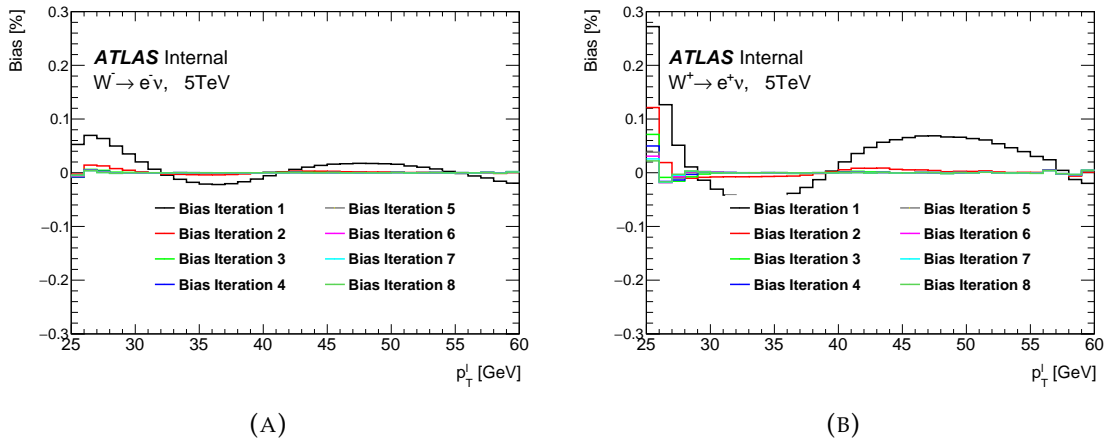


FIGURE 4.9: Comparison of the unfolding bias for different iterations, for  $W^-$  (A) and  $W^+$  (B) at 5 TeV.

1506

## 1507 4.5 Optimisation of the number of iterations

1508 As discussed above, the statistical uncertainty increases with the number of iterations,  
 1509 whereas the unfolding bias, considered as a source of uncertainty, decreases  
 1510 with the number of iterations, as seen in Figure 4.10. Therefore, it is possible to  
 1511 optimise the number of iterations by minimising the combined statistical and bias  
 1512 uncertainties. The other systematic uncertainties are not included in the optimi-  
 1513 sation as they should be independent of the number of iterations as mentioned  
 1514 earlier. Also, the optimisation should be performed for a selected region of the  
 1515 unfolded distribution since we can not use the whole range of the unfolded dis-  
 1516 tribution (the bias is zero). The example in Figure 4.10 shows the information that  
 1517 can be used for the bin-by-bin optimisation around the peak region:  
 1518 For our example shown in Figure 4.11, as the bias is very small comparing to other  
 1519 source of uncertainties, the best choice is to use the first iteration. But to avoid  
 1520 the fluctuation/bias in the first iteration, see Figure 4.9, the 2<sup>nd</sup> iteration is chosen  
 1521 instead.

## 1522 4.6 Bin-by-bin unfolding

1523 The bin-by-bin unfolding consists in applying a correction factor that we extract di-  
 1524 rectly from simulation. This unfolding method is used basically in the case where  
 1525 the variable of interest is characterised with a small migration between truth and  
 1526 reconstructed level and when the number of bins is the same between the truth

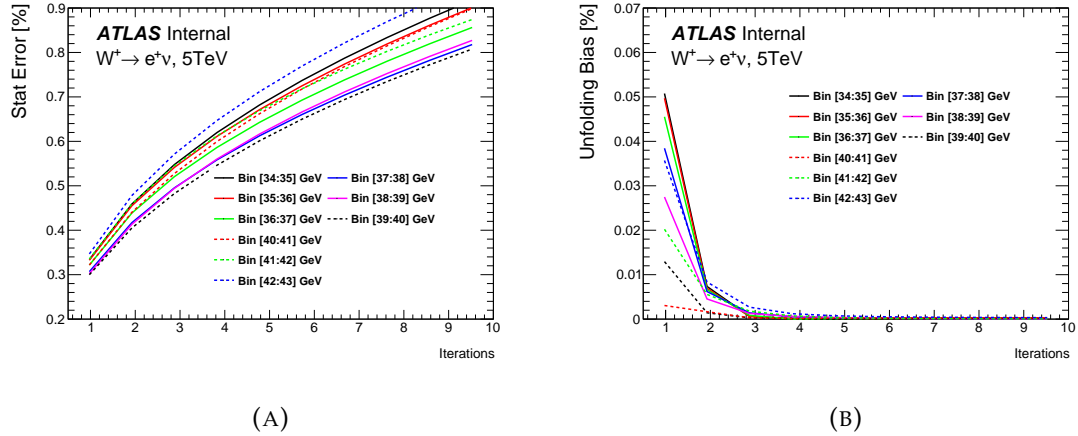


FIGURE 4.10: Statistical (A) and unfolding bias (B) uncertainties as a function of the number of iterations for different bins of  $p_T^\ell$ , around the peak region in our distribution of interest.

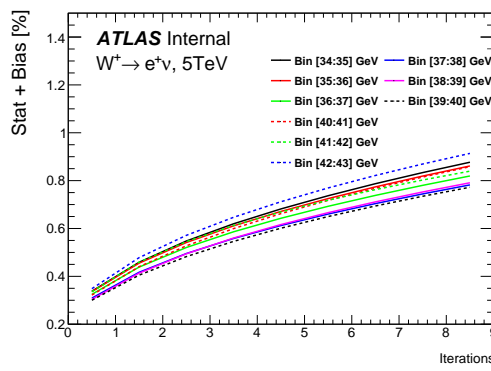


FIGURE 4.11: Sum of the statistical and unfolding bias uncertainties as a function of the number of iterations for different bins of  $p_T^\ell$ , around the peak region in our distribution of interest.

1527 and reconstructed distributions. Let us consider a MC truth distribution  $x_i^{\text{gen}}$  and  
 1528 a MC reconstructed distribution  $y_i^{\text{rec}}$ . The correction factor is calculated as:

$$C_i = \frac{x_i^{\text{gen}}}{y_i^{\text{rec}}}. \quad (4.13)$$

1529 The unfolded data using the bin-by-bin method is calculated as:

$$\text{Unfolded}_i = C_i \times \text{data}_i. \quad (4.14)$$

1530 The bin-by-bin is used only in the case where the detector effects are very small,  
 1531 otherwise this method will introduce a large bias [110]. This method can be used  
 1532 mainly for the unfolding of  $p_T^\ell$  and  $\eta_\ell$ .



1533 **Chapter 5**

1534 **Measurement of the  $W$ -boson  
1535 transverse momentum distribution**

1536 **5.1 Introduction**

1537 One of the most important theoretical sources of uncertainties in the measurement  
1538 of the  $W$ -boson mass, is the extrapolation of the boson  $p_T$  distribution from  $Z$ -  
1539 boson to  $W$ -boson ( $\approx 6$  MeV [155]), where the QCD high order predictions are not  
1540 sufficiently precise to describe the data. A precise direct measurement of  $p_T^W$  will  
1541 provide a direct comparison with QCD predictions, this is equivalent to saying  
1542 that replacing the theoretical extrapolation from  $p_T^Z$  by such a direct measurement  
1543 of the  $p_T^W$  distribution will improve the precision of the measurement of  $M_W$ . Mea-  
1544 suring the  $p_T^W$  distribution in low  $p_T^W$  region ( $p_T^W < 30$  GeV) with an uncertainty  
1545  $\approx 1\%$  in bin of 5 GeV will reduce the QCD modelling uncertainty [115] in the mea-  
1546 surement of  $M_W$  by a factor of two [132]. The  $p_T^W$  distribution is reconstructed  
1547 using  $W \rightarrow \ell\nu$  events, where the charged leptons are measured in the different  
1548 tracking detectors or in the EM calorimeter, as discussed in Chapter 2, while the  
1549 neutrino leaves the detector unseen. Because of the neutrino, the  $p_T^W$  distribution  
1550 is reconstructed through the hadronic recoil,  $\vec{u}_T$ , defined as the vector sum of all  
1551 energy deposits excluding the energy of the lepton. The transverse momentum of  
1552 the  $W$  boson is defined by:

$$\vec{p}_T^W = -\vec{u}_T, \quad (5.1)$$

1553 and the transverse momentum of the decay neutrino  $\vec{p}_T^\nu$  is inferred from the vector  
1554 of the missing transverse momentum  $\vec{p}_T^{\text{miss}}$  which corresponds to the momentum  
1555 imbalance in the transverse plan:

$$\vec{p}_T^{\text{miss}} = -(\vec{p}_T^\ell + \vec{u}_T). \quad (5.2)$$

1556 For the reconstruction of  $p_T^W$ , a good understanding of  $\vec{u}_T$  is needed. The recon-  
1557 struction of the hadronic recoil is described in [101]. The measurement of  $p_T^W$  is  
1558 based on low number of interactions per bunch crossing data (low pile-up  $\mu$ ) to en-  
1559 sure a reasonable resolution on the hadronic recoil, as shown in Figure 5.1, which  
1560 shows the comparison of the resolution on the hadronic recoil between high pile-  
1561 up runs (black circles) and low pile-up runs (red points). In this chapter, we will  
1562 describe the measurement of the  $W$ -boson transverse momentum through the un-  
1563 folding of the  $p_T^W$  distributions at the detector level, using the unfolding method  
1564 described in Chapter 4, with low pile-up data sets collected during Run 2 at  $\sqrt{s}$

= 5 and 13 TeV. Also, a different approach is used to estimate the unfolding bias for the  $p_T^W$  analysis, in order to improve our evaluation of the unfolding bias. The new approach, described in [114], consists of using a different reweighting method to get the best data/MC agreement. The main signal events for  $W$  and  $Z$  boson productions are described in [95]. They are generated using the POWHEG event generator using the CT10 PDF interfaced to PYTHIA8 using the AZ NLO tune, and being interfaced to PHOTOS++ to simulate the effect of final state QED radiation.

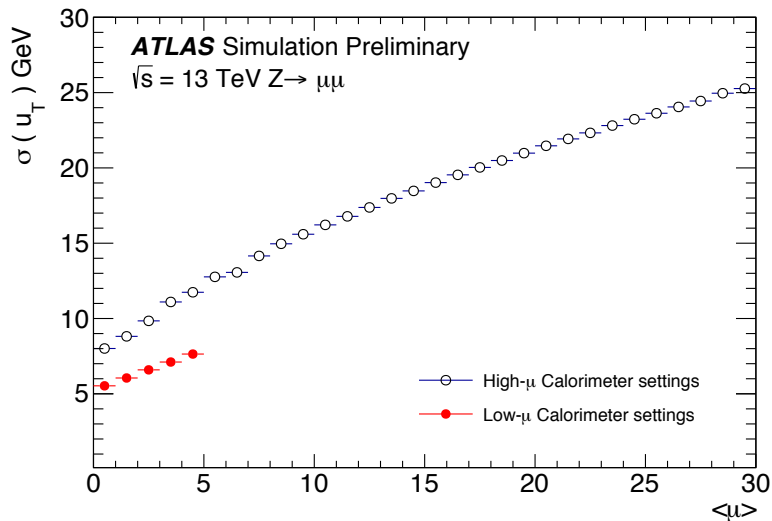


FIGURE 5.1: Hadronic recoil resolution as a function of  $\langle \mu \rangle$  for simulated  $Z \rightarrow \mu\mu$  events with two different calorimeter settings [132], see Chapter 3 for a discussion of the calorimeter settings.

1571

## 1572 5.2 Data and simulated distributions

### 1573 5.2.1 Selections

1574 The selections of  $W \rightarrow \ell\nu$  events for the  $p_T^W$  distribution are based on the following two triggers *HLT\_e15\_Ihloose\_nod0\_L1EM12* and *HLT\_mu14*, for electrons and muons, respectively. In addition, events are required to contain one lepton with  $p_T^\ell > 25$  GeV and  $E_T^{\text{miss}} > 25$  GeV to reduce background effects. In addition, the  $W$  boson transverse mass defined as  $m_T^W = \sqrt{2p_T^\ell p_T^{\text{miss}}(1 - \cos(\Delta\phi))}$ , with  $\Delta\phi$  being the azimuthal opening angle between the charged lepton and the missing transverse momentum, is chosen to be  $m_T^W > 50$  GeV. A detailed description of the selections, with the final number of events which pass all the selections, is given for 5 and 13 TeV samples separately in [114].

### 1583 5.2.2 Control plots for the $p_T^W$ distribution

1584 Once all the events pass the selections described above, we show the distributions of the  $W$ -boson transverse momentum for data compared to MC simulation

TABLE 5.1: Analysis cut flow for  $W^+ \rightarrow e^+ \nu_e$  5 TeV signal selection.

Cut	Data	Signal	$W^\pm \rightarrow \ell^\pm \nu$ BG	$Z \rightarrow \ell\ell$	Top	Diboson	Multijet
One electron	1993720	643610 $\pm$ 260	32940 $\pm$ 190	44338 $\pm$ 71	1754.4 $\pm$ 3.9	772.2 $\pm$ 3.7	-
Electron trig matched	1907724	612940 $\pm$ 250	30790 $\pm$ 190	42100 $\pm$ 69	1698.5 $\pm$ 3.8	741.1 $\pm$ 3.6	-
Isolation	1438941	610320 $\pm$ 250	30590 $\pm$ 190	41923 $\pm$ 69	1663.6 $\pm$ 3.8	722.5 $\pm$ 3.6	-
$p_T^e > 25$ GeV	720284	482240 $\pm$ 220	14790 $\pm$ 130	31955 $\pm$ 53	1464.5 $\pm$ 3.5	592.1 $\pm$ 3.2	-
$E_T^{\text{miss}} > 25$ GeV	440605	421510 $\pm$ 210	9650 $\pm$ 100	1336 $\pm$ 20	1223 $\pm$ 3.2	420.8 $\pm$ 2.4	-
$m_T^W > 50$ GeV	430620	417430 $\pm$ 210	8800 $\pm$ 96	1047 $\pm$ 16	944.3 $\pm$ 2.9	373.5 $\pm$ 2.2	3030 $\pm$ 550

TABLE 5.2: Analysis cut flow for  $W^+ \rightarrow e^+ \nu_e$  13 TeV signal selection.

Cut	Data	Signal	$W^\pm \rightarrow \ell^\pm \nu$ BG	$Z \rightarrow \ell\ell$	Top	Diboson	Multijet
One electron	7915023	1797340 $\pm$ 390	92520 $\pm$ 270	147490 $\pm$ 140	63207 $\pm$ 89	3069 $\pm$ 63	-
Electron trig matched	7840239	1709140 $\pm$ 380	86370 $\pm$ 260	139760 $\pm$ 140	61110 $\pm$ 88	2967 $\pm$ 62	-
Isolation	5143483	1698430 $\pm$ 380	85560 $\pm$ 260	138890 $\pm$ 140	59834 $\pm$ 87	2939 $\pm$ 61	-
$p_T^e > 25$ GeV	2452868	1342200 $\pm$ 330	44450 $\pm$ 190	106270 $\pm$ 110	53811 $\pm$ 82	2565 $\pm$ 58	-
$E_T^{\text{miss}} > 25$ GeV	1275513	1136520 $\pm$ 310	28580 $\pm$ 150	8313 $\pm$ 46	45707 $\pm$ 75	1990 $\pm$ 53	-
$m_T^W > 50$ GeV	1207776	1117560 $\pm$ 310	24760 $\pm$ 130	6443 $\pm$ 36	34580 $\pm$ 65	1718 $\pm$ 50	28000 $\pm$ 1800

TABLE 5.3: Analysis cut flow for  $W^+ \rightarrow \mu^+ \nu_\mu$  5 TeV signal selection.

Cut	Data	Signal	$W^\pm \rightarrow \ell^\pm \nu$ BG	$Z \rightarrow \ell\ell$	Top	Diboson	Multijet
One muon	2434459	760980 $\pm$ 280	35090 $\pm$ 200	37015 $\pm$ 82	2025.3 $\pm$ 4.1	864.7 $\pm$ 3.7	-
Muon trig matched	2353403	664100 $\pm$ 260	30610 $\pm$ 190	32554 $\pm$ 76	1725.6 $\pm$ 3.8	746.6 $\pm$ 3.4	-
Isolation	1186616	659200 $\pm$ 260	30400 $\pm$ 190	32303 $\pm$ 76	1574.6 $\pm$ 3.7	710.1 $\pm$ 3.3	-
$p_T^\mu > 25$ GeV	632016	508270 $\pm$ 230	13900 $\pm$ 130	22556 $\pm$ 57	1335.3 $\pm$ 3.4	568.2 $\pm$ 2.9	-
$E_T^{\text{miss}} > 25$ GeV	470856	442600 $\pm$ 210	8700 $\pm$ 100	9959 $\pm$ 31	1111.8 $\pm$ 3	424.5 $\pm$ 2.5	-
$m_T^W > 50$ GeV	457053	438280 $\pm$ 210	7879 $\pm$ 97	9649 $\pm$ 27	879.7 $\pm$ 2.8	381.7 $\pm$ 2.3	720 $\pm$ 190

TABLE 5.4: Analysis cut flow for  $W^+ \rightarrow \mu^+ \nu_\mu$  13 TeV signal selection.

Cut	Data	Signal	$W^\pm \rightarrow \ell^\pm \nu$ BG	$Z \rightarrow \ell\ell$	Top	Diboson	Multijet
One muon	9570104	2100770 $\pm$ 410	83110 $\pm$ 270	2019400 $\pm$ 2200	71602 $\pm$ 94	3442 $\pm$ 63	-
Muon trig matched	9382783	1840550 $\pm$ 390	72820 $\pm$ 250	1750400 $\pm$ 2000	61519 $\pm$ 87	2956 $\pm$ 59	-
Isolation	3905612	1821750 $\pm$ 380	71780 $\pm$ 250	595700 $\pm$ 1100	56849 $\pm$ 84	2916 $\pm$ 59	-
$p_T^\mu > 25$ GeV	1930655	1393330 $\pm$ 340	34470 $\pm$ 170	170840 $\pm$ 490	49338 $\pm$ 78	2471 $\pm$ 54	-
$E_T^{\text{miss}} > 25$ GeV	1321407	1173860 $\pm$ 310	21450 $\pm$ 140	51090 $\pm$ 180	41956 $\pm$ 72	1930 $\pm$ 49	-
$m_T^W > 50$ GeV	1244892	1153800 $\pm$ 310	18270 $\pm$ 130	38304 $\pm$ 81	32375 $\pm$ 63	1705 $\pm$ 44	9040 $\pm$ 800

TABLE 5.5: Analysis cut flow for  $W^- \rightarrow e^- \bar{\nu}_e$  5 TeV signal selection.

Cut	Data	Signal	$W^\pm \rightarrow \ell^\pm \nu$ BG	$Z \rightarrow \ell\ell$	Top	Diboson	Multijet
One electron	1724472	374900 $\pm$ 200	24150 $\pm$ 160	41995 $\pm$ 70	1590.5 $\pm$ 2.9	684.8 $\pm$ 4	-
Electron trig matched	1645694	359010 $\pm$ 200	22070 $\pm$ 160	39854 $\pm$ 68	1539.9 $\pm$ 2.9	655.7 $\pm$ 3.9	-
Isolation	1176976	357660 $\pm$ 200	21920 $\pm$ 160	39686 $\pm$ 68	1504.6 $\pm$ 2.8	640.7 $\pm$ 3.8	-
$p_T^e > 25$ GeV	529183	302070 $\pm$ 180	11920 $\pm$ 110	30214 $\pm$ 52	1330.8 $\pm$ 2.6	532.9 $\pm$ 3.5	-
$E_T^{\text{miss}} > 25$ GeV	281957	266750 $\pm$ 170	8084 $\pm$ 90	1293 $\pm$ 20	1112.5 $\pm$ 2.4	380 $\pm$ 3	-
$m_T^W > 50$ GeV	274329	264540 $\pm$ 170	7317 $\pm$ 84	994 $\pm$ 16	855.2 $\pm$ 2.1	338.1 $\pm$ 2.9	2400 $\pm$ 500

TABLE 5.6: Analysis cut flow for  $W^- \rightarrow e^- \bar{\nu}_e$  13 TeV signal selection.

Cut	Data	Signal	$W^\pm \rightarrow \ell^\pm \nu$ BG	$Z \rightarrow \ell\ell$	Top	Diboson	Multijet
One electron	7471742	1323710 $\pm$ 330	78230 $\pm$ 230	140980 $\pm$ 140	61951 $\pm$ 86	3059 $\pm$ 58	-
Electron trig matched	7402574	1267710 $\pm$ 330	72240 $\pm$ 230	133580 $\pm$ 140	59950 $\pm$ 85	2968 $\pm$ 57	-
Isolation	4949352	1260540 $\pm$ 330	71550 $\pm$ 230	132740 $\pm$ 140	58689 $\pm$ 84	2937 $\pm$ 57	-
$p_T^e > 25$ GeV	2113364	1053310 $\pm$ 300	39660 $\pm$ 160	101350 $\pm$ 110	52923 $\pm$ 79	2544 $\pm$ 53	-
$E_T^{\text{miss}} > 25$ GeV	1008915	900640 $\pm$ 280	25900 $\pm$ 130	7954 $\pm$ 45	45065 $\pm$ 73	1962 $\pm$ 48	-
$m_T^W > 50$ GeV	949362	887810 $\pm$ 270	22400 $\pm$ 120	6052 $\pm$ 35	34177 $\pm$ 64	1695 $\pm$ 44	27400 $\pm$ 2000

TABLE 5.7: Analysis cut flow for  $W^- \rightarrow \mu^- \bar{\nu}_\mu$  5 TeV signal selection.

Cut	Data	Signal	$W^\pm \rightarrow \ell^\pm \nu$ BG	$Z \rightarrow \ell\ell$	Top	Diboson	Multijet
One muon	2075709	440560 $\pm$ 220	22510 $\pm$ 170	34440 $\pm$ 80	1835.6 $\pm$ 3.1	751.5 $\pm$ 3.3	-
Muon trig matched	2002955	383720 $\pm$ 200	19640 $\pm$ 160	30277 $\pm$ 75	1561.6 $\pm$ 2.9	648 $\pm$ 3.1	-
Isolation	883078	381010 $\pm$ 200	19450 $\pm$ 160	30046 $\pm$ 74	1411 $\pm$ 2.7	616.9 $\pm$ 2.9	-
$p_T^\mu > 25$ GeV	426119	314370 $\pm$ 180	9370 $\pm$ 110	20749 $\pm$ 56	1202.1 $\pm$ 2.5	505 $\pm$ 2.5	-
$E_T^{\text{miss}} > 25$ GeV	298992	276060 $\pm$ 170	5893 $\pm$ 89	8716 $\pm$ 29	1004.2 $\pm$ 2.3	372.6 $\pm$ 2	-
$m_T^W > 50$ GeV	287870	273710 $\pm$ 170	5158 $\pm$ 82	8408 $\pm$ 26	788.2 $\pm$ 2	335.6 $\pm$ 1.9	760 $\pm$ 160

TABLE 5.8: Analysis cut flow for  $W^- \rightarrow \mu^- \bar{\nu}_\mu$  13 TeV signal selection.

Cut	Data	Signal	$W^\pm \rightarrow \ell^\pm \nu$ BG	$Z \rightarrow \ell\ell$	Top	Diboson	Multijet
One muon	8773414	1518070 $\pm$ 360	64930 $\pm$ 230	2019900 $\pm$ 2200	70580 $\pm$ 90	3230 $\pm$ 60	-
Muon trig matched	8597493	1322980 $\pm$ 330	56520 $\pm$ 210	1750300 $\pm$ 2000	60579 $\pm$ 84	2806 $\pm$ 56	-
Isolation	3298569	1310310 $\pm$ 330	55680 $\pm$ 210	593700 $\pm$ 1100	55949 $\pm$ 80	2751 $\pm$ 55	-
$p_T^\mu > 25$ GeV	1561721	1069770 $\pm$ 300	28230 $\pm$ 150	166810 $\pm$ 490	48544 $\pm$ 75	2362 $\pm$ 52	-
$E_T^{\text{miss}} > 25$ GeV	1030406	910150 $\pm$ 280	17380 $\pm$ 120	47370 $\pm$ 180	41259 $\pm$ 69	1842 $\pm$ 46	-
$m_T^W > 50$ GeV	963568	896850 $\pm$ 270	14710 $\pm$ 110	34572 $\pm$ 80	31772 $\pm$ 61	1598 $\pm$ 43	9050 $\pm$ 620

1586 (signal and background) for 5 TeV, in Figure 5.2 and 13 TeV in Figure 5.3 sepa-  
 1587 rately. The bottom panels show the ratio data to simulation, with the green band  
 1588 corresponding to the total uncertainty with the statistical and systematic uncer-  
 1589 tainties added in quadrature. In general, one finds good agreement between the  
 1590 data and the predicted number of events within the uncertainty except for some  
 1591 of the 13 TeV cases.

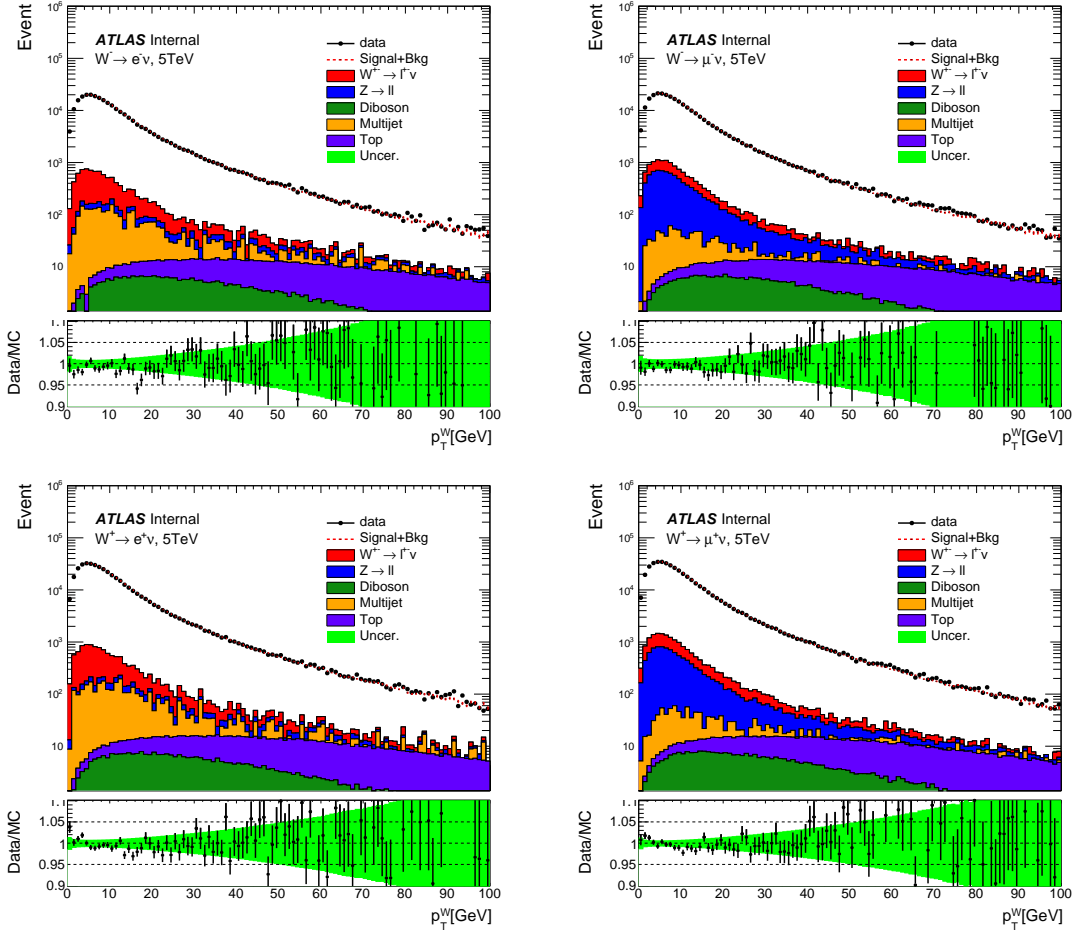


FIGURE 5.2: Reconstructed  $p_T^W$  distributions in data compared to MC (signal and background) in the electron (left) and muon (right) channels for negative (top) and positive (bottom) charges for the  $\sqrt{s} = 5$  TeV data set. The lower panel of each plot shows the data to simulation ratio, together with the total uncertainty at the detector level. The green band is dominated by the uncertainty due to the calibration of the hadronic recoil and the statistical uncertainty. The different sources of uncertainties at the detector level are shown in Appendix B.

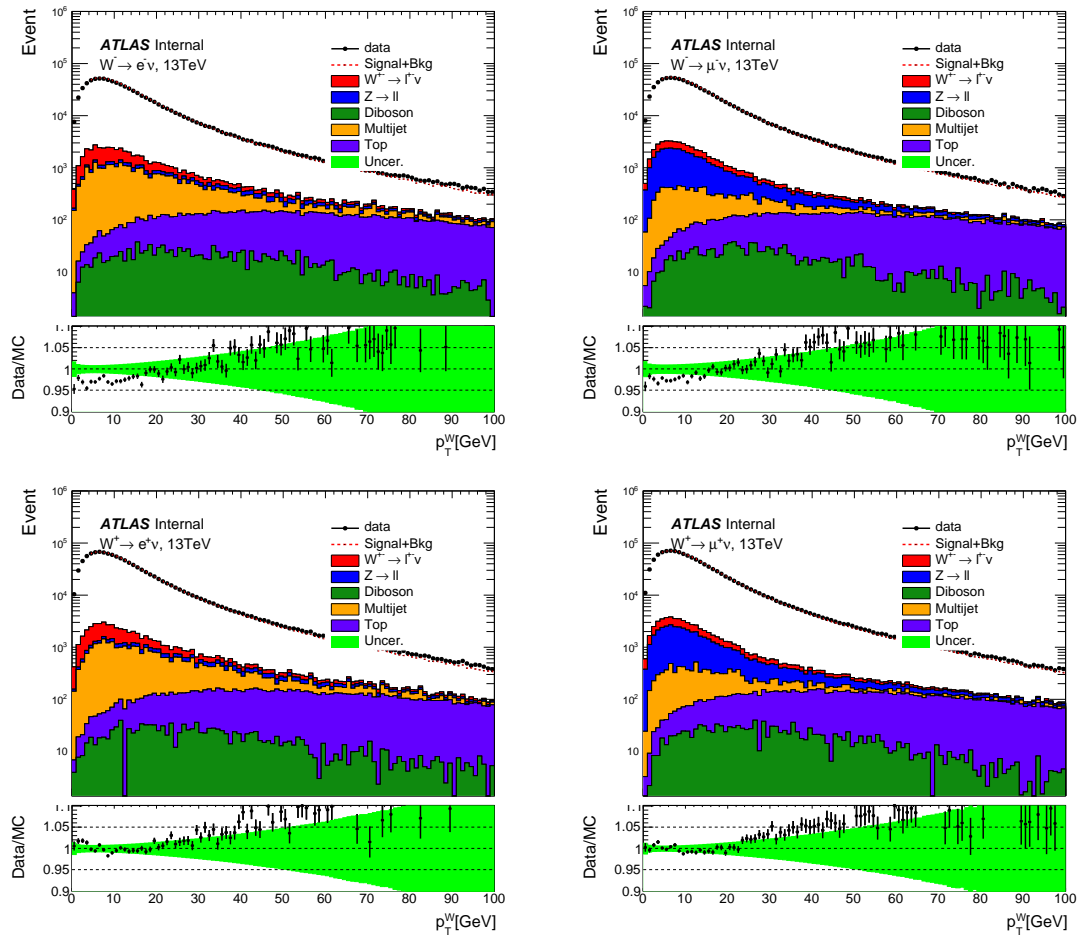


FIGURE 5.3: Same as Figure 5.2 but for the  $\sqrt{s} = 13$  TeV data set. The agreement is generally worse at 13 TeV compared to 5 TeV, because for simulation we use the the same tuning, AZ tuned at 7 TeV, which gives a better agreement between data and simulation for 5 than 13 TeV.

## 1592 5.3 Data unfolding

### 1593 5.3.1 Unfolding description

1594 As described in Chapter 4, the Bayesian unfolding method is used to unfold data  
 1595 distributions. The unfolding procedure starts by subtracting the background ef-  
 1596 fects from data distributions. The background contribution is based on simulation  
 1597 samples, and their effect on the data is estimated using the formula:

$$\text{data}_i^{\text{corrected}} = \text{data}_i \times \left( 1 - \frac{N_i^{\text{Bkgr}}}{N_i^{\text{Sig}} + N_i^{\text{Bkgr}}} \right), \quad (5.3)$$

1598 where  $N_i^{\text{Bkgr}}$  is the sum of all the background contributions in bin  $i$ , showed in  
 1599 Figures 5.2 and 5.3,  $N_i^{\text{Sig}}$  is the number of events in signal in bin  $i$ . Then, the  
 1600 efficiency correction factor, defined in Chapter 4, is applied to data. Figure 5.4  
 1601 shows an example of such efficiency correction factors. Once the data distribu-  
 1602 tions are corrected, it can be unfolded as described in Chapter 4 using the migra-  
 1603 tion matrix. Figure 5.5 shows an example of the migration matrix used for the  $p_T^W$   
 1604 unfolding. The migration matrix is characterised by a large migration between  
 1605 truth and detector variables, which makes the unfolding more involved than that  
 of  $p_T^\ell$  and  $\eta_\ell$ . The migration matrix is determined using the simulation samples,

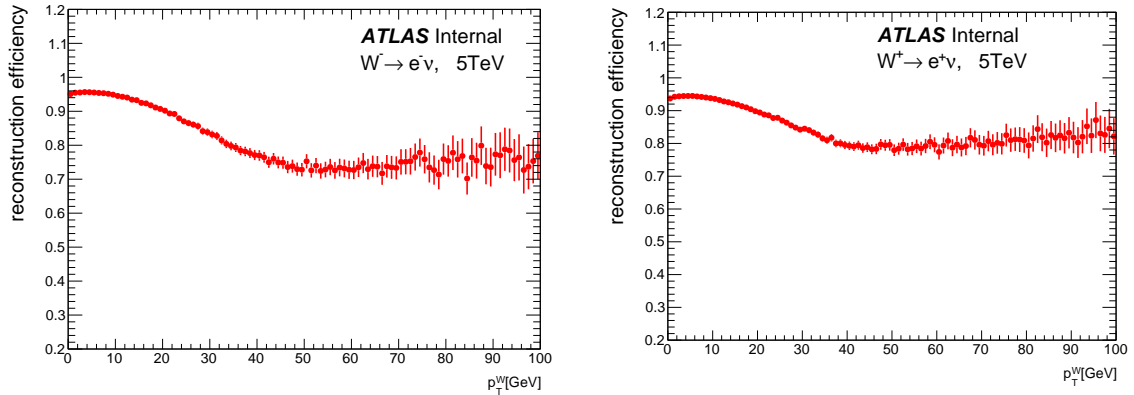


FIGURE 5.4: Example of the unfolding efficiency factor, defined as the ratio of the number of events at the reconstruction level with correspond to a truth level selection divided by the total number of events at the reconstruction level. This efficiency is applied to correct data distributions before unfolding, for electron channels at  $\sqrt{s} = 5$  TeV.

1606 Powheg+Pythia8 [43] in our analysis, where the  $x$ -axis corresponds to the recon-  
 1607 structed bins and the  $y$ -axis to true bins. The migration matrix is constructed in  
 1608 such a way that each event passes both truth and reconstructed selections. The  
 1609 migration between the truth and the reconstructed levels depends on detector ef-  
 1610 ffects (such as the finite resolution of the detector and the limited reconstruc-  
 1611 tion efficiency). After the unfolding, the unfolded distribution can not be compared  
 1612 directly to the truth distribution, since this unfolded distribution corresponds to  
 1613 the truth distribution with both truth and reconstructed selections. For a direct

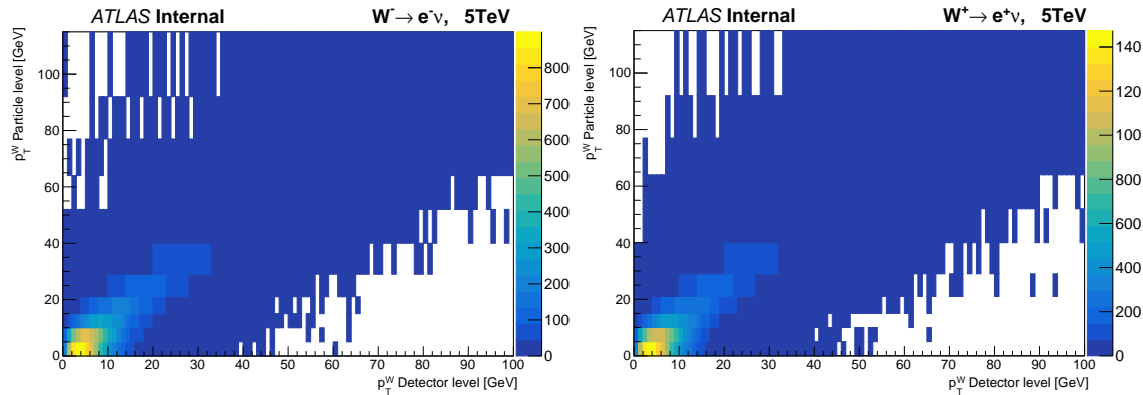


FIGURE 5.5: Example of the migration matrix of  $p_T^W$  for electron channels at  $\sqrt{s} = 5$  TeV. The correlation between bins is more important in the low  $p_T^W$  region ( $p_T^W < 30$  GeV).

1615 comparison, the unfolded distribution needs the acceptance correction, discussed  
 1616 in Chapter 4. After all the corrections, Figure 5.6 shows an example of the compari-  
 1617 son between the truth, reconstructed data and the unfolded data distributions. As  
 1618 described in Chapter 4, the Bayesian unfolding method is characterised by a regu-  
 1619 larisation parameter, used to reduce the bias that we introduce with the unfolding  
 1620 procedure. This parameter is optimised using statistical and bias uncertainties in  
 Sec. 5.3.6.

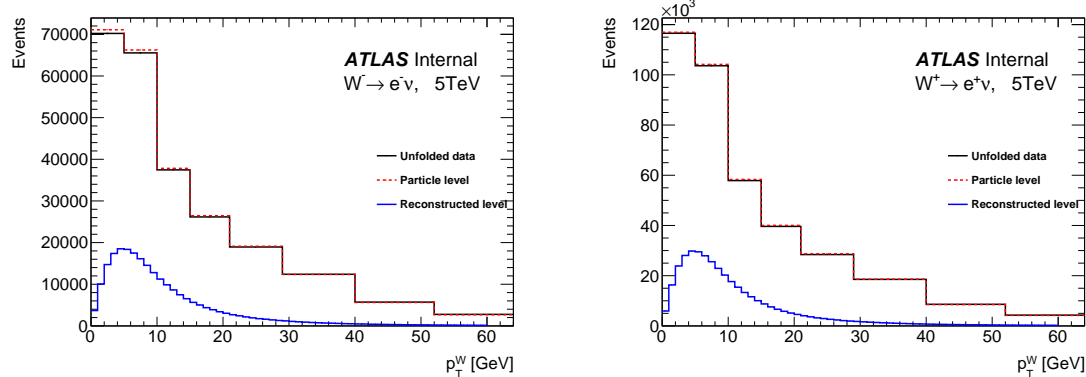


FIGURE 5.6: Example of the unfolded data distribution compared to reconstructed data events and the truth distributions for electron channels at  $\sqrt{s} = 5$  TeV. The acceptance correction is applied to the unfolded distribution to take into account events at the truth level which are not reconstructed.

### 5.3.2 Experimental systematic uncertainties

In this section, we review different sources of systematic uncertainties affecting the measurement of  $p_T^W$  distributions and the measurement of the differential cross sections in Chapter 7:

**Lepton scale factors:** As described in Chapter 3, two factors (energy scale and resolution) are applied to data and MC respectively to correct the residual difference observed between data and simulation. The combined effect of all scale and resolution uncertainties on the distributions of  $p_T^W$  is shown in Figures 5.7 and 5.8. The effect on  $p_T^W$  is up to 0.2% in low  $p_T^W$  region.

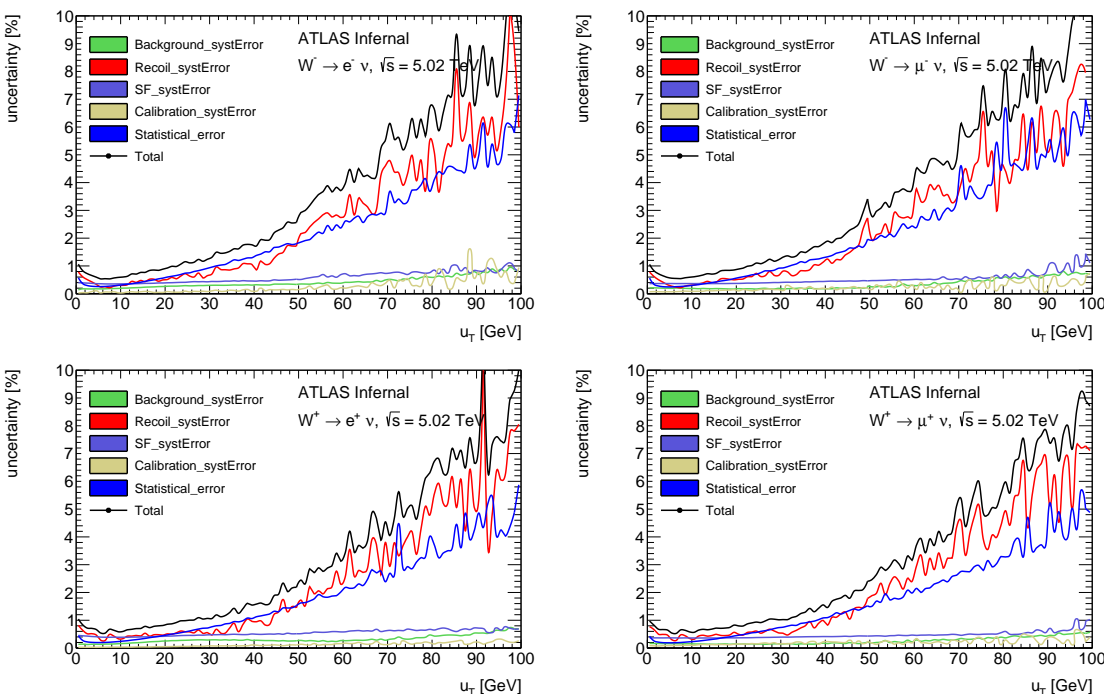


FIGURE 5.7: Different sources of uncertainties on the measurement of  $p_T^W$  distributions at the detector level for the  $\sqrt{s} = 5$  TeV data set. The total uncertainty is less than 1% in the low  $p_T^W$  region ( $p_T^W < 30$  GeV) and around 5% in the high  $p_T^W$  region ( $p_T^W \approx 100$  GeV). The total uncertainty is dominated by the hadronic recoil calibration uncertainty and the statistical uncertainty of the data.

**Lepton selection efficiency:** As detailed in Sec. 7.2, selected leptons are required to pass specific criteria. The efficiency of the selections in the simulation is normalised to that in data and applied to the simulation as product of different scale factors (SFs):

$$W_{\text{event}} = \text{SF}_{\text{reco}} \cdot \text{SF}_{\text{ID}} \cdot \text{SF}_{\text{isolation}} \cdot \text{SF}_{\text{trigger}}, \quad (5.4)$$

which correspond to the reconstruction, identification, isolation and trigger scale factors. The SFs are calculated using a “tag-and-probe” method detailed in [22].

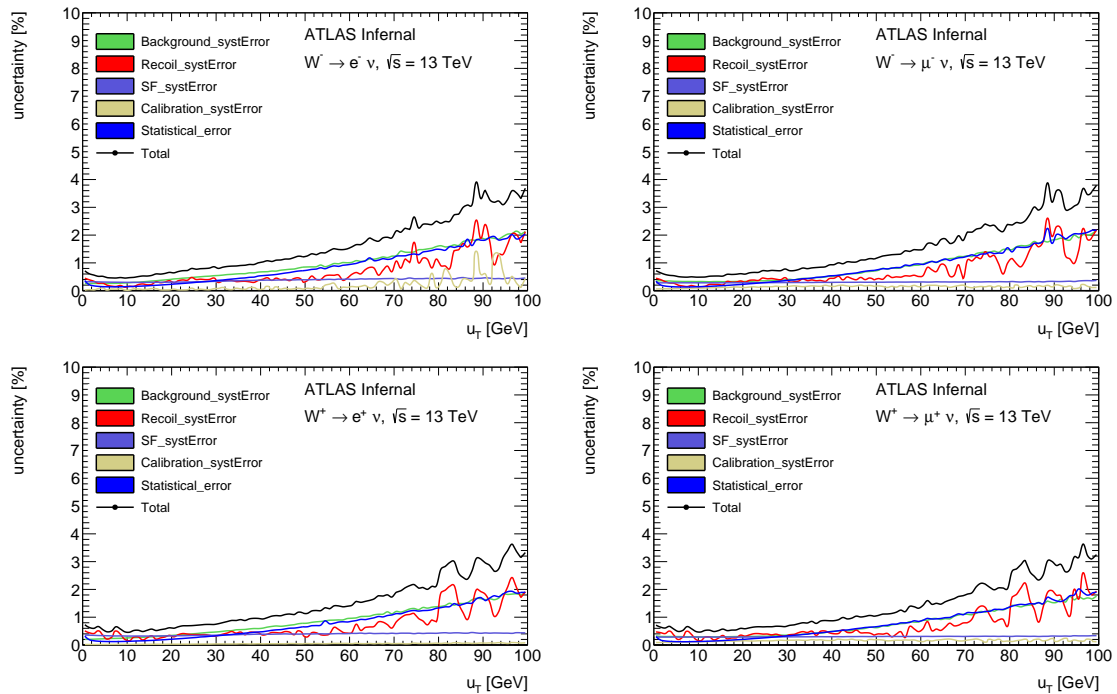


FIGURE 5.8: Different sources of uncertainties on the measurement of  $p_T^W$  distributions at the detector level for the  $\sqrt{s} = 13$  TeV data set. The total uncertainty is less than 1% in the low  $p_T^W$  region ( $p_T^W < 30$  GeV) and around 5% in the high  $p_T^W$  region ( $p_T^W \approx 100$  GeV). The total uncertainty is dominated by the hadronic recoil calibration uncertainty and the background uncertainty (because of the large background contributions of gauge-boson pair production and top quark production).

1638 **Hadronic recoil calibration:** Because the neutrino can not be measured in the AT-  
 1639 LAS detector, the hadronic recoil, defined as the vector sum of all energy  
 1640 deposits excluding energy of lepton, is used in the  $W$  boson analysis to deter-  
 1641 mine  $p_T^{\nu}$  and  $p_T^W$ . The uncertainty coming from the calibration of the hadronic  
 1642 recoil is dominated mainly by data statistics, specially at low  $p_T^W$ . The uncer-  
 1643 tainty on the hadronic recoil calibration is the dominant systematic uncer-  
 1644 tainty compared to other source of uncertainties.

1645 **Background uncertainty:** It is related to the background estimation, in particular  
 1646 to the multi-jet contribution [155], and varies between channels and center-  
 1647 of-mass energies. In general, the background uncertainty is below 0.5% for  
 1648 our regions of interest.

1649 **Luminosity:** The luminosity uncertainty for 13 TeV low pile-up runs is 1.5 % for  
 1650 the combination of 2017+2018 data (2.1% for 2017, 1.5% for 2018 ). The lumi-  
 1651 nosity uncertainty is 1.6% for 5 TeV 2017 low pile-up runs [104].

### 1652 5.3.3 Propagation of statistical uncertainties

1653 The propagation of the statistical uncertainties of the data through the unfolding  
 1654 is done using pseudo-data, constructed by fluctuating the data distribution with  
 1655 Poisson variations, and the covariance matrix of the statistical uncertainties at the  
 1656 unfolded level is built using the unfolding results for each pseudo-data distribu-  
 1657 tion, as described in Chapter 4. There is also another approach to calculate the  
 1658 covariance matrix at the unfolded level, by using internal toys generated by the  
 1659 *RooUnfoldBayes* class. Figure 5.9 shows an example of the statistical uncertainties  
 1660 at the unfolded level, bin-by-bin, for different iterations. The statistical uncertain-  
 1661 ties are smaller than 1% in low  $p_T^W$  region ( $p_T^W < 30$  GeV) and larger than 2 % at  
 1662  $p_T^W = 100$  GeV. Because of the correlation between truth and reconstructed levels  
 1663 (Figure 5.10), the statistical uncertainties increase with the number of iterations as  
 1664 shown in Figure 5.9. In fact, the diagonal elements of the covariance matrix in-  
 1665 crease with the number of iterations, on the other hand, the correlation between  
 1666 bins (non-diagonal elements) decrease to ensure that the total statistical uncertain-  
 1667 ties are independent of the number of iterations when we integrate over all bins.

1668

### 1669 5.3.4 Propagation of systematic uncertainties

1670 The systematic uncertainties are propagated through the unfolding in the same  
 1671 way as described in Chapter 4. In general the propagation of systematic uncer-  
 1672 tainties is based on simulation samples, where the reconstructed distribution and  
 1673 the migration matrix are modified by their uncertainties. The difference between  
 1674 the unfolding of the modified distribution and the unfolding of the nominal dis-  
 1675 tribution is considered as the systematic uncertainty. The systematic uncertainties  
 1676 increase also with the number of iterations, but contrary to the statistical uncer-  
 1677 tainties, the increase for the experimental systematic uncertainties is due to fluc-  
 1678 tuations related to the low statistics. Figure 5.11 shows an example of the recoil  
 1679 systematic uncertainty, the dominant one, as a function of the number of iterations

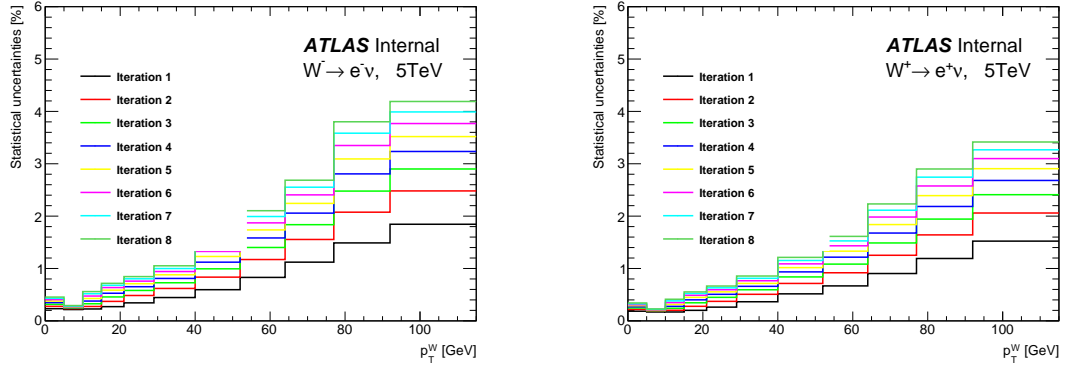


FIGURE 5.9: Statistical uncertainties on the unfolded distribution as a function of the number of iterations, bin-by-bin, for electron channels at  $\sqrt{s} = 5$  TeV.

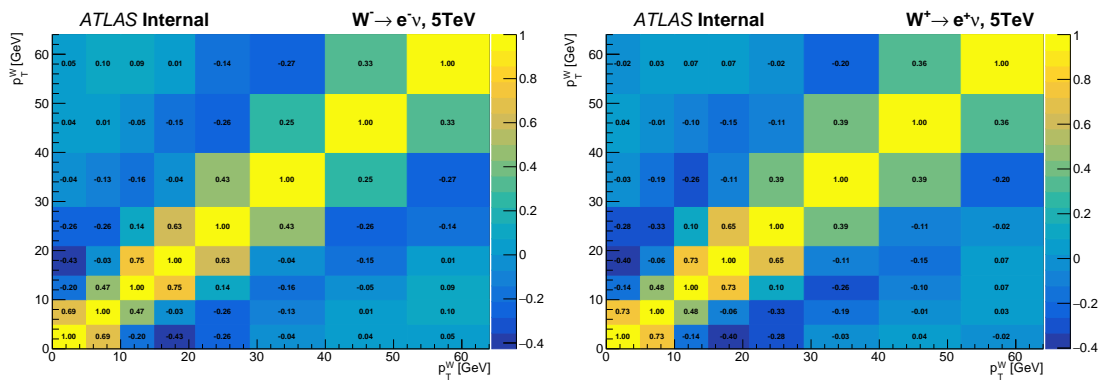


FIGURE 5.10: Correlation matrix of the statistical uncertainties, for electron channels at  $\sqrt{s} = 5$  TeV, corresponding to the iteration 4.

1680 for different bins. As for the statistical uncertainties, the correlation between bins  
 1681 (Figure 5.12) decreases with the number of iterations to ensure that the total uncer-  
 1682 tainty is independent of the number of iterations. All the sources of uncertainties  
 1683 are shown as a function of the number of iterations in Ref. [114]. The different  
 sources of uncertainties at the detector level are shown in Appendix B.

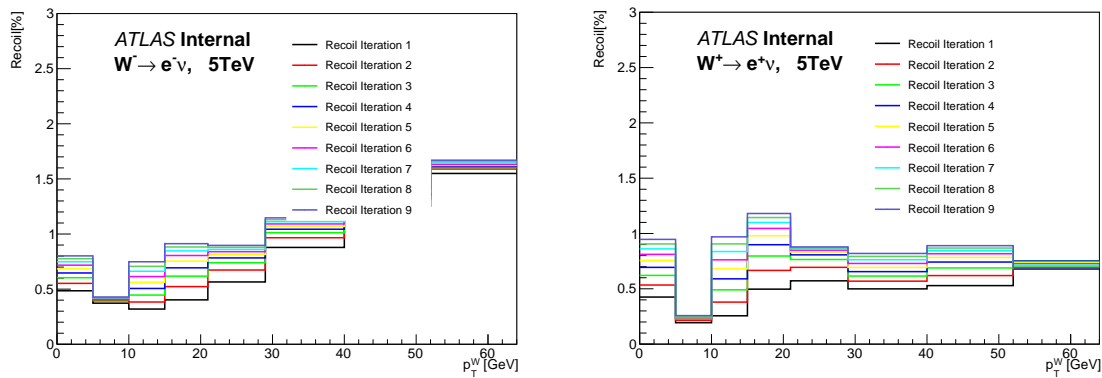


FIGURE 5.11: Example of the recoil systematic uncertainties on the unfolded distribution as a function of the number of iterations, bin-by-bin, for electron channels at  $\sqrt{s} = 5$  TeV.

1684

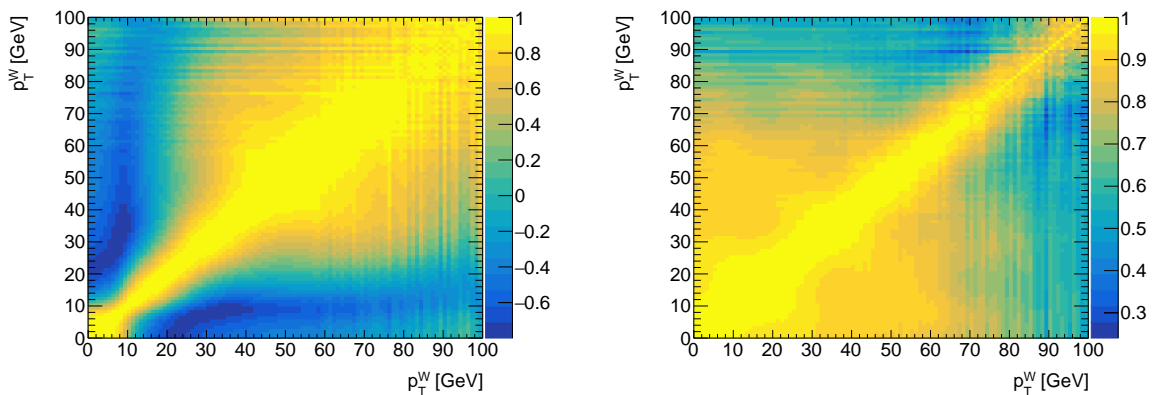


FIGURE 5.12: Correlation matrix for the hadronic recoil calibration uncertainty (left) and lepton calibration uncertainty (right), at 5 TeV, corresponding to iteration 4.

**1685 5.3.5 Comparison of the uncertainties**

1686 The breakdown of the systematic uncertainties is shown in Figure 5.13 at the un-  
1687 folded level. The total experimental measurement uncertainty remains below 1%  
1688 up to  $p_T^W = 25$  GeV at 5 TeV, and below 2% up to 50 GeV at 13 TeV, for each of  
1689 the  $W^+ \rightarrow e^+ \nu_e$  and  $W^- \rightarrow e^- \bar{\nu}_e$  channels. The same results are observed also for  
1690 muon channels [114]. In this range, the statistical uncertainties and recoil calibra-  
1691 tion uncertainties dominate compared to other sources of uncertainty as shown in  
1692 Figure 5.13. At 13 TeV the background uncertainty is more important comparing  
1693 to 5 TeV because of the large contributions of gauge-boson pair production and  
1694 top-quark production [114]. At 100 GeV, the total uncertainties reach 9% and 3%  
1695 for 5 and 13 TeV, respectively. The scale and hierarchy of uncertainties are pre-  
1696 served at the unfolded level. The breakdown of the uncertainties for the electron  
1697 and the muon channels at the detector level are shown in [114]. The uncertain-  
1698 ties are calculated using 3 iterations as a parameter of the Bayesian unfolding. The  
1699 number of iterations is optimised for the measurement of the  $p_T^W$  spectrum in [114].

1700

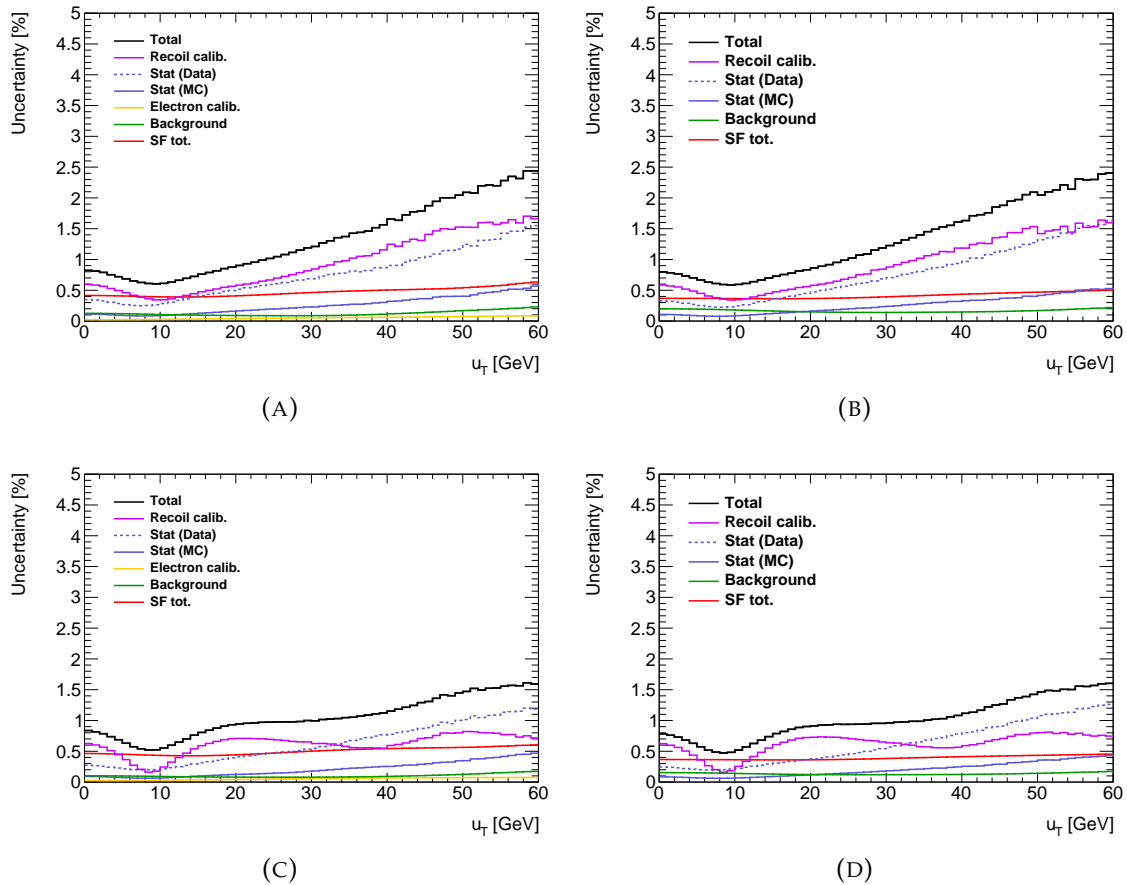


FIGURE 5.13: Different sources of uncertainties on the measurement of  $p_T^W$  distributions at the unfolded level for the  $\sqrt{s} = 5$  TeV data set, for electron channels  $W^-$  (A),  $W^+$  (B) and muon channels  $W^-$  (C), and  $W^+$  (D). The total uncertainty is less than 1% in the low  $p_T^W$  region ( $p_T^W < 30$  GeV) and around 2% in the high  $p_T^W$  region ( $p_T^W \approx 60$  GeV). The total uncertainty is dominated by the hadronic recoil calibration uncertainty and the statistical uncertainty of data.

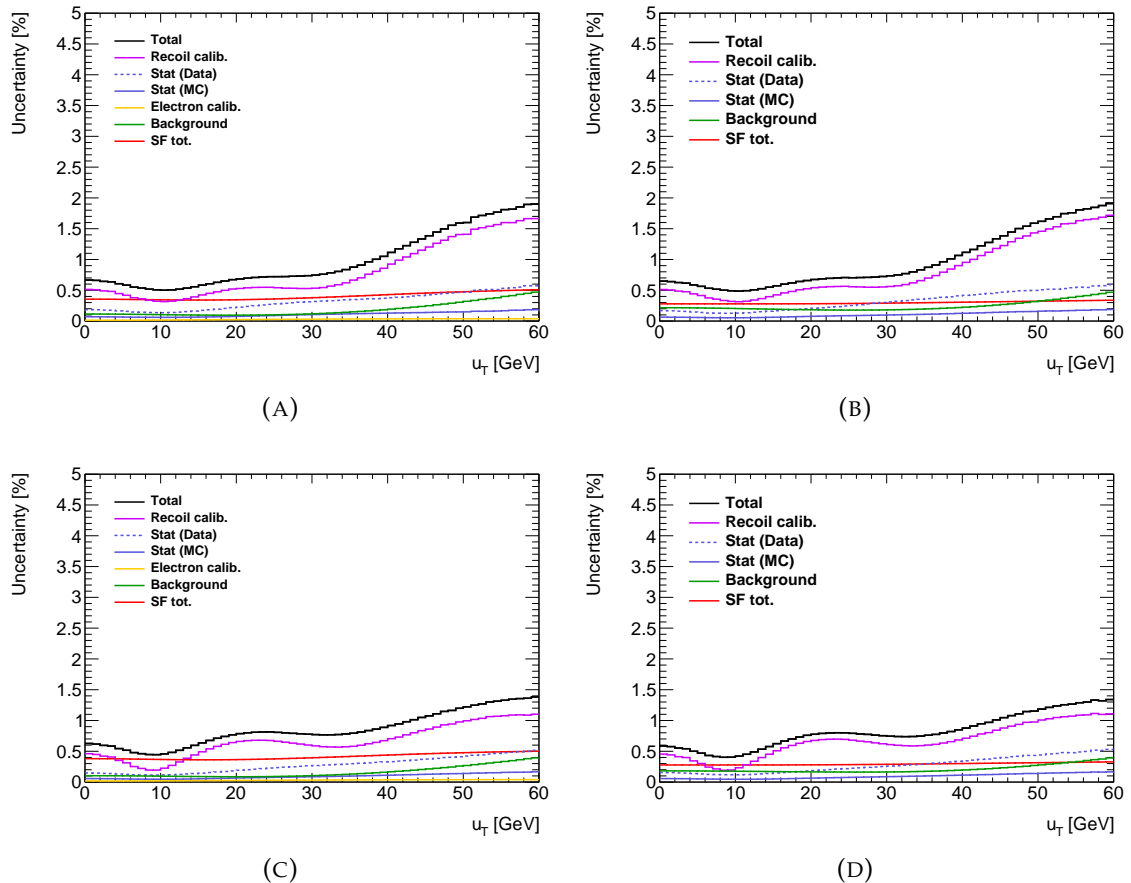


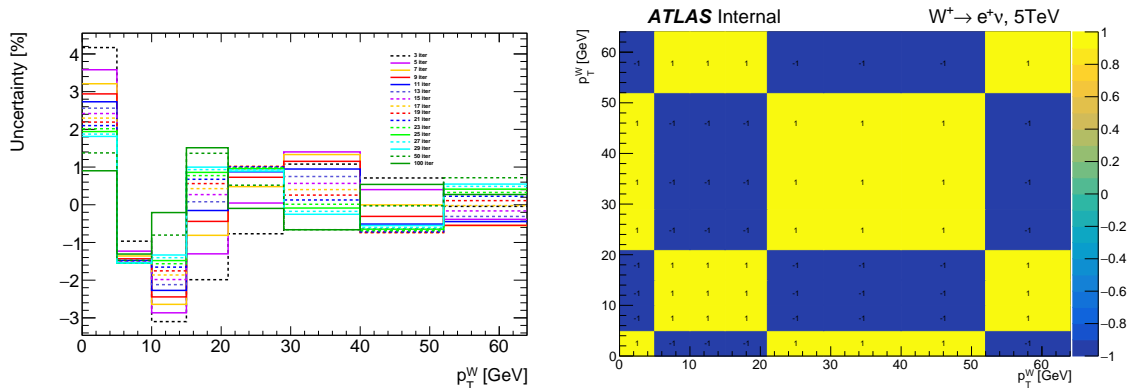
FIGURE 5.14: Different sources of uncertainties on the measurement of  $p_T^W$  distributions at the unfolded level for the  $\sqrt{s} = 13$  TeV data set, for the electron channels  $W^-$  (A),  $W^+$  (B) and the muon channels  $W^-$  (C), and  $W^+$  (D). The total uncertainty is smaller than 1% in the low  $p_T^W$  region ( $p_T^W < 30$  GeV) and around 1.5% for the high  $p_T^W$  region ( $p_T^W \approx 60$  GeV). The total uncertainty is dominated by the hadronic recoil calibration uncertainty and the background uncertainty.

### 5.3.6 Unfolding bias

In the  $p_T^W$  analysis, the unfolding bias estimation is the major concern, because of the large migration between truth and detector levels variables, as shown in Figure 5.5. Contrary to the method used to estimate the bias described in Chapter 4, another more involved approach is used for the  $p_T^W$  analysis. As described in Chapter 4, the unfolding bias can be estimated by:

1. The MC events are reweighted at the truth level to get the best agreement to the data (reconstruction level).
2. The corresponding reconstruction-level distribution is unfolded (as pseudo-data) using the original migration matrix (used for data unfolding).
3. The unfolded result is compared to the reweighted truth distribution, thus providing an estimate of the bias uncertainty.

The new approach is to change the truth level reweighting method. In fact we usually reweight the truth distribution by the data/MC, as discussed in Chapter 4, but for the new approach, we define several reweighting functions at the truth level and we minimise the  $\chi^2$  value in order to get the best agreement at the reconstruction-level with data. Figure 5.15 shows an example of the bias uncertainty for 5 TeV. Contrary to the statistical uncertainty, the bias uncertainty decreases with the number of iterations. The bias is important for the first bins, and starts to decrease after 40 GeV because of the large bins size. The bias uncertainty is considered fully correlated, and the correlation between bins increases in order to ensure that the bias is zero when we add all the bins together, as seen in Figure 5.15.



## 1724 5.4 Results of $p_T^W$ measurement

1725 The results for the unfolded  $p_T^W$  distributions compared to the different predictions  
 1726 are shown in Figures 5.16 and 5.17 for the electron and muon channels, re-  
 1727 spectively. Excluding luminosity, the experimental uncertainties range from less  
 1728 than 1% at low  $p_T^W$  to about 5% (2%) at  $p_T^W=100$  GeV, at 5 TeV (13 TeV). These  
 1729 numbers are smaller than those quoted in Appendix B due to the large size of the  
 1730 binning used. The luminosity uncertainty contributes in addition to 1.6% at 5 TeV,  
 1731 and 1.5% at 13 TeV. The predictions include Powheg AZNLO, Pythia AZ, Sherpa  
 1732 and DYRES. An approximately equal level of agreement with data is visible for  
 1733 Powheg and Pythia. Sherpa predicts a softer spectrum, while DYRES is harder  
 1734 than the data. These features are consistently observed in the electron and muon  
 channels, for both  $W$  boson charges, and at both energies.

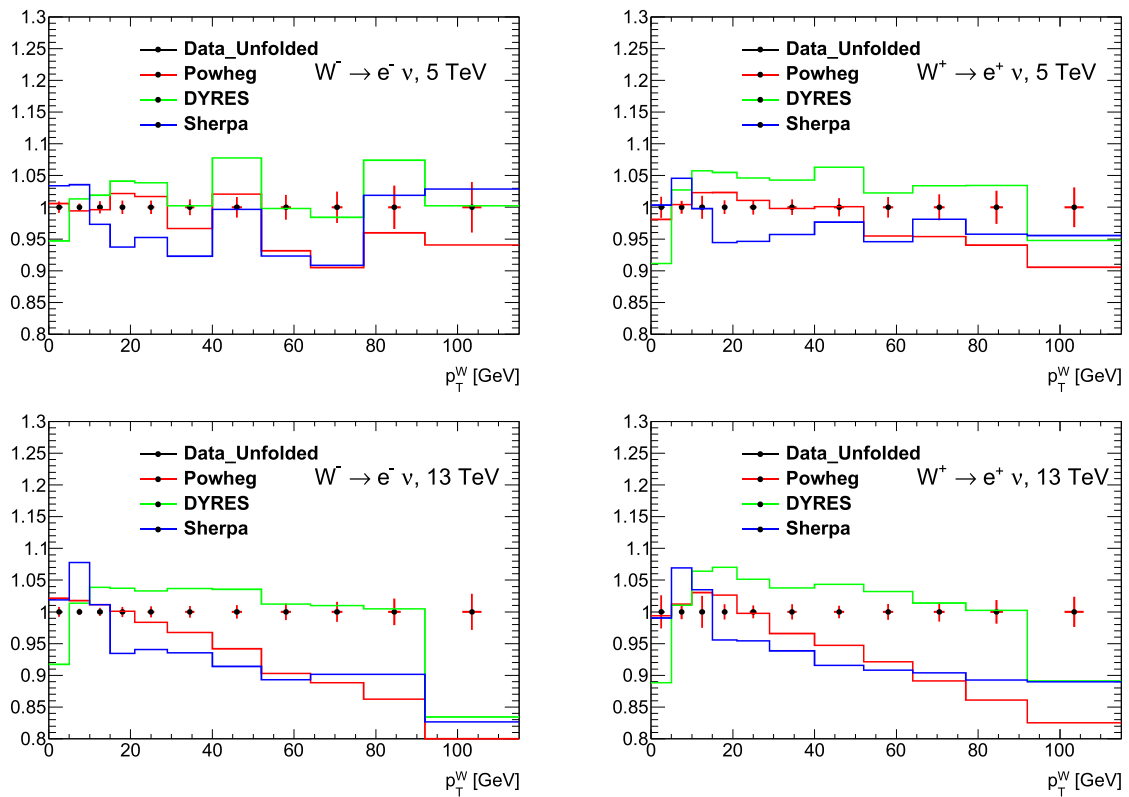


FIGURE 5.16: Unfolded  $P_T^W$  distribution in comparison with various predictions in the  $W^-$  (left) and  $W^+$  (right) electron channels, at 5 TeV (top) and 13 TeV (bottom).

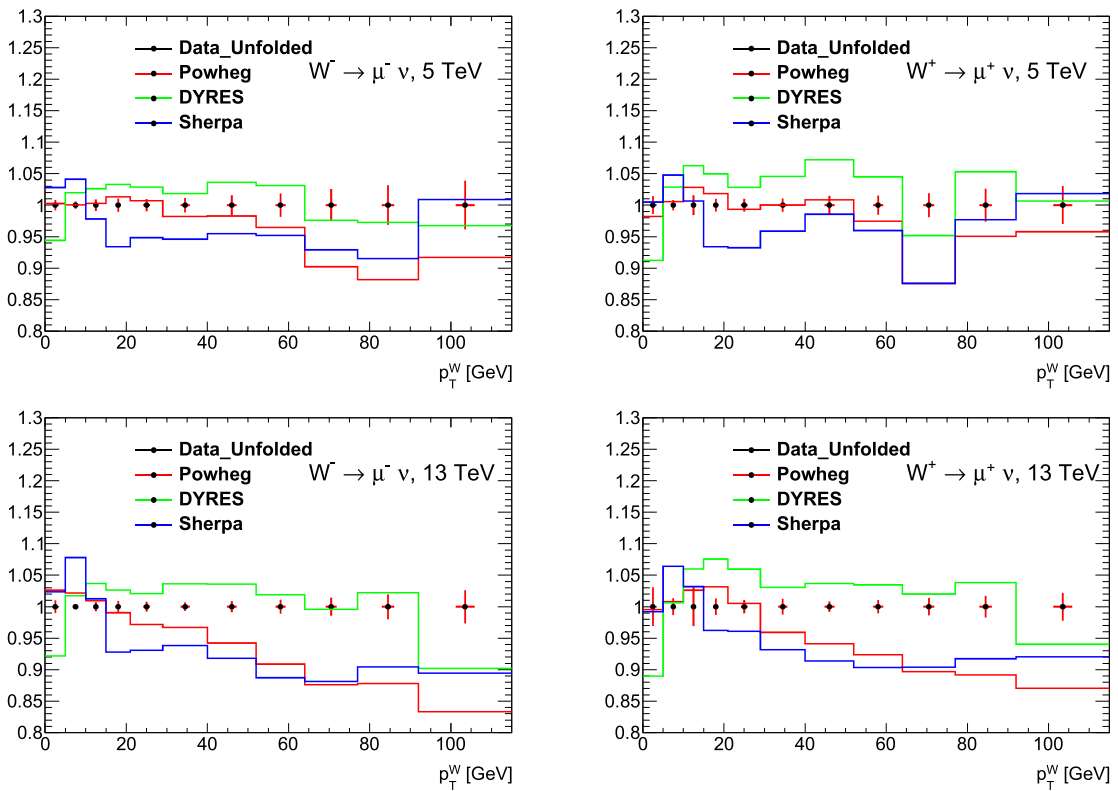


FIGURE 5.17: Unfolded  $P_T^W$  distribution in comparison with various predictions in the  $W^-$  (left) and  $W^+$  (right) muon channels, at 5 TeV (top) and 13 TeV (bottom).



## 1736 Chapter 6

# 1737 $W$ boson production cross sections

### 1738 6.1 Introduction

1739 The  $W$  boson production cross section predictions are available including correc-  
 1740 tions from QCD (at NNLO in the differential case) and EW (at NLO also in the  
 1741 differential case) [12]. Recently an N3LO computation was performed [64], and a  
 1742 mixed QCD-EW differential computation was also done in [34], see also [62] for an  
 1743 almost complete calculation. Therefore, the measurement of  $W$  boson production  
 1744 cross section at the LHC will provide an important test of the SM. Figure 6.1 shows  
 1745 the comparison between the theoretical predictions and measurements from dif-  
 1746 ferent experiments. The production cross sections are based on  $p_T^W$  distributions  
 1747 described in Chapter 5 with the same selections and corrections, and calculated  
 1748 using two methods: using bin-by-bin correction and using the unfolded distribu-  
 1749 tions. This chapter describes the measurement of the inclusive production cross  
 1750 sections of  $W^\pm \rightarrow \ell^\pm \nu$ . The data used correspond to low pile-up runs ( $\mu \approx 2$ )  
 1751 collected during 2017 and 2018 using proton–proton collisions at  $\sqrt{s} = 5$  TeV and  
 1752 13 TeV. The bin-by-bin correction is based on a correction factor  $C$  extracted from  
 1753 simulation by comparing the truth and reconstruction level, whereas the second  
 1754 method consists of using the unfolded distribution already corrected by the un-  
 1755 folding procedure described in Chapter 4.

### 1756 6.2 Fiducial cross-section methodology

1757 The fiducial cross section is calculated using the bin-by-bin correction method and  
 1758 compared to the unfolding method, and a brief comparison of the two approaches  
 1759 is shown below.

#### 1760 6.2.1 The bin-by-bin method

1761 The fiducial cross section is calculated from the observed number of events se-  
 1762 lected in a fiducial phase space after subtracting background contributions and  
 1763 taking into account the detector efficiencies. The resulting fiducial cross section of  
 1764  $W^\pm$  for a given channel ( $W^\pm \rightarrow \ell^\pm \nu$ ) can be expressed with the formula:

$$\sigma_{\text{fid}} = \frac{N^{\text{data}} - N^{\text{bg}}}{\mathcal{L} \cdot C_v} \quad (6.1)$$

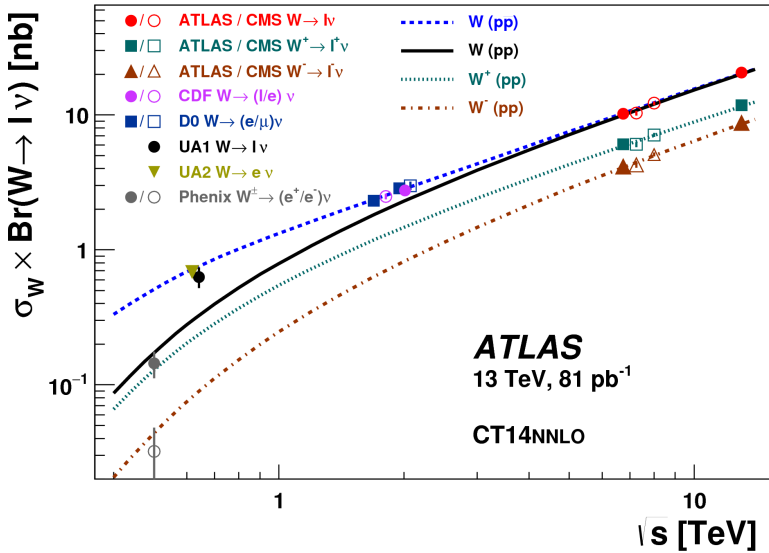


FIGURE 6.1: The measured values of  $\sigma_W \times \text{Br}(W \rightarrow \ell)$  for  $W$  boson compared to the theoretical predictions based on NNLO QCD calculations [117].

1765 where

- 1766 for a given channel,  $N^{\text{data}}$  and  $N^{\text{bg}}$  represent the number of events of data  
1767 in the phase space defined in the section, and the expected number of back-  
1768 ground events.
- 1769  $C_v$  is a correction factor calculated using simulation, corresponding to the  
1770 ratio of the number of selected events at the detector level and the number of  
1771 events at the particle level in the fiducial phase space. This correction factor  
1772 allows to correct the observed difference between data and simulation (due  
1773 to e.g. reconstruction, identification, isolation, and trigger).
- 1774  $\mathcal{L}$  is the integrated luminosity of data.

## 1775 6.2.2 The Bayesian unfolding method

1776 The second option is to use the unfolding method (the Bayesian unfolding  
1777 method) defined in the Chapter 4. In general, the idea behind the unfolding is  
1778 to correct all the detector effects in data distributions, and the total and differential  
1779 cross sections can be calculated using the unfolded distributions.

1780 For the unfolding approach, the cross section is calculated via the formula:

$$\sigma_{\text{fid}} = \frac{N^{\text{Unfolded}}}{\mathcal{L}} \times \frac{N^{\text{truth&reco}}}{N^{\text{truth}}} = \frac{N^{\text{Unfolded}}}{\mathcal{L}} \cdot A_{\text{unf}} \quad (6.2)$$

1781 where

- 1782  $N_{\text{Unfolded}}$  represents the number of events in the unfolded distribution.
- 1783  $A_{\text{unf}}$  is a correction factor related to the unfolding procedure, defined in the  
1784 Chapter 4. This factor represents the fraction of events passing reconstructed

1785 and truth selections to the number of events that meet the selection criteria  
 1786 at truth level.

1787 •  $\mathcal{L}$  is the integrated luminosity of data.

1788 The unfolding method used in this thesis depends on a regularisation parameter  
 1789 related to the number of iterations (Chapter 4). However as the unfolding does  
 1790 not change the normalisation of the input distributions, the fiducial cross section is  
 1791 independent of the number of iterations. For the different sources of uncertainties  
 1792 (statistical and systematic), the uncertainties are independent of the number of  
 1793 iterations when we take the correlation between bins into account. Also, as the  
 1794 unfolding bias (Chapter 4) depends mainly on the shape of a distribution, when  
 1795 we integer aver all the bins we find no bias. Figure 6.2 shows the fiducial cross  
 sections for different iterations.

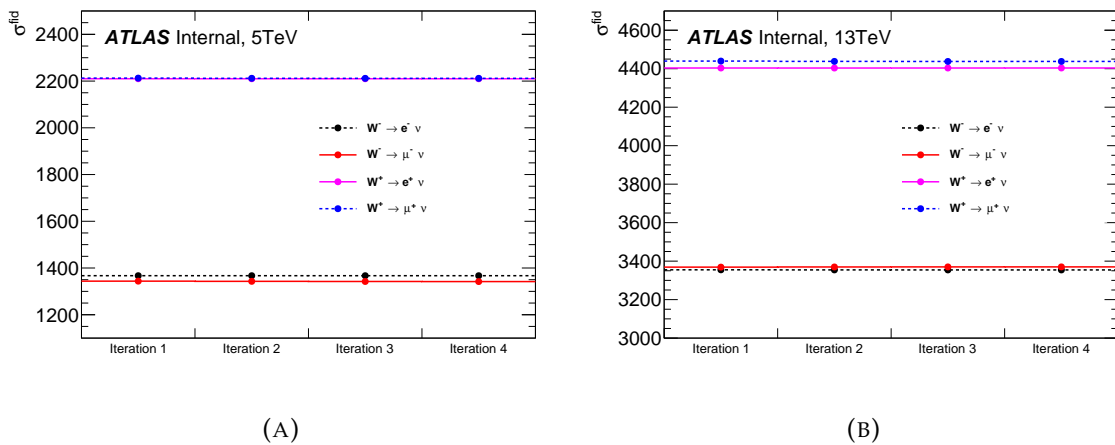


FIGURE 6.2: Fiducial cross section as a function of the number of iterations at 5 TeV (A) and 13 TeV (B).

1796  
 1797 The propagation of systematic uncertainties using bin-by-bin correction is  
 1798 based on the comparison between the fiducial cross section  $\sigma_{\text{fid}}$  and the modified  
 1799 fiducial cross section  $\sigma_{\text{fid}}^{\text{var}}$ , where:

$$\sigma_{\text{fid}} = \frac{N^{\text{data}} - N^{\text{bg}}}{\mathcal{L}} \times \frac{N^{\text{truth}}}{N^{\text{reco}}}, \quad (6.3)$$

$$\sigma_{\text{fid}}^{\text{var}} = \frac{N^{\text{data}} - (N^{\text{bg}} + \text{var})}{\mathcal{L}} \times \frac{N^{\text{truth}}}{N^{\text{reco}} + \text{var}}. \quad (6.4)$$

1800 The systematic uncertainty can be written as:

$$\text{Systematic} = \frac{\sigma_{\text{fid}}^{\text{var}} - \sigma_{\text{fid}}}{\sigma_{\text{fid}}}. \quad (6.5)$$

1801 For the unfolding procedure, the propagation of systematic uncertainty is done as  
 1802 described in Chapter 5, and the total uncertainty is taken as the sum of all the el-  
 1803 ements of the unfolding covariance matrix. Good agreement is observed between  
 1804 the two approaches as shown in table 6.1 as example for the  $W^+ \rightarrow e^+ \nu_e$  at 5 TeV.

TABLE 6.1: An example comparison the  $W^+ \rightarrow e^+ \nu_e$  channel at 5 TeV between systematic uncertainties using bin-by-bin correction and the Bayesian unfolding.

$W^+ \rightarrow e^+ \nu_e$						
Syst. uncer	Reco SF	Id SF	Iso SF	Trigger SF	$e^+$ calib	HR calib
Unfolding	0.30%	0.31%	0.33%	0.23%	0.012%	0.08%
Bin-by-bin	0.30%	0.30%	0.33%	0.22%	0.013%	0.08%

### 1805 6.2.3 Results

1806 The measured fiducial cross sections  $\sigma_{\text{fid}}$  for  $W^\pm \rightarrow \ell^\pm \nu$  are shown in the tables 6.2 and 6.3 with the different sources of uncertainties.

TABLE 6.2: Fiducial cross section with different sources of uncertainties using the bin-by-bin correction and the unfolding approach using 5 TeV samples.

$W^- \rightarrow e^- \bar{\nu}_e, 5 \text{ TeV}, (\text{value} \pm \text{stat} \pm \text{syst} \pm \text{lum}) [\text{pb}]$	
$\sigma_{\text{fid}}$ (Unfolding)	$1379 \pm 2.7 \pm 6.4 \pm 22$
$\sigma_{\text{fid}}$ (Bin-by-bin)	$1380 \pm 2.6 \pm 6.3 \pm 22$
$W^+ \rightarrow e^+ \nu_e, 5 \text{ TeV}, (\text{value} \pm \text{stat} \pm \text{syst} \pm \text{lum}) [\text{pb}]$	
$\sigma_{\text{fid}}$ (Unfolding)	$2227 \pm 3.3 \pm 10 \pm 36$
$\sigma_{\text{fid}}$ (Bin-by-bin)	$2228 \pm 3.4 \pm 10 \pm 36$
$W^- \rightarrow \mu^- \bar{\nu}_\mu, 5 \text{ TeV}, (\text{value} \pm \text{stat} \pm \text{syst} \pm \text{lum}) [\text{pb}]$	
$\sigma_{\text{fid}}$ (Unfolding)	$1377 \pm 2.5 \pm 5.6 \pm 22$
$\sigma_{\text{fid}}$ (Bin-by-bin)	$1376 \pm 2.6 \pm 5.5 \pm 22$
$W^+ \rightarrow \mu^+ \nu_\mu, 5 \text{ TeV}, (\text{value} \pm \text{stat} \pm \text{syst} \pm \text{lum}) [\text{pb}]$	
$\sigma_{\text{fid}}$ (Unfolding)	$2224 \pm 3.3 \pm 8.2 \pm 36$
$\sigma_{\text{fid}}$ (Bin-by-bin)	$2225 \pm 3.3 \pm 8.1 \pm 36$

1807

### 1808 6.2.4 Comparison with theoretical predictions

1809 Theoretical predictions are calculated for the fiducial cross-sections  $\sigma_{\text{fid}}$  using DY-  
 1810 TURBO [45] at NNLO QCD, with different PDF sets: CT18 [93], HERAPDF20 [87],  
 1811 MMHT2014 [91], NNPDF31 [53], ABMP16 [9]. The comparison between measured  
 1812 fiducial cross section and theoretical predictions is shown in Figure 6.3. The un-  
 1813 certainties on the measured  $\sigma_{\text{fid}}$  is dominated by the uncertainty on the luminosity,  
 1814 estimated to 1.6% and 1.5% for 5 TeV and 13 TeV, respectively. The CT18 PDF set  
 1815 describes the data best, while the rest of PDFs shows deviation for at least one data  
 1816 set.

TABLE 6.3: Fiducial cross section with different sources of uncertainties using the bin-by-bin correction and the unfolding approach using 13 TeV samples.

$W^- \rightarrow e^- \bar{\nu}_e, 13 \text{ TeV}, (\text{value} \pm \text{stat} \pm \text{syst} \pm \text{lum}) [\text{pb}]$	
$\sigma_{\text{fid}}$ (Unfolding)	$3445 \pm 3.8 \pm 21 \pm 50$
$\sigma_{\text{fid}}$ (Bin-by-bin)	$3445 \pm 3.8 \pm 20 \pm 50$
$W^+ \rightarrow e^+ \nu_e, 13 \text{ TeV}, (\text{value} \pm \text{stat} \pm \text{syst} \pm \text{lum}) [\text{pb}]$	
$\sigma_{\text{fid}}$ (Unfolding)	$4507 \pm 4.3 \pm 22 \pm 66$
$\sigma_{\text{fid}}$ (Bin-by-bin)	$4505 \pm 4.4 \pm 22 \pm 66$
$W^- \rightarrow \mu^- \bar{\nu}_\mu, 13 \text{ TeV}, (\text{value} \pm \text{stat} \pm \text{syst} \pm \text{lum}) [\text{pb}]$	
$\sigma_{\text{fid}}$ (Unfolding)	$3444 \pm 3.7 \pm 24 \pm 50$
$\sigma_{\text{fid}}$ (Bin-by-bin)	$3445 \pm 3.8 \pm 25 \pm 50$
$W^+ \rightarrow \mu^+ \nu_\mu, 13 \text{ TeV}, (\text{value} \pm \text{stat} \pm \text{syst} \pm \text{lum}) [\text{pb}]$	
$\sigma_{\text{fid}}$ (Unfolding)	$4504 \pm 4.3 \pm 28 \pm 66$
$\sigma_{\text{fid}}$ (Bin-by-bin)	$4505 \pm 4.3 \pm 28 \pm 66$

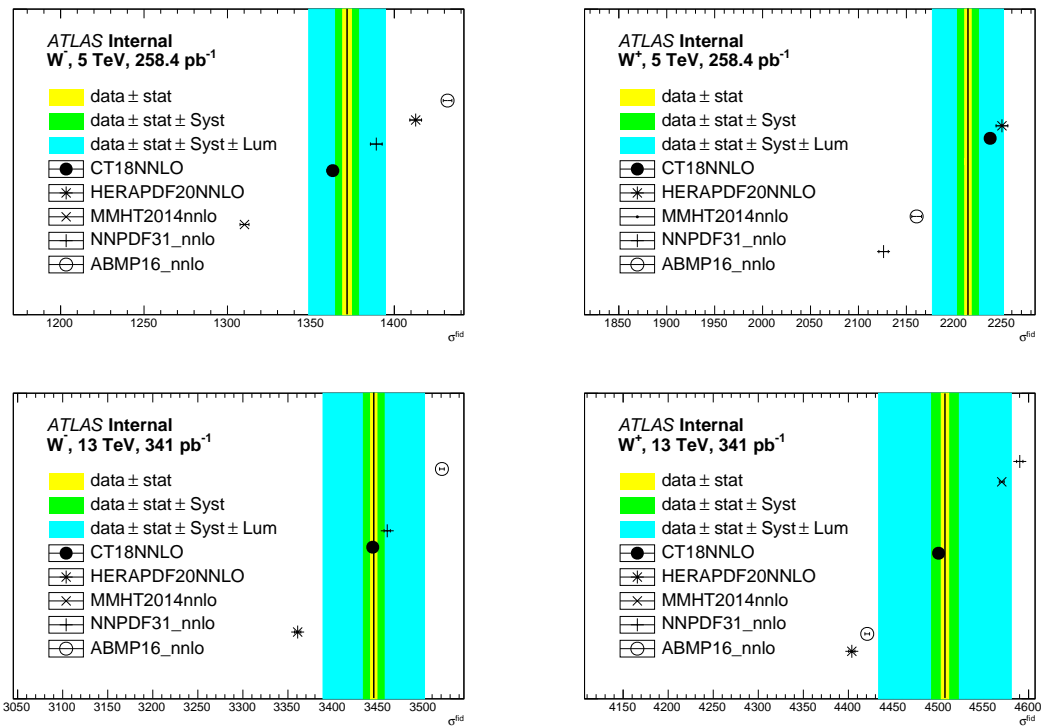


FIGURE 6.3: Measured fiducial cross sections ( $\sigma_{\text{fid}}$ ) compared to different PDFs set using QCD (NNLO) predictions. The yellow band corresponds to the statistical uncertainty, the middle band to the statistical and experimental systematic uncertainties added in quadrature, while the outer band shows the total uncertainty, including the luminosity uncertainty.



1817 **Chapter 7**

1818 **Measurement of single and double  
1819 differential cross sections**

1820 **7.1 Introduction**

1821 In this chapter we present detailed studies of the measurement of the differential  
 1822 cross sections of the  $W^\pm$  boson using the low pile-up runs at  $\sqrt{s} = 5$  and  
 1823 13 TeV, taken in Fall 2017 and July 2018 with the ATLAS detector, corresponding  
 1824 to an integrated luminosity of data of  $258 \text{ pb}^{-1}$  for  $\sqrt{s} = 5 \text{ TeV}$  and  $340 \text{ pb}^{-1}$  for  
 1825  $\sqrt{s} = 13 \text{ TeV}$ . The data, simulation and all the corrections used in this study are de-  
 1826 scribed in Ref. [95]. The differential cross sections are measured in fiducial phase  
 1827 spaces, described in section 4 of Ref. [27], as functions of different variables ( $\eta_\ell, p_T^\ell$ ,  
 1828  $\eta_\ell - p_T^\ell$ ) using the unfolded distributions. Different sources of statistical and sys-  
 1829 tematic uncertainties, described in the section 8 of Ref. [27], are propagated via the  
 1830 unfolding procedure. In addition to these sources of uncertainties, there is a bias  
 1831 related to the unfolding procedure, but as the migrations between bins are low for  
 1832  $\eta_\ell$  and  $p_T^\ell$ , the bias in this case is negligible comparing to other sources of uncertain-  
 1833 ties. The unfolding of data distributions and the propagation of different sources  
 1834 of uncertainties (statistical, systematic and bias) through unfolding, including an  
 1835 optimisation study for the number of iterations needed for the unfolding, are de-  
 1836 scribed in Sec. ???. Section 7.3 shows the results of the differential cross-section  
 1837 measurements and the different sources of uncertainties using the unfolded distri-  
 1838 butions. In Sec. 7.6, a two dimensional unfolding is used to measure the double  
 1839 differential cross sections in bins of  $\eta_\ell$  and  $p_T^\ell$ . A technique is used to transfer the  
 1840 two dimensional unfolding to a one dimensional unfolding as used for differential  
 1841 cross sections of  $\eta_\ell$  and  $p_T^\ell$ , separately. All the sources of uncertainties, discussed  
 1842 in Ref. [27], are propagated through unfolding as described in Sec. ???.

1843 The measurement of differential cross sections in this process provides strin-  
 1844 gent tests of the QCD theory, and is crucial for a deep understanding and mod-  
 1845 elling of QCD interactions. Also, the rapidity dependence of the  $W$  boson pro-  
 1846 duction in the Drell–Yan process provides constraints on the parton distribution  
 1847 functions (PDFs), which are currently the dominant uncertainty source in the  $W$   
 1848 mass measurement (9.2 MeV) [115].

## 1849 7.2 Data and simulation distributions

### 1850 7.2.1 Fiducial phase space

1851 The selection of the  $W$  candidate events follows the  $p_T^W$  measurement described in  
 1852 Chapter 5. The analysis requires lepton candidates satisfying medium identifica-  
 1853 tion criteria based on the EM showers shapes (defined in Ref. [103]). In addition,  
 1854 medium likelihood identification, “ptvarcone20/pT < 0.1” isolation and trigger  
 1855 requirements are applied, trigger requiring the online reconstruction and identi-  
 1856 fication of one lepton passing a  $p_T^\ell$  threshold of 15 GeV, definitions are shown in  
 1857 Ref. [103]. Candidates within the barrel-end-cap crack ( $1.37 < |\eta_\ell| < 1.52$ ) are  
 1858 rejected. Also, the selections:  $E_T^{\text{miss}} > 25$  GeV and  $m_T^W > 50$  GeV are applied in or-  
 1859 der to remove most of the  $Z$ -boson and multi-jet backgrounds in the signal phase  
 1860 space.

### 1861 7.2.2 Experimental systematic uncertainties

1862 In this section, we review the different sources of systematic uncertainty affecting  
 1863 the measurement of the differential cross sections:

1864 **Lepton scale factors:** As described in Chapter 3, two factors (energy scale and res-  
 1865 olution) are applied to data and MC respectively to correct residual differ-  
 1866 ence observed between data and simulation. The energy scale and res-  
 1867 olution factors determined from low pile-up runs are applied. The combined  
 1868 effect of all scale and resolution uncertainties on the distributions of  $\eta_\ell$ ,  $p_T^\ell$   
 1869 are shown in Figure 7.1. The effect on  $p_T^\ell$  is up to 2% for large value of  $p_T^\ell$ , but  
 it’s negligible for  $\eta_\ell$ .

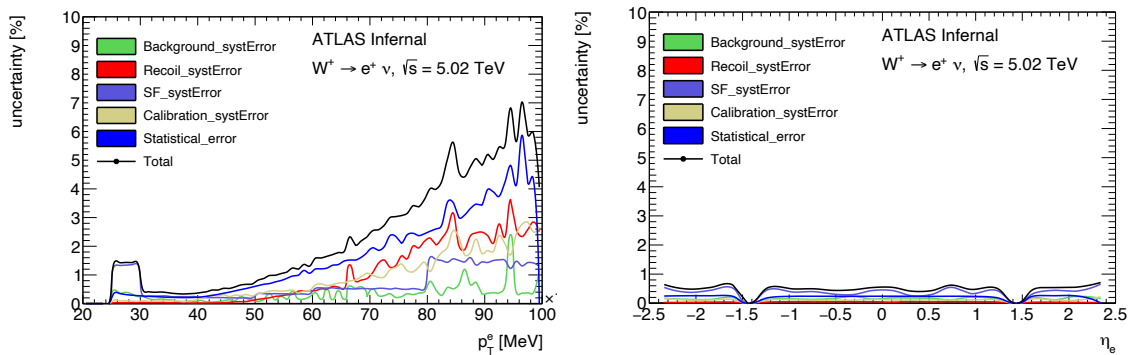


FIGURE 7.1: Uncertainties effect on the distributions of  $\eta_\ell$ ,  $p_T^\ell$  for  $W^+ \rightarrow e^+ \nu_e$  at 5 TeV.  
 Uncertainties for 5 and 13 TeV data sets are described in Appendix B.

1870

1871 **Lepton selection efficiency:** As detailed in Sec. 7.2, selected leptons are required  
 1872 to pass specific criteria. Small differences between data and simulation on  
 1873 the efficiencies of the selections are applied to the simulation as:

$$W_{\text{event}} = \text{SF}_{\text{reco}} \cdot \text{SF}_{\text{ID}} \cdot \text{SF}_{\text{isolation}} \cdot \text{SF}_{\text{trigger}}, \quad (7.1)$$

1874 which correspond to the reconstruction, identification, isolation and trigger  
 1875 scale factors (SFs). The SFs are calculated using “tag-and-probe” method  
 1876 detailed in Ref. [22]. The uncertainty on the selection efficiency is found to  
 1877 be the dominant systematic comparing to other source of uncertainties.

1878 **Hadronic recoil calibration:** Because of the neutrino which can not be measured  
 1879 in the ATLAS detector, the hadronic recoil, defined as the vector sum of all  
 1880 energy deposits excluding energy of lepton, is used in  $W$  boson analysis to  
 1881 determine  $p_T^\nu$ ,  $p_T^W$ , etc. The uncertainty coming from the calibration of the  
 1882 hadronic recoil is related principally to data statistics. This systematic is more  
 1883 important for  $p_T^\ell$  and is of the order of 2% for large value of  $p_T^\ell$ , see Figure 7.1.

1884 **Background uncertainty:** It is related to the background estimation, in particular  
 1885 to the multi-jet contribution [155], and varies between channels and center-  
 1886 of-mass energies. In general, the background uncertainty is below 0.5% for  
 1887 our regions of interest.

1888 **Luminosity:** The luminosity uncertainty for 13 TeV low pile-up runs is 1.5% for  
 1889 the combination of 2017+2018 data (2.1% for 2017, 1.5% for 2018). It is 1.6 %  
 1890 for 5 TeV low pile-up runs.

### 1891 7.2.3 Data and MC comparison

1892 The corrections applied during the unfolding are extracted basically from the mi-  
 1893 gration matrix, determined using MC simulation, which connects the particle and  
 1894 detector levels. The idea is that in order to unfold data distribution, the simulation  
 1895 must describe data perfectly. Otherwise, the unfolded data can not be precisely  
 1896 compared to distributions at truth level. More information about objects defini-  
 1897 tions and all the corrections are described in Section 3 of Ref [27]. Figure 7.2 show  
 1898 the relevant data and MC distributions used for the cross-section measurement.

### 1899 7.2.4 Unfolding of data distributions

1900 The idea of unfolding is to use a migration matrix built from MC which contains  
 1901 all detector effects and allows us to pass from reconstruction to truth level. As  
 1902 detailed in Section 4, the unfolding is done to correct all detector effects. Contrary  
 1903 to the  $p_T^W$  unfolding described in Ref [27], the  $\eta_\ell$  or  $p_T^\ell$  unfolding is easier because of  
 1904 the small migration between bins, due to a negligible difference between truth and  
 1905 reconstructed levels (less detector effects), which means that the migration matrix  
 1906 is more diagonal, see Figure 7.3.

1907 The same unfolding method used for  $p_T^W$  is used also for  $\eta_\ell$ ,  $p_T^\ell$  unfolding, the itera-  
 1908 tive Bayesian unfolding method [55]. Figure 7.4 shows an example of distributions  
 1909 at the unfolding and reconstructed level using 3 iterations. Because of the small  
 1910 migration between bins, the unfolded level distribution is identical to the truth  
 1911 level distribution.

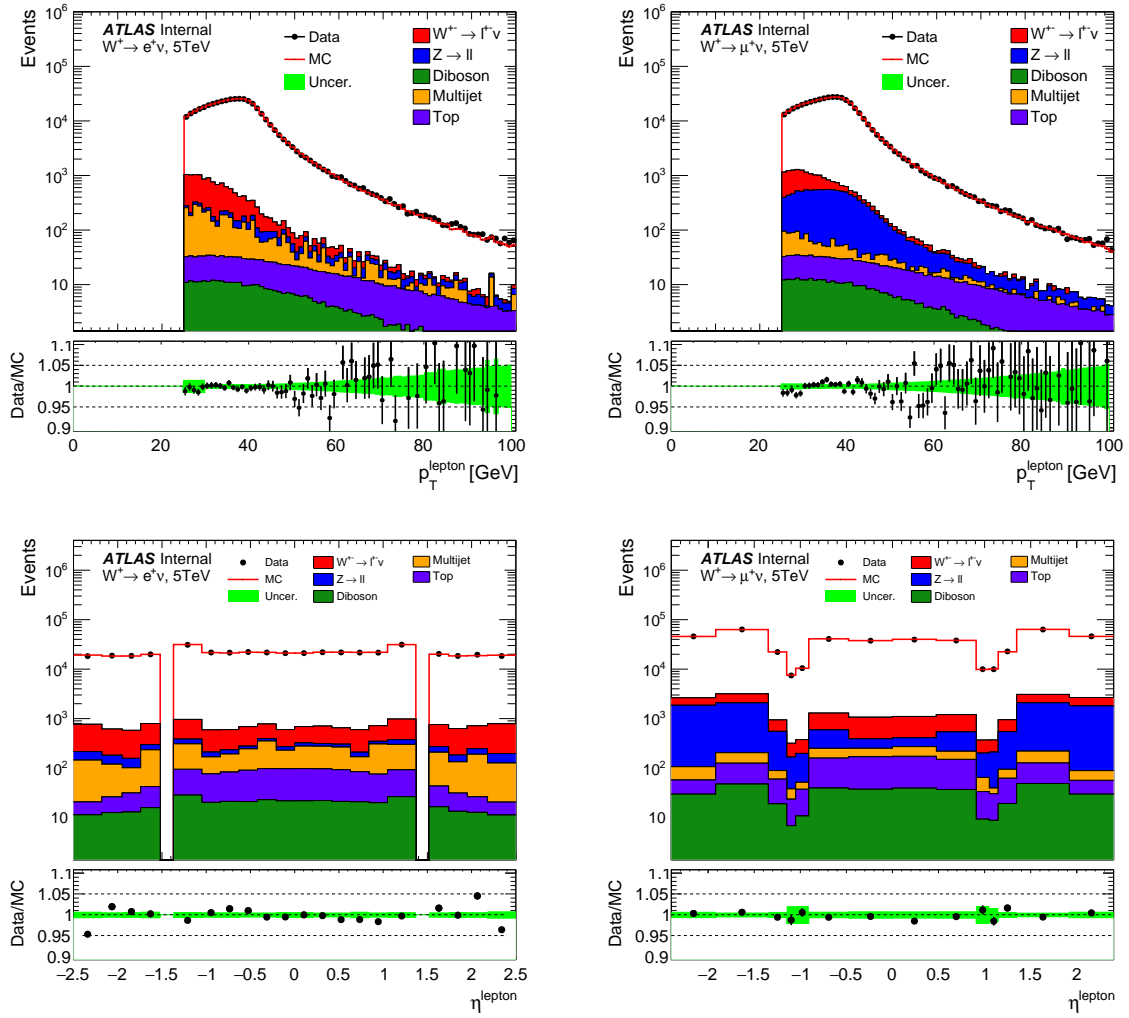


FIGURE 7.2: Example distributions of the observables  $p_T^\ell$  (top) and  $\eta_\ell$  (bottom) chosen to be unfolded for  $W^+$  in the electron (left) and muon (right) channels at 5 TeV in the fiducial phase space. The signal and background are normalised to data. The low panel gives the ratio Data/MC in each bin. The green band shows the statistical and systematic uncertainties. Control plots for other channels are shown in Appendix A.

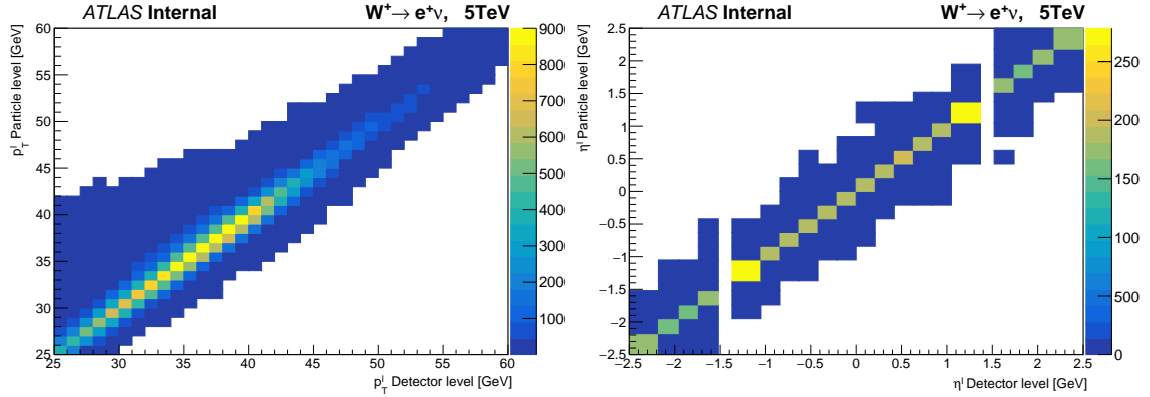


FIGURE 7.3: Example of the migration matrix used in the unfolding of  $p_T^\ell$  (left) and  $\eta_\ell$  (right) for  $W^+ \rightarrow e^+ \nu_e$  at 5 TeV, the migration matrix is quasi diagonal because of the small difference between particle and detector levels.

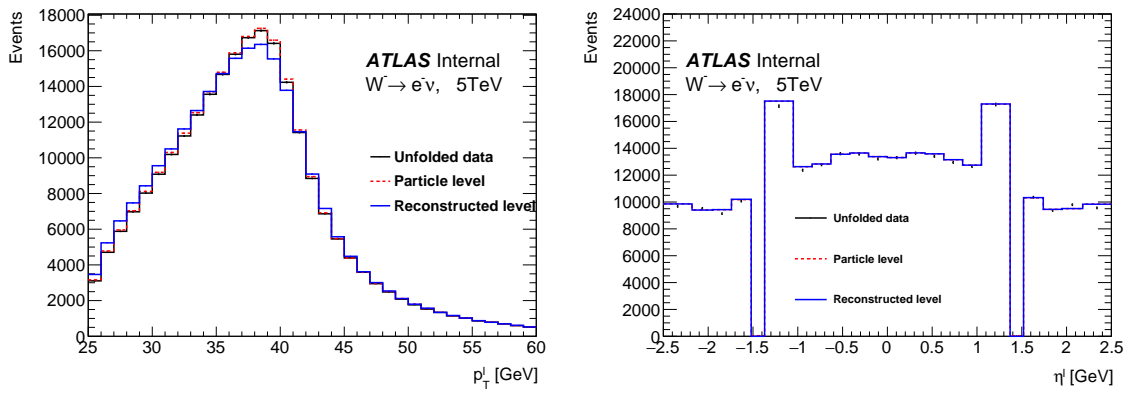


FIGURE 7.4: Example of the unfolded distributions for  $p_T^\ell$  (left) and  $\eta_\ell$  (right) for  $W^- \rightarrow e^- \bar{\nu}_e$  at 5 TeV at detector level, particle level and unfolded level.

### 7.2.5 Propagation of the statistical and systematic uncertainties

The propagation of uncertainties through the unfolding is done in the same way as for  $p_T^W$ , as detailed in Chapter 4. The main difference comes from the degree of migration between bins. Figure 7.5 shows an example of statistical uncertainty at the unfolding level, comparing to  $\eta_e$ ,  $p_T^\ell$  is characterised with slightly larger migration between bins which explains the increase in the statistical error with the number of iterations.

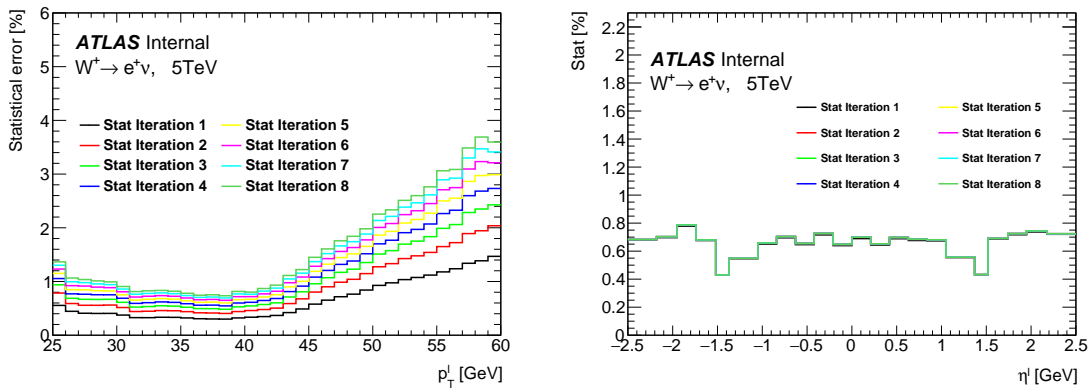


FIGURE 7.5: Example of the statistical uncertainties for  $p_T^\ell$  (left) and  $\eta_e$  (right), for  $W^+ \rightarrow e^+ \nu_e$  at 5 TeV. Statistical error increases with the number of iterations because of the migration between bins. Statistical uncertainties with their correlation matrices are described in Appendix B.

Contrary to the statistical uncertainty, the systematic uncertainties are more stable with the number of iterations, Figure 7.6 shows an example of the dominant systematic uncertainty at the unfolded level as a function of the number of iterations. For  $\eta_e$  and  $p_T^\ell$ , the total uncertainty is dominated by the uncertainty from the efficiency scale factors.

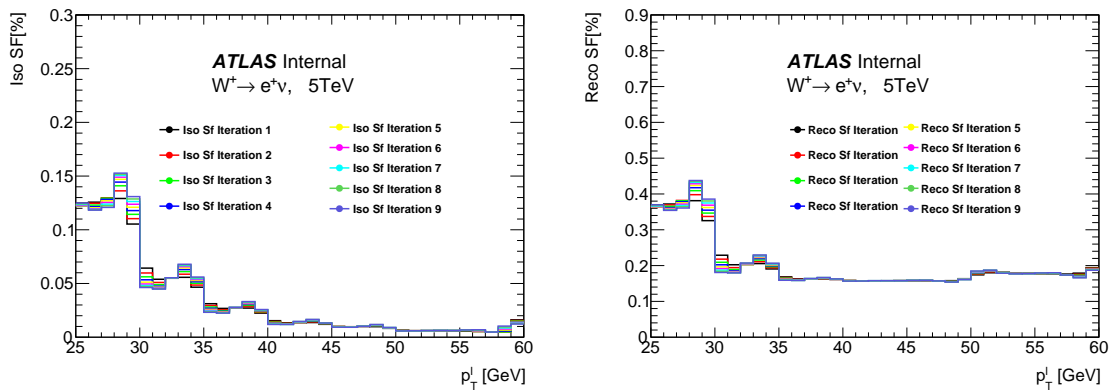


FIGURE 7.6: Example of the systematic uncertainties (isolation (left) and reconstruction (right) SFs) for  $p_T^\ell$  for  $W^+ \rightarrow e^+ \nu_e$  at 5 TeV.

### 7.2.6 Unfolding bias

As detailed in Chapter 4, the unfolding method used in this thesis introduces a bias that should not be dominant. The bias is calculated as explained in Chapter 4. The procedure to estimate the bias can be summarised in two steps (Ref [111]):

- Reweight the MC distribution at truth level with the fitted ratio data/MC, in such a way that the corresponding reconstructed distribution, obtained by the truth level reweighted distribution, matches better the data distribution after the background subtraction.
- The bias is estimated as the difference between the unfolded distribution of the reconstruction-weighted distribution and the truth-weighted distribution.

The procedure used to calculate the bias of unfolding is illustrated in Fig. ???. The reconstruction-weighted distribution must be closer to data compared to the original reconstructed distribution (Fig. 7.7).

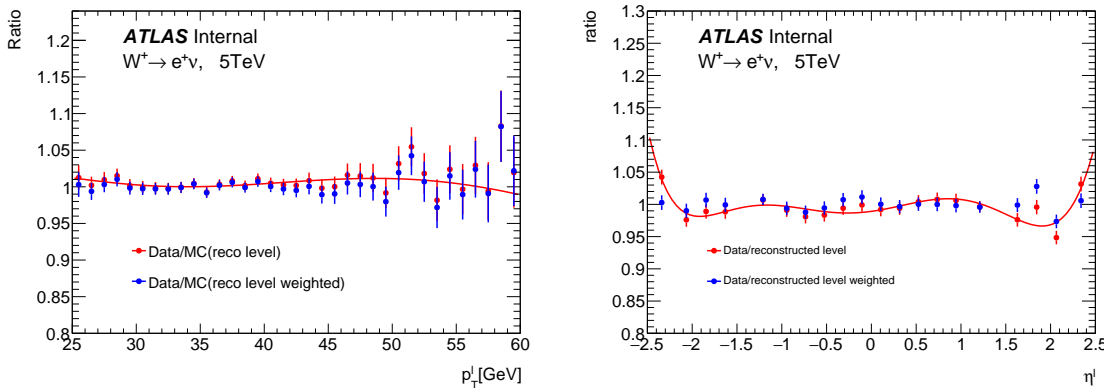


FIGURE 7.7: The ratio of data over the original reconstructed MC distributions for  $p_T^\ell$  (left) and  $\eta_\ell$  (right) compared to the ratio of data over the weighted one. The latter is in better agreement with data (background subtracted).

As the unfolding does not change the normalisation of input distributions, the total unfolding bias when we take the correlation (anti-correlation) between bins into account must be equal to 0. Contrary to other sources of uncertainties, the bias decreases with the number of iterations and the anti-correlation between bins increases with the number of iterations to ensure that the bias integrated in all bins is zero (Fig. 7.8).

### 7.2.7 Optimisation of the number of iterations in iterative Bayesian unfolding

As discussed above, the statistical uncertainty increases with the number of iterations, while the unfolding bias decreases with them. Therefore it is possible to minimise the total uncertainty by optimising the number of iterations. As the bias

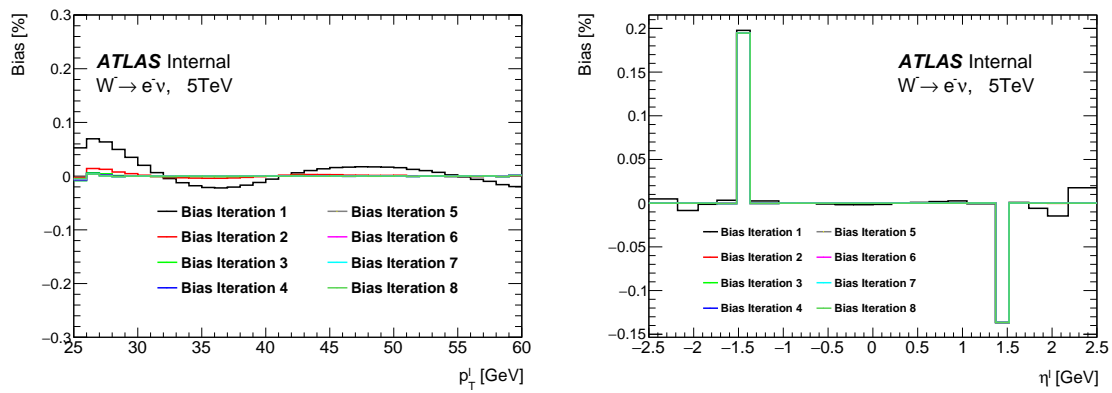


FIGURE 7.8: Example of the unfolding bias of  $p_T^\ell$  (left) and  $\eta_\ell$  (right) as a function of the number of iterations used in the unfolding for  $W^-$  at 5 TeV. After the second iteration, the bias is negligible compared to other sources of uncertainty. The unfolding bias for other channels is shown in Appendix B.

1949 is very small comparing to other sources of uncertainties, the best choice is to use  
 1950 the first iteration. However to avoid the fluctuations in the bias as shown in Figure 7.9, the second iteration is used. As we are interested in the differential cross  
 1951 sections, the optimisation study is done for each bin separately around the peak  
 1952 region.  
 1953

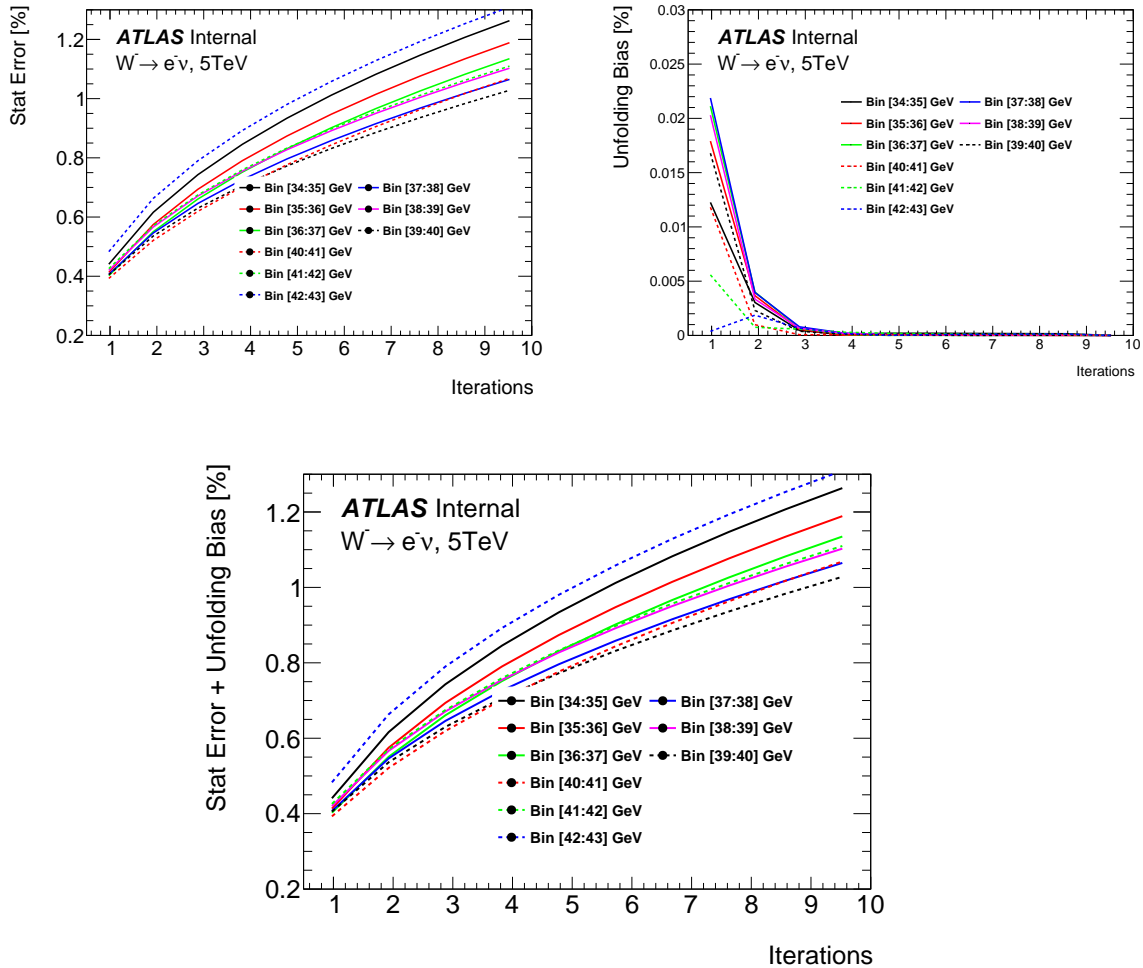


FIGURE 7.9: Example of the statistical uncertainty (top left) and the unfolding bias uncertainty (top right) and their combined uncertainty (bottom) for a few selected bins in  $p_T^\ell$  as a function of the number of iterations used in the unfolding.

### 1954 7.3 Differential cross sections

1955 The differential cross sections can be estimated using a correction factor calculated  
 1956 from simulation, the bin-by-bin unfolding, where the differential cross-section for-  
 1957 mula can be expressed as:

$$\frac{d\sigma_i}{dx^i} = \frac{N_{\text{data}}^i}{\Delta x^i \mathcal{L}} \cdot C_i = \frac{N_{\text{data}}^i}{\Delta x^i \mathcal{L}} \cdot \frac{N_{\text{truth}}^i}{N_{\text{reco}}^i}, \quad (7.2)$$

1958 where  $\Delta x^i$  is the bin width, and  $N^i$  is the number of events in bin  $i$ . On the other  
 1959 hand, there is another option to calculate the differential cross section, replacing  
 1960 the correction bin-by-bin factor  $C_i$ , by the unfolding of the data distribution using  
 1961 the inverse of the migration matrix  $M_{ij}$ . The new formula using the unfolded  
 1962 distribution of data is expressed as:

$$\frac{d\sigma_i}{dx^i} = \frac{N_{\text{Unf}}^i}{\Delta x^i \mathcal{L}} \cdot \frac{1}{A_c} = \frac{1}{\Delta x^i \mathcal{L}} \cdot \sum_j M_{ij}^{-1} (N_{\text{reco}}^j - N_{\text{reco,bkg}}^j) \cdot \frac{1}{A_c}, \quad (7.3)$$

1963 where  $\Delta x^i$  is the bin width,  $N_{\text{Unf}}^i$  is the number of events in the unfolded distri-  
 1964 bution,  $A_c$  is the acceptance correction, used to correct the unfolded distribution  
 1965 and take into account the events that pass the detector-level selection but fail the  
 1966 particle-level selection. Figure 7.10 shows an example of the acceptance correction  
 for  $p_T^\ell$  and  $\eta_\ell$  at 5 TeV.

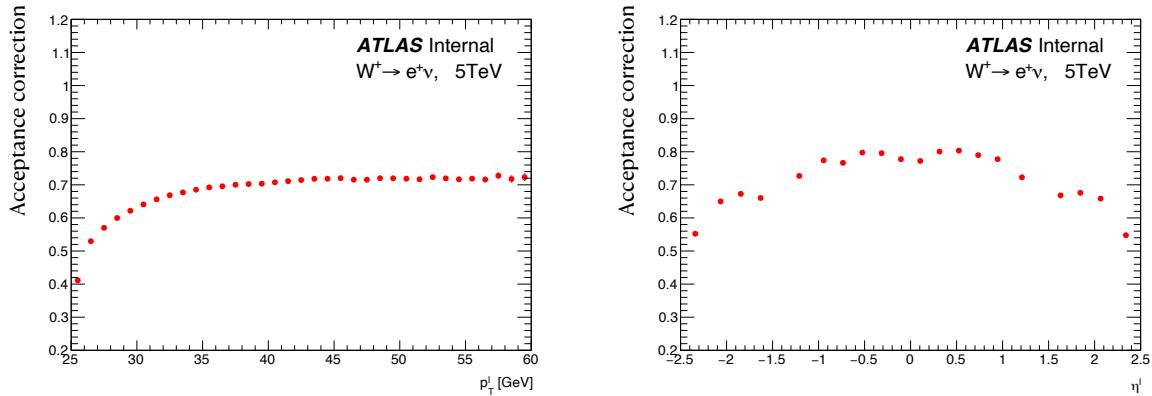


FIGURE 7.10: Fraction of events that pass the detector-level selection but fail the particle-  
 level selection bin-by-bin for  $p_T^\ell$  (left) and  $\eta_\ell$  (right).

1968 **Differential cross sections in the  $e$  channel versus  $p_T^e$  at 5 TeV**

TABLE 7.1: Differential cross sections versus  $p_T^e$  for 5 TeV ( $W^-, e^-$ ). The columns show the bin range, the measured cross section and the corresponding relative uncertainties.

W <sup>-</sup> → e <sup>-</sup> $\bar{\nu}_e$ , 5 TeV, uncertainties in (%)				
Range	$d\sigma/dp_T^e$ [pb/GeV]	Stat uncertainty	Unfolding bias	Syst uncertainty
[26, 27]	18.300	0.895	0.014	1.583
[27, 28]	22.885	0.802	0.013	1.674
[28, 29]	27.240	0.786	0.008	1.783
[29, 30]	31.219	0.747	0.005	1.344
[30, 31]	35.345	0.706	0.002	0.425
[31, 32]	39.692	0.663	0.001	0.310
[32, 33]	43.592	0.653	0.003	0.315
[33, 34]	48.299	0.616	0.003	0.323
[34, 35]	52.746	0.575	0.004	0.313
[35, 36]	57.124	0.551	0.004	0.286
[36, 37]	61.673	0.546	0.004	0.276
[37, 38]	65.344	0.567	0.003	0.280
[38, 39]	66.728	0.536	0.002	0.275
[39, 40]	63.810	0.521	0.001	0.276
[40, 41]	55.319	0.571	0.001	0.292
[41, 42]	44.373	0.663	0.002	0.344
[42, 43]	34.381	0.705	0.003	0.379
[43, 44]	26.705	0.759	0.003	0.408
[44, 45]	21.292	0.828	0.003	0.385

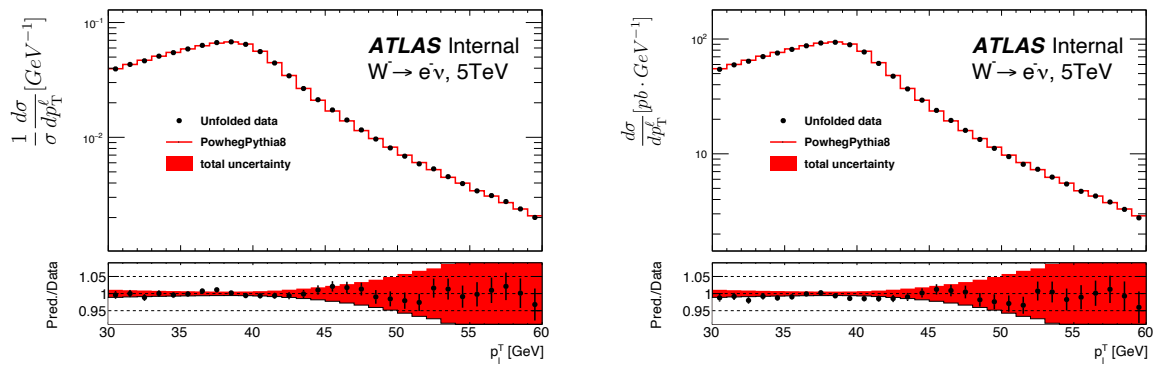


FIGURE 7.11: Differential cross sections (left) and normalised differential cross sections (right) as a function of  $p_T^e$  for 5 TeV ( $W^-, e^-$ ). The bottom panel shows the ratio data to MC (Powheg+Pethia8) together with the red band showing the total uncertainty.

TABLE 7.2: Differential cross sections versus  $p_T^e$  for 5 TeV ( $W^+, e^+$ ). The columns show the bin range, the measured cross section and the corresponding relative uncertainties.

W <sup>+</sup> → e <sup>+</sup> ν <sub>e</sub> , 5 TeV, uncertainties in (%)				
Range	$d\sigma/dp_T^e$ [pb/GeV]	Stat uncertainty	Unfolding bias	Syst uncertainty
[26, 27]	36.907	0.590	0.019	1.536
[27, 28]	44.556	0.557	0.008	1.644
[28, 29]	51.628	0.557	0.010	1.768
[29, 30]	58.724	0.561	0.009	1.308
[30, 31]	65.036	0.515	0.008	0.389
[31, 32]	71.340	0.441	0.007	0.275
[32, 33]	76.950	0.446	0.008	0.281
[33, 34]	81.804	0.459	0.007	0.297
[34, 35]	87.183	0.455	0.007	0.284
[35, 36]	92.366	0.439	0.007	0.261
[36, 37]	95.698	0.417	0.006	0.258
[37, 38]	98.590	0.413	0.005	0.261
[38, 39]	98.572	0.405	0.001	0.260
[39, 40]	92.989	0.440	0.002	0.253
[40, 41]	79.972	0.459	0.006	0.249
[41, 42]	63.485	0.478	0.008	0.275
[42, 43]	48.760	0.504	0.008	0.294
[43, 44]	37.878	0.589	0.009	0.309
[44, 45]	29.757	0.677	0.006	0.287

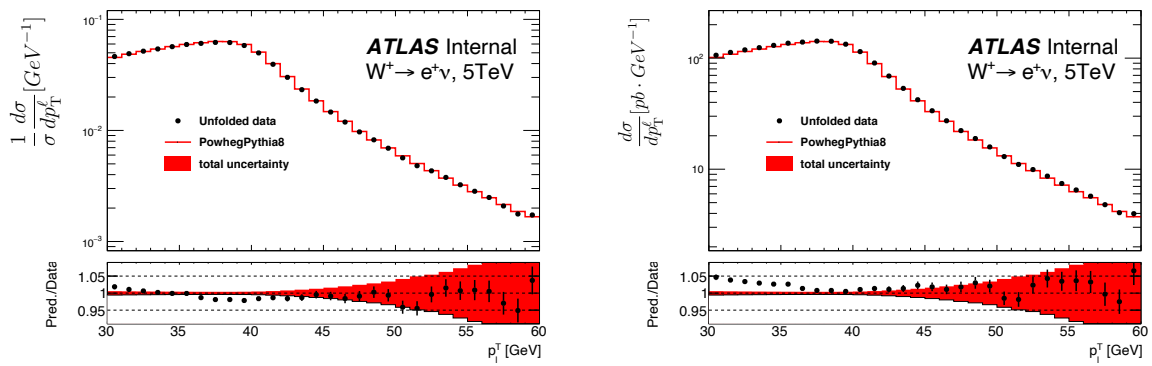


FIGURE 7.12: Differential cross sections (right) and normalised differential cross sections (left) as a function of  $p_T^e$  for 5 TeV ( $W^+, e^+$ ). The bottom panel shows the ratio data to MC (Powheg+Pethia8) together with the red band showing the total uncertainty.

### 1969 Differential cross sections of the $\mu$ channel versus $p_T^\mu$ at 5 TeV

TABLE 7.3: Differential cross sections versus  $p_T^\mu$  for 5 TeV ( $W^-$ ,  $\mu^-$ ). The columns show the bin range, the measured cross section and the corresponding relative uncertainties.

$W^- \rightarrow \mu^- \bar{\nu}_\mu$ , 5 TeV, uncertainties in (%)				
Range	$d\sigma/dp_T^\mu$ [pb/GeV]	Stat uncertainty	Unfolding bias	Syst uncertainty
[26, 27]	20.256	0.928	0.010	0.732
[27, 28]	24.586	0.850	0.023	0.764
[28, 29]	28.525	0.770	0.015	0.846
[29, 30]	32.915	0.782	0.011	0.752
[30, 31]	36.989	0.696	0.007	0.542
[31, 32]	41.858	0.638	0.006	0.650
[32, 33]	46.520	0.645	0.004	0.644
[33, 34]	50.704	0.592	0.002	0.676
[34, 35]	55.074	0.557	0.000	0.586
[35, 36]	59.439	0.559	0.001	0.469
[36, 37]	63.851	0.503	0.001	0.564
[37, 38]	67.492	0.499	0.002	0.580
[38, 39]	69.177	0.508	0.002	0.579
[39, 40]	66.828	0.510	0.000	0.498
[40, 41]	58.303	0.531	0.002	0.467
[41, 42]	46.584	0.562	0.005	0.550
[42, 43]	35.949	0.629	0.005	0.563
[43, 44]	27.695	0.736	0.004	0.548
[44, 45]	22.101	0.809	0.004	0.494

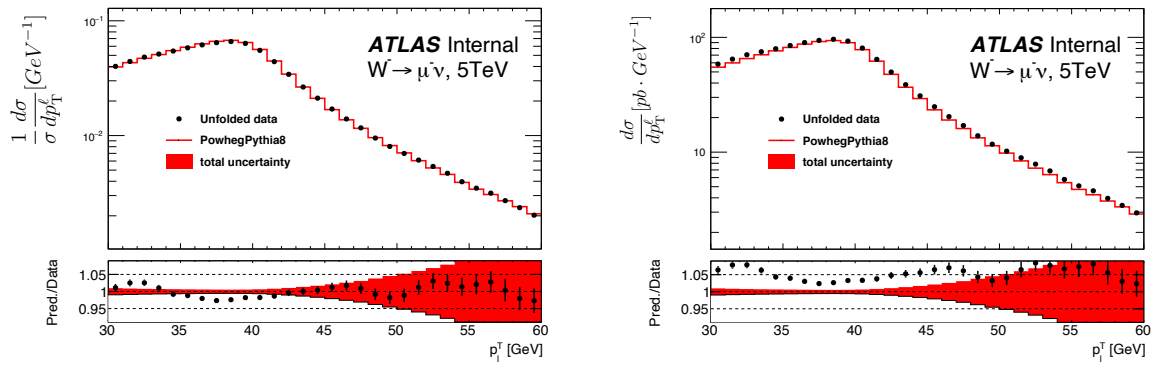


FIGURE 7.13: Differential cross sections (right) and normalised differential cross sections (left) as a function of  $p_T^\mu$  for 5 TeV ( $W^-$ ,  $\mu^-$ ). The bottom panel shows the ratio data to MC (Powheg+Pythia8) together with the red band showing the total uncertainty.

TABLE 7.4: Differential cross sections versus  $p_T^\mu$  for 5 TeV ( $W^+, \mu^+$ ). The columns show the bin range, the measured cross section and the corresponding relative uncertainties.

W <sup>+</sup> → $\mu^+ \nu_\mu$ , 5 TeV, uncertainties in (%)				
Range	$d\sigma/dp_T^\mu$ [pb/GeV]	Stat uncertainty	Unfolding bias	Syst uncertainty
[26, 27]	40.943	0.613	0.025	0.707
[27, 28]	49.223	0.592	0.014	0.734
[28, 29]	56.081	0.572	0.013	0.814
[29, 30]	62.909	0.555	0.006	0.713
[30, 31]	69.407	0.518	0.001	0.521
[31, 32]	75.895	0.483	0.001	0.632
[32, 33]	81.579	0.458	0.006	0.634
[33, 34]	87.212	0.439	0.009	0.660
[34, 35]	92.731	0.435	0.013	0.562
[35, 36]	98.205	0.420	0.014	0.457
[36, 37]	102.257	0.414	0.017	0.547
[37, 38]	104.721	0.411	0.017	0.565
[38, 39]	104.533	0.405	0.014	0.567
[39, 40]	97.729	0.432	0.008	0.493
[40, 41]	83.991	0.457	0.002	0.464
[41, 42]	66.658	0.479	0.012	0.539
[42, 43]	51.638	0.534	0.018	0.546
[43, 44]	39.754	0.619	0.020	0.526
[44, 45]	30.943	0.718	0.017	0.476

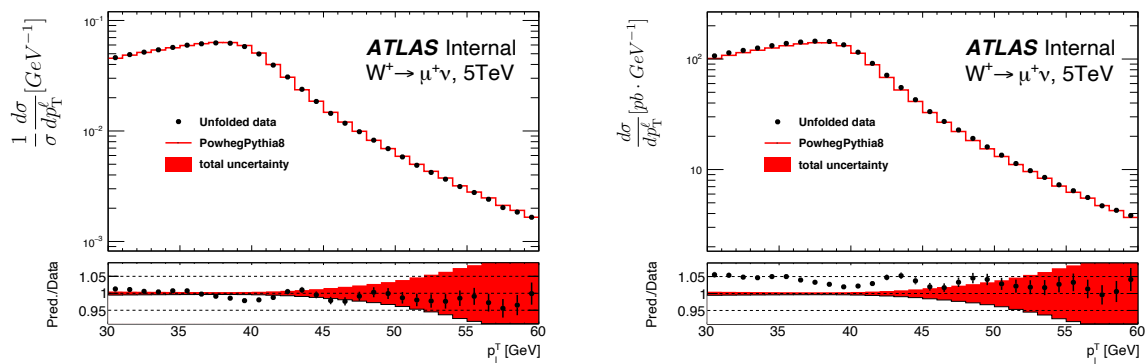


FIGURE 7.14: Differential cross sections (right) and normalised differential cross sections (left) as a function of  $p_T^\mu$  for 5 TeV ( $W^+, \mu^+$ ). The bottom panel shows the ratio data to MC (Powheg+Pythia8) together with the red band showing the total uncertainty.

1970 **Differential cross sections of the  $e$  channel versus  $p_T^e$  at 13 TeV**

TABLE 7.5: Differential cross sections versus  $p_T^e$  for 13 TeV ( $W^-, e^-$ ). The columns show the bin range, the measured cross section and the corresponding relative uncertainties.

$W^- \rightarrow e^- \bar{\nu}_e$ , 13 TeV, uncertainties in (%)				
Range	$d\sigma/dp_T^e$ [pb/GeV]	Stat uncertainty	Unfolding bias	Syst uncertainty
[26, 27]	48.398	0.448	0.058	0.888
[27, 28]	59.710	0.442	0.026	0.942
[28, 29]	69.166	0.406	0.012	0.997
[29, 30]	78.766	0.376	0.034	0.758
[30, 31]	88.430	0.371	0.041	0.468
[31, 32]	97.272	0.370	0.039	0.501
[32, 33]	106.339	0.360	0.031	0.523
[33, 34]	115.313	0.331	0.019	0.538
[34, 35]	124.252	0.317	0.006	0.418
[35, 36]	133.374	0.312	0.007	0.258
[36, 37]	141.726	0.294	0.020	0.251
[37, 38]	146.909	0.280	0.029	0.256
[38, 39]	148.526	0.273	0.033	0.259
[39, 40]	141.766	0.283	0.030	0.246
[40, 41]	125.030	0.305	0.021	0.230
[41, 42]	104.001	0.351	0.007	0.237
[42, 43]	83.848	0.375	0.006	0.252
[43, 44]	67.814	0.394	0.015	0.263
[44, 45]	55.272	0.458	0.023	0.273

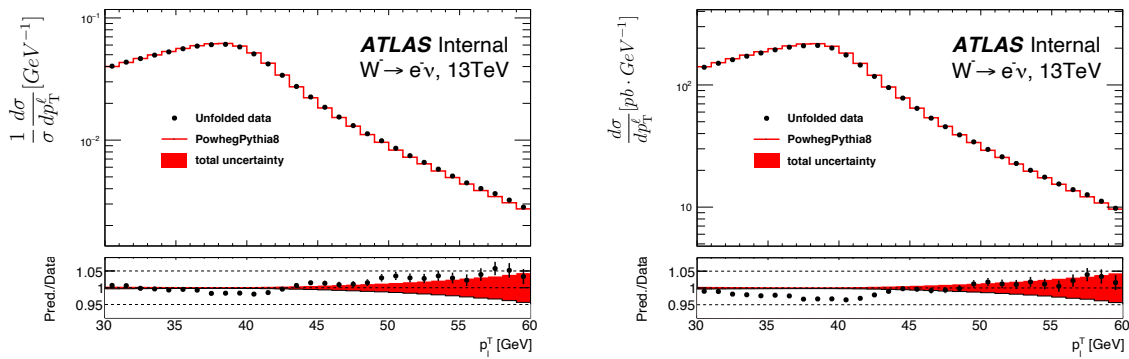


FIGURE 7.15: Differential cross sections (right) and normalised differential cross sections (left) as a function of  $p_T^e$  for 13 TeV ( $W^-, e^-$ ). The bottom panel shows the ratio data to MC (Powheg+Pethia8) together with the red band showing the total uncertainty.

TABLE 7.6: Differential cross sections versus  $p_T^e$  for 13 TeV ( $W^+, e^+$ ). The columns show the bin ranges, the measured cross section and the corresponding relative uncertainties.

$W^+ \rightarrow e^+ \nu_e$ , 13 TeV, uncertainties in (%)				
Range	$d\sigma/dp_T^e$ [pb/GeV]	Stat uncertainty	Unfolding bias	Syst uncertainty
[26, 27]	73.773	0.372	0.106	0.879
[27, 28]	89.046	0.354	0.123	0.932
[28, 29]	101.290	0.328	0.051	0.988
[29, 30]	112.455	0.316	0.006	0.750
[30, 31]	124.343	0.326	0.035	0.453
[31, 32]	135.555	0.296	0.044	0.481
[32, 33]	145.498	0.293	0.040	0.499
[33, 34]	154.658	0.292	0.029	0.510
[34, 35]	163.823	0.281	0.016	0.398
[35, 36]	172.351	0.276	0.001	0.254
[36, 37]	179.925	0.268	0.016	0.248
[37, 38]	183.698	0.265	0.028	0.252
[38, 39]	182.920	0.270	0.036	0.256
[39, 40]	172.858	0.268	0.034	0.243
[40, 41]	151.985	0.297	0.025	0.226
[41, 42]	125.704	0.317	0.011	0.230
[42, 43]	100.523	0.308	0.002	0.240
[43, 44]	81.060	0.339	0.015	0.251
[44, 45]	65.895	0.395	0.024	0.253

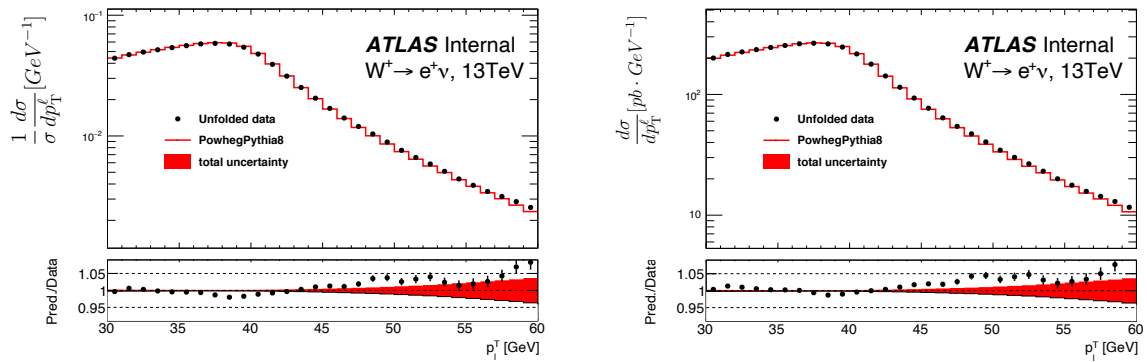


FIGURE 7.16: Differential cross sections (right) and normalised differential cross sections (left) as a function of  $p_T^e$  for 13 TeV ( $W^+, e^+$ ). The bottom panel shows the ratio data to MC (Powheg+Pythia8) together with the red band showing the total uncertainty.

1971 **Differential cross sections of the  $\mu$  channel versus  $p_T^\mu$  at 13 TeV**

TABLE 7.7: Differential cross sections versus  $p_T^\mu$  for 13 TeV ( $W^-$ ,  $\mu^-$ ). The columns show the bin range, the measured cross section and the corresponding relative uncertainties.

$W^- \rightarrow \mu^- \bar{\nu}_\mu$ , 13 TeV, uncertainties in (%)				
Range	$d\sigma/dp_T^\mu$ [pb/GeV]	Stat uncertainty	Unfolding bias	Syst uncertainty
[26, 27]	52.018	0.476	0.066	0.392
[27, 28]	62.789	0.464	0.085	0.400
[28, 29]	72.624	0.450	0.056	0.431
[29, 30]	81.235	0.390	0.037	0.393
[30, 31]	90.532	0.395	0.023	0.317
[31, 32]	100.091	0.373	0.011	0.360
[32, 33]	109.480	0.328	0.001	0.361
[33, 34]	119.185	0.314	0.009	0.372
[34, 35]	127.754	0.306	0.017	0.340
[35, 36]	136.933	0.291	0.024	0.305
[36, 37]	144.898	0.272	0.029	0.340
[37, 38]	150.402	0.273	0.030	0.347
[38, 39]	152.265	0.289	0.024	0.347
[39, 40]	146.020	0.295	0.011	0.320
[40, 41]	128.869	0.307	0.004	0.311
[41, 42]	107.394	0.334	0.020	0.341
[42, 43]	86.287	0.370	0.026	0.348
[43, 44]	69.418	0.384	0.033	0.346
[44, 45]	56.634	0.403	0.032	0.334

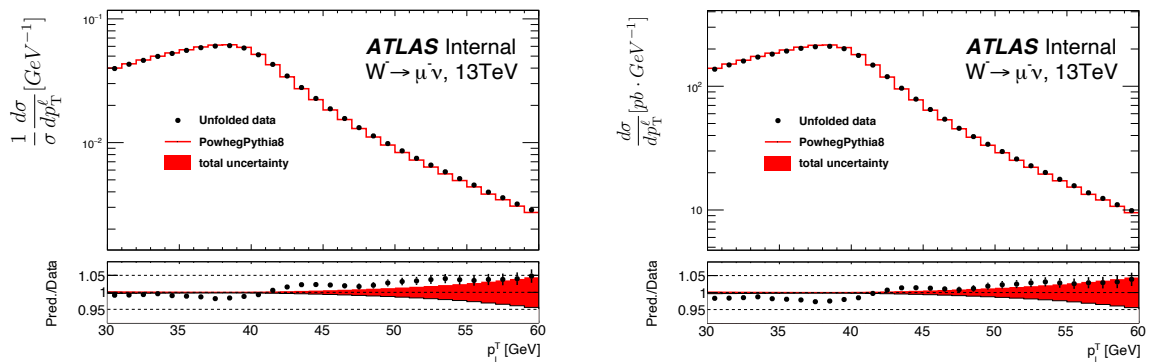


FIGURE 7.17: Differential cross sections (right) and normalised differential cross sections (left) as a function of  $p_T^\mu$  for 13 TeV ( $W^-$ ,  $\mu^-$ ). The bottom panel shows the ratio data to MC (Powheg+Pythia8) together with the red band showing the total uncertainty.

TABLE 7.8: Differential cross sections versus  $p_T^\mu$  for 13 TeV ( $W^+, \mu^+$ ). The columns show the bin range, the measured cross sections and the corresponding relative uncertainties.

$W^+ \rightarrow \mu^+ \nu_\mu$ , 13 TeV, uncertainties in (%)				
Range	$d\sigma/dp_T^\mu$ [pb/GeV]	Stat uncertainty	Unfolding bias	Syst uncertainty
[26, 27]	80.886	0.359	0.030	0.374
[27, 28]	96.188	0.390	0.007	0.383
[28, 29]	108.856	0.382	0.010	0.411
[29, 30]	120.804	0.352	0.020	0.373
[30, 31]	131.932	0.317	0.024	0.305
[31, 32]	142.772	0.310	0.023	0.345
[32, 33]	152.768	0.294	0.020	0.348
[33, 34]	162.641	0.287	0.014	0.359
[34, 35]	172.353	0.269	0.006	0.325
[35, 36]	180.673	0.265	0.002	0.294
[36, 37]	187.665	0.265	0.011	0.327
[37, 38]	190.965	0.257	0.020	0.336
[38, 39]	190.346	0.262	0.026	0.337
[39, 40]	179.390	0.260	0.025	0.311
[40, 41]	157.157	0.278	0.020	0.305
[41, 42]	128.185	0.303	0.010	0.335
[42, 43]	102.682	0.326	0.000	0.341
[43, 44]	82.328	0.367	0.008	0.335
[44, 45]	66.918	0.413	0.015	0.318

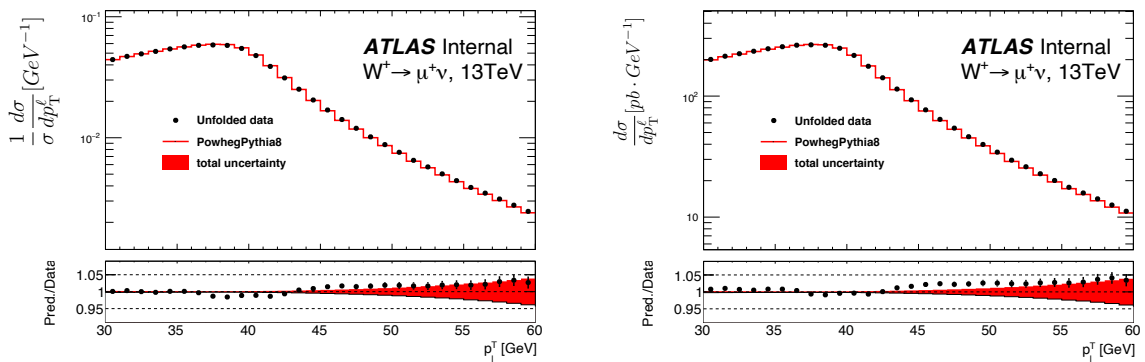


FIGURE 7.18: Differential cross sections (right) and normalised differential cross sections (left) as a function of  $p_T^\mu$  for 13 TeV ( $W^+, \mu^+$ ). The bottom panel shows the ratio data to MC (Powheg+Pythia8) together with the red band showing the total uncertainty.

1972 **Differential cross sections of the  $e$  channel versus  $\eta_e$**

TABLE 7.9: Differential cross sections versus  $\eta_e$  at 5 TeV ( $W^+, e^+$ ). The columns show the bin range, measured cross section, relative uncertainties.

$W^+ \rightarrow e^+ \nu_e$ , 5 TeV, uncertainties in (%)				
Range	$d\sigma/d\eta_e$	Stat uncertainty	Unfolding bias	Syst uncertainty
[-2.50, -2.18]	367.836	0.678	0.000	0.642
[-1.95, -1.74]	461.329	0.775	0.000	0.525
[-1.74, -1.52]	469.095	0.667	0.000	0.641
[-1.52, -1.37]	468.811	0.427	0.146	0.587
[-1.37, -1.05]	464.068	0.543	0.000	0.568
[-1.05, -0.84]	465.592	0.643	0.000	0.492
[-0.84, -0.63]	464.723	0.683	0.000	0.433
[-0.63, -0.42]	460.784	0.637	0.000	0.380
[-0.42, -0.21]	452.088	0.705	0.000	0.375
[-0.21, 0.00]	449.530	0.637	0.000	0.537
[ 0.00, 0.21]	453.114	0.681	0.000	0.495
[ 0.21, 0.42]	456.250	0.643	0.000	0.325
[ 0.42, 0.63]	452.126	0.683	0.000	0.370
[ 0.63, 0.84]	454.408	0.662	0.000	0.645
[ 0.84, 1.05]	459.436	0.666	0.000	0.432
[ 1.05, 1.37]	469.338	0.537	0.000	0.555
[ 1.37, 1.52]	472.773	0.413	0.030	0.490
[ 1.52, 1.74]	474.614	0.670	0.000	0.467
[ 1.74, 1.95]	457.307	0.715	0.000	0.511
[ 2.18, 2.50]	371.495	0.694	0.000	0.797

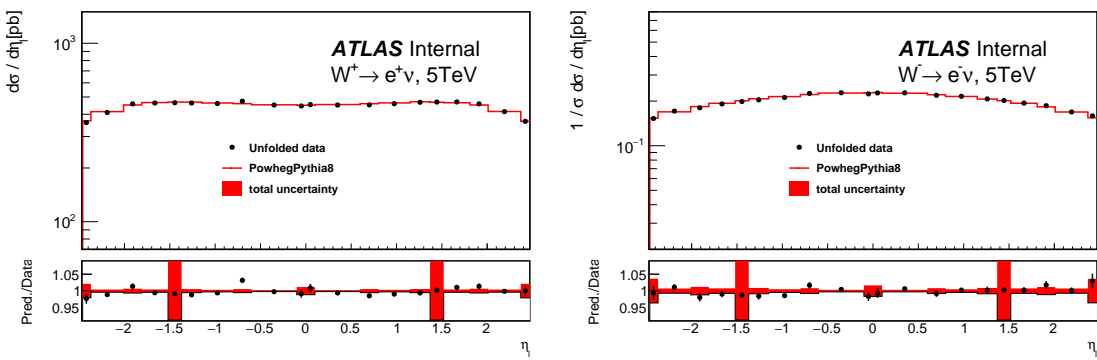


FIGURE 7.19: Differential cross sections (left) and normalised differential cross sections (right) as a function of  $p_T^e$  for 13 TeV ( $W^+, e^+$ ). The bottom panel shows the ratio data to MC (Powheg+Pythia8) together with the red band showing the total uncertainty.

TABLE 7.10: Differential cross sections versus  $\eta_e$  at 5 TeV ( $W^-, e^-$ ). The columns show the bin range, measured cross section, relative uncertainties.

$W^- \rightarrow e^- \bar{\nu}_e, 5 \text{ TeV}$ , uncertainties in (%)				
Range	$d\sigma / d\eta_e$	Stat uncertainty	Unfolding bias	Syst uncertainty
[-2.50, -2.18]	216.082	0.935	0.944	0.688
[-2.18, -1.95]	249.183	0.929	0.491	0.450
[-1.95, -1.74]	250.450	0.972	0.067	0.531
[-1.74, -1.52]	268.866	0.997	0.578	0.617
[-1.52, -1.37]	275.843	0.602	0.948	0.550
[-1.37, -1.05]	284.339	0.720	0.999	0.519
[-1.05, -0.84]	293.295	0.888	0.591	0.463
[-0.84, -0.63]	305.781	0.838	0.119	0.421
[-0.63, -0.42]	312.623	0.853	0.303	0.353
[-0.42, -0.21]	315.281	0.818	0.569	0.344
[-0.21, 0.00]	311.796	0.802	0.623	0.486
[0.00, 0.21]	317.227	0.796	0.457	0.448
[0.21, 0.42]	314.936	0.842	0.165	0.304
[0.42, 0.63]	308.392	0.770	0.150	0.343
[0.63, 0.84]	302.388	0.800	0.361	0.581
[0.84, 1.05]	298.429	0.797	0.345	0.389
[1.05, 1.37]	289.149	0.712	0.084	0.501
[1.37, 1.52]	280.873	0.552	0.762	0.467
[1.52, 1.74]	272.492	0.908	1.314	0.447
[1.74, 1.95]	256.505	0.972	1.667	0.493
[1.95, 2.18]	250.888	0.912	1.039	0.481
[2.18, 2.50]	215.071	0.924	2.373	0.858

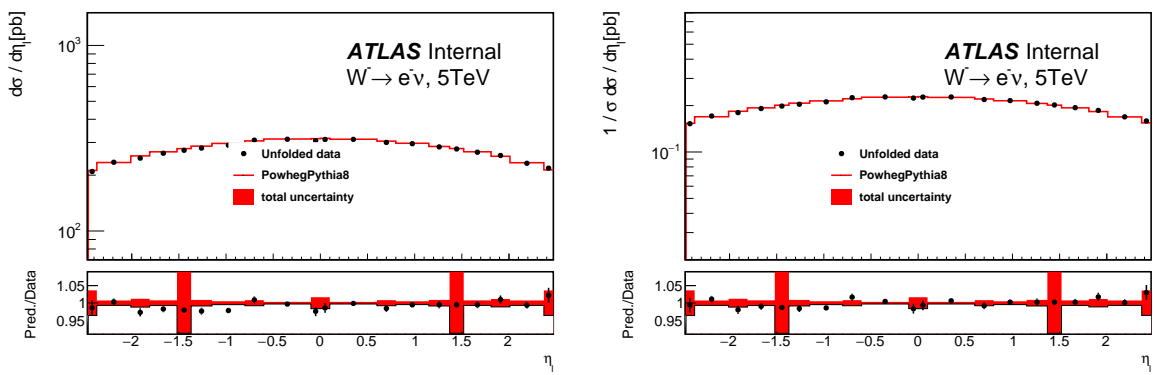


FIGURE 7.20: Differential cross sections (left) and normalised differential cross sections (right) as a function of  $p_T^e$  for 13 TeV ( $W^-, e^-$ ). The bottom panel shows the ratio data to MC (Powheg+Pythia8) together with the red band showing the total uncertainty.

1973 **Differential cross sections of the  $\mu$  channel versus  $\eta_\mu$** TABLE 7.11: Differential cross-sections versus  $\eta^\mu$  at 5 TeV ( $W^+, \mu^+$ ). The columns show the bin range, measured cross section, relative uncertainties.

$W^+ \rightarrow \mu^+ \nu_\mu$ , 5 TeV, uncertainties in (%)				
Range	$d\sigma / d\eta_\mu$	Stat uncertainty	Unfolding bias	Syst uncertainty
[-2.40, -1.92]	417.143	0.470	0.000	0.761
[-1.92, -1.35]	464.547	0.411	0.000	0.571
[-1.35, -1.15]	462.196	0.670	0.000	0.697
[-1.15, -1.05]	458.964	1.183	0.000	2.246
[-1.05, -0.91]	461.993	0.987	0.000	2.243
[-0.91, -0.48]	453.411	0.504	0.000	0.782
[-0.48, 0.00]	446.514	0.529	0.000	0.896
[0.00, 0.48]	443.203	0.493	0.000	0.886
[0.48, 0.91]	454.335	0.489	0.000	0.893
[0.91, 1.05]	466.137	1.020	0.000	2.233
[1.05, 1.15]	455.781	1.055	0.000	1.775
[1.15, 1.35]	474.952	0.689	0.000	0.664
[1.35, 1.92]	459.009	0.412	0.000	0.543
[1.92, 2.40]	417.343	0.470	0.000	0.769

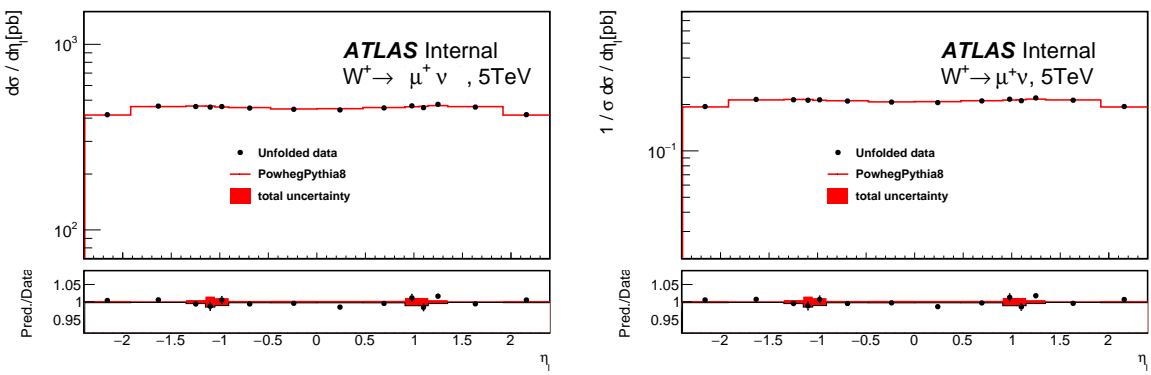
FIGURE 7.21: Differential cross sections (left) and normalised differential cross sections (right) as a function of  $p_T^\mu$  for 13 TeV ( $W^+, \mu^+$ ). The bottom panel shows the ratio data to MC (Powheg+Pythia8) together with the red band showing the total uncertainty

TABLE 7.12: Differential cross-sections versus  $\eta^\mu$  at 5 TeV ( $W^-, \mu^-$ ). The columns show the bin range, measured cross section, relative uncertainties.

$W^- \rightarrow \mu^- \bar{\nu}_\mu, 5 \text{ TeV, uncertainties in (\%)}$				
Range	$d\sigma/d\eta_\mu$	Stat uncertainty	Unfolding bias	Syst uncertainty
[-2.40, -1.92]	234.738	0.621	0.000	0.752
[-1.92, -1.35]	268.060	0.508	0.000	0.501
[-1.35, -1.15]	285.380	0.881	0.000	1.307
[-1.15, -1.05]	306.520	1.296	0.000	3.090
[-1.05, -0.91]	297.537	1.314	0.000	0.024
[-0.91, -0.48]	302.886	0.607	0.000	1.061
[-0.48, 0.00]	311.382	0.569	0.000	0.738
[0.00, 0.48]	309.306	0.633	0.000	0.707
[0.48, 0.91]	303.490	0.635	0.000	0.778
[0.91, 1.05]	293.061	1.202	0.000	2.989
[1.05, 1.15]	284.430	1.390	0.000	3.657
[1.15, 1.35]	285.125	0.837	0.000	1.393
[1.35, 1.92]	264.657	0.512	0.000	0.550
[1.92, 2.40]	239.405	0.592	0.000	0.775

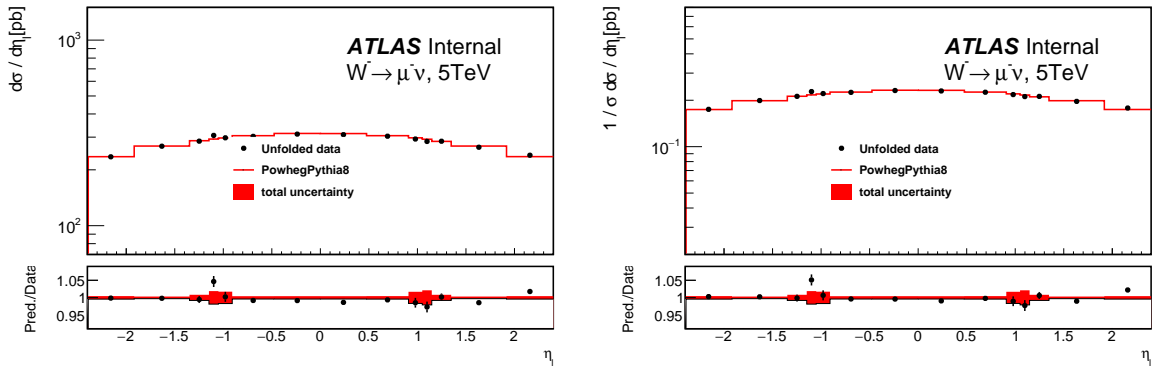


FIGURE 7.22: Differential cross sections (left) and normalised differential cross sections (right) as a function of  $p_T^\mu$  for 13 TeV ( $W^-, \mu^-$ ). The bottom panel shows the ratio data to MC (Powheg+Pythia8) together with the red band showing the total uncertainty

## 7.4 Comparison of electron and muon channels

The differential cross sections for electron and muon are calculated using different binning in  $\eta$  direction. The choose of  $\eta$  binning is related mainly to the scale factor (SF) binning (reconstruction, trigger, isolation and identification SFs) that we apply to simulation in order to correct the difference between data and simulation. The electron SFs are calculated in the same binning, Table 7.13, while for muon, the SFs are calculated using different binning, Table 7.14.

TABLE 7.13: Values of  $\eta$  bin boundaries for electron SFs.

-2.47	-2.37	-2.01	-1.81	-1.37	-1.15	-0.8	-0.6	-0.1	0	0.1	0.6	0.8	1.15	1.37	1.52	1.81	2.01	2.37	2.47
-------	-------	-------	-------	-------	-------	------	------	------	---	-----	-----	-----	------	------	------	------	------	------	------

TABLE 7.14: Values of  $\eta$  bin boundaries for muon trigger SF.

-2.4	-1.918	-1.348	-1.1479	-1.05	-0.908	-0.476	0	0.476	0.908	1.05	1.1479	1.348	1.918	2.4
------	--------	--------	---------	-------	--------	--------	---	-------	-------	------	--------	-------	-------	-----

The idea to compare the differential cross sections in the electron and muon channels, is to keep the binning at the reconstruction level unchanged, to conserve the SFs effects, and change the binning at the unfolded level to a common binning for the two channels. The new binning is chosen in a such a way that we conserve the bin boundaries similar to the SFs binning at the reconstructed level, Table 7.15. Figure 7.23 shows the comparison between the different SFs for electron and muon and the proposed binning at the unfolded level.

TABLE 7.15: Values of  $\eta$  bin boundaries for new binning at the unfolded level.

-2.5	-1.85	-1.36	-1.05	-0.85	-0.5	0	0.5	0.85	1.05	1.36	1.85	2.5
------	-------	-------	-------	-------	------	---	-----	------	------	------	------	-----

The distributions of  $\eta$  for electron and muon are unfolded to a common unfolded level, Figure 7.24 shows the comparison between distributions at the reconstruction and unfolded level, together with differential cross sections for electron and muon. The comparison of the cross sections shows in a good agreement for electrons and muons, excepting for the around  $\eta \approx 1.2$ , where the difference is related mainly to the variation of trigger SF for muon, shown in Figure 7.23. The difference observed is around 1.8% and included in the uncertainty. For the comparison with theoretical predictions, the binning defined in the Tables 7.13 and 7.14 are used in order to conserve the effect of scale factors.

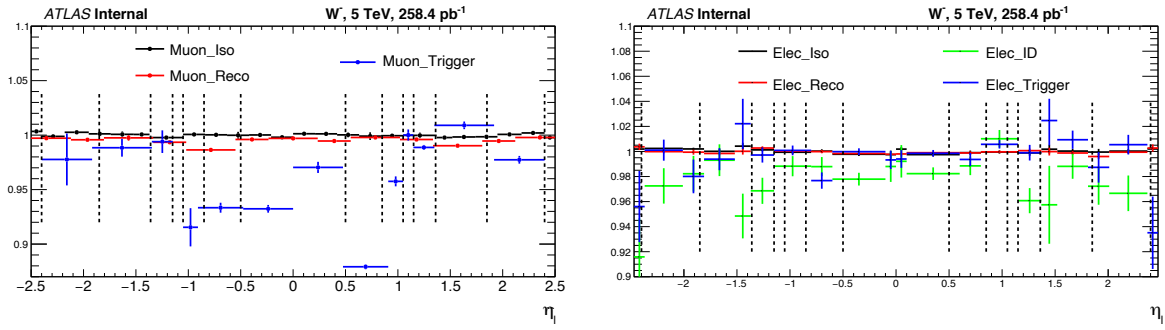


FIGURE 7.23: Muon (left) and electron (right) scale factors (SFs) used to correct simulation. The muons SFs are calculated using different binning, while the electron SFs are calculated in the same binning. The dotted vertical line shows the boundaries for proposed common binning at the unfolded level.

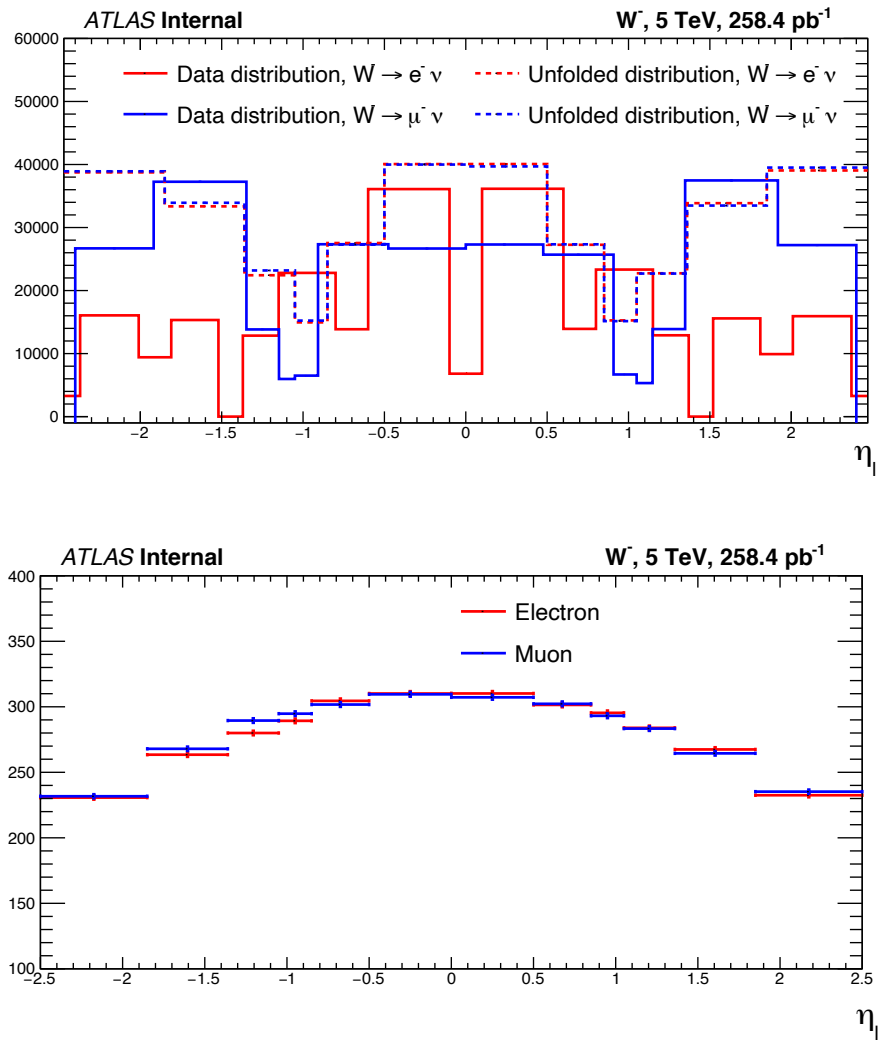


FIGURE 7.24: (Top) Distributions of data as a function of  $\eta_\ell$  for electron and muon at the reconstructed and the unfolded levels using the new common binning at the unfolded level. (Bottom) Comparison of the differential cross sections as a function of  $\eta_\ell$  for electron and muon.

## 1997 7.5 Comparison with theoretical predictions

1998 The measured differential cross sections for  $W^\pm \rightarrow \ell^\pm \nu$  are compared to theoretical  
 1999 predictions using DYTURBO [45] at NNLO QCD and LO in the EW theory, with  
 2000 different PDF sets: CT18 [93], HERAPDF20 [87], MMHT2014 [91], in the fiducial  
 2001 phase space defined in Section 7.2. The differential cross sections are compared  
 2002 separately for electron and muon without combination. The uncertainties of the  
 2003 theoretical predictions arise from the limited knowledge of proton PDFs. The DY-  
 2004 TURBO uses input parameters ( $G_F$ ,  $M_W$ ,  $M_Z$ ) for the theoretical predictions. The  
 2005 PDF sets used were extracted from analyses of various experimental data sets using  
 the corresponding predictions at NNLO in QCD.

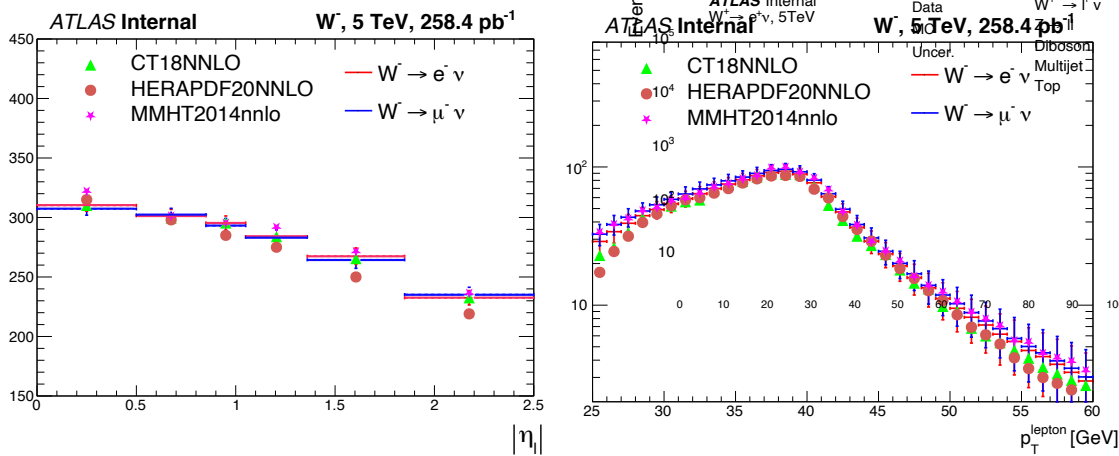


FIGURE 7.25: (left) Differential cross sections as a function of  $\eta_\ell$  for electron and muon compared to different PDF sets. (right) Differential cross sections as a function of  $p_T^\ell$  for electron and muon compared to different PDF sets.

2006 The PDF uncertainty on the  $M_W$  measurement, the dominant source of physics  
 2007 modelling uncertainty  $\approx 9.2$  MeV, arises from our imperfect knowledge of the  
 2008 PDFs affecting the differential cross section as a function of boson rapidity, the  
 2009 angular coefficients, and the  $W$  boson transverse momentum distribution. The  
 2010 measurements of the differential cross sections of the  $W$  boson, as a function of  $\eta_\ell$ ,  
 2011 are used to validate and constrain the PDF uncertainty on the measurement of  $W$   
 2012 boson, by comparing the uncertainties on the measured level and the uncertainties  
 2013 on the PDF predictions.  
 2014

## 2015 7.6 Double differential cross sections in $p_T^\ell$ and $\eta_\ell$ bins

### 2016 7.6.1 Introduction

2017 Double differential cross sections in  $p_T^\ell$  and  $\eta_\ell$  bins are measured using a two di-  
 2018 mensional (2d) unfolding of data distributions. The two dimensional unfolding  
 2019 can be transferred to a one dimensional (1d) unfolding by splitting the data dis-  
 2020 tributions of  $\eta_\ell$ , in different ranges of  $p_T^\ell$  as shown in Fig. 7.26. The statistical and  
 2021 systematic uncertainties are evaluated in the same way as we did for one dimen-  
 2022 sional unfolding described in Sec. 7.6.2. The bin-by-bin correction method can not  
 2023 be used because of the large migration between bins (Fig. 7.27).

2024 The double differential cross sections can be expressed as:

$$\frac{d\sigma}{dp_{T,i}^l d\eta_j^l} = \frac{N_{i,j}^{\text{Unfolded}}}{\mathcal{L} \Delta p_T^l \Delta \eta^l} \cdot \frac{1}{A_{\text{unf}}} \quad (7.4)$$

2025 where  $N_{\text{Unfolded}}$  represents the number of events in the unfolded distribution, and  
 2026  $A_{\text{unf}}$  is a correction factor related to the unfolding procedure. This factor represents  
 2027 the fraction of the entries in a truth bin that are in the same bin at reconstruction  
 level,  $\mathcal{L}$  is the integrated luminosity of data, and  $\Delta p_T^l$ ,  $\Delta \eta^l$  are the bin widths.

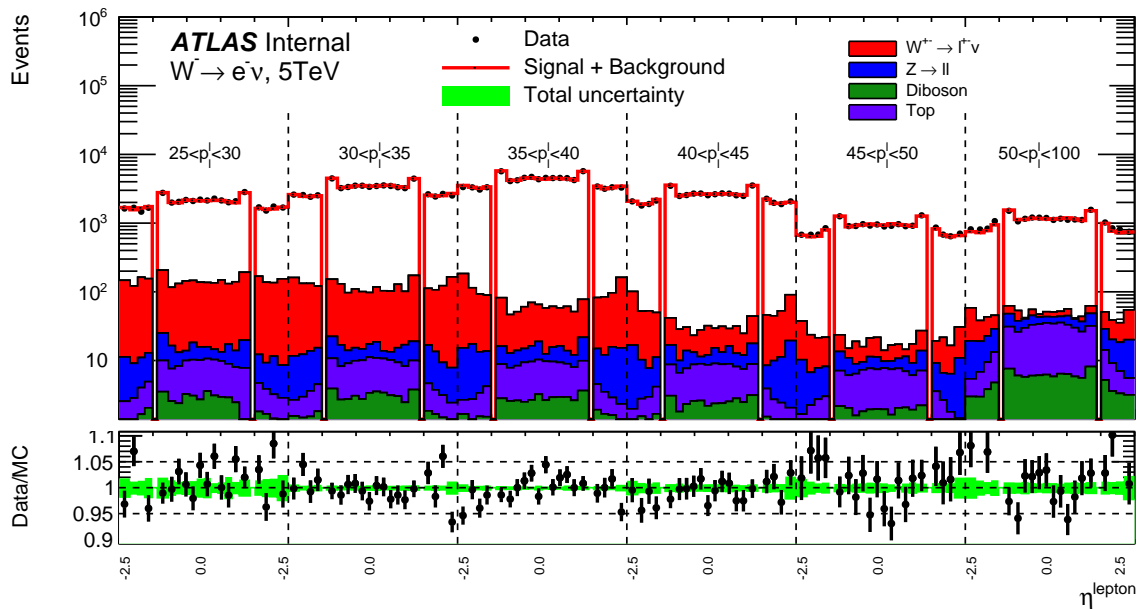


FIGURE 7.26: Distributions of the observables chosen to be unfolded  $\eta_\ell$  in bins of  $p_T^\ell$  for 5 TeV in the fiducial phase space. The signal and backgrounds are normalised to data. The low panel gives the ratio of the numbers of observed events to the total prediction in each bin. The green band shows the total statistical and systematic uncertainties. All the comparisons data/MC for 5 and 13 TeV are shown in Appendix B.

2029 **7.6.2 Migration matrix**

2030 In a migration matrix, one axis, e.g. the  $x$ -axis corresponds to reconstructed bins,  
 2031 the  $y$ -axis to true bins. For the double differential cross sections, the migration ma-  
 2032 trix is constructed in the same way but we take into account the different ranges of  
 2033  $p_T^\ell$ . The  $x$ -axis, corresponds to reconstructed  $\eta_\ell$  in different ranges of reconstructed  
 $p_T^\ell$ . The  $y$ -axis, corresponds to true  $\eta_\ell$  in different ranges of true  $p_T^\ell$ .

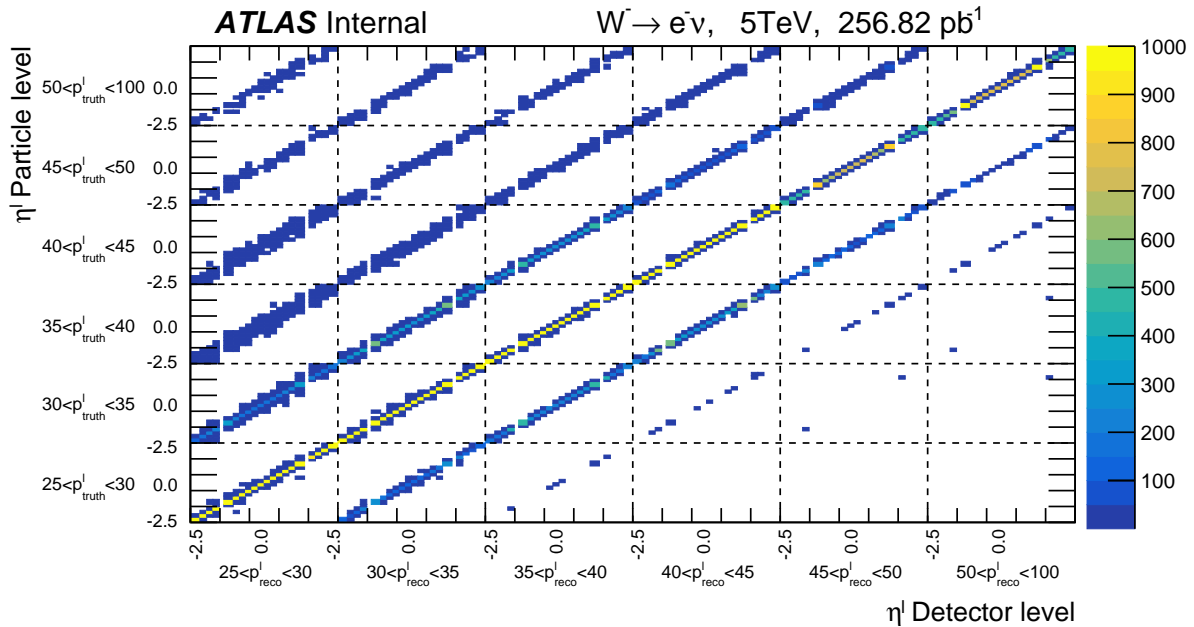


FIGURE 7.27: Example of the migration matrix used to unfold the data distribution for the measurement of the double differential cross sections, for  $W^- \rightarrow e^- \nu$  at 5 TeV.

2034

2035 **7.6.3 Statistical uncertainty**

2036 As the 2d unfolding problem is transformed into 1d unfolding, the statistical and  
 2037 systematic uncertainties are calculated as described in Sec. 7.6.2. As shown in  
 2038 Fig. 7.27, the 2d unfolding is characterised with a large migration between bins  
 2039 which explains the variation of statistical uncertainty with the number of iterations  
 2040 (Fig. 7.28).

2041 **7.6.4 Unfolding bias**

2042 The bias is calculated as described for 1d unfolding (Sec. 7.6.2). The only differ-  
 2043 ence is that we fit the ratio data/MC separately for each range of  $p_T^\ell$  as shown in  
 2044 Fig. 7.29.

2045 Because of the migration in the 2 dimensional unfolding, the bias is in the order  
 2046 of 1% for the first iteration and decreases with the number of iterations. For the  
 2047 double differential cross-sections results, 4 iterations are used in the final results to  
 2048 ensure that bias contribution is negligible comparing to other source of uncertain-  
 2049 ties. There are some bins where the bias is in the order 1.5% and does not change

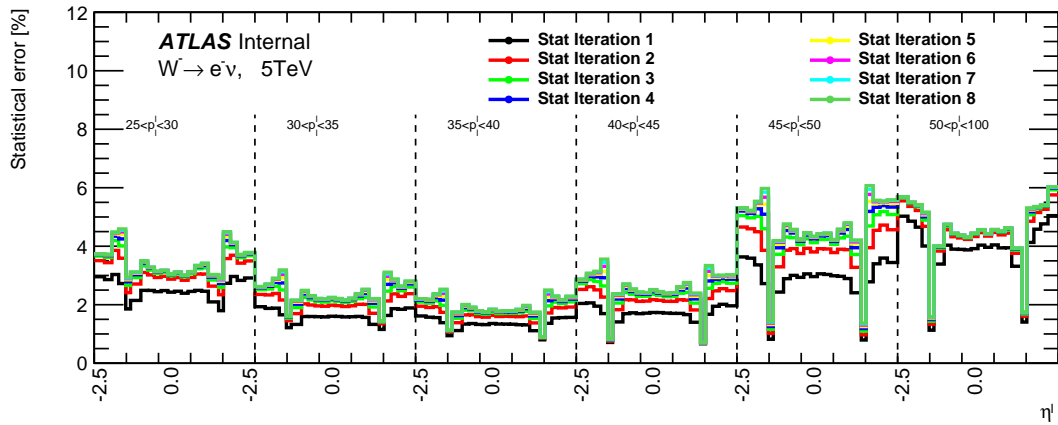


FIGURE 7.28: Example of the statistical uncertainty of unfolded distribution of  $\eta_\ell$  in different ranges of  $p_T^\ell$

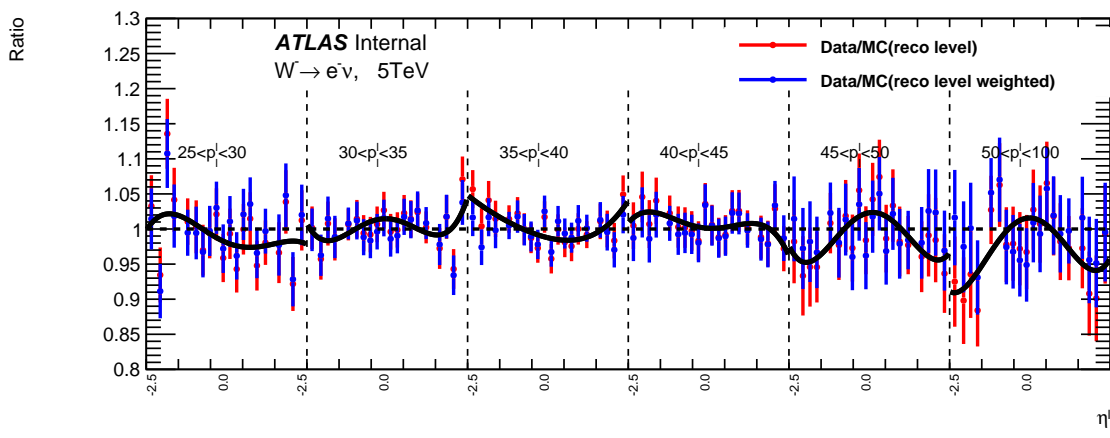


FIGURE 7.29: Example of the fitted ratio data/MC of  $\eta_\ell$  in different ranges of  $p_T^\ell$

2050 with iterations. Basically, the bias values in these bins have no signification as bins correspond to empty bin [1.52, 1.37] (Fig. 7.30).

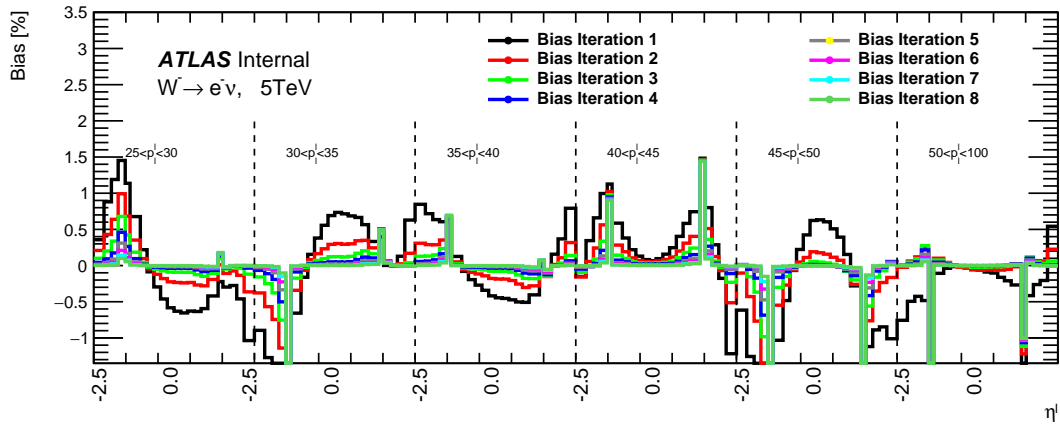


FIGURE 7.30: Example of the bias uncertainty as a function of  $\eta_\ell$  in different ranges of  $p_T^\ell$ .

### 2052 7.6.5 Double differential cross sections

2053 The double differential cross section results, together with the statistical, exper-  
 2054 imental systematic and unfolding bias uncertainties, are shown in Figures 7.31 and  
 2055 7.32 for 5 TeV and Figures 7.33 and 7.34 for 13 TeV.

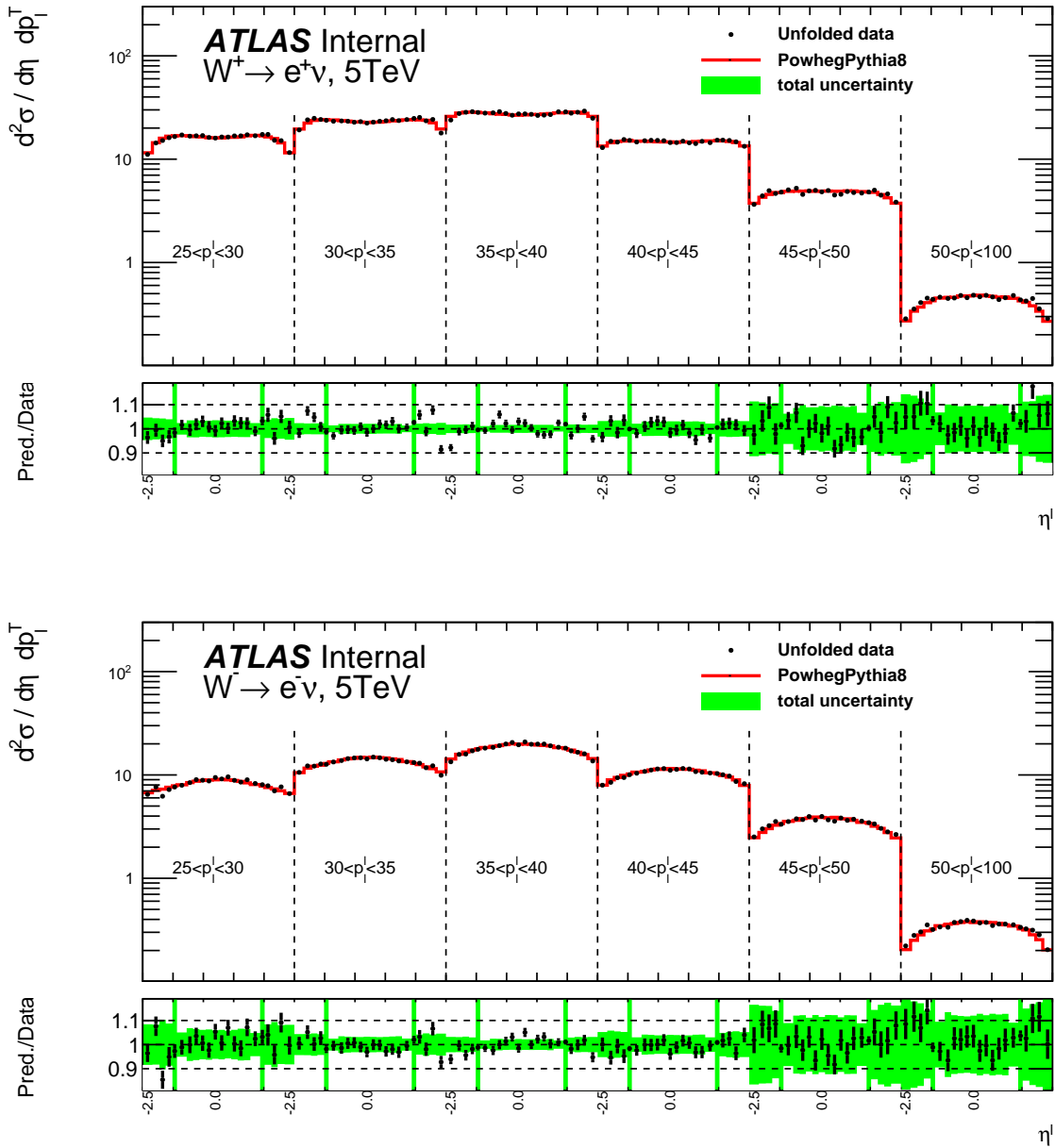


FIGURE 7.31: Double differential cross sections in bins of  $\eta_\ell$  and  $p_T^\ell$  compared to Powheg+Pythia8 for  $W^+ \rightarrow e^+\nu$  and  $W^- \rightarrow e^-\nu$  at 5 TeV. The low panel shows the ratio data/MC and the green band represents the statistical and systematic uncertainties added in quadrature.

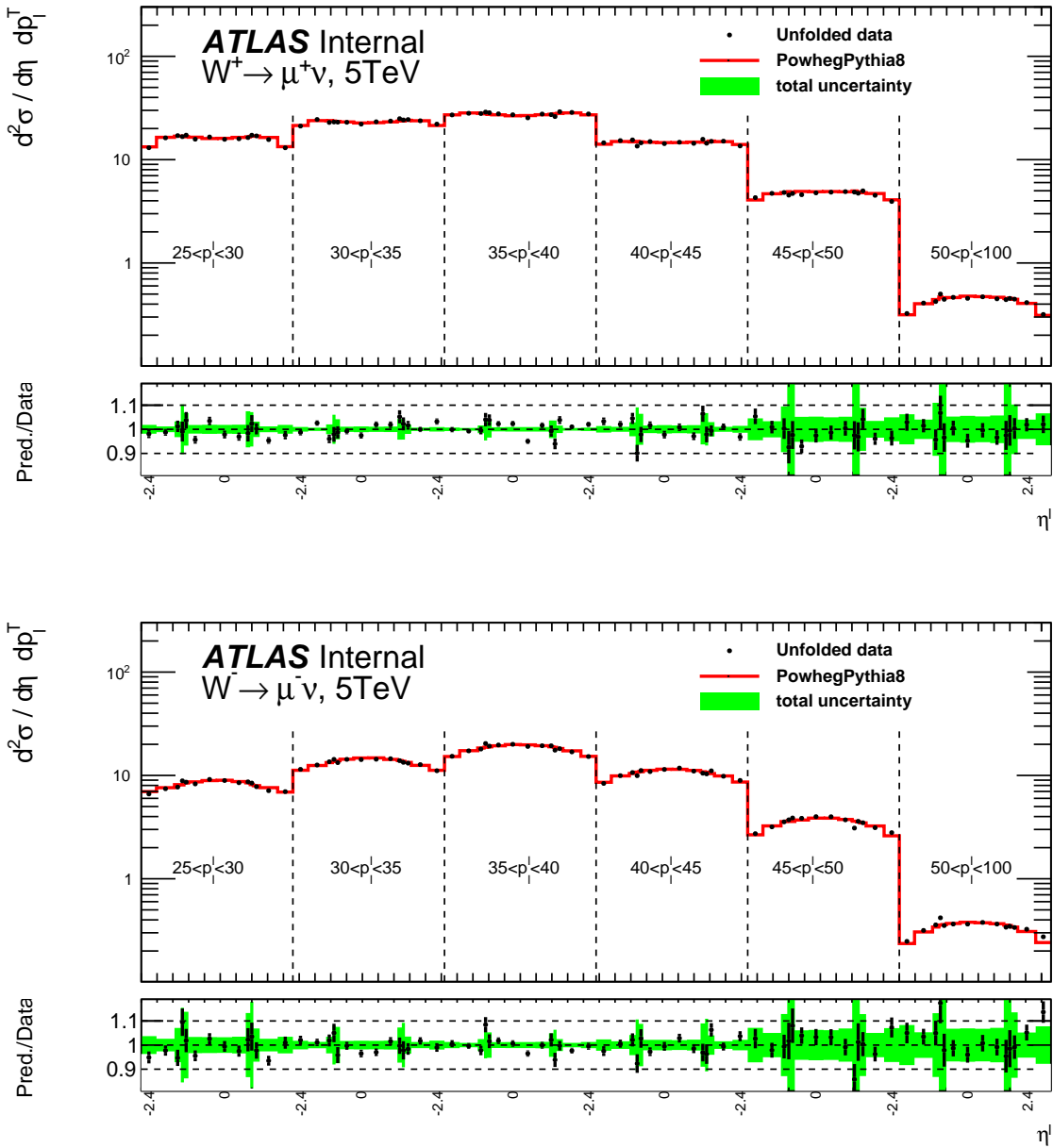


FIGURE 7.32: Double differential cross sections in bins of  $\eta_\ell$  and  $p_T^\ell$  compared to Powheg+Pythia8 for  $W^+ \rightarrow \mu^+ \nu$  and  $W^- \rightarrow \mu^- \nu$  at 5 TeV. The low panel shows the ratio data/MC and the green band represents the statistical and systematic uncertainties added in quadrature.

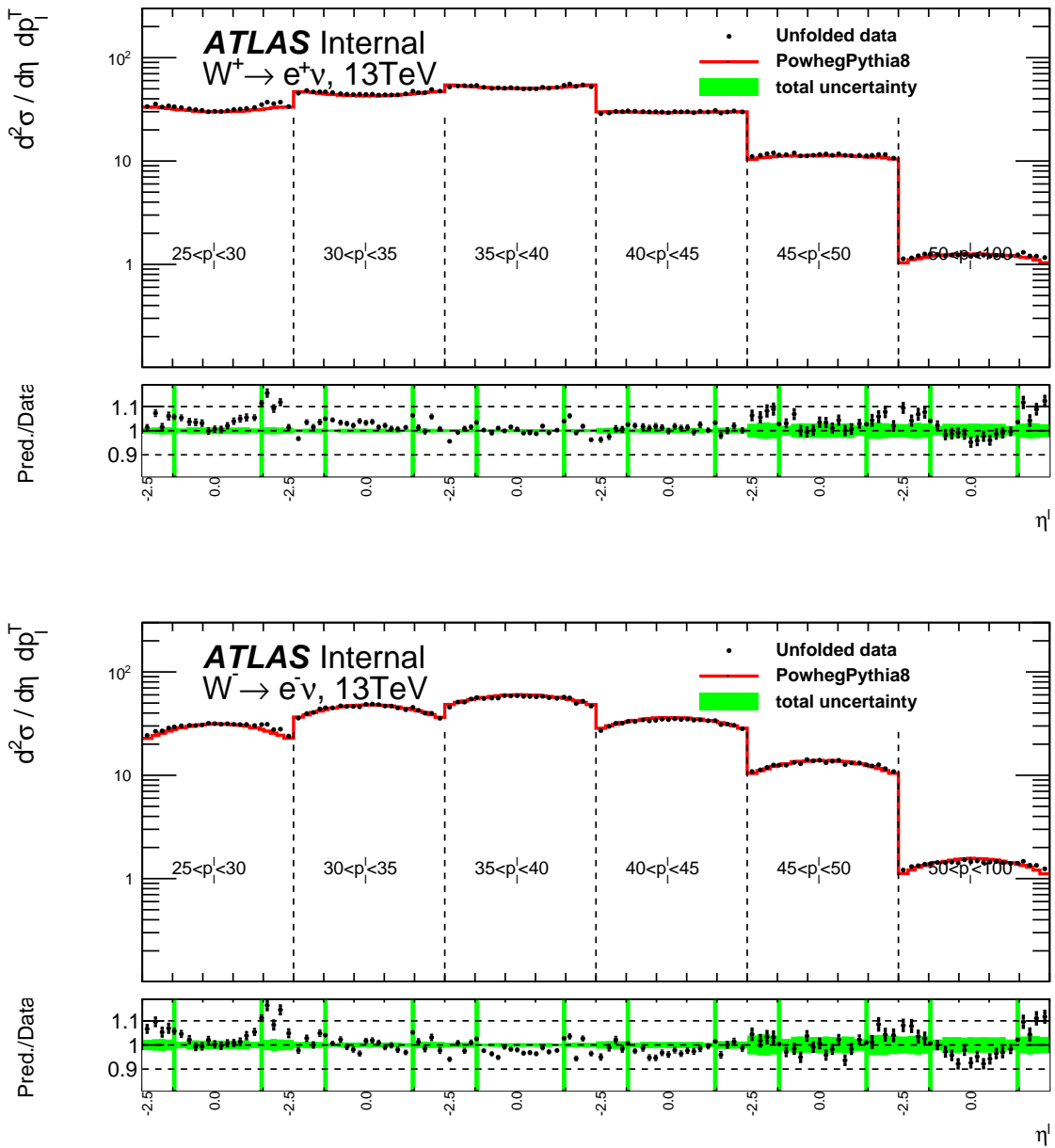


FIGURE 7.33: Double differential cross sections in bins of  $\eta_\ell$  and  $p_T^\ell$  compared to Powheg+Pythia8 for  $W^+ \rightarrow e^+\nu$  and  $W^- \rightarrow e^-\nu$  at 13 TeV. The low panel shows the ratio data/MC and the green band represents the statistical and systematic uncertainties added in quadrature.

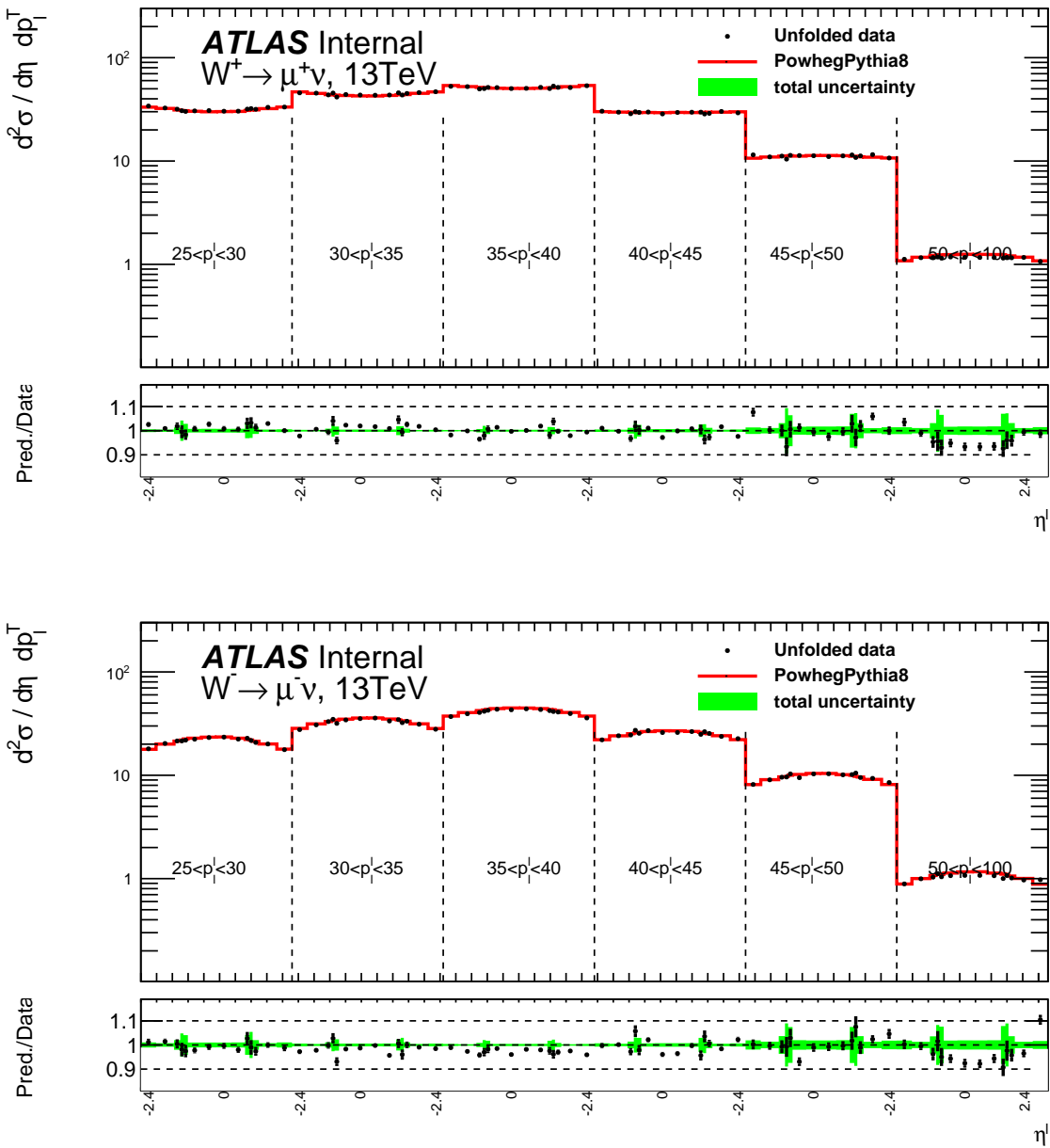


FIGURE 7.34: Double differential cross sections in bins of  $\eta_\ell$  and  $p_T^\ell$  compared to Powheg+Pythia8 for  $W^+ \rightarrow \mu^+ \nu$  and  $W^- \rightarrow \mu^- \nu$  at 13 TeV. The low panel shows the ratio data/MC and the green band represents the stat and systematic uncertainties added in quadrature.



2056 **Chapter 8**

2057 **Measurement of the  $W$ -boson mass**

2058 **8.1 Introduction**

2059 This chapter will show preliminary results of the measurement of  $W$  boson mass  
 2060 using low pile-up data set at  $\sqrt{s} = 5$  TeV and 13 TeV with two approaches: us-  
 2061 ing the templates method [17], developed before for Run 1 analysis, and using the  
 2062 unfolded distributions of our variables of interest. The methodology of using the  
 2063 unfolded distributions for  $W$  boson mass is described in Sec. 8.3. In parallel of  
 2064 those methods, there is another approach, using a new fitting algorithm in global  
 2065  $W$  mass, with the profile likelihood approach [77], which treats the correlation be-  
 2066 tween uncertainties differently from the template method. However, in this chap-  
 2067 ter, we will focus on the evaluation of statistical uncertainty on the  $W$  boson mass  
 2068 measurement using the two approaches described above, and the dominated ex-  
 2069 perimental uncertainties: lepton efficiency, lepton calibration and hadronic recoil  
 2070 calibration.

2071 **8.2 Template fit method methodology**

2072 The  $W$  boson is an unstable particle which decays to a charged lepton and a neu-  
 2073 trino. The mass of the  $W$  boson is determined using the distributions of the trans-  
 2074 verse mass of  $W$  ( $m_T^W$ ) and of the transverse momentum of lepton ( $p_T^\ell$ ), where the  
 2075  $p_T^\ell$  distribution has a Jacobian peak at  $M_W/2$ , while the transverse mass peak at  
 2076  $M_W$ , Figure 8.1 shows the distributions of  $p_T^\ell$  and  $m_T^W$  at the Jacobian peaks. The  
 2077 basic idea of the template method consists in computing the  $p_T^\ell$  and  $m_T^W$  distribu-  
 2078 tions for different assumed values of  $M_W$ , called the templates, and the compari-  
 2079 son between templates and data gives the best fit value.

2080 To generate templates with different  $W$  masses, the truth level distributions are  
 2081 reweighted using the Breit-Wigner equation:

$$f(m_W) = \frac{d\sigma}{dm} \propto \frac{m^2}{(m^2 - m_W^2)^2 + m^4 \Gamma_W^2 / m_W^2}, \quad (8.1)$$

2082 where  $m_W$  is the  $W$  boson mass, and the weight applied to truth distributions is  
 2083 considered as:

$$\text{weight} = \frac{f(m'_W)}{f(m_W)}, \quad (8.2)$$

2084 where  $m'_W$  is the modified mass.

2085 Figure 8.6 shows an example of  $p_T^{\ell}$  and  $m_T^W$  distributions compared to the  
 2086 templates generated with different mass values. Then, the comparison between tem-  
 2087 plates and data is based on  $\chi^2$  defined as:

$$\chi^2 = \sum_{i=1}^N \frac{(n_i^{\text{data}} - n_i^{\text{template}})^2}{(\sigma_{n_i}^{\text{data}})^2 + (\sigma_{n_i}^{\text{template}})^2}, \quad (8.3)$$

2088 where  $n_i^{\text{data}}$  ( $n_i^{\text{template}}$ ) is the number of entries in bin  $i$  of data (template), and  $\sigma_{n_i}^{\text{data}}$   
 2089 ( $\sigma_{n_i}^{\text{template}}$ ) is the uncertainty in bin  $i$  of data (template). The background is sub-  
 2090 tracted from the number of entries in data  $n_i^{\text{data}}$ .

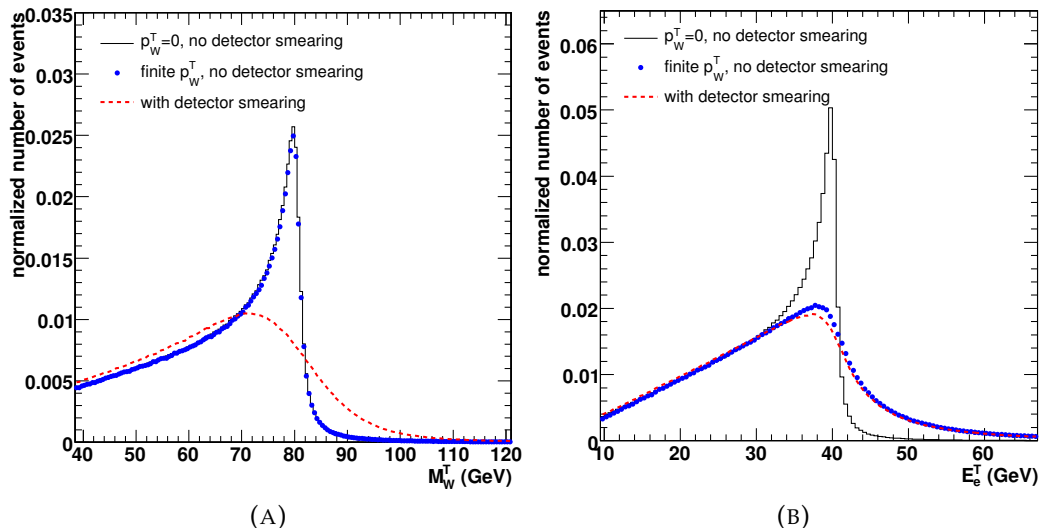


FIGURE 8.1: Transverse mass of  $W$  (A) and lepton transverse momentum (B) distributions in  $W$  decays. The distributions at the generator level with  $p_W^T = 0$  (blackline), with finite  $W$  boson  $p_W^T$  (blue dots) and including the experimental resolution in the low luminosity phase (red dashed line) are shown [112].

2090 The  $\chi^2$  is calculated between data and each template separately, then the com-  
 2091 puted  $\chi^2$  values are fitted using a polynomial function. The minimum of  $\chi^2$  distri-  
 2092 bution gives the best  $M_W$  value. Figure 8.3 shows an example of the fitted  $\chi^2$  dis-  
 2093 tribution. The templates used in the  $W$ -mass fit are signal MC samples reweighted  
 2094 to  $M_W \pm [0, 25, 50, 100, 150, 200]$  MeV.

2095 This method has been used in previous experiments (CDF and DO) for the  $W$   
 2096 mass measurement. In parallel to the template method, there is a new method [77]  
 2097 being developed called “profile likelihood” approach, which allows to deal with  
 2098 systematic uncertainties and their correlations in a different way.

### 2100 8.3 $W$ boson mass using the unfolded distribution

2101 In addition to the method described above, there is a different approach consist-  
 2102 ing in using the distributions at the unfolded level instead of the distributions at  
 2103 the reconstructed level. The main idea is to use distributions which are already

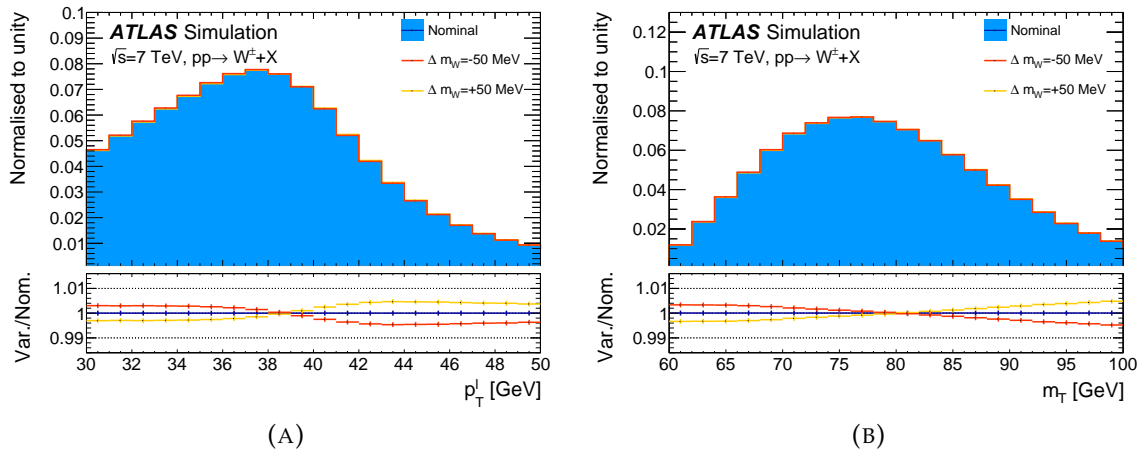


FIGURE 8.2: Kinematic distributions of  $p_T^\ell$  (A) and  $m_T^W$  (B) in simulated events for the  $W$ -boson mass nominal value  $M_W = 80370$  MeV and the shifted values  $M_W = 80320$  MeV and  $M_W = 80420$  MeV [115].

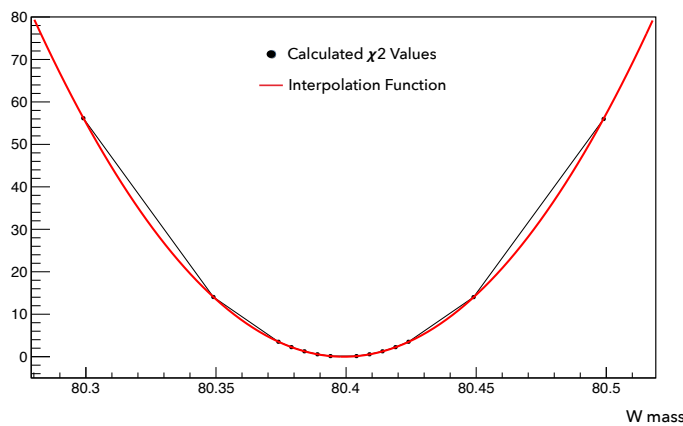


FIGURE 8.3: Fit to  $\chi^2$  distribution at different template mass values.

2104 corrected by the unfolding procedure and does not contain undesirable detector  
 2105 effects. The extraction of the  $M_W$  boson is the same as described with the template  
 2106 method, except for the  $\chi^2$  formula which have to be changed to take into account  
 2107 the correlation between bins at the unfolded level, introduced by the unfolding  
 2108 procedure. The new  $\chi^2$  formula is expressed as:

$$\chi^2 = (n_{\text{data}}^{\text{Unf}} - n_{\text{template}}^{\text{Unf}})^T \cdot (V_{\text{data}} + V_{\text{template}})^{-1} \cdot (n_{\text{data}}^{\text{Unf}} - n_{\text{template}}^{\text{Unf}}), \quad (8.4)$$

2109 where  $n_{\text{data}}^{\text{Unf}}$  is the unfolded distribution of data,  $n_{\text{template}}^{\text{Unf}}$  is the unfolded distribution  
 2110 of template,  $V_{\text{data}}$  ( $V_{\text{template}}$ ) represents the covariance matrix of the statistical  
 2111 uncertainty for the unfolded distribution of data (template) calculated as described  
 2112 in Chapter 4. Once the  $\chi^2$  is calculated for all the unfolded templates, the proce-  
 2113 dure is the same as described for the template method. Ideally for both meth-  
 2114 ods, we expect to have the same results but with an additional bias for the second  
 2115 method due to the unfolding of the variables of interest.

## 2116 8.4 Statistical uncertainty

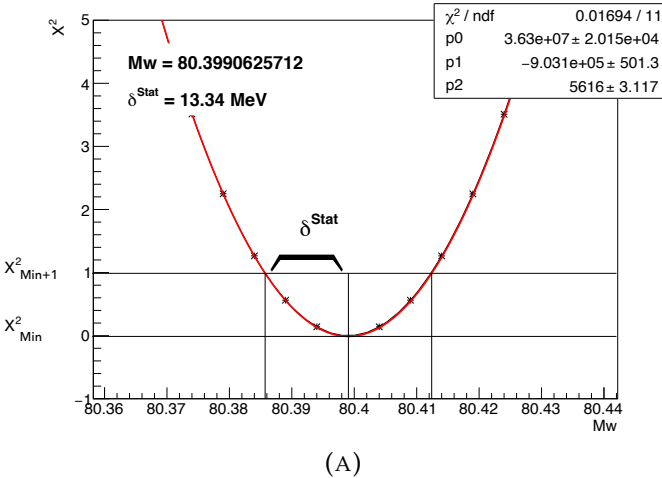
2117 The evaluation of statistical uncertainty is based on data distributions and MC  
 2118 templates, calculated from the  $\chi^2$  fit using a parabola function and estimated as  
 2119 the deviation from the measured value of  $M_W$  and  $M'_W$  correspond to  $\chi^2_{\text{min}} + 1$ .  
 2120 Figure 8.4 shows an example of the statistical uncertainty estimation. The statis-  
 2121 tical uncertainties are calculated using distributions of  $p_T^\ell$  and  $m_T^W$  separately and  
 2122 then combined. Since our distributions of interest are generated using the same  
 2123 events, we have to take into account the correlation between this two variables.  
 2124 The correlation is calculated using toys of MC (400 toys), generated by varying the  
 2125  $p_T^\ell$  and  $m_T^W$  distributions simultaneous with a random Poisson variation, and for  
 2126 each toy the  $W$  mass is calculated. Then the correlation factor is calculated as:

$$r = \frac{\sum_{i=1}^N (X_i - \bar{X})(Y_i - \bar{Y})}{\sqrt{\sum_{i=1}^N (X_i - \bar{X})^2} \sqrt{\sum_{i=1}^N (Y_i - \bar{Y})^2}}, \quad (8.5)$$

2127 where  $N$  is the number of toys,  $X_i$  ( $Y_i$ ) represent the  $W$  mass results for toy  $i$  of  $p_T^\ell$   
 2128 ( $m_T^W$ ),  $\bar{X}$  ( $\bar{Y}$ ) is the average of all the measured values  $X_i$  ( $Y_i$ ). The final measured  
 2129 value of the  $W$ -boson statistical uncertainty is obtained from the combination of  
 2130 various measurements performed in the electron and muon channels, and in  $|\eta|$ -  
 2131 dependent categories, as defined in Table 8.1. The boundaries of the  $|\eta|$  categories  
 2132 were defined as for Run 1 analysis, driven mainly by experimental and statisti-  
 2133 cal constraints [115]. Figure B.8 shows an example of the correlation between  $p_T^\ell$   
 2134 and  $m_T^W$  with the corresponding correlation factor for different ranges of  $|\eta|$ . The

TABLE 8.1: Summary of categories and kinematic distributions used in the  $W$  mass analysis for the electron and muon decay channels [115].

Decay channel	$W \rightarrow ev$	$W \rightarrow \mu v$
Kinematic distributions	$p_T^\ell, m_T$	$p_T^\ell, m_T$
Charge categories	$W^+, W^-$	$W^+, W^-$
$ \eta_\ell $ categories	$[0,0.6], [0.6,1.2], [1.8,2.4]$	$[0,0.8], [0.8,1.4], [1.4,2.0], [2.0,2.4]$

FIGURE 8.4: Statistical uncertainty calculation from  $\chi^2$  distribution.

2135 average is done using BLUE [109].

## 2136 8.5 Systematic uncertainties

2137 In this section, we will describe the propagation of systematic uncertainties for  
 2138 the  $W$  boson mass measurement, focusing on the dominant uncertainties: lepton  
 2139 efficiency corrections, lepton calibration and hadronic recoil calibration. The mod-  
 2140 eling uncertainties: QCD, Electroweak and PDF's uncertainties are not included in  
 2141 the work described in this thesis. The propagation of uncertainties is based on the  
 2142 templates method introduced in Sec.8.2, where for each uncertainty source, a new  
 2143 set of MC templates is produced. The fitting is then performed separately for the  
 2144 modified and nominal MC templates, and the difference between the fitted values  
 2145 is considered as a systematic uncertainty. The resulting uncertainty for each error  
 2146 source is combined quadratically in order to have for the total uncertainty. The  
 2147 advantage of the template fit method is that it allows a detailed study of the im-  
 2148 pact of different experimental uncertainties independently, contrary to the profile  
 2149 likelihood approach [77] which gives a total uncertainty.

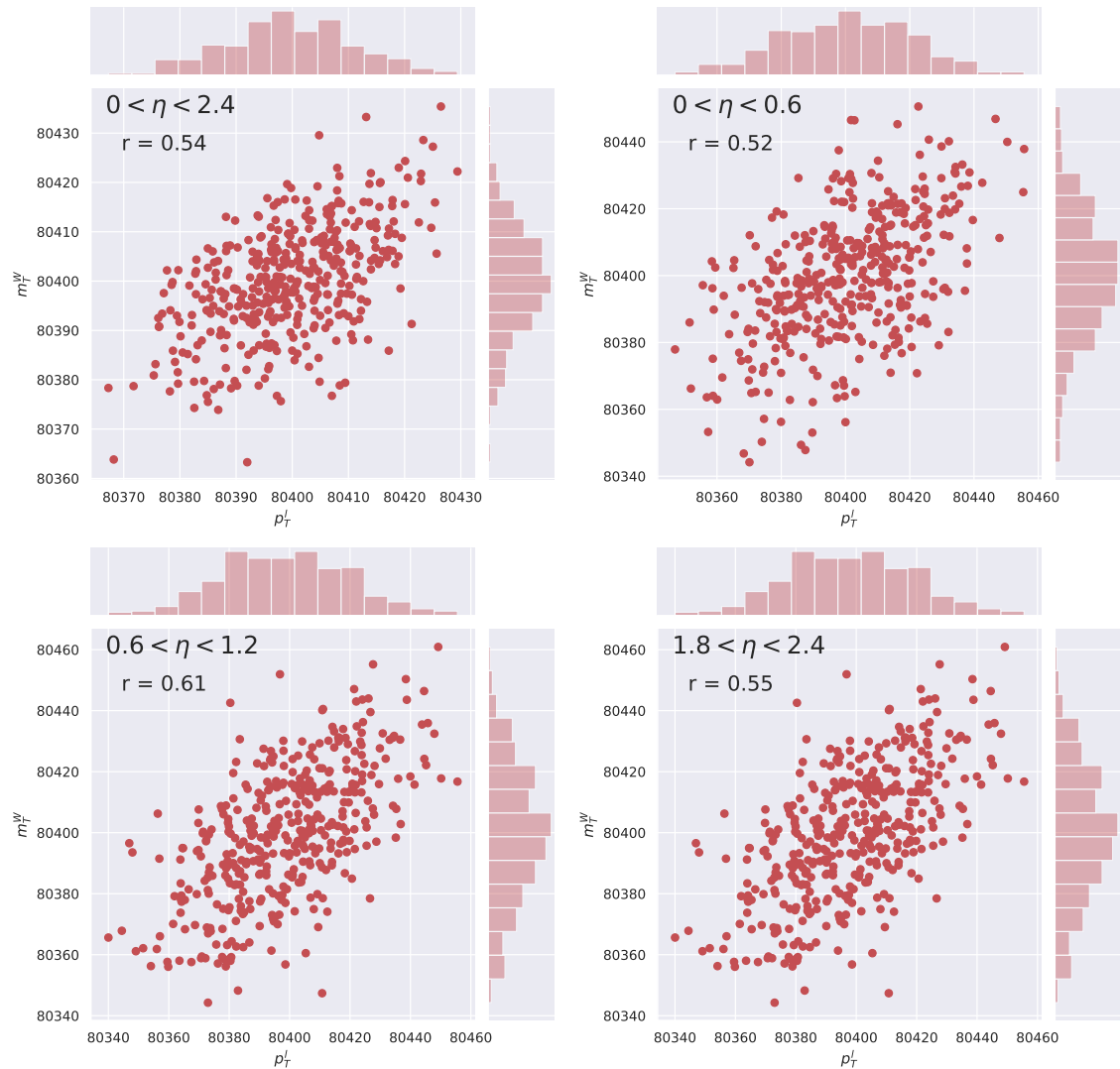


FIGURE 8.5: Correlation between  $p_T^l$  and  $m_T^W$  with the corresponding correlation factor for different ranges of  $|\eta_\ell|$ .

TABLE 8.2: Statistical uncertainties in the  $M_W$  measurement for the different kinematic distributions and their combination in  $|\eta_\ell|$  regions using data sets of 5 TeV.

$\eta_\ell$ range	[0, 0.6]		[0.6, 1.2]		[1.2, 1.8]		[1.8, 2.4]		[0, 2.4]	
Kinematic distribution	$p_T^\ell$	$m_T^W$								
$W^- \rightarrow e^- \bar{\nu}_e, 5 \text{ TeV}$										
Stat[MeV]	55	49	58	53	78	70	61	71	32	29
Correlation		0.52		0.61		0.44		0.55		0.54
Combined		45		50		63		58		27
$W^+ \rightarrow e^+ \nu_e, 5 \text{ TeV}$										
Stat[MeV]	54	48	55	49	64	59	53	48	28	25
Correlation		0.57		0.60		0.59		0.57		0.56
Combined		45		46		55		45		23
$W^- \rightarrow \mu^- \bar{\nu}_\mu, 5 \text{ TeV}$										
Stat[MeV]	55	48	59	53	58	55	78	73	31	28
Correlation		0.50		0.52		0.55		0.52		0.53
Combined		44		49		50		66		26
$W^+ \rightarrow \mu^+ \nu_\mu, 5 \text{ TeV}$										
Stat[MeV]	51	46	56	50	50	46	54	50	27	25
Correlation		0.51		0.59		0.60		0.50		0.56
Combined		42		48		43		45		23

TABLE 8.3: Statistical uncertainties in the  $M_W$  measurement for the different kinematic distributions and their combination in  $|\eta_\ell|$  regions using data sets of 13 TeV.

$\eta_\ell$ range	[0, 0.6]		[0.6, 1.2]		[1.2, 1.8]		[1.8, 2.4]		[0, 2.4]	
Kinematic distribution	$p_T^\ell$	$m_T^W$								
$W^- \rightarrow e^- \bar{\nu}_e, 13 \text{ TeV}$										
Stat[MeV]	37	35	39	36	51	49	44	42	21	20
Correlation		0.56		0.57		0.60		0.61		0.54
Combined		32		33		45		39		18
$W^+ \rightarrow e^+ \nu_e, 13 \text{ TeV}$										
Stat[MeV]	36	34	37	36	48	45	40	38	20	19
Correlation		0.59		0.63		0.60		0.67		0.59
Combined		31		33		41		36		17
$W^- \rightarrow \mu^- \bar{\nu}_\mu, 13 \text{ TeV}$										
Stat[MeV]	35	33	39	38	39	37	48	47	20	19
Correlation		0.55		0.60		0.58		0.60		0.63
Combined		30		31		34		42		18
$W^+ \rightarrow \mu^+ \nu_\mu, 13 \text{ TeV}$										
Stat[MeV]	35	34	39	37	36	35	46	44	19	18
Correlation		0.57		0.60		0.64		0.64		0.62
Combined		31		34		32		41		17

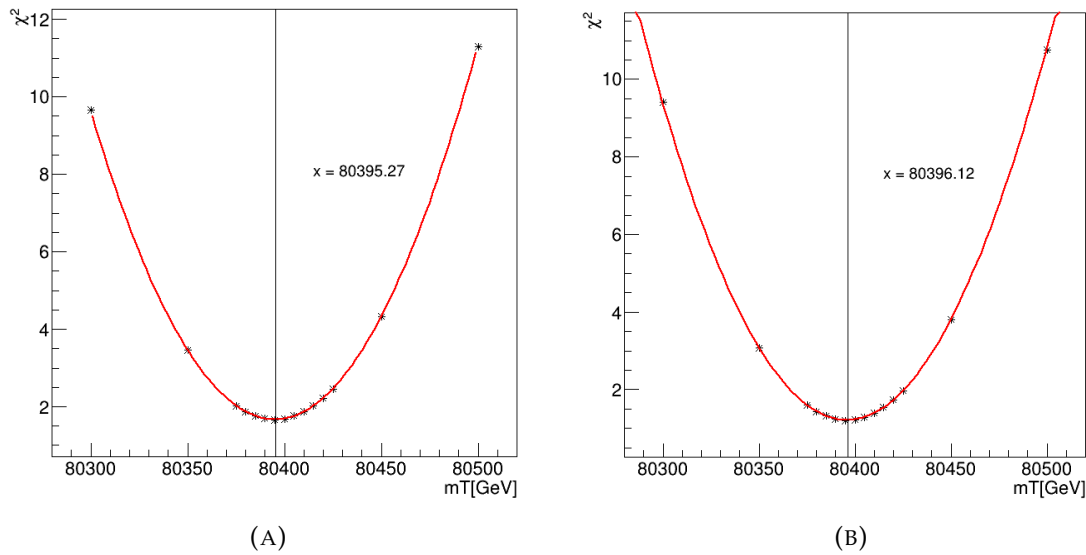


FIGURE 8.6: Example of  $M_W$  fitting results using the nominal MC templates (A) and varied MC templates (B) [155], the difference between the fitted values is considered as the propagated uncertainty on the  $M_W$  mass measurement.

- Lepton selection efficiency: lepton efficiency corrections are determined using tag-and-prob [1], and measured separately for electron reconstruction, identification and trigger efficiencies [47], using  $p_T^\ell$  and  $m_T^W$  separately for different range of  $|\eta_\ell|$ . For  $p_T^\ell$  and  $m_T^W$  ranges, and without including the extracted crack region ( $1.2 < \eta_\ell < 1.8$ ), the reconstruction and identification efficiency corrections have an uncertainty of  $\approx 4.5$  MeV in the barrel region, and around 4 MeV in the end-cap region. The isolation and trigger efficiency corrections are smaller and have an uncertainty of 1 to 2 MeV in the barrel and end-cap.

TABLE 8.4: Lepton selection efficiency uncertainties (in MeV) on the measurement of  $W$ -boson mass, for  $W^- \rightarrow e^- \bar{\nu}_e$  at 5 TeV.

$\eta_\ell$ range	[0, 0.6]		[0.6, 1.2]		[1.2, 1.8]		[1.8, 2.4]		[0, 2.4]	
Kinematic distribution	$p_T^\ell$	$m_T^W$	$p_T^\ell$	$m_T^W$	$p_T^\ell$	$m_T^W$	$p_T^\ell$	$m_T^W$	$p_T^\ell$	$m_T^W$
Channel										
	$W^- \rightarrow e^- \bar{\nu}_e$ , 5 TeV									
Identification efficiency	4.6	4.7	3.9	3.9	6.8	5.9	4.9	4.2	4.3	4.5
Isolation efficiency	2.1	1.3	2.3	1.3	3.6	2.2	2.3	1.4	2.1	1.2
Reconstruction efficiency	4.7	2.4	5.7	2.9	6.7	3.3	4.5	1.6	5.1	2.2
Trigger efficiency	1.9	1.7	1.3	1.2	2.4	1.9	7.1	4.9	1.4	0.9

- Lepton energy calibration: as shown in Ref. [152] for muons and in Chapter 3 for electrons, lepton energies are calibrated in order to correct the difference between data and simulation. For electrons, the uncertainty related to the lepton energy calibration is in particular due to the limited size of the  $Z \rightarrow ee$  sample, used in the calibration procedure, while for muons, the uncertainty

2164 is related mainly to the limited knowledge of the detector alignment and res-  
 2165 olution [155]. The uncertainty for electron channel is in the order of 18 MeV,  
 and larger when we split bins of  $\eta_l$  because of statistical fluctuations.

TABLE 8.5: Lepton energy calibration uncertainties (in MeV) on the measurement of  $W$ -  
 boson mass, for  $W^- \rightarrow e^- \bar{\nu}_e$  at 5 TeV.

$\eta_\ell$ range	[0, 0.6]		[0.6, 1.2]		[1.2, 1.8]		[1.8, 2.4]		[0, 2.4]	
Kinematic distribution	$p_T^\ell$	$m_T^W$	$p_T^\ell$	$m_T^W$	$p_T^\ell$	$m_T^W$	$p_T^\ell$	$m_T^W$	$p_T^\ell$	$m_T^W$
Channel	$W^- \rightarrow e^- \bar{\nu}_e$ , 5 TeV									
Energy scale	27	28	30	33	44	48	44	48	19	20
Energy resolution	1.3	2.3	2.8	4.1	4.1	7.2	3.2	7.7	1.4	2.5

2166

- Hadronic recoil calibration:

TABLE 8.6: Hadronic recoil calibration uncertainties (in MeV) on the measurement of  $W$ -  
 boson mass, for  $W^- \rightarrow e^- \bar{\nu}_e$  at 5 TeV.

$\eta_l$ range	[0, 0.6]		[0.6, 1.2]		[1.2, 1.8]		[1.8, 2.4]		[0, 2.4]	
Kinematic distribution	$p_T^\ell$	$m_T^W$	$p_T^\ell$	$m_T^W$	$p_T^\ell$	$m_T^W$	$p_T^\ell$	$m_T^W$	$p_T^\ell$	$m_T^W$
channel	$W^- \rightarrow e^- \bar{\nu}_e$ , 5 TeV									
$\sum E_T$ reweighting	4.1	6.2	3.9	6.5	6.5	11.2	4.3	7.9	3.8	6.7
Resolution correction	1.9	2.7	2.0	3.4	5.3	8.6	2.3	3.2	2.0	2.9
Response correction	2.9	3.3	3.9	3.2	4.1	7.2	3.5	3.5	3.2	3.3

2167

## 2168 8.6 Statistical uncertainty with the unfolded distribution

2169

2170 As described in Sec. 8.3, unfolded distributions are already corrected by the un-  
 2171 folding procedure and do not include detector effects. The  $m_T^W$  and  $p_T^\ell$  distribu-  
 2172 tions with the corresponding templates are unfolded using the iterative Bayesian  
 2173 unfolding. The comparison between the modified templates and the nominal dis-  
 2174 tributions at the reconstructed and unfolded levels is shown in Figure 8.7.

2175 The main particularity of the unfolded distributions is that the unfolding pro-  
 2176 cedure introduces a correlation between bins that we have to take into account  
 2177 in the  $\chi^2$  formula, while the statistical uncertainties of the different bins of the  
 2178 reconstructed distributions are fully uncorrelated. The correlation matrix for the  
 2179 statistical uncertainty of the unfolded distribution is calculated with the RooUn-  
 2180 fold framework [7]. Figure 8.8 shows an example of the correlation matrix at the  
 2181 reconstructed and unfolded levels for the transverse mass  $m_T^W$ . Then, the tem-  
 2182 plate distributions are also unfolded using the corresponding migration matrix.  
 2183 As shown in Sec 8.3, the  $\chi^2$  is calculated as:

$$\chi^2 = (n_{\text{data}}^{\text{Unf}} - n_{\text{template}}^{\text{Unf}})^T \cdot (V)^{-1} \cdot (n_{\text{data}}^{\text{Unf}} - n_{\text{template}}^{\text{Unf}}), \quad (8.6)$$

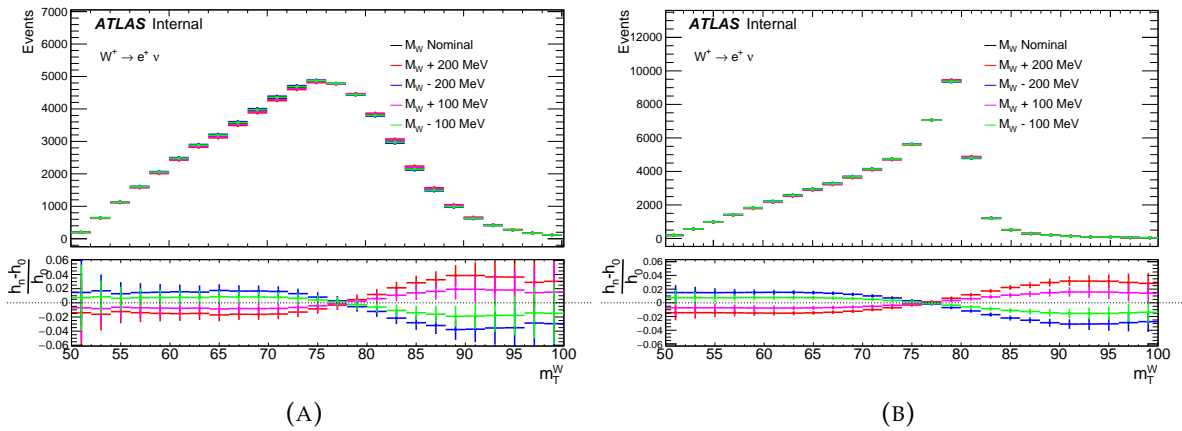


FIGURE 8.7: Distributions of  $m_T^W$  with the corresponding templates at the reconstructed level (A) and at the unfolded level (B).

2184 where the total covariance matrix  $V$  is considered as the sum of the covariance  
 2185 matrix of the unfolded data and the unfolded templates,  $V = V_{\text{data}} + V_{\text{template}}$ . The same procedure is applied also separately for  $p_T^\ell$  distributions.

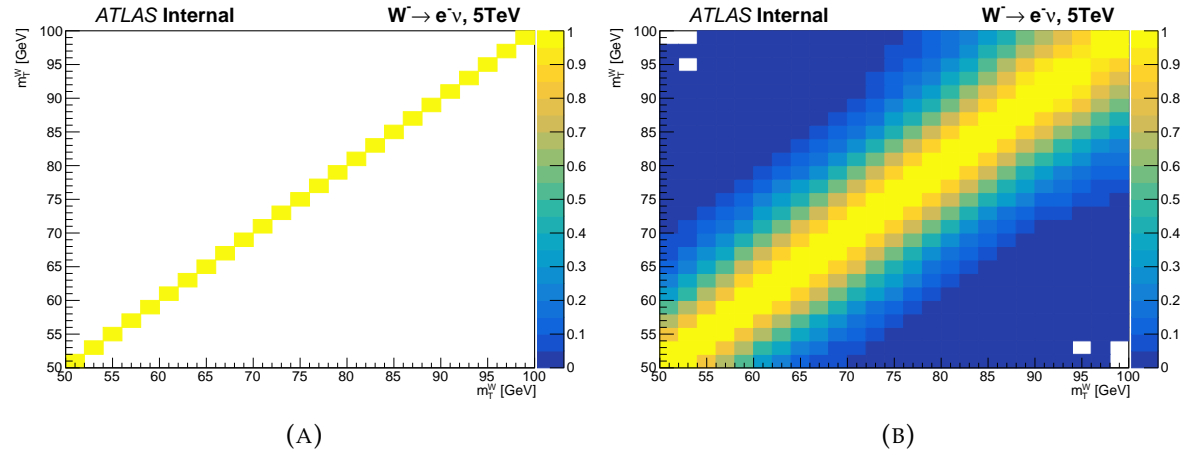


FIGURE 8.8: Correlation matrix for the statistical uncertainty for  $m_T^W$  distribution at the reconstructed level (A) and at the unfolded level (B), the correlation between bins is introduced by the unfolding procedure.

2186 Table 8.7 shows an example of the statistical uncertainties calculated using the  
 2187 unfolded and the reconstructed distributions, for different regions of  $\eta$ . In general,  
 2188 the results are similar for the statistical uncertainty for both methods. Then, the  
 2189 correlation between  $p_T^\ell$  and  $m_T^W$  is evaluated using the unfolded toys as described  
 2190 for the templates method in Sec. 8.4. In general, using the unfolded distribution  
 2191 does not change the results for the statistical uncertainties, but it is not the case  
 2192 when we treat the systematic uncertainties because of the statistical fluctuations  
 2193 in  $p_T^\ell$  and  $m_T^W$  and also because of the bias that we introduce with the unfolding  
 2194 procedure.

TABLE 8.7: Statistical uncertainties (in MeV) on the  $M_W$  measurement using the unfolded and reconstructed distributions, for  $p_T^\ell$  and  $m_T^W$  separately, using different regions of  $\eta_\ell$  at 5 TeV.

$\eta_\ell$ range	[0, 0.6]		[0.6, 1.2]		[1.2, 1.8]		[1.8, 2.4]		[0, 2.4]	
Kinematic distribution	$p_T^\ell$	$m_T^W$	$p_T^\ell$	$m_T^W$	$p_T^\ell$	$m_T^W$	$p_T^\ell$	$m_T^W$	$p_T^\ell$	$m_T^W$
Channel	$W^- \rightarrow e^- \bar{\nu}_e, 5 \text{ TeV}$									
Stat [Unfolded]	55	49	58	53	78	70	61	71	32	29
Stat [Reconstructed]	54	49	57	53	76	71	62	71	31	29



2196 **Chapter 9**

2197 **Conclusion**

2198 This thesis describes mainly my personal work on the in-situ calibration of the  
 2199 electromagnetic calorimeter of the ATLAS detector, and on the measurement  
 2200 of  $W$  boson properties using low pile-up data set collected by ATLAS in 2017  
 2201 and 2018 during Run 2 corresponding to an integrated luminosity of  $258 \text{ pb}^{-1}$  at  
 2202  $\sqrt{s} = 5 \text{ TeV}$  and  $340 \text{ pb}^{-1}$  at  $\sqrt{s} = 13 \text{ TeV}$ .

2203  
 2204 The in-situ calibration is the last step in the calibration procedure. It is based  
 2205 on the  $Z \rightarrow e^+e^-$  event samples and aims for correcting for residual difference in  
 2206 the energy scale and resolution between data and MC simulation. The calibration  
 2207 using the template method developed for Run 1 analysis has been performed  
 2208 for all nominal data samples taken in Run 2 in 2015, 2016, 2017 and 2018 under  
 2209 different running conditions. The number of interactions per bunch crossing  $\mu$  of  
 2210 these nominal data samples varies typically between 10 and 70, being lower in  
 2211 2015 and 2016 and higher in 2017 and 2018. Year dependence of the calibration  
 2212 corrections has been studied. The same procedure has also been applied to the  
 2213 low pile-up data showing larger uncertainties due to the limited statistics of the  
 2214 samples. The low pile-up data have a  $\mu$  value around 2. We have thus developed  
 2215 a new approach by studying the  $\mu$  dependence of the energy scale correction  
 2216 of the nominal data samples and extrapolating the correction of the nominal  
 2217 samples to  $\mu \sim 2$  to be compared with that obtained directly from the low pile-up  
 2218 data samples. It is found that the two sets of the corrections are consistent and  
 2219 the extrapolated correction has better precision even when the extrapolation  
 2220 uncertainties are taken into account.

2221  
 2222 The measurement of the  $W$  boson properties includes three parts. The first  
 2223 part corresponds to a measurement of the transverse momentum of the  $W$  boson,  
 2224  $p_T^W$ . The modelling uncertainty of  $p_T^W$  by a theoretical extrapolation from  $Z$ -boson  
 2225 measurements has been one of the dominant systematic uncertainties of the pre-  
 2226 vious mass determination of the  $W$  boson by ATLAS. A direct measurement of  
 2227  $p_T^W$  would avoid such an extrapolation and the corresponding theoretical mod-  
 2228 elling uncertainty. The second part is on the measurement of the fiducial, single  
 2229 and double differential cross sections of the  $W$  boson production in the electron  
 2230 and muon decay channels at 5 and 13 TeV. The measurement has been compared  
 2231 with a NNLO QCD prediction using different PDF sets, showing its potential in  
 2232 constraining the uncertainty of the PDFs which was the dominant source for the  
 2233 determination of the  $W$  boson mass. The third part represents preliminary results

2234 for the  $W$  boson mass determination using the templates method and a new ap-  
2235 proach which relies on unfolded distributions. In this thesis, we focused on the  
2236 measurement of the dominant experimental uncertainties. The final result for the  
2237  $W$  boson mass must take into account the theoretical and modeling uncertainties  
2238 that are not studied in this thesis.

2239 **Appendix A**

2240 **Control plots**

2241 **Comparison data/simulation for  $p_T^\ell$**

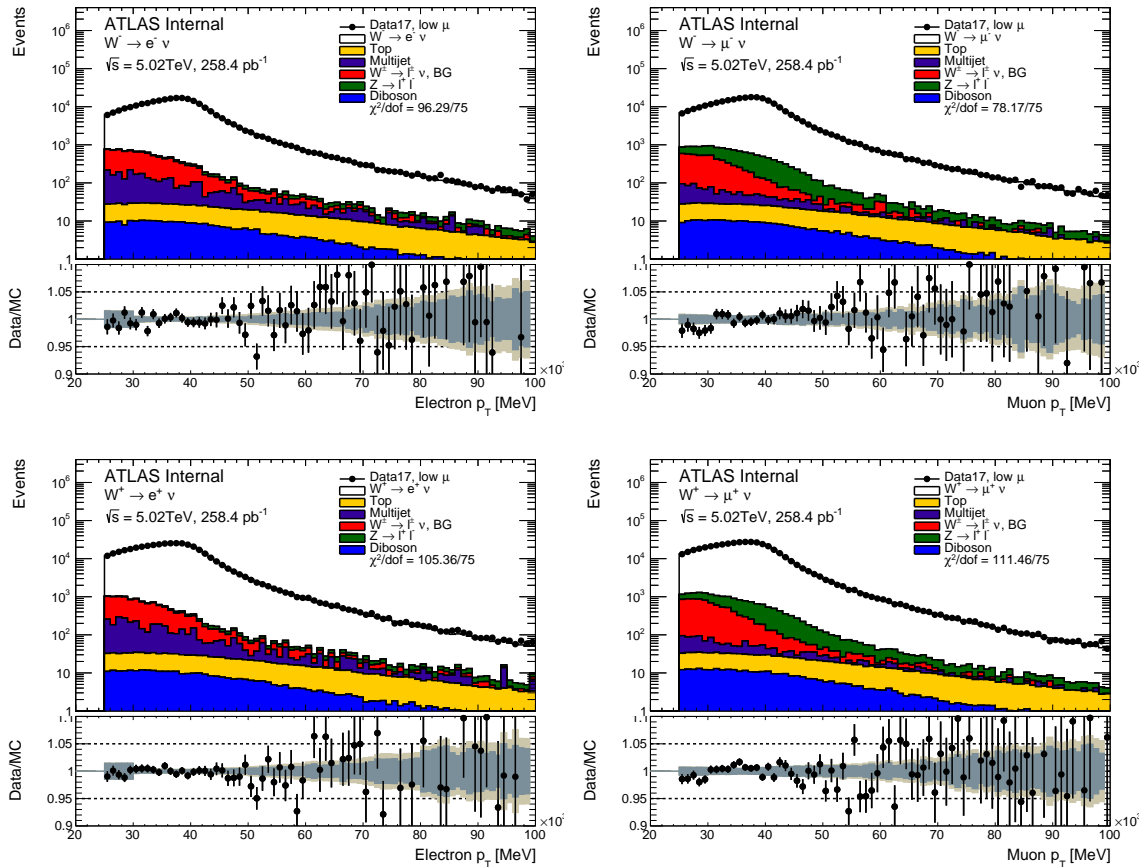


FIGURE A.1: Reconstructed  $p_T^\ell$  distributions at detector level for  $\sqrt{s} = 5$  TeV data set in the fiducial phase space. The signal and backgrounds are normalised to data. The low panel gives the ratio data/MC in each bin. The green band shows the statistical and systematic uncertainties added in quadrature. The total uncertainty is dominated by the uncertainty in the efficiency corrections applied to lepton.

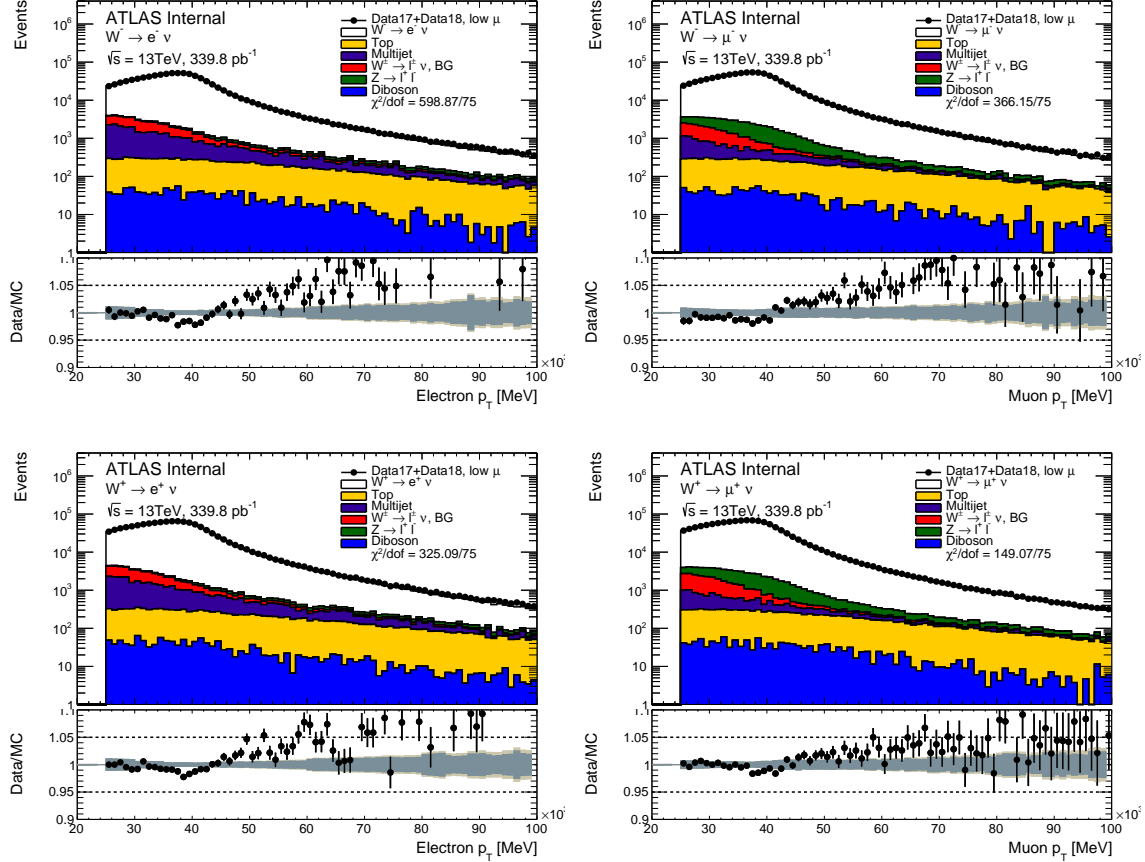


FIGURE A.2: Reconstructed  $p_T^l$  distributions at the detector level for  $\sqrt{s} = 13$  TeV data set in the fiducial phase space. The signal and backgrounds are normalised to data. The low panel gives the ratio data/MC in each bin. The green band shows the statistical and systematic uncertainties added in quadrature. The total uncertainty is dominated by the uncertainty on the efficiency corrections applied to lepton.

2242 **Comparison data/simulation for  $m_T^W$**

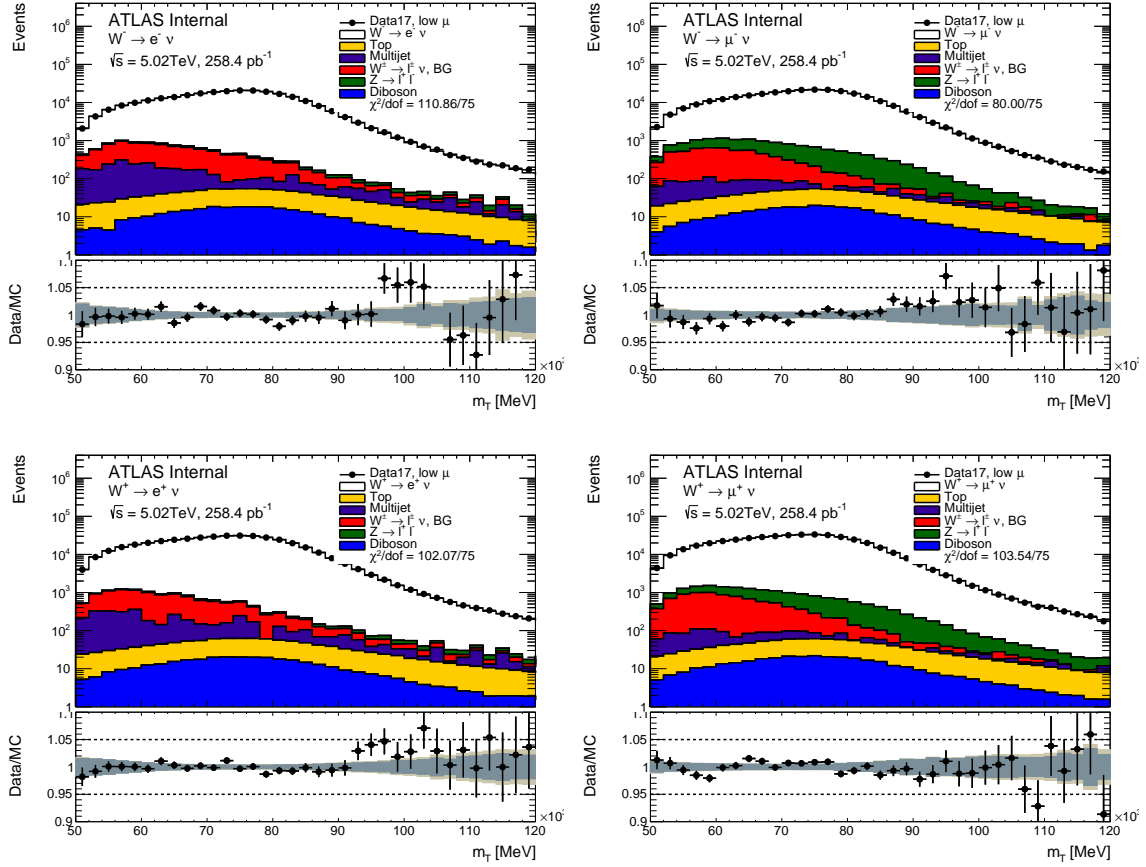


FIGURE A.3: Reconstructed  $m_T^W$  distributions at detector level for  $\sqrt{s} = 5$  TeV data set in the fiducial phase space. The signal and backgrounds are normalised to data. The low panel gives the ratio data/MC in each bin. The green band shows the statistical and systematic uncertainties added in quadrature. The total uncertainty is dominated by the uncertainty on the efficiency corrections applied to lepton.

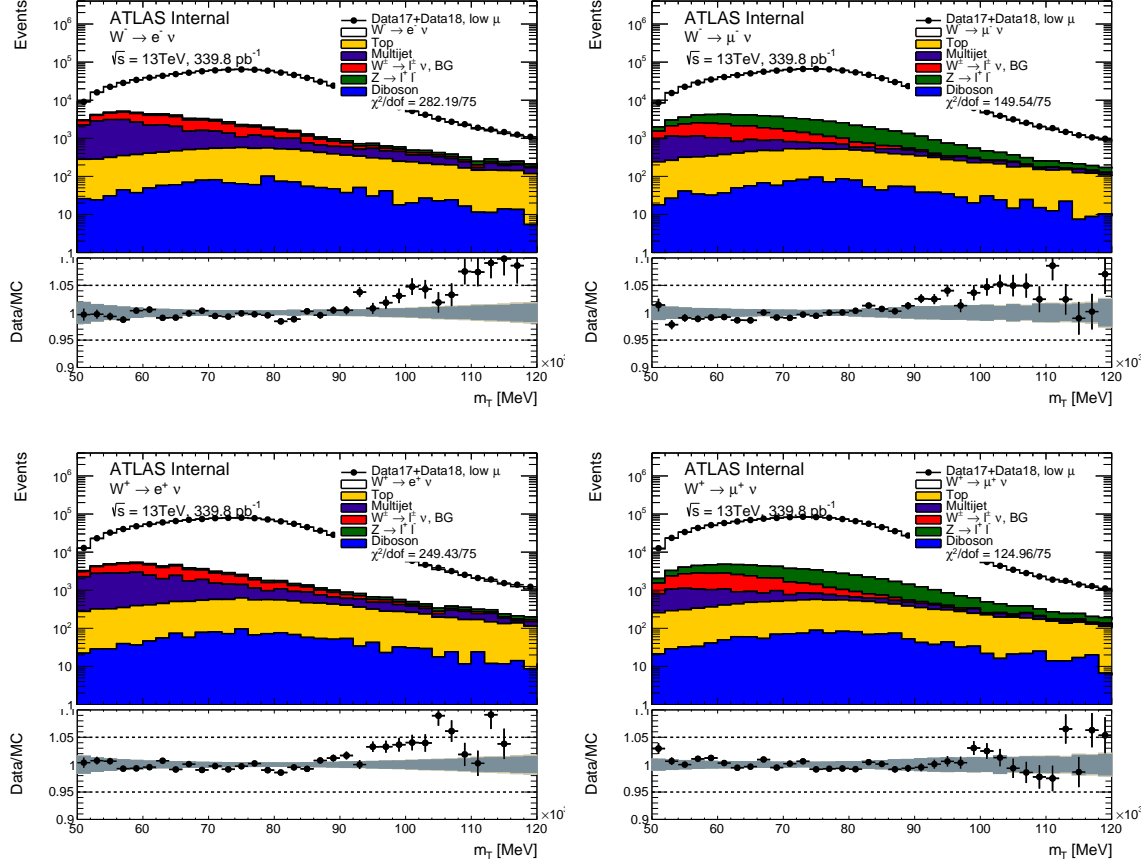


FIGURE A.4: Reconstructed  $m_T^W$  distributions at detector level for  $\sqrt{s} = 13$  TeV data set in the fiducial phase space. The signal and backgrounds are normalised to data. The low panel gives the ratio data/MC in each bin. The green band shows the statistical and systematic uncertainties added in quadrature. The total uncertainty is dominated by the uncertainty on the efficiency corrections applied to lepton.

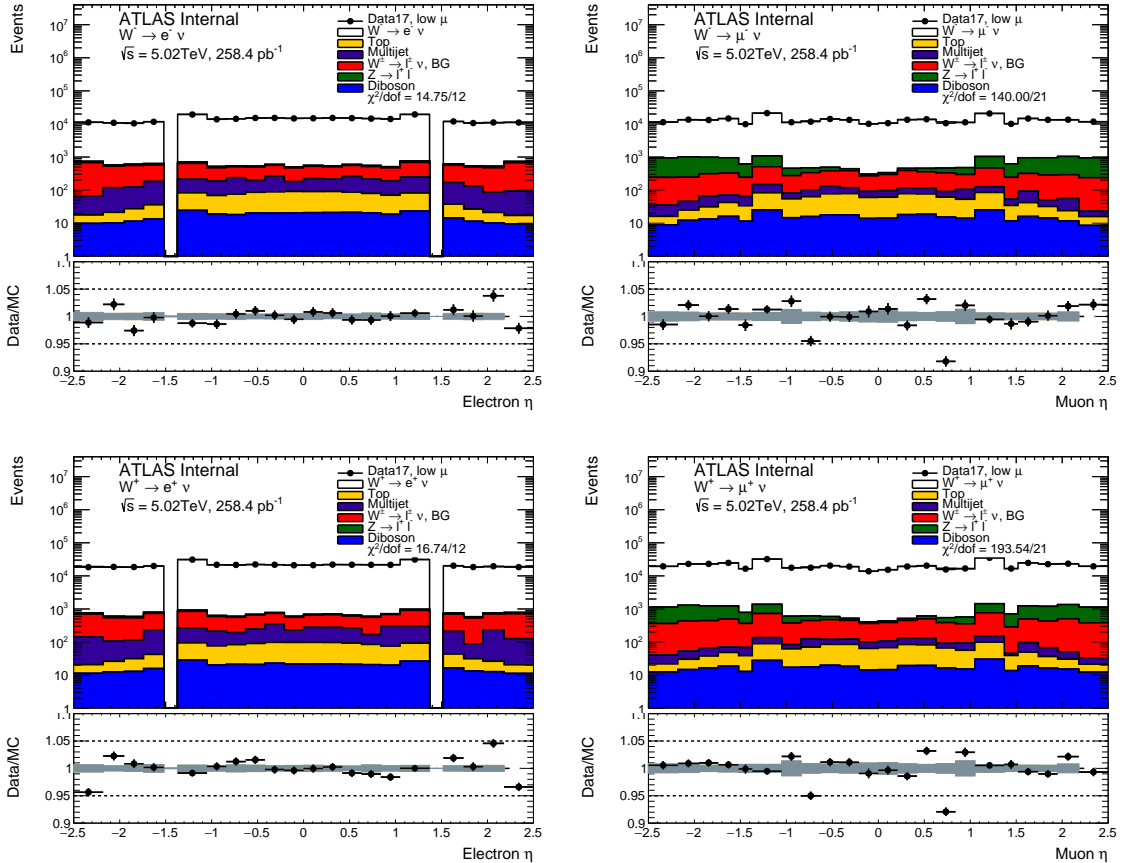
2243 **Comparison data/simulation for  $\eta_\ell$** 

FIGURE A.5: Reconstructed  $\eta_\ell$  distributions at detector level for  $\sqrt{s} = 5$  TeV data set in the fiducial phase space. The signal and backgrounds are normalised to data. The low panel gives the ratio data/MC in each bin. The green band shows the statistical and systematic uncertainties added in quadrature. The total uncertainty is dominated by the uncertainty on the efficiency corrections applied to lepton.

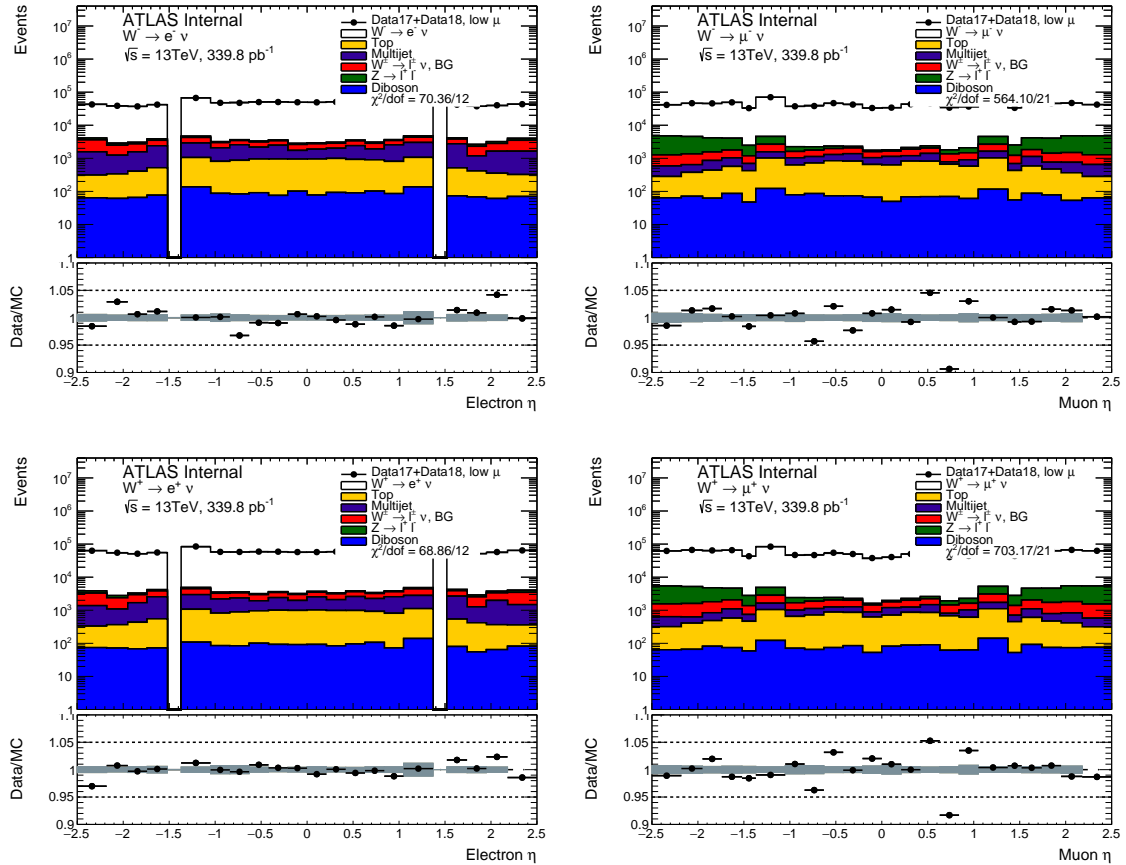


FIGURE A.6: Reconstructed  $\eta_\ell$  distributions at detector level for  $\sqrt{s} = 13$  TeV data set in the fiducial phase space. The signal and backgrounds are normalised to data. The low panel gives the ratio data/MC in each bin. The green band shows the statistical and systematic uncertainties added in quadrature. The total uncertainty is dominated by the uncertainty on the efficiency corrections applied to lepton.

2244 **Appendix B**

2245 **Breakdown of uncertainties**

2246 **Uncertainties in the measurement of  $p_T^\ell$  at detector level**

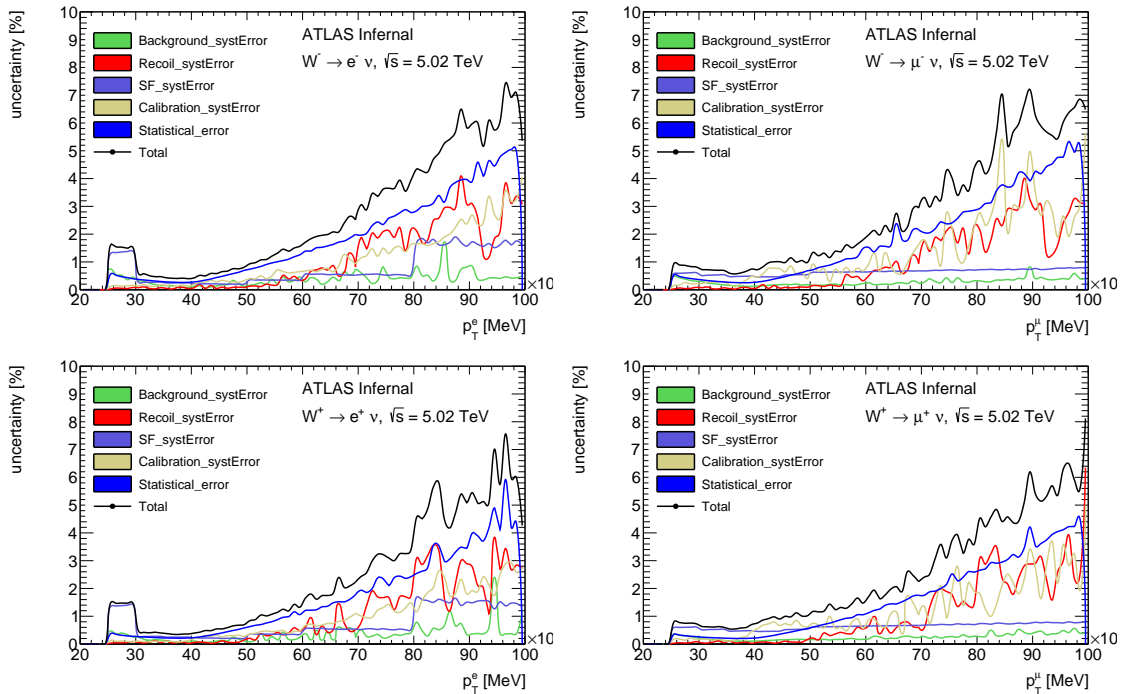


FIGURE B.1: Different sources of uncertainties on the measurement of  $p_T^\ell$  distributions at detector level for the  $\sqrt{s} = 5$  TeV data set. The total uncertainty is less than 2% at low  $p_T^\ell$  region ( $p_T^\ell < 50$  GeV) and around 6% for high  $p_T^\ell$  region ( $p_T^\ell \approx 100$  GeV). The total uncertainty is dominated by SF systematic uncertainty and the statistical uncertainty of data.

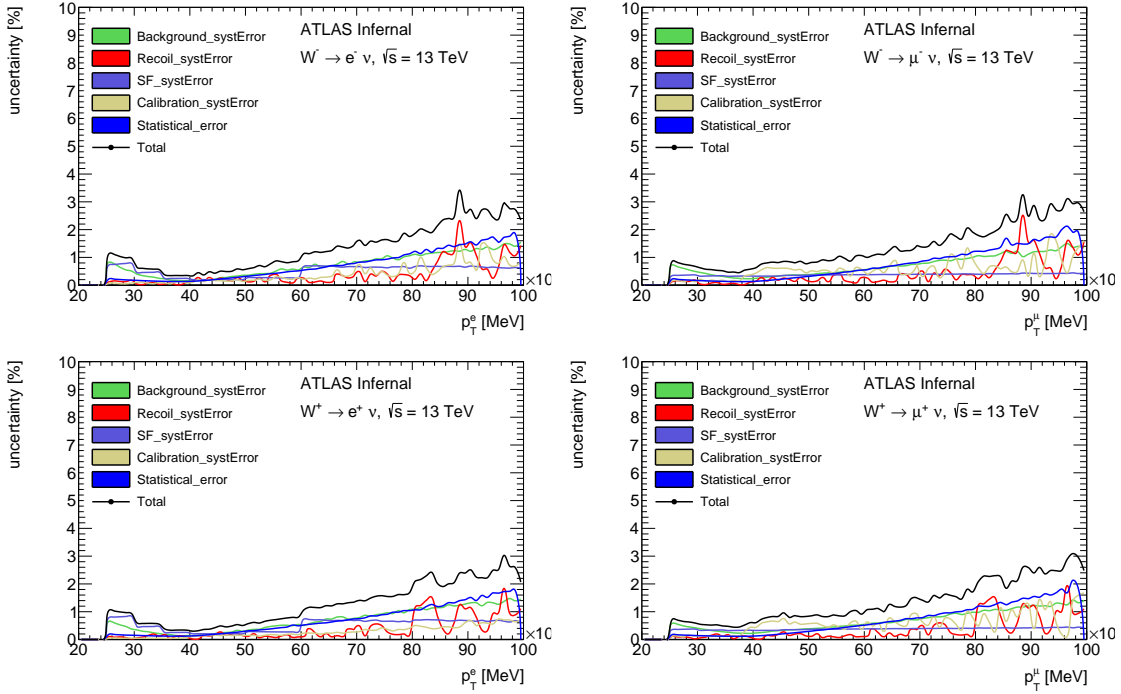


FIGURE B.2: Different sources of uncertainties on the measurement of  $p_T^\ell$  distributions at detector level for the  $\sqrt{s} = 13$  TeV data set. The total uncertainty is less than 1% at low  $p_T^\ell$  region ( $p_T^\ell < 50$  GeV) and around 3% for high  $p_T^\ell$  region ( $p_T^\ell \approx 100$  GeV). The total uncertainty is dominated by SF systematic uncertainty and the statistical uncertainty of data.

## 2247 Uncertainties in the measurement of $\eta_\ell$ at detector level

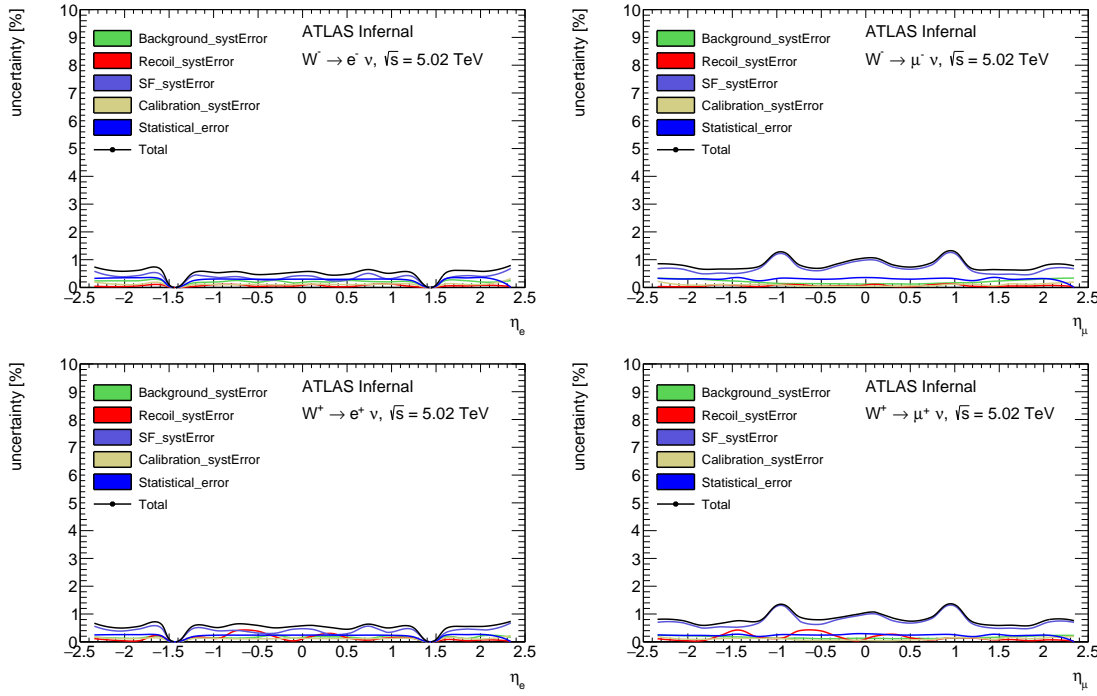


FIGURE B.3: Different sources of uncertainties on the measurement of  $\eta_\ell$  distributions at detector level for the  $\sqrt{s} = 5$  TeV data set. The total uncertainty is less than 1% and dominated by SF systematic uncertainty and the statistical uncertainty of data.

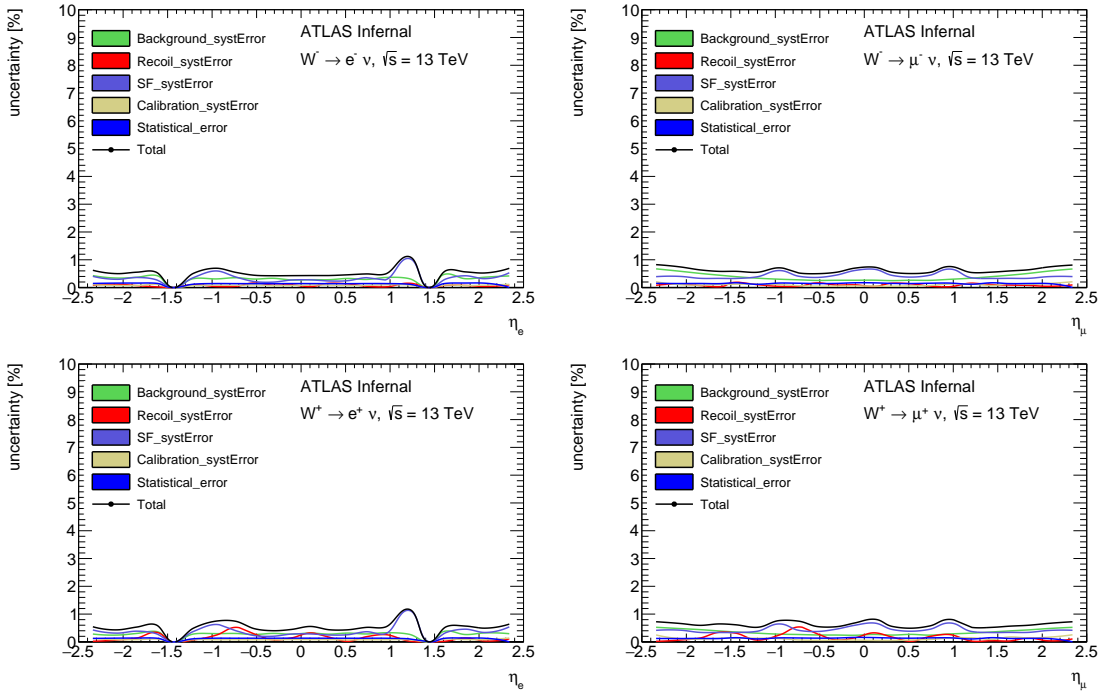


FIGURE B.4: Different sources of uncertainties on the measurement of  $\eta_\ell$  distributions at the detector level for the  $\sqrt{s} = 13$  TeV data set. The total uncertainty is less than 1% and dominated by SF systematic uncertainty and the statistical uncertainty of data.

2248 **Uncertainties in the measurement of  $p_T^W$  at detector**  
 2249 **level**

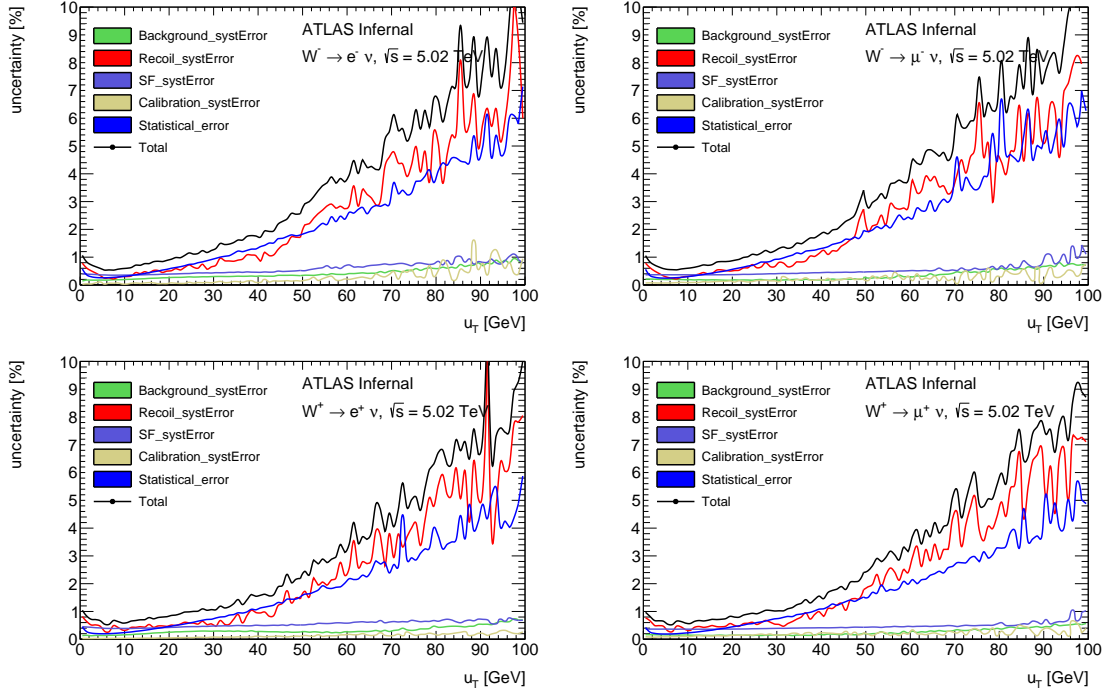


FIGURE B.5: Different sources of uncertainties in the measurement of  $p_T^W$  distributions at detector level for the  $\sqrt{s} = 5$  TeV data set. The total uncertainty is less than 1% at low  $p_T^W$  region ( $p_T^W < 30$  GeV) and around 5% for high  $p_T^W$  region ( $p_T^W \approx 100$  GeV). The total uncertainty is dominated by hadronic recoil calibration uncertainty and the statistical uncertainty of data.

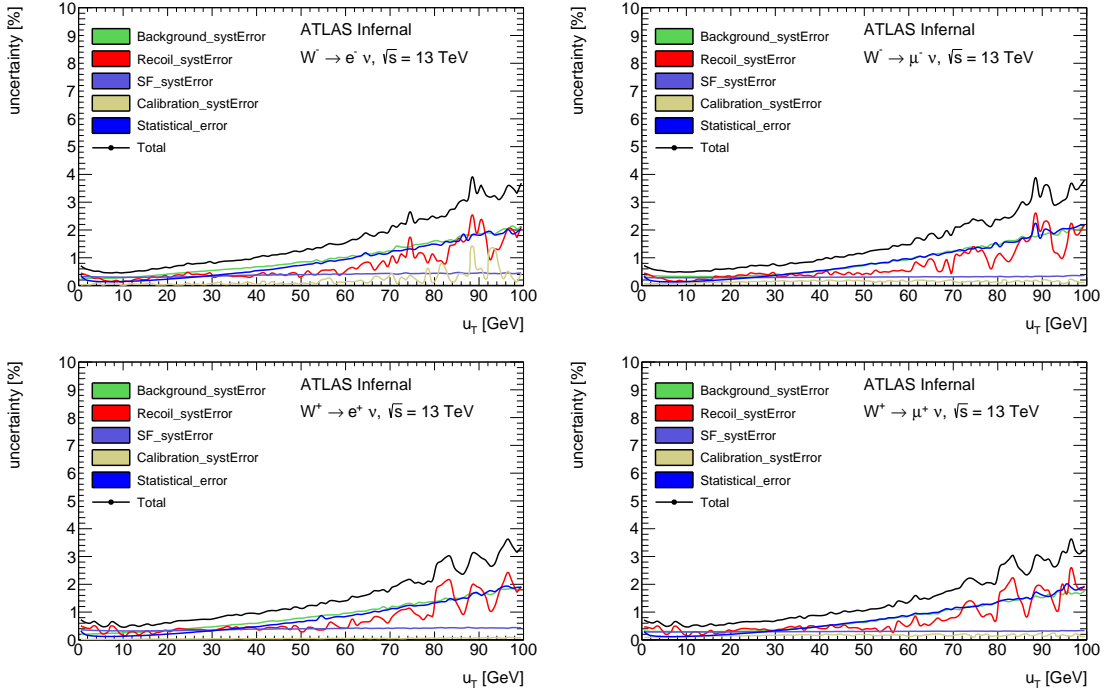


FIGURE B.6: Different sources of uncertainties on the measurement of  $p_T^W$  distributions at detector level for the  $\sqrt{s} = 13$  TeV data set. The total uncertainty is less than 1% at low  $p_T^W$  region ( $p_T^W < 30$  GeV) and around 3% for high  $p_T^W$  region ( $p_T^W \approx 100$  GeV). The total uncertainty is dominated by hadronic recoil calibration uncertainty and background uncertainty (because of the large contributions of gauge-boson pair production and top-quark production in background).

2250 **Uncertainties in the measurement of  $p_T^W$  at unfolded**  
 2251 **level**

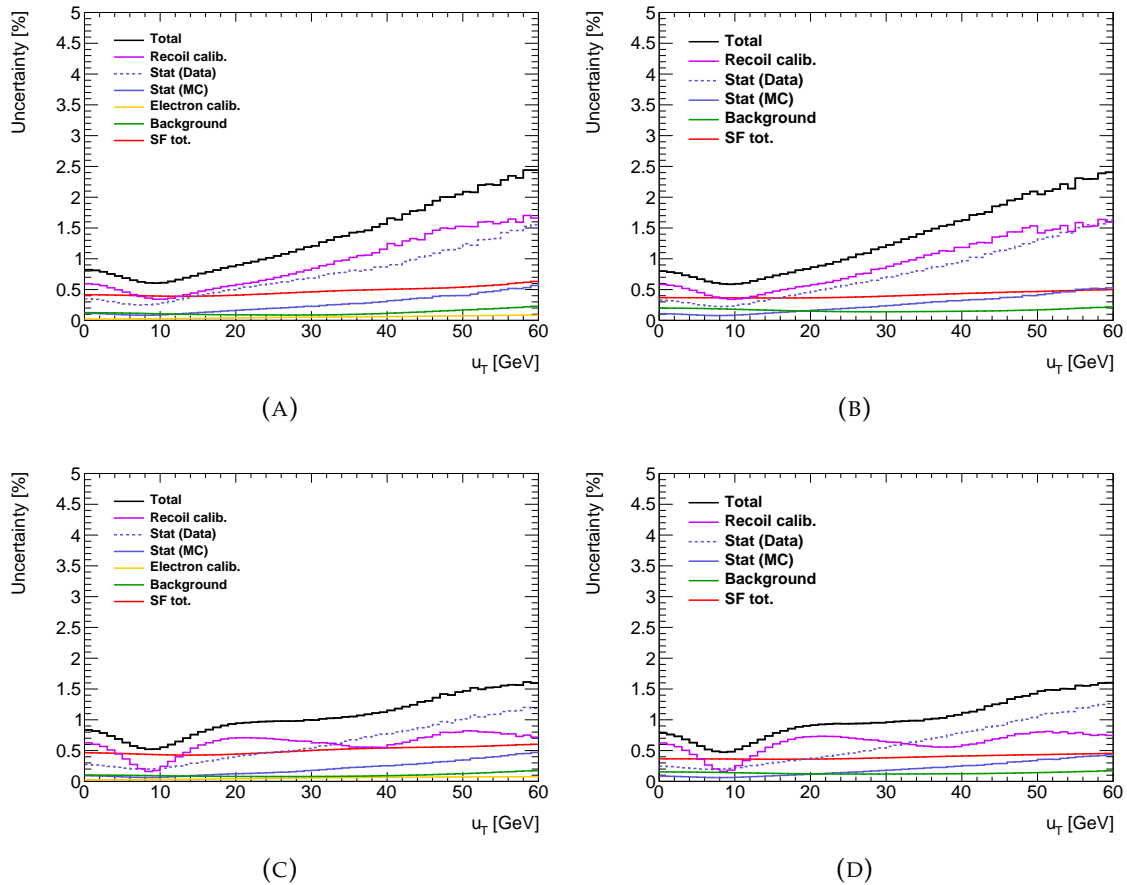


FIGURE B.7: Different sources of uncertainties on the measurement of unfolded  $p_T^W$  distributions for the  $\sqrt{s} = 5$  TeV data set, for the electron (A, B) and muon (C, D) channels. The total uncertainty is less than 1% at low  $p_T^W$  region ( $p_T^W < 30$  GeV) and around 2% for high  $p_T^W$  region ( $p_T^W \approx 60$  GeV). The total uncertainty is dominated by hadronic recoil calibration uncertainty and the statistical uncertainty of data.

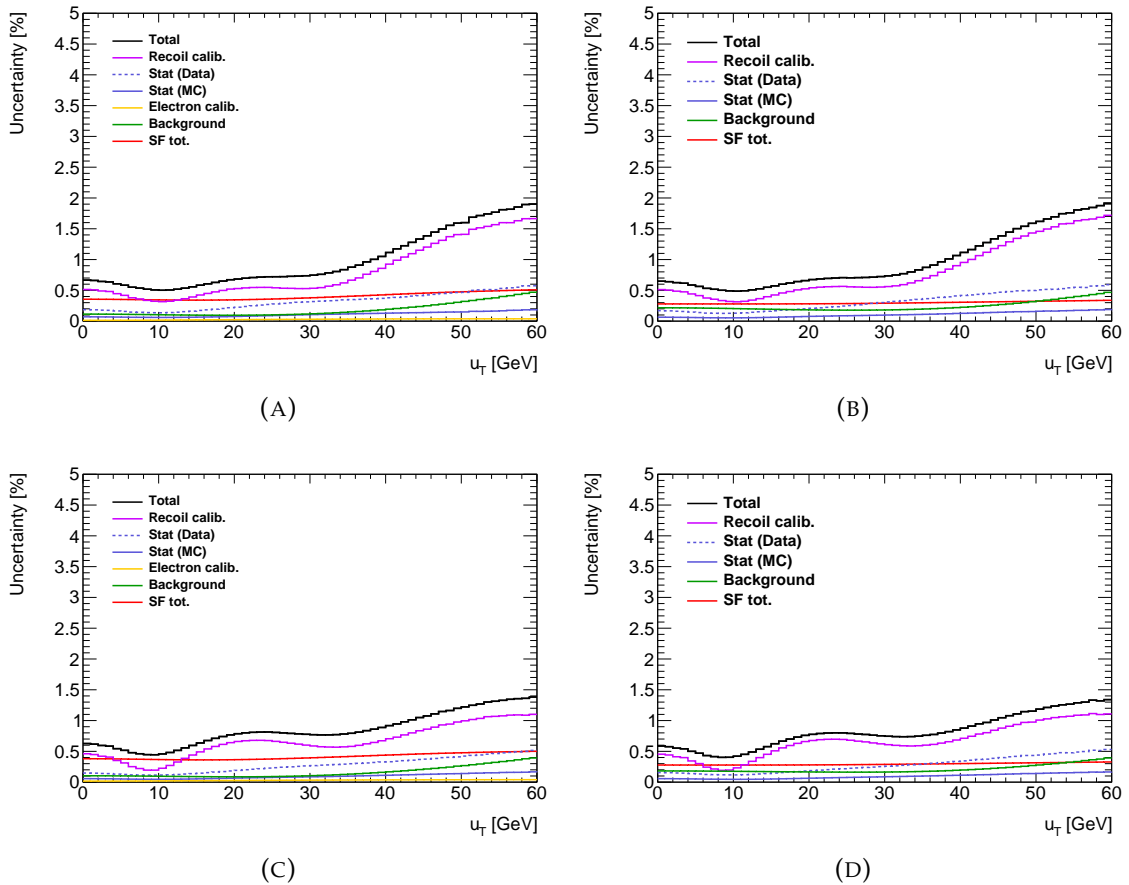


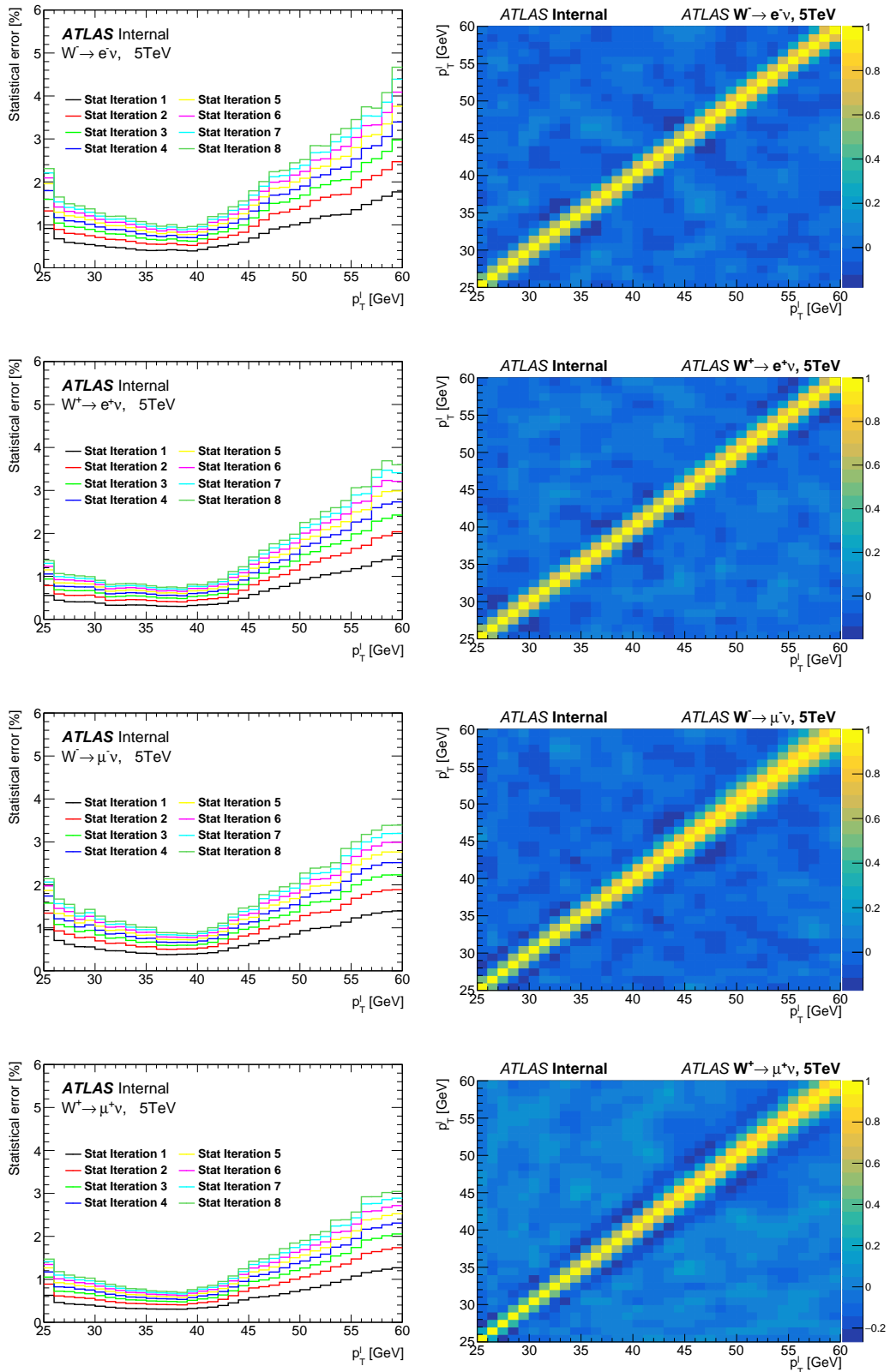
FIGURE B.8: Different sources of uncertainties on the measurement of unfolded  $p_T^W$  distributions for the  $\sqrt{s} = 13$  TeV data set, for the electron (A, B) and muon (C, D) channels. The total uncertainty is less than 1% at low  $p_T^W$  region ( $p_T^W < 30$  GeV) and around 1.5% for high  $p_T^W$  region ( $p_T^W \approx 60$  GeV). The total uncertainty is dominated by hadronic recoil calibration uncertainty and the background uncertainty.

2252 **Appendix C**

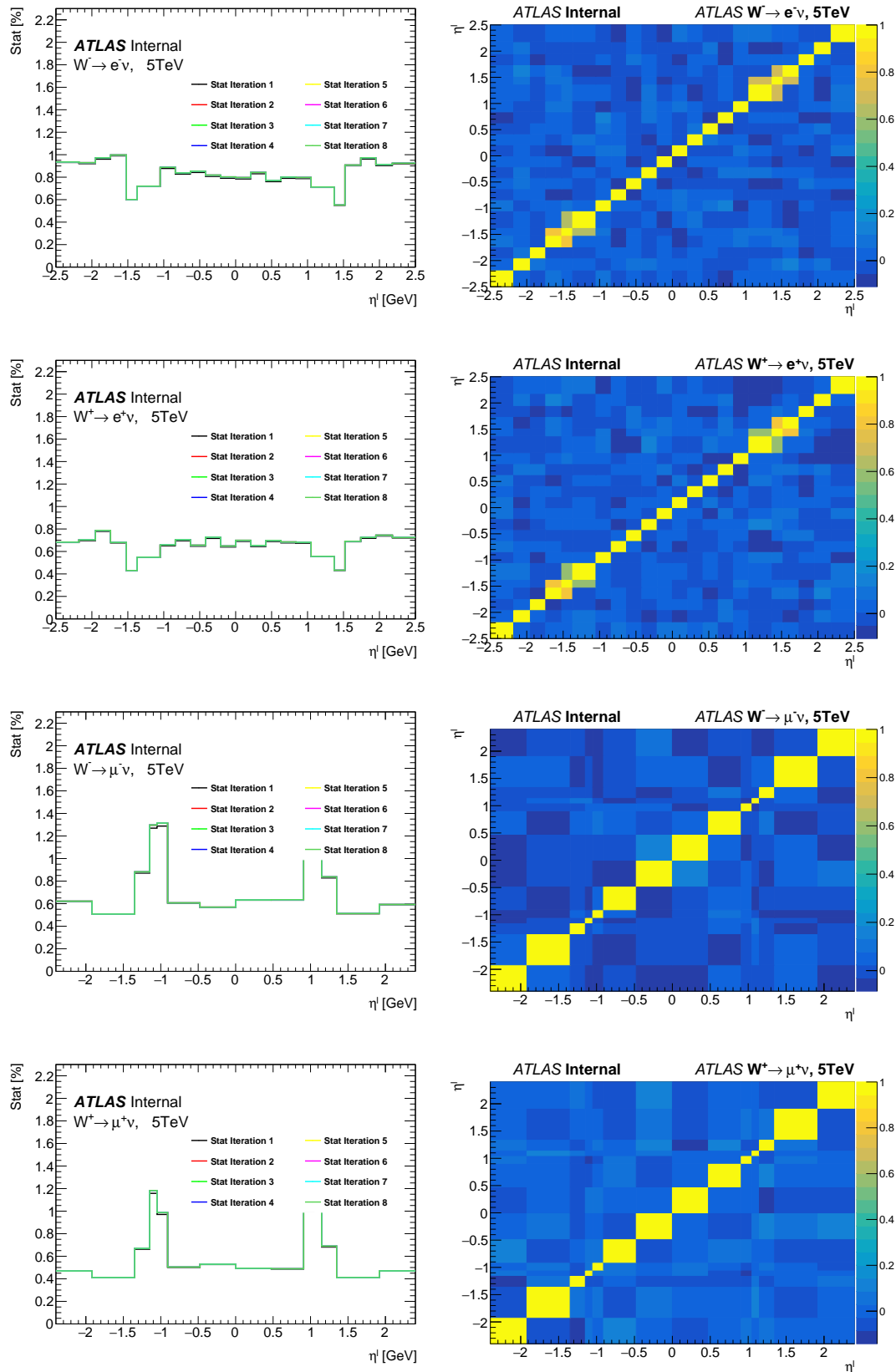
2253 **Uncertainties for the differential cross  
sections**

2254

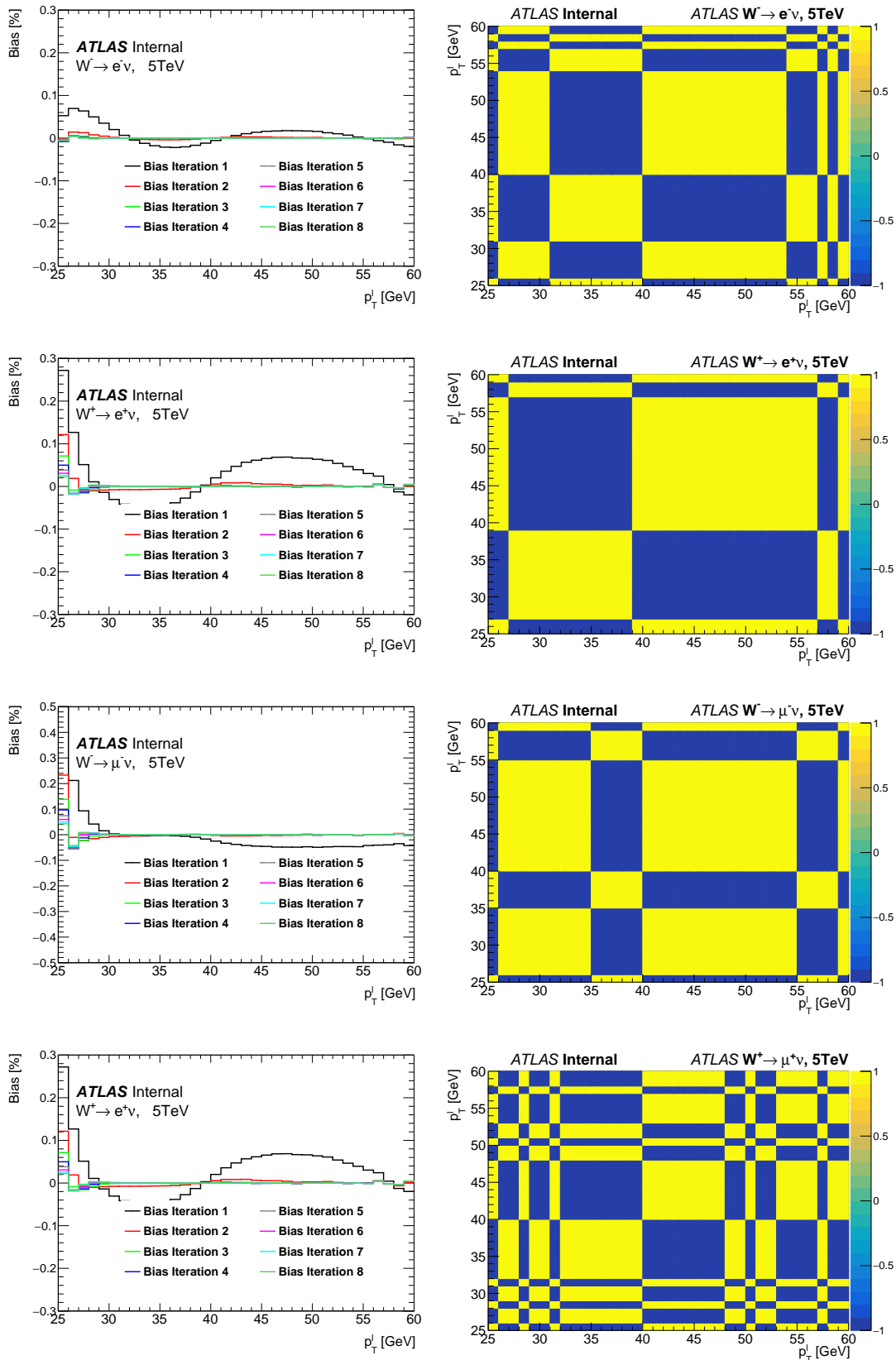
2255 **Statistical uncertainties with their correlation matrix of**  
 2256  **$p_T^\ell$  at 5 TeV**



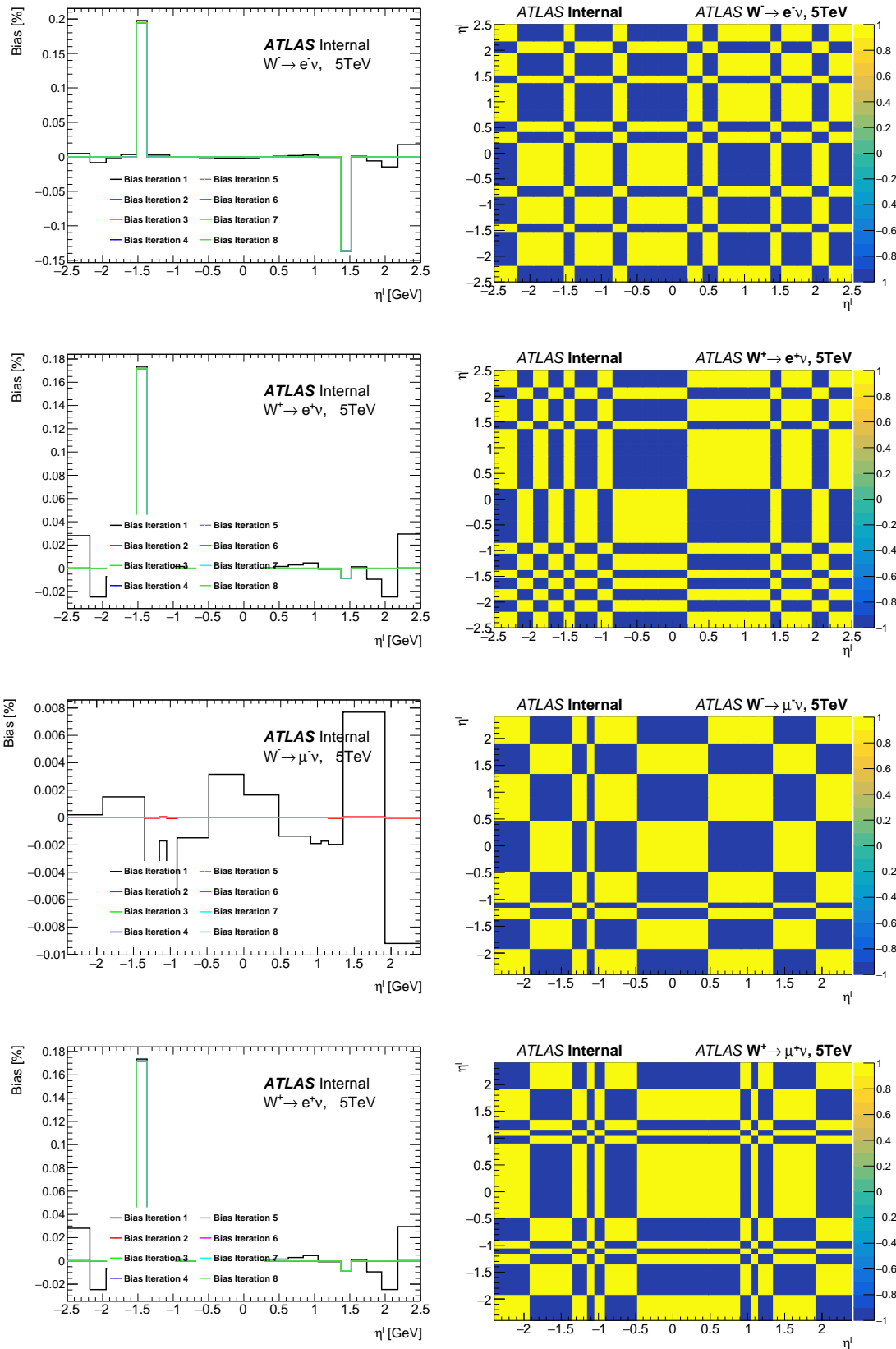
2257 **Statistical uncertainties with their correlation matrix of**  
 2258  **$\eta_\ell$  at 5 TeV**



2259 **Unfolding bias with their correlation matrix of  $p_T^\ell$  at**  
 2260 **5 TeV**



2261 **Unfolding bias with their correlation matrix of  $\eta_\ell$  at**  
 2262 **5 TeV**



2263 **Statistical uncertainties for double differential cross**  
 2264 **sections at 5 TeV**

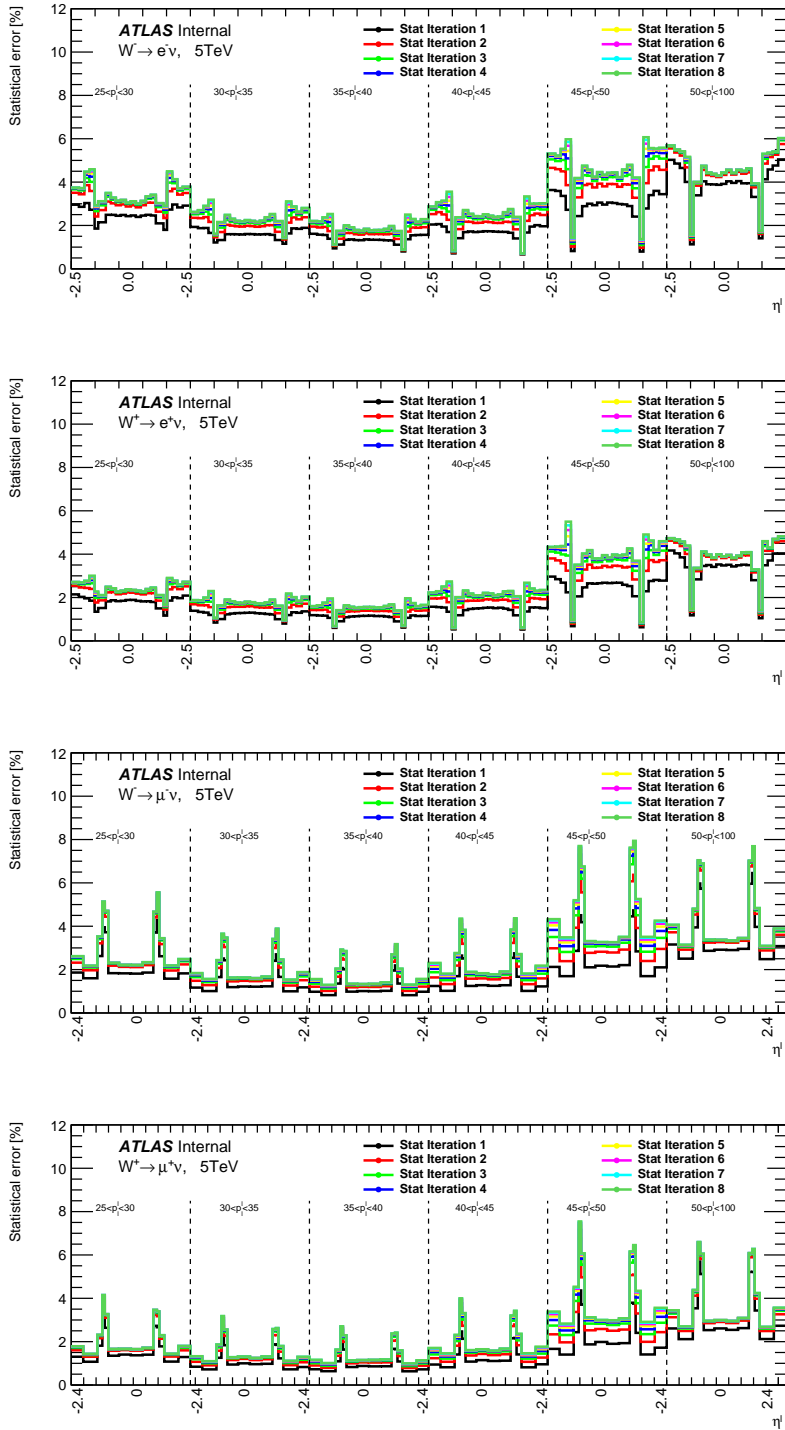


FIGURE C.1: Statistical uncertainties of unfolded distributions used for double differential cross sections at 5 TeV

2265 **Statistical uncertainties for double differential cross**  
 2266 **sections at 13 TeV**

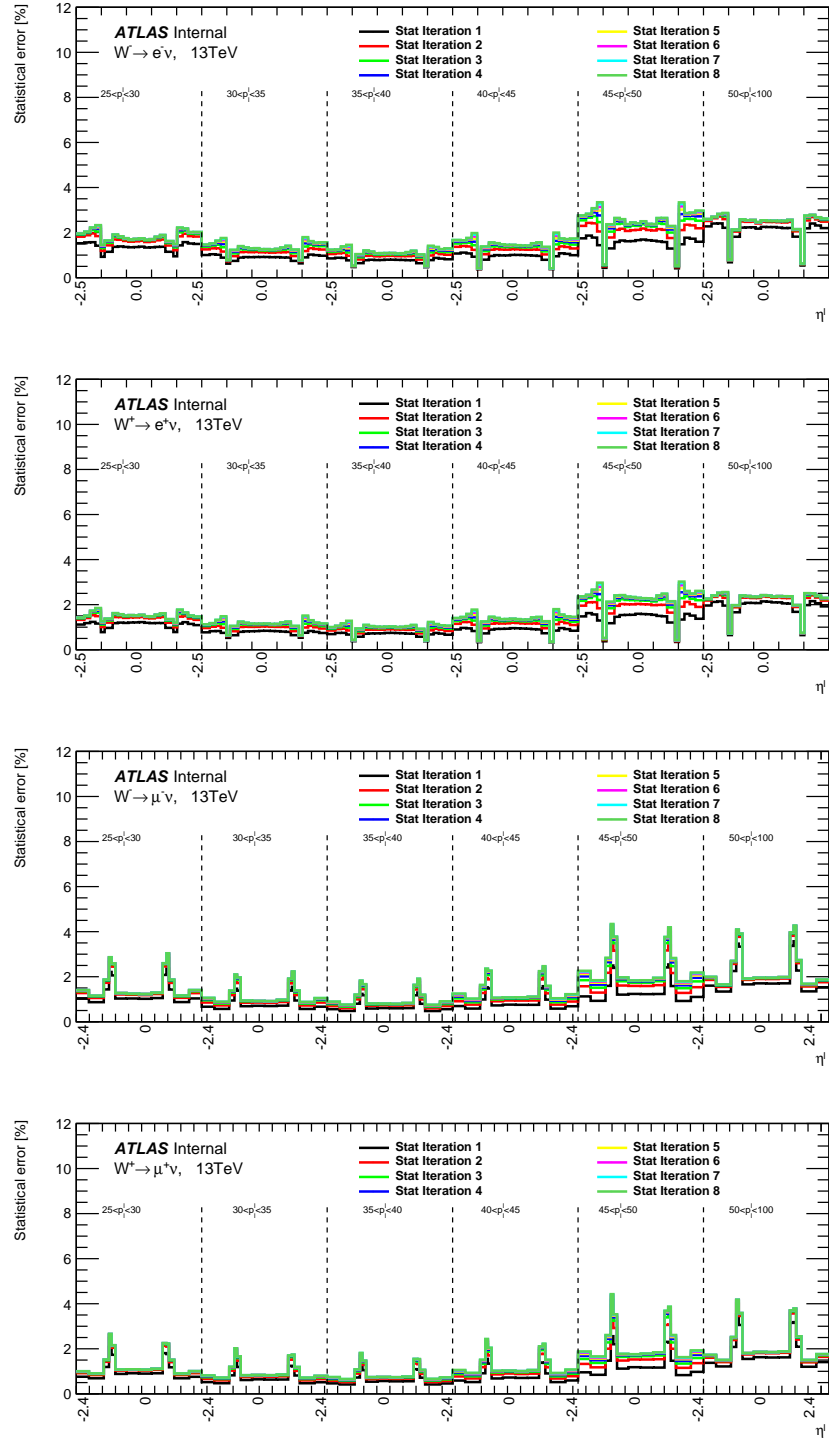


FIGURE C.2: Statistical uncertainties of unfolded distributions used for double differential cross sections at 13 TeV

2267 **Unfolding bias for double differential cross sections at**  
 2268 **5 TeV**

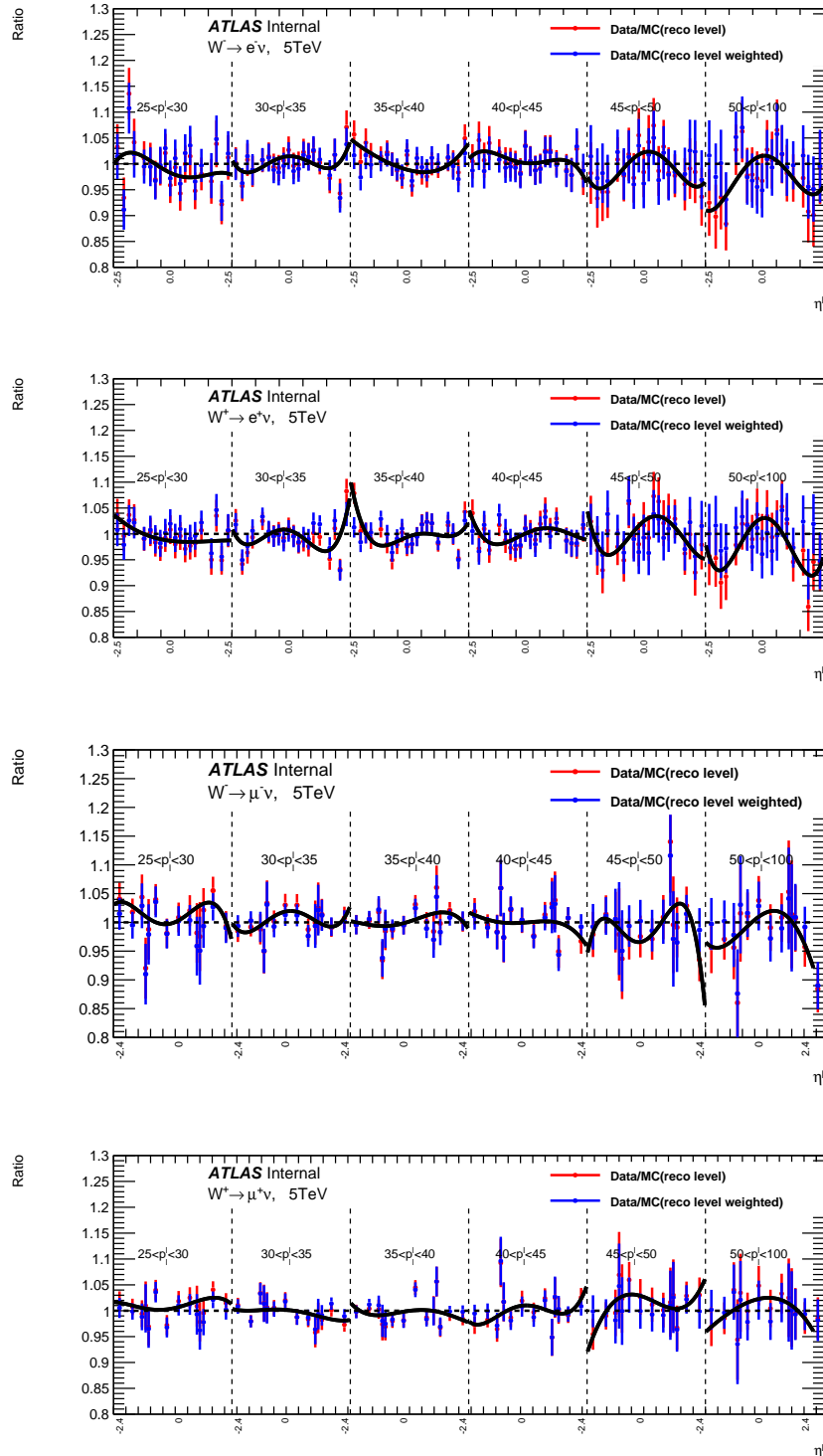


FIGURE C.3: Ratio data/MC used to calculate the unfolding bias for double differential cross sections at 5 TeV

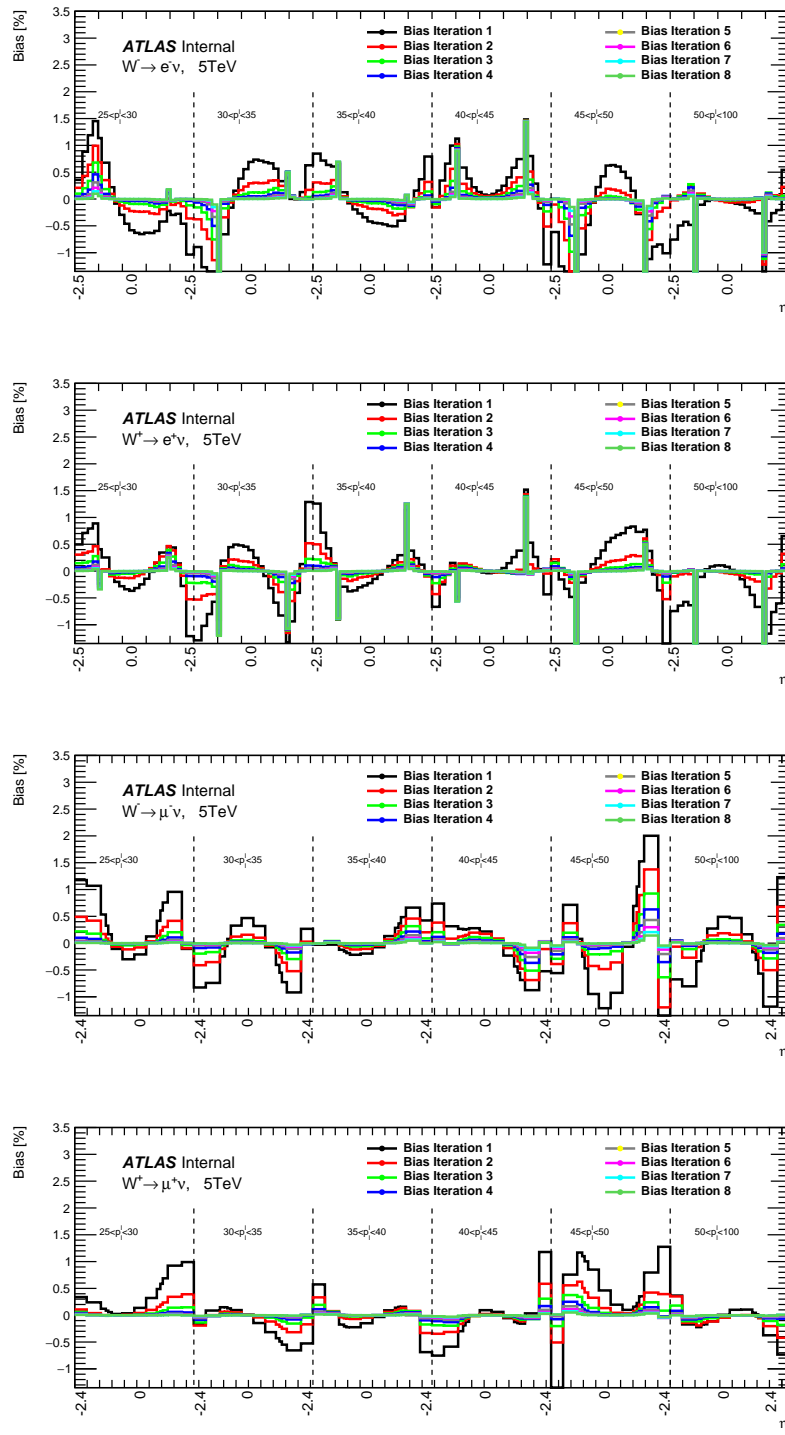


FIGURE C.4: Unfolding bias for double differential cross sections at 5 TeV

2269 **Unfolding bias for double differential cross sections at**  
 2270 **13 TeV**

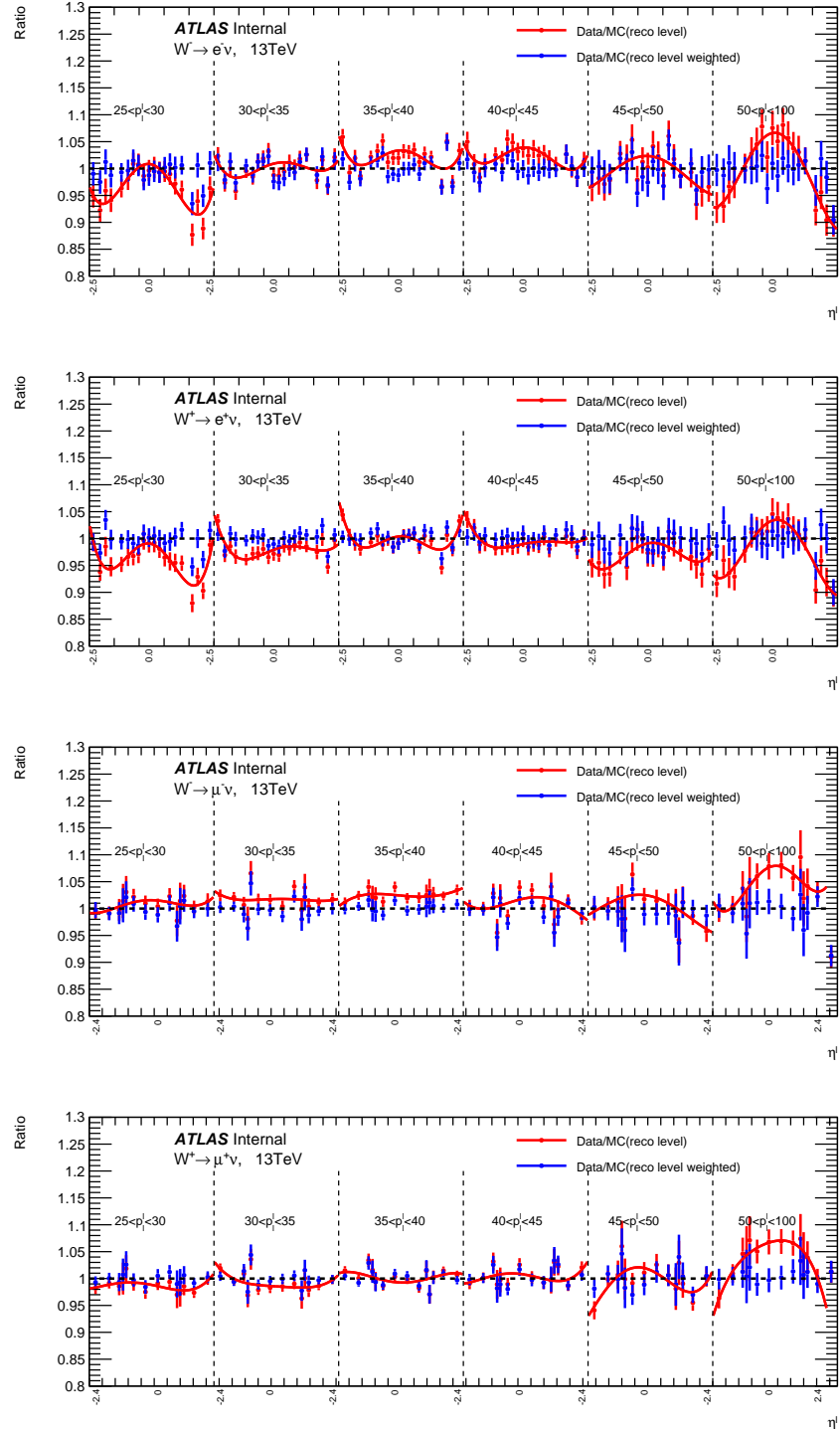


FIGURE C.5: Ratio data/MC used to calculate the unfolding bias for double differential cross sections at 13 TeV

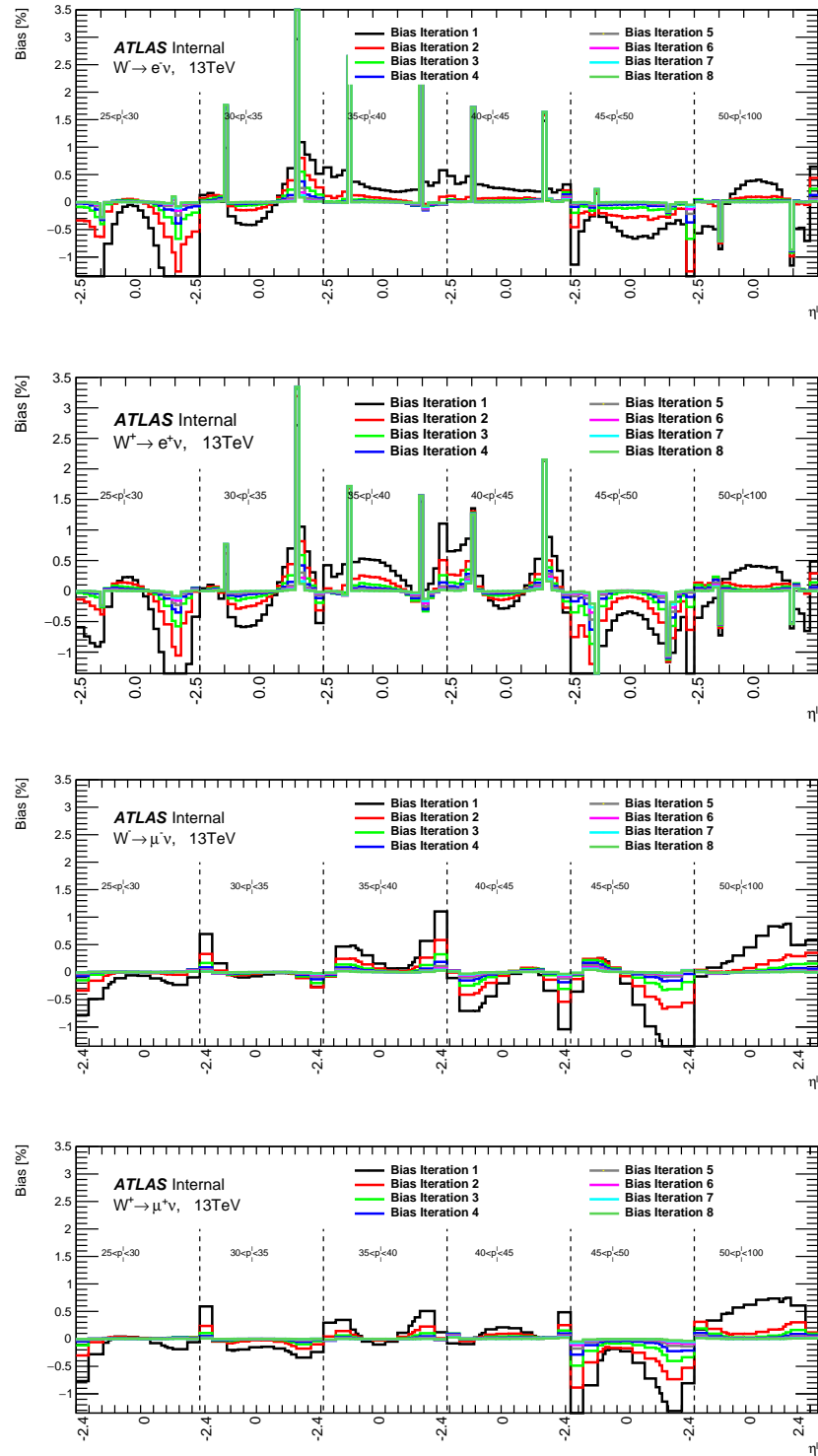


FIGURE C.6: Unfolding bias for double differential cross sections at 13 TeV



# 2272 Bibliography

2273 [1] M. Aaboud et al. "Electron efficiency measurements with the ATLAS detec-  
 2274 tor using 2012 LHC proton–proton collision data". In: *The European Physical*  
 2275 *Journal C* 77.3 (Mar. 2017). ISSN: 1434-6052. DOI: [10.1140/epjc/s10052-017-4756-2](https://doi.org/10.1140/epjc/s10052-017-4756-2). URL: <http://dx.doi.org/10.1140/epjc/s10052-017-4756-2> (cit. on p. 138).

2276 [2] Morad Aaboud et al. "Electron and photon energy calibration with the AT-  
 2277 LAS detector using 2015–2016 LHC proton-proton collision data". In: *JINST*  
 2278 14.03 (2019), P03017. DOI: [10.1088/1748-0221/14/03/P03017](https://doi.org/10.1088/1748-0221/14/03/P03017). arXiv:  
 2279 [1812.03848 \[hep-ex\]](https://arxiv.org/abs/1812.03848) (cit. on p. 42).

2280 [3] G. Aad et al. "The ATLAS Experiment at the CERN Large Hadron Col-  
 2281 llider". In: *JINST* 3 (2008), S08003. DOI: [10.1088/1748-0221/3/08/S08003](https://doi.org/10.1088/1748-0221/3/08/S08003) (cit. on p. 26).

2282 [4] G. Aad et al. "Observation of a new particle in the search for the Standard  
 2283 Model Higgs boson with the ATLAS detector at the LHC". In: *Physics Letters*  
 2284 *B* 716.1 (Sept. 2012), pp. 1–29. DOI: [10.1016/j.physletb.2012.08.020](https://doi.org/10.1016/j.physletb.2012.08.020). arXiv: [1207.7214 \[hep-ex\]](https://arxiv.org/abs/1207.7214) (cit. on p. 2).

2285 [5] Timo Antero Aaltonen et al. "Combination of CDF and D0  $W$ -Boson Mass  
 2286 Measurements". In: *Phys. Rev. D* 88.5 (2013), p. 052018. DOI: [10.1103/PhysRevD.88.052018](https://doi.org/10.1103/PhysRevD.88.052018). arXiv: [1307.7627 \[hep-ex\]](https://arxiv.org/abs/1307.7627) (cit. on p. 11).

2287 [6] Henso Abreu. "Measurement of the inclusive prompt photon cross section  
 2288 and preparation of the search of the Higgs boson decaying into two pho-  
 2289 tons with the ATLAS detector at the LHC". PhD thesis. Orsay, 2011 (cit. on  
 2290 p. 23).

2291 [7] Tim Adye. "Unfolding algorithms and tests using RooUnfold". In: *arXiv*  
 2292 *e-prints*, arXiv:1105.1160 (May 2011), arXiv:1105.1160. arXiv: [1105.1160](https://arxiv.org/abs/1105.1160)  
 2293 [*physics.data-an*] (cit. on pp. 61, 139).

2294 [8] S. Agostinelli et al. "GEANT4—a simulation toolkit". In: *Nucl. Instrum. Meth.*  
 2295 *A* 506 (2003), pp. 250–303. DOI: [10.1016/S0168-9002\(03\)01368-8](https://doi.org/10.1016/S0168-9002(03)01368-8) (cit.  
 2296 on p. 33).

2297 [9] S. Alekhin, J. Blümlein, and S. Moch. "NLO PDFs from the ABMP16 fit".  
 2298 In: *The European Physical Journal C* 78.6 (June 2018). ISSN: 1434-6052. DOI:  
 2299 [10.1140/epjc/s10052-018-5947-1](https://doi.org/10.1140/epjc/s10052-018-5947-1). URL: <http://dx.doi.org/10.1140/epjc/s10052-018-5947-1> (cit. on p. 94).

2300 [10] M Alekša and M Diemoz. *Discussion on the electromagnetic calorimeters of*  
 2301 *ATLAS and CMS*. Tech. rep. ATL-LARG-PROC-2013-002. Geneva: CERN,  
 2302 May 2013. URL: <https://cds.cern.ch/record/1547314> (cit. on  
 2303 p. 20).

2304

2305

2306

2307

2308

2309

2310 [11] J. Alitti et al. "An Improved determination of the ratio of  $W$  and  $Z$  masses  
2311 at the CERN  $\bar{p}p$  collider". In: *Phys. Lett. B* 276 (1992), pp. 354–364. DOI: [10.1016/0370-2693\(92\)90332-X](https://doi.org/10.1016/0370-2693(92)90332-X) (cit. on p. 11).

2312

2313 [12] Charalampos Anastasiou et al. "High-precision QCD at hadron colliders:  
2314 Electroweak gauge boson rapidity distributions at next-to-next-to leading  
2315 order". In: 69.9, 094008 (May 2004), p. 094008. DOI: [10.1103/PhysRevD.69.094008](https://doi.org/10.1103/PhysRevD.69.094008). arXiv: [hep-ph/0312266](https://arxiv.org/abs/hep-ph/0312266) [hep-ph] (cit. on p. 91).

2316

2317 [13] Nansi Andari. "Observation of a BEH-like boson decaying into two photons with the ATLAS detector at the LHC". PhD thesis. Orsay, LAL, Sept.  
2318 Sept. 2012 (cit. on pp. 23, 29).

2319

2320 [14] Nansi Andari. *W mass measurement*. Tech. rep. ATL-PHYS-PROC-2017-051.  
2321 Geneva: CERN, May 2017. DOI: [oai:cds.cern.ch:2264497](https://cds.cern.ch/record/2264497). URL:  
2322 <https://cds.cern.ch/record/2264497> (cit. on p. 23).

2323

2324 [15] Nansi Andari et al. *Electron and photon energy calibration with the ATLAS de-*  
2325 *tector using 2015-2017 LHC proton-proton collision data*. Tech. rep. ATL-COM-  
2326 PHYS-2018-1720. Geneva: CERN, Dec. 2018. URL: <https://cds.cern.ch/record/2651890> (cit. on pp. 37, 42, 48, 55).

2327

2328 [16] Nansi Andari et al. *Measurement of  $m_W$  at 7 TeV: Physics modeling*. Tech. rep.  
2329 ATL-COM-PHYS-2014-1436. Geneva: CERN, Nov. 2014. URL: <https://cds.cern.ch/record/1966965> (cit. on p. 12).

2330

2331 [17] Nansi Andari et al. *Measurement of  $m_W$  with 7 TeV data:  $W$  boson mass mea-*  
2332 *surement*. Tech. rep. ATL-COM-PHYS-2014-1569. Geneva: CERN, Dec. 2014.  
2333 URL: <https://cds.cern.ch/record/1976186> (cit. on pp. 11, 12, 131).

2334

2335 [18] Samir. S. Arfaoui. "The ATLAS liquid argon calorimeter high-voltage sys-  
2336 tem: commissioning, optimisation, and LHC relative luminosity mea-  
2337 surement". Theses. Université de la Méditerranée - Aix-Marseille II, Oct. 2011.  
2338 URL: <https://tel.archives-ouvertes.fr/tel-00658194> (cit. on  
2339 p. 34).

2340

2341 [19] Theodoros Argyropoulos et al. "Cathode strip chambers in ATLAS: Instal-  
2342 lation, commissioning and in situ performance". In: *IEEE Trans. Nucl. Sci.*  
2343 56 (2009), pp. 1568–1574. DOI: [10.1109/TNS.2009.2020861](https://doi.org/10.1109/TNS.2009.2020861) (cit. on  
2344 p. 26).

2345

2346 [20] A. Armbruster et al. *Practical considerations for unfolding*. Tech. rep. ATL-  
2347 COM-PHYS-2014-277. Geneva: CERN, Apr. 2014. URL: <https://cds.cern.ch/record/1694351> (cit. on p. 62).

2348

2349 [21] G. Arnison et al. "Experimental Observation of Isolated Large Transverse  
2350 Energy Electrons with Associated Missing Energy at  $s^{**}(1/2) = 540\text{-GeV}$ ".  
2351 In: *Phys. Lett. B* 122 (1983), pp. 103–116. DOI: [10.1016/0370-2693\(83\)91177-2](https://doi.org/10.1016/0370-2693(83)91177-2) (cit. on p. 11).

2352

2353 [22] ATLAS Collaboration. "Electron efficiency measurements with the AT-  
2354 LAS detector using 2012 LHC proton-proton collision data". In: *arXiv e-*  
2355 *prints*, arXiv:1612.01456 (Dec. 2016), arXiv:1612.01456. arXiv: [1612.01456](https://arxiv.org/abs/1612.01456)  
2356 [hep-ex] (cit. on pp. 79, 99).

2353 [23] ATLAS Collaboration. "Measurement of the muon reconstruction performance of the ATLAS detector using 2011 and 2012 LHC proton-proton collision data". In: *arXiv e-prints*, arXiv:1407.3935 (July 2014), arXiv:1407.3935. arXiv: [1407.3935 \[hep-ex\]](https://arxiv.org/abs/1407.3935) (cit. on p. 11).

2354

2355

2356

2357 [24] *ATLAS detector and physics performance: Technical Design Report*, 1. Technical Design Report ATLAS. Geneva: CERN, 1999. URL: <https://cds.cern.ch/record/391176> (cit. on p. 17).

2358

2359

2360 [25] *ATLAS Liquid Argon Calorimeter Phase-I Upgrade Technical Design Report*. Tech. rep. CERN-LHCC-2013-017. ATLAS-TDR-022. Final version presented to December 2013 LHCC. Sept. 2013. URL: <https://cds.cern.ch/record/1602230> (cit. on p. 24).

2361

2362

2363

2364 [26] *ATLAS liquid-argon calorimeter: Technical Design Report*. Technical Design Report ATLAS. Geneva: CERN, 1996. URL: <https://cds.cern.ch/record/331061> (cit. on pp. 22, 23).

2365

2366

2367 [27] Hicham Atmani et al. *Measurement of the  $p_T$  spectrum of  $W$ - and  $Z$ -bosons produced in  $pp$  collisions at  $\sqrt{s} = 5$  TeV and 13 TeV in low-pileup runs*. Tech. rep. ATL-COM-PHYS-2018-1084. Geneva: CERN, July 2018. URL: <https://cds.cern.ch/record/2632159> (cit. on pp. 97, 99).

2368

2369

2370

2371 [28] M. Baak et al. "The global electroweak fit at NNLO and prospects for the LHC and ILC". In: *European Physical Journal C* 74, 3046 (Sept. 2014), p. 3046. DOI: [10.1140/epjc/s10052-014-3046-5](https://doi.org/10.1140/epjc/s10052-014-3046-5). arXiv: [1407.3792 \[hep-ph\]](https://arxiv.org/abs/1407.3792) (cit. on p. 10).

2372

2373

2374

2375 [29] M. Banner et al. "Observation of Single Isolated Electrons of High Transverse Momentum in Events with Missing Transverse Energy at the CERN anti-p p Collider". In: *Phys. Lett. B* 122 (1983), pp. 476–485. DOI: [10.1016/0370-2693\(83\)91605-2](https://doi.org/10.1016/0370-2693(83)91605-2) (cit. on p. 11).

2376

2377

2378

2379 [30] J Beacham et al. "Physics beyond colliders at CERN: beyond the Standard Model working group report". In: *Journal of Physics G: Nuclear and Particle Physics* 47.1 (Dec. 2019), p. 010501. ISSN: 1361-6471. DOI: [10.1088/1361-6471/ab4cd2](https://doi.org/10.1088/1361-6471/ab4cd2). URL: [http://dx.doi.org/10.1088/1361-6471/ab4cd2](https://dx.doi.org/10.1088/1361-6471/ab4cd2) (cit. on p. 15).

2380

2381

2382

2383

2384 [31] Cyril Pascal Becot. "Diphoton lineshape of the BEH boson using the ATLAS detector at the LHC: calibration, mass, width and interferences". PhD thesis. Diderot U., Paris, Sept. 2015 (cit. on pp. 23, 42).

2385

2386

2387 [32] V. A. Bednyakov, N. D. Giokaris, and A. V. Bednyakov. "On the Higgs mass generation mechanism in the Standard Model". In: *Physics of Particles and Nuclei* 39.1 (Jan. 2008), pp. 13–36. DOI: [10.1007/s11496-008-1002-9](https://doi.org/10.1007/s11496-008-1002-9). arXiv: [hep-ph/0703280 \[hep-ph\]](https://arxiv.org/abs/hep-ph/0703280) (cit. on p. 6).

2388

2389

2390

2391 [33] W. Beenakker, F. A. Berends, and A. P. Chapovsky. "Final-state radiation and line-shape distortion in resonance pair production". In: *Physics Letters B* 435.1-2 (Sept. 1998), pp. 233–239. DOI: [10.1016/S0370-2693\(98\)00760-6](https://doi.org/10.1016/S0370-2693(98)00760-6). arXiv: [hep-ph/9805327 \[hep-ph\]](https://arxiv.org/abs/hep-ph/9805327) (cit. on p. 12).

2392

2393

2394

2395 [34] Arnd Behring et al. "Mixed QCD-electroweak corrections to W-boson  
2396 production in hadron collisions". In: (Sept. 2020). arXiv: 2009 . 10386  
2397 [hep-ph] (cit. on p. 91).

2398 [35] Jacob D. Bekenstein and Bibhas Ranjan Majhi. "Is the principle of least ac-  
2399 tion a must?" In: *Nuclear Physics B* 892 (Mar. 2015), pp. 337–352. DOI: 10 .  
2400 1016/j.nuclphysb.2015.01.015. arXiv: 1411 . 2424 [hep-th] (cit.  
2401 on p. 3).

2402 [36] Carsten Bittrich et al. *In-situ scale factors from Zee events*. Tech. rep. ATL-  
2403 COM-PHYS-2017-757. Geneva: CERN, June 2017. URL: <https://cds.cern.ch/record/2268800> (cit. on pp. 37, 46).

2405 [37] Serguei I. Bityukov. "Signal Significance in the Presence of Systematic and  
2406 Statistical Uncertainties". In: *Journal of High Energy Physics* 2002.9, 060 (Sept.  
2407 2002), p. 060. DOI: 10 . 1088/1126-6708/2002/09/060. arXiv: hep-  
2408 ph/0207130 [hep-ph] (cit. on p. 64).

2409 [38] J-B Blanchard, J-B de Vivie, and P Mastrandrea. *In situ scales and smear-  
2410 ings from Z and J/Ψ events*. Tech. rep. ATL-COM-PHYS-2013-1653. Geneva:  
2411 CERN, Dec. 2013. URL: <https://cds.cern.ch/record/1637533> (cit.  
2412 on pp. 37, 57).

2413 [39] Jorge de Blas et al. "The Global Electroweak and Higgs Fits in the LHC  
2414 era". In: *PoS EPS-HEP2017* (2017). Ed. by Paolo Checchia et al., p. 467. DOI:  
2415 10 . 22323/1 . 314 . 0467. arXiv: 1710 . 05402 [hep-ph] (cit. on p. 10).

2416 [40] Volker Blobel. "Unfolding Methods in Particle Physics". In: (Jan. 2011), 240–  
2417 251. 12 p. DOI: 10 . 5170/CERN-2011-006 . 240. URL: <https://cds.cern.ch/record/2203257> (cit. on p. 59).

2419 [41] Maarten Boonekamp and Jean-Baptiste Blanchard. *Measurement of  $m_W$  at 7  
2420 TeV: Electron performance corrections and uncertainties*. Tech. rep. ATL-COM-  
2421 PHYS-2014-1434. Geneva: CERN, Nov. 2014. URL: <https://cds.cern.ch/record/1966963> (cit. on pp. 11, 46, 57).

2423 [42] Maximilien Brice and Claudia Marcelloni. "View of the Detector ATLAS  
2424 open." Feb. 2007. URL: <https://cds.cern.ch/record/1206860> (cit.  
2425 on p. 18).

2426 [43] Andrew Buckley. *ATLAS Pythia 8 tunes to 7 TeV data*. Tech. rep. Dec. 2014,  
2427 p. 29 (cit. on p. 77).

2428 [44] C.Wang. "presentation at the egamma calibration meeting". In: (Sept.  
2429 2020). URL: <https://indico.cern.ch/event/957069/contributions/4031631/attachments/2108689/3546663/ElectronCalibration.pdf> (cit. on p. 57).

2432 [45] Stefano Camarda et al. "DYTurbo: fast predictions for Drell–Yan processes".  
2433 In: *The European Physical Journal C* 80.3 (Mar. 2020). ISSN: 1434-6052. DOI:  
2434 10 . 1140/epjc/s10052-020-7757-5. URL: <http://dx.doi.org/10.1140/epjc/s10052-020-7757-5> (cit. on pp. 94, 121).

2436 [46] John M. Campbell, J.W. Huston, and W.J. Stirling. "Hard Interactions of  
2437 Quarks and Gluons: A Primer for LHC Physics". In: *Rept. Prog. Phys.* 70  
2438 (2007), p. 89. DOI: [10.1088/0034-4885/70/1/R02](https://doi.org/10.1088/0034-4885/70/1/R02). arXiv: [hep-ph/0611148](https://arxiv.org/abs/hep-ph/0611148) (cit. on p. 8).

2440 [47] Leonor Cerdá Alberich. *Photon and electron identification with the ATLAS de-*  
2441 *tector.* Tech. rep. ATL-PHYS-PROC-2016-230. Geneva: CERN, Nov. 2016.  
2442 DOI: [10.22323/1.282.1235](https://doi.org/10.22323/1.282.1235). URL: <https://cds.cern.ch/record/2233097> (cit. on p. 138).

2444 [48] Olmo Cerri. "Hadronic recoil in the W boson production at LHC for a  
2445 W mass measurement with the CMS experiment". Presented 20 Sep 2017.  
2446 2017. URL: <https://cds.cern.ch/record/2285935> (cit. on p. 11).

2447 [49] Georgios Choudalakis. "Fully Bayesian Unfolding". In: 2012 (cit. on p. 59).

2448 [50] P.J. Clark. "The ATLAS Detector Simulation". In: *Nuclear Physics B - Pro-*  
2449 *ceedings Supplements* 215.1 (2011). Proceedings of the 12th Topical Seminar  
2450 on Innovative Particle and Radiation Detectors (IPRD10), pp. 85–88. ISSN:  
2451 0920-5632. DOI: <https://doi.org/10.1016/j.nuclphysbps.2011.03.142>. URL: <http://www.sciencedirect.com/science/article/pii/S092056321100212X> (cit. on p. 17).

2454 [51] W.E. Cleland and E.G. Stern. "Signal processing considerations for liquid  
2455 ionization calorimeters in a high rate environment". In: *Nuclear Instruments*  
2456 *and Methods in Physics Research Section A: Accelerators, Spectrometers, Detec-*  
2457 *tors and Associated Equipment* 338.2 (1994), pp. 467–497. ISSN: 0168-9002.  
2458 DOI: [https://doi.org/10.1016/0168-9002\(94\)91332-3](https://doi.org/10.1016/0168-9002(94)91332-3).  
2459 URL: <http://www.sciencedirect.com/science/article/pii/0168900294913323> (cit. on p. 29).

2461 [52] The ATLAS Collaboration. "The ATLAS Experiment at the CERN Large  
2462 Hadron Collider". In: *Journal of Instrumentation* 3.08 (Aug. 2008), S08003–  
2463 S08003. DOI: [10.1088/1748-0221/3/08/s08003](https://doi.org/10.1088/1748-0221/3/08/s08003). URL: <https://doi.org/10.1088/1748-0221/3/08/s08003> (cit. on  
2464 p. 17).

2466 [53] The NNPDF Collaboration et al. *Parton distributions from high-precision col-*  
2467 *lider data.* 2017. arXiv: [1706.00428 \[hep-ph\]](https://arxiv.org/abs/1706.00428) (cit. on p. 94).

2468 [54] *Computation and validation of the electronic calibration constants for the ATLAS*  
2469 *Liquid Argon Calorimeters.* Tech. rep. ATL-LARG-INT-2010-007. Geneva:  
2470 CERN, July 2010. URL: <https://cds.cern.ch/record/1278462>  
2471 (cit. on p. 28).

2472 [55] G. D'Agostini. *Improved iterative Bayesian unfolding.* 2010. arXiv: [1010.0632 \[physics.data-an\]](https://arxiv.org/abs/1010.0632) (cit. on pp. 59, 99).

2474 [56] G. D'Agostini. "Improved iterative Bayesian unfolding". In: *arXiv e-*  
2475 *prints*, arXiv:1010.0632 (Oct. 2010), arXiv:1010.0632. arXiv: [1010.0632](https://arxiv.org/abs/1010.0632)  
2476 [physics.data-an] (cit. on p. 61).

2477 [57] Delgove David. “presentation at the egamma calibration meeting”. In:  
 2478 (Mar. 2019). URL: <https://indico.cern.ch/event/804207/contributions/3353868/attachments/1811758/2959326/Linearity.pdf> (cit. on p. 57).

2481 [58] W. de Boer. “Precision Experiments at LEP”. In: *60 YEARS OF CERN EXPERIMENTS AND DISCOVERIES*. Edited by SCHOPPER HERWIG ET AL. Published by World Scientific Publishing Co. Pte. Ltd 23 (July 2015), pp. 107–136. DOI: [10.1142/9789814644150\\_0005](https://doi.org/10.1142/9789814644150_0005). arXiv: [1509.06050](https://arxiv.org/abs/1509.06050) [hep-ex] (cit. on p. 34).

2486 [59] *Design Report Tevatron 1 project*. Tech. rep. FERMILAB-DESIGN-1984-01. 1984. URL: <https://cds.cern.ch/record/1478620> (cit. on p. 11).

2488 [60] Luigi Di Lella and Carlo Rubbia. “The Discovery of the W and Z Particles”. In: *Adv. Ser. Dir. High Energy Phys.* 23 (2015), pp. 137–163. DOI: [10.1142/9789814644150\\_0006](https://doi.org/10.1142/9789814644150_0006). URL: <https://cds.cern.ch/record/2103277> (cit. on p. 11).

2492 [61] Günther Dissertori. “The Determination of the Strong Coupling Constant”. In: *The Standard Theory of Particle Physics: Essays to Celebrate CERN’s 60th Anniversary*. Ed. by Luciano Maiani and et al. Oct. 2016, pp. 113–128. DOI: [10.1142/9789814733519\\_0006](https://doi.org/10.1142/9789814733519_0006). arXiv: [1506.05407](https://arxiv.org/abs/1506.05407) [hep-ex] (cit. on p. 5).

2497 [62] Stefan Dittmaier, Timo Schmidt, and Jan Schwarz. “Mixed NNLO QCD  $\times$  electroweak corrections of  $\mathcal{O}(N_f \alpha_s \alpha)$  to single-W/Z production at the LHC”. In: (Sept. 2020). arXiv: [2009.02229](https://arxiv.org/abs/2009.02229) [hep-ph] (cit. on p. 91).

2500 [63] Daniel Dominguez. “Standard Model. Le modèle standard”. In: (Mar. 2015). General Photo. URL: <https://cds.cern.ch/record/2002395> (cit. on p. 2).

2503 [64] Claude Duhr, Falko Dulat, and Bernhard Mistlberger. “Charged Current Drell-Yan Production at N<sup>3</sup>LO”. In: (July 2020). arXiv: [2007.13313](https://arxiv.org/abs/2007.13313) [hep-ph] (cit. on p. 91).

2506 [65] Sayipjamal Dulat et al. “New parton distribution functions from a global analysis of quantum chromodynamics”. In: *Phys. Rev. D* 93.3 (2016), p. 033006. DOI: [10.1103/PhysRevD.93.033006](https://doi.org/10.1103/PhysRevD.93.033006). arXiv: [1506.07443](https://arxiv.org/abs/1506.07443) [hep-ph] (cit. on p. 8).

2510 [66] Miguel G. Echevarria, Ahmad Idilbi, and Ignazio Scimemi. “Factorization Theorem For Drell-Yan At Low q\_T And Transverse Momentum Distributions On-The-Light-Cone”. In: *JHEP* 07 (2012), p. 002. DOI: [10.1007/JHEP07\(2012\)002](https://doi.org/10.1007/JHEP07(2012)002). arXiv: [1111.4996](https://arxiv.org/abs/1111.4996) [hep-ph] (cit. on p. 8).

2514 [67] “Electron and photon energy calibration with the ATLAS detector using LHC Run 1 data”. In: *European Physical Journal C* 74, 3071 (Oct. 2014), p. 3071. DOI: [10.1140/epjc/s10052-014-3071-4](https://doi.org/10.1140/epjc/s10052-014-3071-4). arXiv: [1407.5063](https://arxiv.org/abs/1407.5063) [hep-ex] (cit. on pp. 11, 33, 34, 46).

2518 [68] “Electron and photon performance measurements with the ATLAS detector  
2519 using the 20152017 LHC proton-proton collision data”. In: *Journal of Instru-*  
2520 *mentation* 14.12 (Dec. 2019), P12006. DOI: [10.1088/1748-0221/14/12/P12006](https://doi.org/10.1088/1748-0221/14/12/P12006). arXiv: [1908.00005](https://arxiv.org/abs/1908.00005) [hep-ex] (cit. on p. 31).

2522 [69] *Electron and photon reconstruction and performance in ATLAS using a dynami-*  
2523 *cal, topological cell clustering-based approach*. Tech. rep. ATL-PHYS-PUB-2017-  
2524 022. Geneva: CERN, Dec. 2017. URL: <https://cds.cern.ch/record/2298955> (cit. on pp. 29, 30).

2526 [70] *Energy Resolution of the Barrel of the CMS Electromagnetic Calorimeter*. Tech.  
2527 rep. CMS-NOTE-2006-148. Geneva: CERN, Nov. 2006. DOI: [10.1088/1748-0221/2/04/P04004](https://doi.org/10.1088/1748-0221/2/04/P04004). URL: <https://cds.cern.ch/record/1009081> (cit. on p. 22).

2530 [71] Jens Erler and Matthias Schott. “Electroweak precision tests of the Standard  
2531 Model after the discovery of the Higgs boson”. In: *Progress in Particle and*  
2532 *Nuclear Physics* 106 (May 2019), pp. 68–119. DOI: [10.1016/j.ppnp.2019.02.007](https://doi.org/10.1016/j.ppnp.2019.02.007). arXiv: [1902.05142](https://arxiv.org/abs/1902.05142) [hep-ph] (cit. on p. 2).

2534 [72] “Experimental observation of isolated large transverse energy electrons  
2535 with associated missing energy at  $\sqrt{s} = 540\text{GeV}$ ”. In: *Phys. Lett. B*  
2536 122.CERN-EP-83-13 (Jan. 1983), 103–116. 31 p. DOI: [10.5170/CERN-1983-004.123](https://doi.org/10.5170/CERN-1983-004.123). URL: <https://cds.cern.ch/record/142059> (cit.  
2537 on p. 11).

2539 [73] Christian Wolfgang Fabjan and F. Gianotti. “Calorimetry for Particle  
2540 Physics”. In: *Rev. Mod. Phys.* 75.CERN-EP-2003-075 (Oct. 2003), 1243–1286.  
2541 96 p. DOI: [10.1103/RevModPhys.75.1243](https://doi.org/10.1103/RevModPhys.75.1243). URL: <https://cds.cern.ch/record/692252> (cit. on p. 22).

2543 [74] Saskia Falke. “Measurement of the Higgs boson properties with Run 2 data  
2544 collected by the ATLAS experiment. Mesure des propriétés du boson de  
2545 Higgs avec les données du Run 2 collectées par l’expérience ATLAS”. Pre-  
2546 sented 17 Sep 2019. 2019. URL: <https://cds.cern.ch/record/2691944> (cit. on pp. 44, 45).

2548 [75] J. Feltesse. “Introduction to Parton Distribution Functions”. In: *Scholarpedia*  
2549 5.11 (2010). revision #186761, p. 10160. DOI: [10.4249/scholarpedia.10160](https://doi.org/10.4249/scholarpedia.10160) (cit. on p. 7).

2551 [76] Joel Feltesse. “Introduction to deep inelastic scattering: Past and present”.  
2552 In: *20th International Workshop on Deep-Inelastic Scattering and Related Sub-*  
2553 *jects*. 2012, pp. 3–12. DOI: [10.3204/DESY-PROC-2012-02/6](https://doi.org/10.3204/DESY-PROC-2012-02/6) (cit. on  
2554 p. 7).

2555 [77] “Fits for W mass analysis”. In: () $\sin^2\theta$  and low mu run analyses work-  
2556 shop 2019. URL: [https://indico.cern.ch/event/776453/contributions/3284036/attachments/1792310/2920446/PeregoMarta\\_2019-02-07-workshopOrsay.pdf](https://indico.cern.ch/event/776453/contributions/3284036/attachments/1792310/2920446/PeregoMarta_2019-02-07-workshopOrsay.pdf) (cit. on pp. 131,  
2557 132, 135).

2558

2559

2560 [78] D. Fournier. "Liquid argon calorimetry". In: *ECFA Large Hadron Collider*  
 2561 (*LHC*) *Workshop: Physics and Instrumentation*. Oct. 1990, pp. 356–359 (cit. on  
 2562 p. 22).

2563 [79] Paolo Francavilla. "The ATLAS Tile Hadronic Calorimeter performance at  
 2564 the LHC". In: *Journal of Physics: Conference Series* 404 (Dec. 2012), p. 012007.  
 2565 DOI: [10.1088/1742-6596/404/1/012007](https://doi.org/10.1088/1742-6596/404/1/012007). URL: <https://doi.org/10.1088%2F1742-6596%2F404%2F1%2F012007> (cit. on p. 20).

2567 [80] Juerg Froehlich. "Relativistic Quantum Theory". In: *arXiv e-prints*,  
 2568 arXiv:1912.00726 (Dec. 2019), arXiv:1912.00726. arXiv: [1912 . 00726](https://arxiv.org/abs/1912.00726)  
 2569 [quant-ph] (cit. on p. 2).

2570 [81] Cecilia E. Gerber. *LHC Highlights and Prospects*. Sept. 2019. arXiv: [1909 . 10919](https://arxiv.org/abs/1909.10919) [hep-ex] (cit. on p. 15).

2572 [82] Christophe Goudet. "Etalonnage du calorimètre électromagnétique de  
 2573 l'expérience ATLAS et application à la mesure des couplages du boson de  
 2574 (Brout-Englert-)Higgs dans le canal diphoton dans le cadre du Run 2 du  
 2575 LHC." PhD thesis. Saclay, 2017 (cit. on pp. 23, 37, 39, 44).

2576 [83] "Grand collisionneur électron-positon (LEP)". In: (Jan. 2013). URL: <https://cds.cern.ch/record/1997707> (cit. on pp. 11, 39).

2578 [84] Andrey Grozin. "Quantum Chromodynamics". In: *arXiv e-prints*,  
 2579 arXiv:1205.1815 (May 2012), arXiv:1205.1815. arXiv: [1205 . 1815](https://arxiv.org/abs/1205.1815)  
 2580 [hep-ph] (cit. on p. 4).

2581 [85] Linghua Guo. *Electron energy in-situ calibration and linearity measurements*  
 2582 from  $Z\text{-}gt;ee$  events. Tech. rep. ATL-COM-PHYS-2020-757. Geneva: CERN,  
 2583 Oct. 2020. URL: <https://cds.cern.ch/record/2742791> (cit. on  
 2584 p. 57).

2585 [86] Manuel Guth. "Signal Region Optimisation Studies Based on BDT and  
 2586 Multi-Bin Approaches in the Context of Supersymmetry Searches in  
 2587 Hadronic Final States with the ATLAS Detector". Presented 27 Mar 2018.  
 2588 Mar. 2018. URL: <https://cds.cern.ch/record/2308793> (cit. on  
 2589 p. 25).

2590 [87] H1 and ZEUS collaborations. *Combination and QCD analysis of charm and*  
 2591 *beauty production cross-section measurements in deep inelastic ep scattering at*  
 2592 *HERA*. 2018. arXiv: [1804 . 01019](https://arxiv.org/abs/1804.01019) [hep-ex] (cit. on pp. 94, 121).

2593 [88] A. K. Halder, Andronikos Paliathanasis, and P. G. L. Leach. "Noether's  
 2594 Theorem and Symmetry". In: *arXiv e-prints*, arXiv:1812.03682 (Dec. 2018),  
 2595 arXiv:1812.03682. arXiv: [1812 . 03682](https://arxiv.org/abs/1812.03682) [math-ph] (cit. on p. 4).

2596 [89] Johannes Haller et al. "Update of the global electroweak fit and constraints  
 2597 on two-Higgs-doublet models". In: *Eur. Phys. J. C* 78.8 (2018), p. 675. DOI:  
 2598 [10.1140/epjc/s10052-018-6131-3](https://doi.org/10.1140/epjc/s10052-018-6131-3). arXiv: [1803 . 01853](https://arxiv.org/abs/1803.01853) [hep-ph]  
 2599 (cit. on pp. 5, 10).

2600 [90] P. Hansen. "Results from the UA1 and UA2 Experiments". In: *International*  
 2601 *School of Physics Enrico Fermi: Elementary Particles*. June 1984, pp. 1–18 (cit.  
 2602 on pp. 2, 11).

2603 [91] L. A. Harland-Lang et al. "Parton distributions in the LHC era: MMHT 2014  
2604 PDFs". In: *The European Physical Journal C* 75.5 (May 2015). ISSN: 1434-6052.  
2605 DOI: [10.1140/epjc/s10052-015-3397-6](https://doi.org/10.1140/epjc/s10052-015-3397-6). URL: <http://dx.doi.org/10.1140/epjc/s10052-015-3397-6> (cit. on pp. 94, 121).

2606

2607 [92] B J Holzer. "Introduction to Particle Accelerators and their Limitations". In:  
2608 *arXiv e-prints*, arXiv:1705.09601 (May 2017), arXiv:1705.09601. arXiv: [1705.09601](https://arxiv.org/abs/1705.09601) [physics.acc-ph] (cit. on p. 15).

2609

2610 [93] Tie-Jiun Hou et al. "New CTEQ global analysis of quantum chromodynamics  
2611 with high-precision data from the LHC". In: (Dec. 2019). arXiv: [1912.10053](https://arxiv.org/abs/1912.10053) [hep-ph] (cit. on pp. 94, 121).

2612

2613 [94] Tafoya Juan. "presentation at the egamma calibration meeting". In: (Nov.  
2614 2020). URL: [https://indico.cern.ch/event/973758/contributions/4100232/attachments/2141733/3609191/calibration\\_Egamma.pdf](https://indico.cern.ch/event/973758/contributions/4100232/attachments/2141733/3609191/calibration_Egamma.pdf) (cit. on p. 57).

2615

2616

2617 [95] Jan Kretzschmar. *Samples and Physics modelling for low pile-up runs taken in  
2618 2017 and 2018*. Tech. rep. ATL-COM-PHYS-2019-075. Geneva: CERN, Feb.  
2619 2019. URL: <https://cds.cern.ch/record/2657141> (cit. on pp. 47,  
2620 72, 97).

2621

2622 [96] L.Iconomou-Fayard. "Status of the E1/E2 investigations with electrons".  
In: (cit. on pp. 23, 44).

2623

2624 [97] C de La Taille and L Serin. *Temperature dependance of the ATLAS electromagnetic  
2625 calorimeter signal. Preliminary drift time measurement*. Tech. rep. ATL-  
2626 LARG-95-029. ATL-A-PN-29. Geneva: CERN, Nov. 1995. URL: <https://cds.cern.ch/record/686091> (cit. on pp. 42, 57).

2627

2628 [98] W. Lampl, Christian Fabjan, and M. Alekса. "Optimizing the Energy Mea-  
2629 surement of the ATLAS Electromagnetic Calorimeter". In: (Jan. 2006) (cit.  
on p. 22).

2630

2631 [99] "LAr temperature vs luminosity and impact on energy calibration". In: ().  
2632 URL: <https://indico.cern.ch/event/748648/contributions/3222929/subcontributions/273194/attachments/1785880/2907510/temperature-2017-ws.pdf> (cit. on pp. 43, 56).

2633

2634 [100] B Lenzi and R Turra. *Monte Carlo calibration update for electrons and  
2635 photons using multivariate techniques*. Tech. rep. ATL-COM-PHYS-2013-1426.  
2636 Geneva: CERN, Oct. 2013. URL: <https://cds.cern.ch/record/1609589> (cit. on p. 33).

2637

2638 [101] Mengran Li et al. *Hadronic recoil reconstruction and calibration for low pile-up  
2639 runs taken in 2017 and 2018*. Tech. rep. ATL-COM-PHYS-2019-078. Geneva:  
2640 CERN, Feb. 2019. URL: <https://cds.cern.ch/record/2657182> (cit.  
2641 on pp. 12, 71).

2642

2643 [102] Peilian Liu. "Expected performance of the upgrade ATLAS experi-  
2644 ment for HL-LHC". In: *arXiv e-prints*, arXiv:1809.02181 (Sept. 2018),  
2645 arXiv:1809.02181. arXiv: [1809.02181](https://arxiv.org/abs/1809.02181) [physics.ins-det] (cit. on  
p. 15).

2646 [103] “Low Mu W Z Analyses”. In: (). URL: <https://twiki.cern.ch/twiki/bin/viewauth/AtlasProtected/LowMuWZAnalyses> (cit. on p. 98).

2647

2648

2649 [104] “Luminosity determination for low-pileup datasets at  $\sqrt{s} = 5$  and 13 TeV using the ATLAS detector at the LHC”. In: (July 2020) (cit. on p. 81).

2650

2651 [105] *Luminosity determination in pp collisions at  $\sqrt{s} = 13$  TeV using the ATLAS detector at the LHC*. Tech. rep. ATLAS-CONF-2019-021. Geneva: CERN, June 2019. URL: <https://cds.cern.ch/record/2677054> (cit. on p. 16).

2652

2653

2654 [106] “Luminosity determination in pp collisions at  $\sqrt{s} = 7$  TeV using the ATLAS detector at the LHC”. In: *European Physical Journal C* 71, 1630 (Apr. 2011), p. 1630. DOI: [10.1140/epjc/s10052-011-1630-5](https://doi.org/10.1140/epjc/s10052-011-1630-5). arXiv: [1101.2185 \[hep-ex\]](https://arxiv.org/abs/1101.2185) (cit. on p. 17).

2655

2656

2657

2658 [107] Melina Luthi. “Multivariate analysis techniques for Particle Flow-based neutral pileup suppression at the ATLAS experiment”. In: (Jan. 2019). URL: <https://cds.cern.ch/record/2655145> (cit. on p. 33).

2659

2660

2661 [108] Simon Lyddon, Chris Holmes, and Stephen Walker. “General Bayesian Updating and the Loss-Likelihood Bootstrap”. In: *arXiv e-prints*, arXiv:1709.07616 (Sept. 2017), arXiv:1709.07616. arXiv: [1709.07616 \[stat.ME\]](https://arxiv.org/abs/1709.07616) (cit. on p. 39).

2662

2663

2664

2665 [109] Louis Lyons, Duncan Gibaut, and Peter Clifford. “How to Combine Correlated Estimates of a Single Physical Quantity”. In: *Nucl. Instrum. Meth. A* 270 (1988), p. 110. DOI: [10.1016/0168-9002\(88\)90018-6](https://doi.org/10.1016/0168-9002(88)90018-6) (cit. on p. 135).

2666

2667

2668

2669 [110] Bogdan Malaescu. *Discussions on unfolding problems, methods and solutions*. Tech. rep. 2016. URL: [http://dpnc.unige.ch/~sfyrla/teaching/Statistics/lectures/Unfolding\\_Lecture\\_UGE\\_Malaescu.pdf](http://dpnc.unige.ch/~sfyrla/teaching/Statistics/lectures/Unfolding_Lecture_UGE_Malaescu.pdf) (cit. on p. 69).

2670

2671

2672

2673 [111] Bogdan Malaescu. *Standard Model Unfolding twiki-page*. Tech. rep. 2016. URL: <https://twiki.cern.ch/twiki/bin/viewauth/AtlasProtected/StandardModelUnfoldingNew> (cit. on pp. 66, 103).

2674

2675

2676 [112] Martina Malberti. “Prospects for the precision determination of the W boson mass with the CMS detector at the LHC”. PhD thesis. Milan Bicocca U., 2007 (cit. on p. 132).

2677

2678

2679 [113] Neil Fraser Mcblane. “Energy Dependence of the Intermodule Widening Correction”. In: (Aug. 2017). URL: <https://cds.cern.ch/record/2281006> (cit. on p. 34).

2680

2681

2682 [114] *Measurement of the  $p_T$  spectrum of W- and Z-bosons produced in pp collisions at  $\sqrt{s} = 5$  TeV and 13 TeV in low-pileup runs*. Tech. rep. ATL-COM-PHYS-2018-1084. Geneva: CERN, July 2018. URL: <https://cds.cern.ch/record/2632159> (cit. on pp. 72, 83, 84).

2683

2684

2685

2686 [115] “Measurement of the W-boson mass in pp collisions at  $\sqrt{s} = 7$  TeV with the ATLAS detector”. In: *Eur. Phys. J. C* 78.2, 110 (Feb. 2018), p. 110. DOI: [10.1140/epjc/s10052-017-5475-4](https://doi.org/10.1140/epjc/s10052-017-5475-4). arXiv: [1701.07240 \[hep-ex\]](https://arxiv.org/abs/1701.07240) (cit. on pp. 11, 12, 13, 46, 57, 71, 97, 133, 134, 135).

2687

2688

2689

2690 [116] "Measurement of the response of the ATLAS liquid argon barrel calorimeter to electrons at the 2004 combined test-beam". In: *Nucl. Instrum. Methods Phys. Res., A* 614 (2010), 400–432. 33 p. DOI: [10.1016/j.nima.2009.12.055](https://doi.org/10.1016/j.nima.2009.12.055). URL: <https://cds.cern.ch/record/1273537> (cit. on p. 28).

2691

2692

2693

2694 [117] "Measurement of  $W^\pm$  and Z-boson production cross sections in pp collisions at  $\sqrt{s} = 13$  TeV with the ATLAS detector". In: *Physics Letters B* 759 (Aug. 2016), pp. 601–621. DOI: [10.1016/j.physletb.2016.06.023](https://doi.org/10.1016/j.physletb.2016.06.023). arXiv: [1603.09222 \[hep-ex\]](https://arxiv.org/abs/1603.09222) (cit. on p. 92).

2695

2696

2697

2698 [118] Krzysztof A. Meissner and Hermann Nicolai. "Standard Model Fermions and Infinite-Dimensional R Symmetries". In: 121.9, 091601 (Aug. 2018), p. 091601. DOI: [10.1103/PhysRevLett.121.091601](https://doi.org/10.1103/PhysRevLett.121.091601). arXiv: [1804.09606 \[hep-th\]](https://arxiv.org/abs/1804.09606) (cit. on p. 1).

2699

2700

2701

2702 [119] Esma Mobs. "The CERN accelerator complex - 2019. Complexe des accélérateurs du CERN - 2019". In: (July 2019). General Photo. URL: <https://cds.cern.ch/record/2684277> (cit. on p. 16).

2703

2704

2705 [120] J.W. Monk and C. Oropesa-Barrera. "The HBOM method for unfolding detector effects". In: *Nuclear Instruments and Methods in Physics Research Section A: Accelerators, Spectrometers, Detectors and Associated Equipment* 701 (Feb. 2013), pp. 17–24. ISSN: 0168-9002. DOI: [10.1016/j.nima.2012.09.045](https://doi.org/10.1016/j.nima.2012.09.045). URL: <http://dx.doi.org/10.1016/j.nima.2012.09.045> (cit. on p. 59).

2706

2707

2708

2709

2710

2711 [121] N. Andari. "presentation at the ATLAS W precision analyses informal meeting 27Th October 2020". In: (Sept. 2020). URL: [https://indico.cern.ch/event/969042/contributions/4078527/attachments/2130404/3587822/presentation\\_271020\\_andari.pdf](https://indico.cern.ch/event/969042/contributions/4078527/attachments/2130404/3587822/presentation_271020_andari.pdf) (cit. on p. 43).

2712

2713

2714

2715

2716 [122] Jason Nielsen. "Fundamentals of LHC Experiments". In: *String Theory and its Applications - TASI 2010, From meV to the Planck Scale*. Ed. by Michael Dine, Thomas Banks, and Subir Sachdev. Nov. 2012, pp. 127–152. DOI: [10.1142/9789814350525\\_0003](https://doi.org/10.1142/9789814350525_0003). arXiv: [1106.2516 \[hep-ex\]](https://arxiv.org/abs/1106.2516) (cit. on p. 15).

2717

2718

2719

2720

2721 [123] Nikiforos Nikiforou. *Performance of the ATLAS Liquid Argon Calorimeter after three years of LHC operation and plans for a future upgrade*. Tech. rep. arXiv:1306.6756. June 2013. DOI: [10.1109/ANIMMA.2013.6728060](https://doi.org/10.1109/ANIMMA.2013.6728060). URL: [http://cds.cern.ch/record/1558820](https://cds.cern.ch/record/1558820) (cit. on p. 23).

2722

2723

2724

2725 [124] Tadej Novak. "ATLAS Pile-up and Overlay Simulation". In: (June 2017). URL: <https://cds.cern.ch/record/2270396> (cit. on p. 17).

2726

2727 [125] J. Nowell. "A Measurement of the W Boson Mass with the ALEPH Detector". Presented on Nov 2000. 2000. URL: <https://cds.cern.ch/record/537297> (cit. on p. 11).

2728

2729

2730 [126] “Observation of a new boson at a mass of 125 GeV with the CMS experiment at the LHC”. In: *Physics Letters B* 716.1 (2012), pp. 30–61. ISSN: 0370-2731 2693. DOI: <https://doi.org/10.1016/j.physletb.2012.08.021>. URL: <http://www.sciencedirect.com/science/article/pii/S0370269312008581> (cit. on p. 2).

2735 [127] D Oliveira Damazio. *Signal Processing for the ATLAS Liquid Argon Calorimeter : studies and implementation*. Tech. rep. ATL-LARG-PROC-2013-015. 2736 Geneva: CERN, Nov. 2013. URL: <https://cds.cern.ch/record/1630826> (cit. on p. 28).

2739 [128] ATLAS Outreach. “ATLAS Fact Sheet : To raise awareness of the ATLAS 2740 detector and collaboration on the LHC”. 2010. URL: <https://cds.cern.ch/record/1457044> (cit. on pp. 19, 26).

2742 [129] “Performance of the ATLAS Transition Radiation Tracker in Run 1 of the 2743 LHC: tracker properties”. In: *Journal of Instrumentation* 12.5 (May 2017), 2744 P05002. DOI: [10.1088/1748-0221/12/05/P05002](https://doi.org/10.1088/1748-0221/12/05/P05002). arXiv: [1702.06473 \[hep-ex\]](https://arxiv.org/abs/1702.06473) (cit. on p. 19).

2746 [130] Antonio Pich. “The Standard Model of Electroweak Interactions; rev. 2747 version”. In: hep-ph/0502010. FTUV-2005-0201. IFIC-2005-13 (Feb. 2005), 48 p. 2748 DOI: [10.5170/CERN-2006-003.1](https://doi.org/10.5170/CERN-2006-003.1). URL: <https://cds.cern.ch/record/819632> (cit. on p. 3).

2750 [131] “presnetation at the egamma calibration meeting”. In: (July 2019). URL: 2751 [https://indico.cern.ch/event/827055/contributions/3506176/attachments/1885454/3110615/Slide\\_ES.pdf](https://indico.cern.ch/event/827055/contributions/3506176/attachments/1885454/3110615/Slide_ES.pdf) (cit. on 2753 pp. 43, 57).

2754 [132] *Prospects for the measurement of the W-boson transverse momentum with a low 2755 pileup data sample at  $\sqrt{s} = 13$  TeV with the ATLAS detector*. Tech. rep. ATL- 2756 PHYS-PUB-2017-021. Geneva: CERN, Dec. 2017. URL: <https://cds.cern.ch/record/2298152> (cit. on pp. 6, 71, 72).

2758 [133] Chris Quigg. “The Electroweak Theory”. In: *arXiv e-prints*, hep-ph/0204104 2759 (Apr. 2002), hep-ph/0204104. arXiv: [hep-ph/0204104 \[hep-ph\]](https://arxiv.org/abs/hep-ph/0204104) (cit. on 2760 p. 5).

2761 [134] Giulia Ripellino. *The alignment of the ATLAS Inner Detector in Run 2*. Tech. 2762 rep. ATL-INDET-PROC-2016-003. Geneva: CERN, Sept. 2016. DOI: [10.22323/1.276.0196](https://doi.org/10.22323/1.276.0196). URL: <https://cds.cern.ch/record/2213441> (cit. on p. 20).

2765 [135] Valerio Rossetti. “Performance of the ATLAS Calorimeters and Commis- 2766 sioning for LHC Run-2”. In: (July 2015). URL: <https://cds.cern.ch/record/2037117> (cit. on p. 25).

2768 [136] Aranzazu Ruiz-Martinez and ATLAS Collaboration. *The Run-2 ATLAS Trig- 2769 ger System*. Tech. rep. ATL-DAQ-PROC-2016-003. Geneva: CERN, Feb. 2016. 2770 DOI: [10.1088/1742-6596/762/1/012003](https://doi.org/10.1088/1742-6596/762/1/012003). URL: <https://cds.cern.ch/record/2133909> (cit. on pp. 26, 27).

2772 [137] S. Schael et al. "Electroweak Measurements in Electron-Positron Collisions  
2773 at W-Boson-Pair Energies at LEP". In: *Phys. Rept.* 532 (2013), pp. 119–  
2774 244. DOI: [10.1016/j.physrep.2013.07.004](https://doi.org/10.1016/j.physrep.2013.07.004). arXiv: [1302.3415](https://arxiv.org/abs/1302.3415)  
2775 [hep-ex] (cit. on p. 11).

2776 [138] Christoph Schäfer. "The  $Z$  lineshape at LEP". In: *Nuclear Physics B - Proceedings Supplements* 65.1 (1998). The Irresistable Rise of the Standard Model, pp. 93–97. ISSN: 0920-5632. DOI: [https://doi.org/10.1016/S0920-5632\(97\)00982-1](https://doi.org/10.1016/S0920-5632(97)00982-1). URL: <http://www.sciencedirect.com/science/article/pii/S0920563297009821> (cit. on p. 10).

2781 [139] Stefan Schmitt. "Data Unfolding Methods in High Energy Physics". In: *EPJ Web of Conferences* 137 (2017). Ed. by Y. Foka, N. Brambilla, and V. Editors Kovalenko, p. 11008. ISSN: 2100-014X. DOI: [10.1051/epjconf/201713711008](https://doi.org/10.1051/epjconf/201713711008). URL: <http://dx.doi.org/10.1051/epjconf/201713711008> (cit. on pp. 59, 62).

2786 [140] Matthias Schott et al. *Measurement of  $m_W$  at 7 TeV: Reconstruction of the hadronic recoil*. Tech. rep. ATL-COM-PHYS-2014-1435. Geneva: CERN, Nov. 2014. URL: <https://cds.cern.ch/record/1966964> (cit. on p. 11).

2789 [141] Estelle Scifo. "Measurement of the Brout-Englert-Higgs boson couplings in its diphoton decay channel with the ATLAS detector at the LHC". PhD thesis. Orsay, LAL, July 2014 (cit. on pp. 9, 23).

2792 [142] Steffen Starz. "ATLAS Calorimeter system: Run-2 performance, Phase-1 and Phase-2 upgrades". In: (July 2018). URL: <https://cds.cern.ch/record/2628123> (cit. on p. 21).

2795 [143] John Strologas and Steven Errede. "Study of the angular coefficients and corresponding helicity cross sections of the  $W$  boson in hadron collisions". In: 73.5, 052001 (Mar. 2006), p. 052001. DOI: [10.1103/PhysRevD.73.052001](https://doi.org/10.1103/PhysRevD.73.052001). arXiv: [hep-ph/0503291](https://arxiv.org/abs/hep-ph/0503291) [hep-ph] (cit. on p. 12).

2799 [144] Robin G. Stuart. "An Improved Determination of the Fermi Coupling Constant,  $G_F$ ". In: *arXiv e-prints*, hep-ph/9902257 (Feb. 1999), hep-ph/9902257. arXiv: [hep-ph/9902257](https://arxiv.org/abs/hep-ph/9902257) [hep-ph] (cit. on p. 10).

2802 [145] "Summary Report of Physics Beyond Colliders at CERN". In: *arXiv e-prints*, arXiv:1902.00260 (Feb. 2019), arXiv:1902.00260. arXiv: [1902.00260](https://arxiv.org/abs/1902.00260) [hep-ex] (cit. on p. 15).

2805 [146] M. Tanabashi et al. "Review of Particle Physics". In: *Phys. Rev. D* 98.3 (2018), p. 030001. DOI: [10.1103/PhysRevD.98.030001](https://doi.org/10.1103/PhysRevD.98.030001) (cit. on p. 10).

2807 [147] The ATLAS Collaboration. "Operation and performance of the ATLAS  
2808 semiconductor tracker". In: *Journal of Instrumentation* 9.8, P08009 (Aug.  
2809 2014), P08009. DOI: [10.1088/1748-0221/9/08/P08009](https://doi.org/10.1088/1748-0221/9/08/P08009). arXiv: [1404.7473](https://arxiv.org/abs/1404.7473) [hep-ex] (cit. on p. 19).

2811 [148] "The ATLAS Experiment at the CERN Large Hadron Collider". In: *JINST* 3  
2812 (2008). Also published by CERN Geneva in 2010, S08003. 437 p. DOI: [10.1088/1748-0221/3/08/S08003](https://doi.org/10.1088/1748-0221/3/08/S08003). URL: <https://cds.cern.ch/record/1129811> (cit. on p. 6).

2815 [149] “The ATLAS Inner Detector commissioning and calibration”. In: *European*  
2816 *Physical Journal C* 70.3 (Dec. 2010), pp. 787–821. DOI: [10.1140/epjc/s10052-010-1366-7](https://doi.org/10.1140/epjc/s10052-010-1366-7). arXiv: [1004.5293 \[physics.ins-det\]](https://arxiv.org/abs/1004.5293) (cit. on  
2817 p. 19).

2819 [150] “The ATLAS silicon pixel sensors”. In: *Nuclear Instruments and Methods in*  
2820 *Physics Research Section A: Accelerators, Spectrometers, Detectors and Associated*  
2821 *Equipment* 456.3 (2001), pp. 217–232. ISSN: 0168-9002. DOI: [https://doi.org/10.1016/S0168-9002\(00\)00574-X](https://doi.org/10.1016/S0168-9002(00)00574-X). URL:  
2822 [http://www.sciencedirect.com/science/article/pii/S016890020000574X](https://www.sciencedirect.com/science/article/pii/S016890020000574X) (cit. on p. 19).

2825 [151] Ruggero Turra, Stefano Manzoni, and Archil Durglishvili. *Monte Carlo energy*  
2826 *calibration of electrons and photons for release 20.7*. Tech. rep. ATL-COM-  
2827 PHYS-2017-761. Geneva: CERN, June 2017. URL: <https://cds.cern.ch/record/2268813> (cit. on p. 33).

2829 [152] Nenad Vranjes, Troels Petersen, and Mikhail Karnevskiy. *Measurement of*  
2830  *$m_W$  at 7 TeV: Muon momentum corrections and uncertainties*. Tech. rep. ATL-  
2831 COM-PHYS-2014-1433. Geneva: CERN, Nov. 2014. URL: <https://cds.cern.ch/record/1966962> (cit. on pp. 11, 138).

2833 [153] Jorg Wenninger. “Operation and Configuration of the LHC in Run 2”. In:  
2834 (Mar. 2019). URL: <https://cds.cern.ch/record/2668326> (cit. on  
2835 p. 43).

2836 [154] Scott Willenbrock. “Hadron Colliders, the Standard Model, and Beyond”. In:  
2837 *arXiv e-prints*, hep-ph/0212032 (Dec. 2002), hep-ph/0212032. arXiv:  
2838 [hep-ph/0212032 \[hep-ph\]](https://arxiv.org/abs/hep-ph/0212032) (cit. on p. 1).

2839 [155] Tairan Xu. “Measurements of W boson properties at  $\sqrt{s} = 5$  and 13 TeV  
2840 with the ATLAS detector at the LHC”. Presented 25 Sep 2019. 2019. URL:  
2841 <https://cds.cern.ch/record/2689846> (cit. on pp. 12, 71, 81, 99,  
2842 138, 139).

2843 [156] Tairan Xu, Hicham Atmani, and Ludovica Aperio Bella. *Electron corrections*  
2844 *for low pile-up runs taken in 2017 and 2018*. Tech. rep. ATL-COM-PHYS-2019-  
2845 077. Geneva: CERN, Feb. 2019. URL: <https://cds.cern.ch/record/2657152> (cit. on p. 39).

2847 [157] Tairan Xu and Maarten Boonekamp. *Multi-jet background in low-pile-up*  
2848 *runs taken in 2017 and 2018*. Tech. rep. ATL-COM-PHYS-2019-076. Geneva:  
2849 CERN, July 2019. URL: <https://cds.cern.ch/record/2657146> (cit.  
2850 on p. 12).

2851 [158] Christoph Zimmermann, Matthias Schott, and Mikhail Karnevskiy. *Measurement*  
2852 *of  $m_W$  at 7 TeV : Muon efficiency corrections and uncertainties*. Tech.  
2853 rep. ATL-COM-PHYS-2015-073. Geneva: CERN, Feb. 2015. URL: <https://cds.cern.ch/record/1987497> (cit. on p. 11).